



## Aspects of characterization methods and product development within applied photovoltaics

Thorsteinsson, Sune

*Publication date:*  
2021

*Document Version*  
Publisher's PDF, also known as Version of record

[Link back to DTU Orbit](#)

*Citation (APA):*  
Thorsteinsson, S. (2021). *Aspects of characterization methods and product development within applied photovoltaics*. Technical University of Denmark.

---

### General rights

Copyright and moral rights for the publications made accessible in the public portal are retained by the authors and/or other copyright owners and it is a condition of accessing publications that users recognise and abide by the legal requirements associated with these rights.

- Users may download and print one copy of any publication from the public portal for the purpose of private study or research.
- You may not further distribute the material or use it for any profit-making activity or commercial gain
- You may freely distribute the URL identifying the publication in the public portal

If you believe that this document breaches copyright please contact us providing details, and we will remove access to the work immediately and investigate your claim.

# Aspects of characterization methods and product development within applied photovoltaics.



PhD Thesis by: Sune Thorsteinsson, February 2021.

Supervisor/Mentor: Jørgen Schou, Senior Scientist at the Photovoltaic Materials and Systems group

## Preface

This thesis is created in order to fulfil the requirements for a Doctor of Philosophy (PhD) degree at the Technical University of Denmark (DTU) according to a special clause (the Danish Ph.d.- act §15 clause 2) where a candidate can deliver a PhD thesis without previous PhD education.

I have been working with research, demonstration and development projects within applied photovoltaics at DTU Fotonik since 2012, and since 2019 been heavily involved in teaching within Photovoltaics where I have developed a studyline within solar energy, and further been a leading part of developing 4 new courses within solar energy.

The scientific work presented in this thesis, represents the work in which I have been involved the recent years during my job at DTU Fotonik.

The work was financed by several EUDP, Elforsk and Innovation fund projects and listing them all would be quite extensive.

Jørgen Schou, Senior Scientist at the Photovoltaic Materials and Systems group at DTU supervised the process of making this thesis.

Bagsværd, Denmark  
February, 2021  
Sune Thorsteinsson

## Acknowledgements

I am grateful to have the opportunity to hand in a PhD thesis under these circumstances. During the past years my involvement in the lab has been limited and my focus has been to secure funding for our activities within applied photovoltaics together with especially my colleague Peter Poulsen, and the establishment of the studyline within Solar Energy combined with development of the new courses which have taken a lot of my time.

Therefore being able to submit this thesis would not have been possible without my colleagues. So I would like to thank Gisele, Adrian, Nicholas for their great effort in making great research within our field, and Peter Poulsen for keeping a great overview within these many diverse projects. In addition I would like to thank all the authors and co-authors for the contributions with their great work.

I am also very grateful to Jørgen Schou, who has been a great support and done great supervision in the process of writing this thesis.

Also I would like to thank Lars Ulrik Aen Andersen, Stela Canulescu, Peter Poulsen and the rest of the organization to be supportive during this process and encourage me to finish.

## List of abbreviations

**AOI:** Angle of incidence

**BIPV:** Building Integrated Photovoltaics

**CCD:** Charge Coupled Device

**CdTe:** Cadmium Telluride

**CI(G)S:** Copper Indium (Gallium) Selenide

**CIE:** International Commission on Illumination

**DHI:** Diffuse Horizontal Irradiance

**DNI:** Direct Normal Irradiance

**EL:** Electroluminescence

**EQE:** External Quantum Efficiency

**GHI:** Global Horizontal Irradiance

**IAM:** Incidence Angle Modifier

**InGaAs:** Indium Gallium Arsenide

**ISC:** Short Circuit Current

**IQE:** Internal Quantum Efficiency

**LCOE:** Levelized Cost of Energy

**L2L:** Light to Light system

**MPP:** Maximum Power Point

**O&M:** Operation and Maintenance

**OPEX:** Operating Expenditures

**OLED:** Organic Light Emitting Diode

**PID:** Potential Induced Degradation

**PIPV:** Product Integrated Photovoltaics

**PL:** Photoluminescence

**PV:** Photovoltaic

**SNR:** Signal to Noise Ratio

**SOC:** State of Charge

**TMY:** Typical Meteorological Year

**VOC:** Open Circuit Voltage

## Contents

Preface .....	2
Acknowledgements.....	3
List of abbreviations.....	4
Abstract.....	6
Dansk sammenfatning .....	7
List of Contributions.....	8
First Author .....	8
Co author .....	8
Introduction .....	10
Fault detection in the field.....	13
Introduction .....	13
Electrochemical Impedance Spectroscopy .....	13
Outdoor Electro luminescence .....	17
Part conclusion.....	20
Optical characterization and development for PV applications .....	20
Introduction .....	20
Optical Characterization .....	21
Reflector systems.....	26
Part Conclusion .....	28
Development and Characterization of product integrated photovoltaic systems .....	28
Introduction .....	28
Product integrated photovoltaic development and characterization.....	29
Part Conclusion .....	33
Conclusion.....	34
Bibliography .....	35
Total list of publications.....	39
Journal articles .....	39
Conference proceedings: .....	39
Contributions .....	45

## Abstract

Photovoltaic energy has within the last decade transformed itself from being a small niche to be a significant energy source and has during the same time, undergone huge capacity expansions. In the future photovoltaic energy is predicted to be the main driver in the expansion of renewable energy. This development is facilitated by large cost reductions, however to achieve a low price of energy additional measures including low operating costs as well as confidence by the financial stakeholders are required. The operating costs can be reduced by automatic fault finding methods where the labor effort is greatly reduced, and the confidence from financial stakeholders is increased via accurate performance estimates backed up by lab measurement.

In addition, building integrated photovoltaics offers great advantages contributing to the energy transformation in the build environment such as cost efficiency, production at the place of consumption but are also subjected to physical and aesthetical constraints.

Solar powered products that uses a battery and a solar panel can be developed to be aesthetically pleasing, and if right engineered, provide reliable functionality and at the same time provide huge savings on cabling especially in the urban environment.

This thesis presents result on work within two methods for automatic fault detection. Impedance spectroscopy is used to find early traces of degradation and it is shown that impedance spectroscopy can be used to identify micro cracks and potential induced degradation on crystalline PV modules.

Methods for acquiring daylight electroluminescent images from a drone are also presented, where it is shown that biasing a string with a waveform a luminescent signal can be achieved by subtracting images without bias from images under bias. This technique allows, together with the use of optical bandpass filters, to filter the ambient light. Images of sufficient quality can be acquired, and hereby proof of concept for outdoors electroluminescent imaging is presented.

Further, this thesis presents results from an optical characterization setup which is developed for characterizing the relative transmission loss as a function of incident angle, and the measurement system is validated via a round robin measurement campaign. These results can be used to increase confidence to the performance models used as input for the financial calculations. Further work on optimizing appearance for building integrated modules are presented where an inorganic coating is used to blacken the ribbons. The optical measurement setup is expanded to conduct single plane reflection measurements, where the results can be used for color assessment of photovoltaic devices as well as glare assessment. These measurements are highly relevant in the assessment of BIPV and provides documentation towards aesthetical constraints.

The optical work is concluded by demonstrating a reflector system for solar powered sensor masts, where a prototype is modelled, developed and tested.

The thesis concludes by presenting the development of a laboratory and products for product integrated photovoltaics focused on lighting product for the high end market segments. Here results on characterization of subcomponents as well as performance models for products and examples product developments are presented. This effort has created one new company and increased the sales for other involved companies. All in all the work within this thesis covers many aspects of applied photovoltaics, and progress within all the presented fields is demonstrated.

## Dansk sammenfatning

Fotovoltaisk energi er i løbet af de sidste 10 år gået fra at være en mindre niche i energimarkedet til at være en væsentlig energikilde, og antallet af anlæg er blevet væsentligt forøget. Fotovoltaisk energi er forudset til at blive den væsentligste drivkraft bag udbygning af vedvarende energi og denne udvikling er båret af store prisreduktioner. For at opnå lav energipris kræves også lave drifts omkostninger samt tillid fra finansielle institutioner. Driftsomkostningerne kan reduceres ved udvikling af automatiske fejlfindings metoder, der i stort omfang reducerer den nødvendige arbejdskraft, og tillid fra finansielle institutioner kan øges ved hjælp af nøjagtige ydelsesmodeller der tager udgangspunkt i laboratoriemålinger.

Bygningsintegrerede solceller kan udgøre et stort bidrag til den grønne omstilling i byggeriet, hvor der kan drages fordel af omkostningseffektivitet samt produktion af elektricitet på forbrugsstedet, men produkterne er underlagt fysiske og æstetiske krav.

Soldrevne produkter, der benytter et batteri og et solpanel, kan blive udviklet med høj æstetik og kan, hvis det er rigtig dimensioneret, yde pålidelig drift og på samme tid give store besparelser på kabling især i bymiljøet.

Denne afhandling præsenterer resultater baseret på arbejde med to metoder for automatisk fejl detektering. Impedans spektroskopi er benyttet til at finde tidlige signaler for nedbrydning i paneler og det er vist at impedans spektroskopi kan benyttes til at identificerer mikrorevner og spændings induceret nedbrydning på krystallinske solcellemoduler.

Metoder til at optage billeder fra elektroluminescens i dagslys fra en drone er også præsenteret, hvor det er vist, at dagslyset kan blive filtreret væk ved at forsyne solcellestrengen med en pulserede strøm hvorved baggrunds billeder taget uden strøm bliver subtraheret fra billeder taget med en påtrykket strøm i panelet. Herved opnås tilstrækkelig billede kvalitet, når der også anvendes et båndpas filter.

Afhandlingen præsenterer også resultater fra en optisk måleopstilling udviklet til at måle det normaliserede transmissions tab som funktion af vinkel og målesystemet er valideret i en "round robin" målekampagne. Resultaterne kan benyttes til at øge tiltroen til ydelsesmodellerne, der bruges som input til de finansielle beregninger. Optimering af det visuelle indtryk fra bygningsintegrerede moduler er præsenteret, hvor en uorganisk belægning er benyttet til at sortfarve lodde-tabene, og den optiske måleopstilling er udvidet til også at kunne måle refleksion i ét plan. Disse målinger kan benyttes til farvegengivelsesmålinger og målinger af genskin. Målingerne er meget relevante i forhold til vurdering og tilvejebringelse af dokumentation vedr. æstetiske krav for opsætning af solcellepanelerne på bygninger.

Det optiske arbejde er afsluttet med at demonstrere et reflektor system for soldrevne sensormaster, hvor en prototype er modelleret, udviklet og testet.

Afhandlingen afsluttes med en præsentation af udviklingen af et laboratorium og produkter for såkaldte produkt-integrerede solcelle systemer med fokus på belysningsystemer til det eksklusive marked. Resultater for karakterisering af delkomponenter samt ydelsesmodeller for produkter og eksempler på produktudvikling er præsenteret. Denne indsats har øget omsætningen hos de involverede virksomheder og skabt et nyt firma.

Denne afhandling præsenterer mange aspekter inden for anvendt solcelleteknologi og der er demonstreret fremskridt inden for alle de præsenterede felter.

## List of Contributions

### First Author

- S. Thorsteinsson *et al.*, “Novel field test design for acquisition of DC and AC parameters during service,” *Conf. Rec. IEEE Photovolt. Spec. Conf.*, vol. 2016-Novem, pp. 1608–1610, 2016, doi: 10.1109/PVSC.2016.7749892.
- S. Thorsteinsson *et al.*, “PV LED ENGINE CHARACTERIZATION LAB FOR STANDALONE LIGHT TO LIGHT SYSTEMS,” in *29th European Photovoltaic Solar Energy Conference and Exhibition PV*, 2014, pp. 3059–3061.

### Co author

- M. I. Oprea *et al.*, “Impedance Characterization of PV Modules in Outdoor Conditions,” *32nd Eur. Photovolt. Sol. Energy Conf. Exhib.*, no. 64014, pp. 1849–1853, 2016.
- M. I. Oprea *et al.*, “Detection of potential induced degradation in c-Si PV panels using electrical impedance spectroscopy,” in *Conference Record of the IEEE Photovoltaic Specialists Conference*, 2016, vol. 2016-Novem, doi: 10.1109/PVSC.2016.7749885.
- J. Symonowicz, N. Riedel, S. Thorsteins S. Thorsteinsson *et al.*, “New Method of Silicon Photovoltaic Panel Fault Detection Using Impedance Spectroscopy,” *33rd Eur. Photovolt. Sol. Energy Conf. Exhib.*, pp. 1831–1835, 1831.
- G. A. D. R. Benatto *et al.*, “Development of outdoor luminescence imaging for drone-based PV array inspection,” in *Proceedings of the 44th IEEE Photovoltaic Specialists Conference, PVSC 2017*, 2017, pp. 2682–2687, doi: 10.1109/PVSC.2017.8366602.
- G. Alves dos Reis Benatto *et al.*, “Luminescence Imaging Strategies for Drone-Based PV Array Inspection,” *33rd Eur. Photovolt. Sol. Energy Conf. Exhib.*, pp. 2016–2020, 2017.
- G. A. Dos Reis Benatto *et al.*, “Outdoor Electroluminescence Acquisition Using a Movable Testbed,” in *2018 IEEE 7th World Conference on Photovoltaic Energy Conversion, WCPEC 2018 - A Joint Conference of 45th IEEE PVSC, 28th PVSEC and 34th EU PVSEC*, 2018, doi: 10.1109/PVSC.2018.8547628.
- G. Alves Dos Reis Benatto *et al.*, “Drone-Based Daylight Electroluminescence Imaging of PV Modules,” *IEEE J. Photovoltaics*, vol. 10, no. 3, pp. 872–877, 2020, doi: 10.1109/JPHOTOV.2020.2978068.
- R. S. Davidsen *et al.*, “BLACK SILICON SOLAR CELLS WITH BLACK RIBBONS,” in *32nd European Photovoltaic Solar Energy Conference and Exhibition*, 2016, pp. 631–634.
- M. Amdemeskel *et al.*, “Indoor Measurement of Angle Resolved Light Absorption by Antireflective Glass in Solar Panels,” *33rd Eur. Photovolt. Sol. Energy Conf. Exhib.*, pp. 1723–1726, 2017, doi: 10.4229/EUPVSEC20172017-5BV.4.78.
- M. W. Amdemeskel *et al.*, “Indoor Measurement of Angle Resolved Light Absorption by Black Silicon,” no. i, pp. 2672–2676, 2018, doi: 10.1109/pvsc.2017.8366366.
- N. Riedel-Lyngskær *et al.*, “Interlaboratory comparison of methodologies for measuring the angle of incidence dependence of solar cells,” *35th Eur. Photovolt. Sol. Energy Conf. Exhib.*, no. i, pp. 1034–1039, 2018, doi: 10.4229/35thEUPVSEC20182018-5BO.10.4.
- M. Babin, A. Thorseth, A. A. S. Lancia, and S. Thorsteinsson, “CHARACTERISATION OF ANGULAR DEPENDENT OPTICAL PROPERTIES OF DIFFERENT COLORING TECHNOLOGIES EMPLOYED IN BIPV PRODUCTS,” in *36th European Photovoltaic Solar Energy Conference and Exhibition*, 2020, pp. 1136–1142.
- M. L. Jakobsen, S. Thorsteinsson, P. B. Poulsen, P. M. Rodder, and K. Rodder, “Vertical reflector for bifacial PV-panels,” *2016 IEEE 44th Photovolt. Spec. Conf. PVSC 2016*, pp. 1–4, 2016, doi: 10.1109/PVSC.2017.8366625.
- M. L. Jakobsen, S. Thorsteinsson, P. B. Poulsen, P. M. Rødder, and K. Rødder, “RAY TRACING MODELLING OF REFLECTOR FOR VERTICAL BIFACIAL PANEL,” in *32nd European Photovoltaic Solar Energy Conference and Exhibition*, 2016, pp. 1418–1420.

- M. L. Jakobsen, S. Thorsteinsson, P. B. Poulsen, N. Riedel, P. M. Rødder, and K. Rødder, "Bifacial PV cell with reflector for stand-alone mast for sensor powering purposes," in *AIP Conference Proceedings*, 2017, vol. 1881, doi: 10.1063/1.5001437.
- R. O. Ploug *et al.*, "DESIGNING HIGH EFFICIENT SOLAR POWERED OLED LIGHTING SYSTEMS," in *32nd European Photovoltaic Solar Energy Conference and Exhibition*, 2016, pp. 2523–2527.
- P. Nymann *et al.*, "DESIGN, CHARACTERIZATION AND MODELLING OF HIGH EFFICIENT SOLAR POWERED LIGHTING SYSTEMS," in *32nd European Photovoltaic Solar Energy Conference and Exhibition*, 2016, pp. 2832–2836.
- P. B. Poulsen *et al.*, "Designing high efficient solar powered lighting systems," in *Conference Record of the IEEE Photovoltaic Specialists Conference*, 2016, vol. 2016-Novem, doi: 10.1109/PVSC.2016.7750143.
- P. B. Poulsen *et al.*, "Sun Hub – Energy Hub for Outdoor Tables," *33rd Eur. Photovolt. Sol. Energy Conf. Exhib.*, pp. 2771–2774, 2017, doi: 10.4229/EUPVSEC20172017-6BV.3.105.
- A. Adrian Santamaria Lancia, N. Riedel, R. O. Ploug, S. Thorsteinsson, P. B. Poulsen, and A. Gisele Dos Reis Benatto, "Synchronization of Solar Stand-alone Devices and Autonomous Energy Management through Solar Time Measurements," in *2018 IEEE 7th World Conference on Photovoltaic Energy Conversion, WCPEC 2018 - A Joint Conference of 45th IEEE PVSC, 28th PVSEC and 34th EU PVSEC*, 2018, doi: 10.1109/PVSC.2018.8548183.

## Introduction

Terrestrial photovoltaic (PV) energy has especially during the last decade showed huge price declines and a huge capacity expansion exceeding 630 GW worldwide [1]. In the future photovoltaic energy is predicted to be the main driver for expansion of renewable energy, since it offers consistently lower electricity prices than energy from coal and many other energy resources [2]. Facilitating energy production using photovoltaics requires a photovoltaic system, comprising of the photovoltaic modules, in which photovoltaic cells are interconnected and protected against the environment, as well as the balance of system hardware. The balance of system hardware is anything else required than the modules being inverters, mounting structures and the remaining electrical infrastructure. Approximately 95% of the deployed PV systems are wafer based silicon and the remaining 5% is thin films mostly based on cadmium telluride CdTe and copper indium (gallium) selenide  $\text{Cu(In,Ga)}\text{S}_2$  [3]. The success of photovoltaic energy, is a result of a long term dedicated effort in developing and upscaling especially the solar cells. A similar development and maturing effort has also undergone the module technologies and the balance of system hardware. This effort has resulted in a system price decline of 60% [3], a module price decline of approximately 85% [4] and a balance of system price decline of 40% [3], over that last decade, making photovoltaic energy one of the cheapest electricity sources in most places of the world.

This development has been supported by attractive support schemes in Europe and particular Germany in the beginning of last decade and from the middle of the decade China and India were the major market drivers [1]. These schemes have paid off since grid parity of solar PV is reached in most countries enabling unsubsidized Photovoltaic Energy. Solar PV will thus be a great part of the solution towards a carbon neutral energy sector, but expansion of other renewable sources and development of grid integration, storage and electrification are also important [2].

The system price reduction of PV plants is great however is only partly contributing to the energy price, quantified as the levelized cost of energy (LCOE), which is the total lifetime cost divided by the lifetime energy production. For a photovoltaic plant the contributors are the installation cost, the operating costs (OPEX) and the decommissioning costs. The OPEX is insurance, equipment management and operation and maintenance (O&M) and is according to [5] around 1.2% per year of the installed cost for the US. For the total LCOE, OPEX is thus 20-30% of the LCOE depending on financial assumptions, location and cost of labor. The O&M costs (maintenance, fault finding, land management etc.) are being estimated to 44% of the OPEX cost in [6]. O&M methods are historically quite labor intensive and efficient means of faultfinding, contributes to lowering the O&M cost of photovoltaic energy as well as increasing the security of the supply, since preventive maintenance becomes more attractive. With the rapid increase of the global photovoltaic capacity to more than 630 GW and with a worldwide addition exceeding 100 GW/ year, efficient O&M procedures are even more important ensuring high long term performance [7].

Photovoltaic power plants are constructed and paid before they produce energy and revenue, and requires therefor confidence in performance from the investors [8]. The risk assessed by the investors, will therefore influence the cost of financing, with high risks increasing financing costs. The energy production of photovoltaic plants is based on yield predictions (using software packages) where historic and characteristic weather data and performance models of the system components are used to predict the power flow in the PV system, and the income is estimated based on forecasts for the electricity price

and the predicted energy production. Therefore accurate and validated energy yield prediction methods are needed. The energy yield predictions are getting more well established, and a great effort in creating confidence to these energy prediction tools has been done [9]. The commercial software tool PVsyst is being the de-facto standard energy yield prediction tool trusted by financial stakeholders however many software tools exists. The technical uncertainties in these energy yield prediction tools can be reduced by establishing and standardizing the characterization procedures from which the performance models are derived. Validated performance models based on accurate lab measurements improve this confidence and reduce the uncertainty of the energy yield simulations that are used to predict the revenue in the financial models. Confidence in measurement procedures and comparability between labs are therefore a contributor to a lower LCOE.

Building integrated photovoltaics (BIPV), where photovoltaic modules are used as building skins has in recent years become more attractive due to the price decline of the photovoltaic modules, and due to the focus on buildings contributing to the green transition. Here the photovoltaic modules serve a dual functionality as both building skins and an as energy producing unit [7]. BIPV offers several advantages such as cost efficiency, reduced need for grid expansion and better utilization of the land [10]. Cost efficiency is achieved by the dual functionality of the material, saving conventional building materials. Reduced need for grid expansion is enabled since buildings in Europe is responsible for 49 % of the energy consumption, making the energy from BIPV produced at the place of consumption. Large scale deployment of BIPV can therefore reduce massive electrical grid expansions and further BIPV improves the utilization of the land, since the land area already occupied by the building is also used for energy production [10].

Deployment of BIPV are subjected to physical and aesthetically constraints, related to urban planning and heritage conservation [10], however it is possible to integrate BIPV solutions with a high degree of aesthetics and in multiple colors [11]. The BIPV industry is still fairly young and new standardization procedures are under development, adapting the requirements from the stakeholders [12]. Thorough optical characterization on both angular performance, glare assessment and color performance are suggested by the PVPS<sup>1</sup> program in order qualify BIPV products [12], and development of good characterization methods helps this standardization.

Photovoltaics has also proved to be an efficient power source for application outside a centralized grid. In fact the first PV terrestrial applications were powering transmitter stations, remote cottages etc. all placed far from the electrical grid [13]. For these uses alternative sources of energy are generators based on combustible fuels, and photovoltaic energy in combination with battery storage reduces the operating cost and simplifies operation - often to a such dramatic extent, where the application often changes to become feasible. The off grid concept can be downscaled to products, where comfort lighting products, lanterns, solar powered calculators etc., can be powered from the sun - in some cases completely, however reliable performance requires battery integration [14]. Introducing solar power to already existing rechargeable products can enable a battery reduction of certain products of 30 % [14]. Our own research experience shows, that accurate performance models are needed to validate customer expectations and enable functionality during the periods of the year with small amounts of sunlight. Several of our industrial collaborators have various kind of these product integrated

---

<sup>1</sup> IEA Photovoltaic Power Systems Program T15 BIPV

photovoltaic (PIPV) products in their portfolio and performance assessment, characterization and design of these products, are important to support this development.

In this thesis 3 overall research topics are presented, where progress towards solving the challenges outlined above are presented.

The first section is presenting research within two methods for efficient fault detection and identification of PV panels. The first method is electrical impedance spectroscopy by which the electrical impedance response of a photovoltaic string is analyzed to detect abnormalities, and progress towards fault detection of pv-modules is presented.

The other method is developments towards a drone-based acquisition of electroluminescence imaging under outdoor conditions under daylight. Here development of first a stationary daylight based electroluminescence method is presented, and developments towards a moveable acquisition system is presented demonstrating that the developed methods can be applied on an Unmanned Aerial Vehicle (drone).

The second section is presenting research progress in quantifying the reflection loss, where confidence in the measurement method increased through comparison with other research labs.

Within this work developments toward improved appearance, and a methods for quantification of the colored appearance is also presented.

The section concludes on presenting the development of a reflector system with improved winter performance of a solar powered sensor mast where a bifacial panel is used.

The third section describes and exemplifies development of a methodology and a laboratory for developing and performance assessing PIPV products, with emphasis on lighting products.

## Fault detection in the field

### Introduction

Photovoltaic energy is a distributed energy resource, and on the utility scale deployment, generally only few sources of monitoring are available covering 1000's of panels. Contact based characterization methods, where individual panels/ substrings are disconnected and investigated, are therefore extremely expensive, expose the operators to electrical shock hazard risks and are in practice not realistic.

However, a single faulty panel, can, due to the serial connection in the substrings, be the cause of significantly reduced power from the whole substring/ array. Therefore efficient fault detection methods that both locate the fault spatially and can advise on which action to perform, in an automated way, are in great demand.

A fault in a PV module is according to [15] defined as either an effect that degrades the module's power which is not reversed by normal operation or a fault that creates a safety issue. Within this definition, e.g. cosmetic faults are not defined as a fault, as well as increased soiling.

Additionally the authors of [15] have made a systematic mapping of faults that can be detected from each matured characterization technique used in the industry (in 2014).

Within this thesis, two promising methods are investigated and contributions towards the fully automated fault detection and location are presented:

1. Impedance spectroscopy on strings
2. Outdoor Electroluminescence imaging.

### Electrochemical Impedance Spectroscopy

Electrochemical Impedance spectroscopy (EIS) has been used for many years for characterizing fuel cells, batteries as well as dye synthesized solar cells. Work within this thesis has contributed to also apply the EIS methods for fault detection of Silicon PV panels in strings, and some of the findings are successfully commercialized via the Danish company Emazys [16].

The basis of electric impedance spectroscopy is to measure the electrical impedance at a range of frequencies by applying a sinusoidal electrical potential with an angular frequency  $\omega$  and measure the response, and similar to Ohms law the impedance can be calculated as the voltage divided by the current:

$$Z(\omega) = \frac{E(\omega)}{I(\omega)}$$

where  $Z(\omega)$  is the complex impedance, with resistors contributing to the real part of the Impedance by  $R$ , and capacitances and inductances contribute with  $\frac{1}{j\omega C}$  and  $j\omega L$ , respectively. DC equivalent circuit models for PV cells and panels are well established and [17] established useful AC equivalent circuits, by introducing a parallel capacitance. Using these models, the characteristic impedances can be calculated for the single diode model.

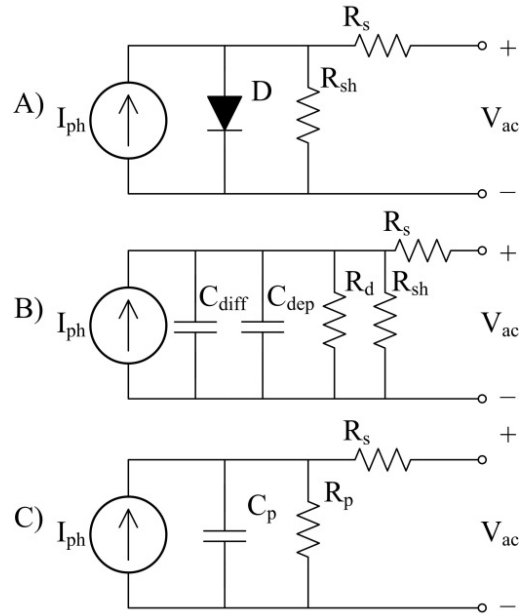


Figure 1: A: Single diode DC equivalent circuit, B: Detailed AC circuit with division of the parallel capacitance into a diffusion and depletion capacitance, C: The circuit seen from the impedance spectrum [18].

These equivalent circuit models are used in the contributions for fitting the measured spectra enabling estimation of circuit parameters.

In [18] outdoor panel and string impedance spectroscopy measurements have been performed using an automated setup capable of measuring in the frequency range of 200 -1000 Hz.

The results show that impedance spectroscopy is applicable to obtain circuit parameters under operation and the parallel resistance decreases with illumination and the parallel capacitance increase with illumination. Both measurements on an individual panel as well as a string have been measured and the results on both the string and the panels show the same trends with varying irradiance.

In [19] faulty modules with potential induced degradation (PID) s-type faults were identified on a residential installation with the Emazys Z100. The apparently best performing module and the five worst performing modules were brought to the lab for further investigation using Light IV curves, dark IV curves and Impedance spectroscopy. For the PIDs degraded modules only around 20 % of the original power was left compared to the label value, and a decrease in shunt resistance was evident on both the light IV curves, Dark IV curves and the IS measurements. Using the IS measurement for fitting equivalent circuit parameters revealed a more than 2 orders of magnitude decrease in parallel resistances and a one order of magnitude increase in parallel capacitance. These results are consistent with PID, and the results, indicate that IS measurements can be a useful tool to detect PIDs faults.

In [20] a field station is designed in order to investigate how impedance spectroscopy can be used for early detection of degraded modules in the field.

10 panels are mounted and connected to relays that switches the panels individually into a measurement circuitry either allowing for first Quadrant IV curves or impedance spectroscopy measurement using the commercial Z 100. When the panels are not measured, the panels are

connected to a string inverter via a power-optimizer which enables the modules to most of the time operate in their individual maximum powerpoint, despite different power outputs due to different states of degradation. The station is further equipped with 2 irradiance sensors and thermocouples mounted on the back of the modules to monitor irradiance and temperatures. The system measures continuously, by switching the panels out 1 by 1 for IV and IS measurements, facilitating a measurement cycle giving a new measurement for each panel around every few minutes. To minimize the IV-sweep time the voltage points for the IV-curve are implemented to be more dense around the Short circuit current (ISC), the open circuit voltage (VOC) and the expected maximum power point (MPP). These voltage points are created based on a VOC measurement prior to the IV sweep. The electronic load used for this system needs around 10-20 seconds to perform a 50 points IV sweep. Further quality procedures are implemented, where re-measurements are taken if the irradiation changes more than few percent during the IV measurement. The principal operation of the field station is shown in Figure 2.

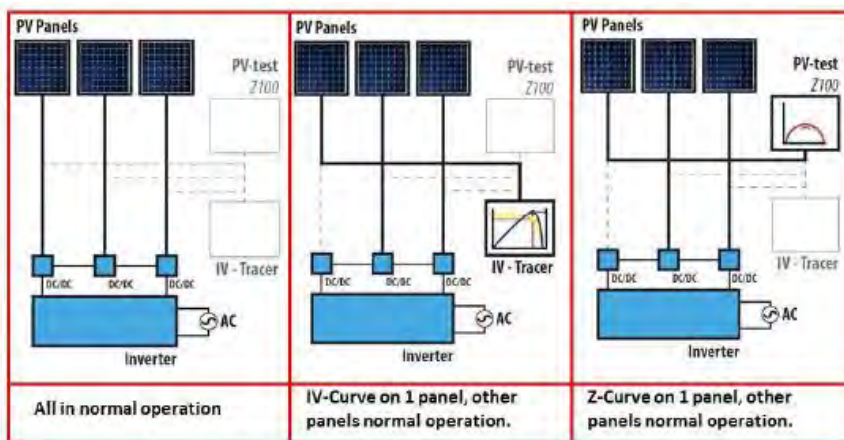


Figure 2: Operation of the field station [20] © 2016 IEEE.

The station is equipped with panels that were degraded in the laboratory; 5 which had undergone mechanical load testing via sand bags to introduce  $\mu$ -cracks, a few that had under gone PID stress and a few that had received damp heat stress. For the PID modules and the damp heat modules no measurable power-loss was detected.



Figure 3: Population of the field station with panels that have undergone stress [21].

The results from the station is published in [21].

The power derived from the light IV measurements show that the outdoor measurements is about 5 W larger than the indoors measurements. The difference can be due to temperature variations, and different measurement equipment. However the approximately 5 W difference is acceptable since the purpose is fault detection and not accurate power rating. Using the outdoors IV curves to fit the parallel and series resistances shows no difference between the healthy and degraded modules and thus concludes that IV curves cannot be used for early fault detection.

For the impedance spectroscopy, the data show range limitations of the Emazys Z 100 instrument only allowing for Dark IS measurement when using the chosen instrumentation. The analyzed data shows a decrease in Dark IS parallel resistance is a good indicator to determine early stages of degradation both for PID modules and for micro cracked modules. Overall the work concludes IS data as being a promising method for detecting  $\mu$ -cracks, however further investigations are needed [21].

The perspective of this fault detection method is to implement the technology in string inverters and combiner boxes and during nighttime perform impedance spectroscopy to monitor for faults. The nighttime analysis is beneficial since it does not compromise power production, and further it can be done in an automated manner. Future work to achieve efficient use of this technology is first to establish a more solid foundation for fault signals from the impedance spectroscopy that with a high degree of certainty can be used to detect faults. The optimal end achievement is correlating power loss with the data from the IS spectra to provide guidance on panel replacements. In addition, for practical applications string based IS will be needed and therefore work towards string based IS should be investigated, both for fault detection and location. The company Emazys [16] already claims that their Z

200, can detect faults in a string and measure series resistance based on IS measurements and further the same device can locate disconnects in a PV string. The Z200 device is a field measurement device that requires disconnection of the PV string. Lately Huawei [22] have implemented IV curve tracing for monitoring in their inverters, which might be an indication of that monitoring is entering the inverters [23].

### Outdoor Electro luminescence

Electro luminescence (EL) imaging, where the PV-panel is biased and the radiative emission is imaged, can, in the lab and between dusk and dawn, provide qualitative information about e.g. micro-cracks and potential induced degradation in photovoltaic modules [15]. Research on quantitative analysis of the acquired images is ongoing [24], [25], and promising results are achieved. Compared to visual and infrared imaging EL imaging provides a direct visualization of the photo-activity in a spatially resolved manner. Lock-in thermography can increase the resolution of IR images and locate the sources, but is not well suited for field inspection since the optimal lock-in frequency allowed due to the thermal time constant in the vertical direction of the PV module is around 10 minutes [26]. Further biasing of the modules are needed and luminescence images provide a higher resolution in general.

Electroluminescence is achieved by biasing the PV module with a forward bias and radiative recombination will provide emission of light at the wavelength corresponding to the bandgap of the semiconductor in question. For crystalline silicon, the peak wavelength is 1150 nm with a broad peak expanding up to approx. 900 nm, allowing silicon based CCD detectors to be used as cameras. Using silicon detectors a long exposure time of 30-60 s is required, since the quantum efficiency of a silicon based sensor is low (less than approximately 20-30 % [27]) in the wavelength region of interest. Indium gallium arsenide (InGaAs) sensors with a quantum efficiency of approximately 80 % in the relevant wavelength region allows for much shorter exposure times ~10 ms compared to exposure times of silicon, however the InGaAs sensors are significantly more expensive as well as they also offer lower resolution.

Electroluminescence imaging can also be attractive as a fault diagnostic tool in the field provided the following challenges are met.

1. Acquisition of images of sufficiently good quality under sunlight from a movable camera mounted on an autonomous ground based or aerial vehicle - e.g. a drone.
2. Biasing of the PV strings needs to be implemented preferable in a contact less manner e.g. with the relevant electronics to be placed either in the inverter or in the combiner box. Since power to the modules during image acquisition is required, the inverters or combiner boxes need adaption to support biasing the panels with a reverse power flow.
3. Image correction for preparation of image for analysis
4. Automated image analysis, providing quantitative feedback to the O&M operator of the plant.

The following contributions have made significant progress towards this goal.

In [28] requirements for drone based acquisition of outdoors photo and electroluminescent images are analyzed. For image acquisition, the use of an InGaAs sensor was concluded to be the best suited technology due to the high quantum efficiency around the emission peak of silicon at a wavelength of 1150 nm.

For electroluminescence a trigger circuit capable of providing a square waveform to the PV panel was developed, enabling acquisition of images with forward bias (light images) and acquisition of images without bias (dark images). The difference between these two images is the EL signal. The contribution shows that the difference in signal between the light and the dark images is statistically significant for most irradiance levels, using 50 light images and 50 dark images (Figure 4). Further an analysis was made where the number of pictures for averaging was varied and it concludes that averaging 8 light and 8 dark pictures with the used camera settings gives an acceptable noise reduction for outdoor acquisition.

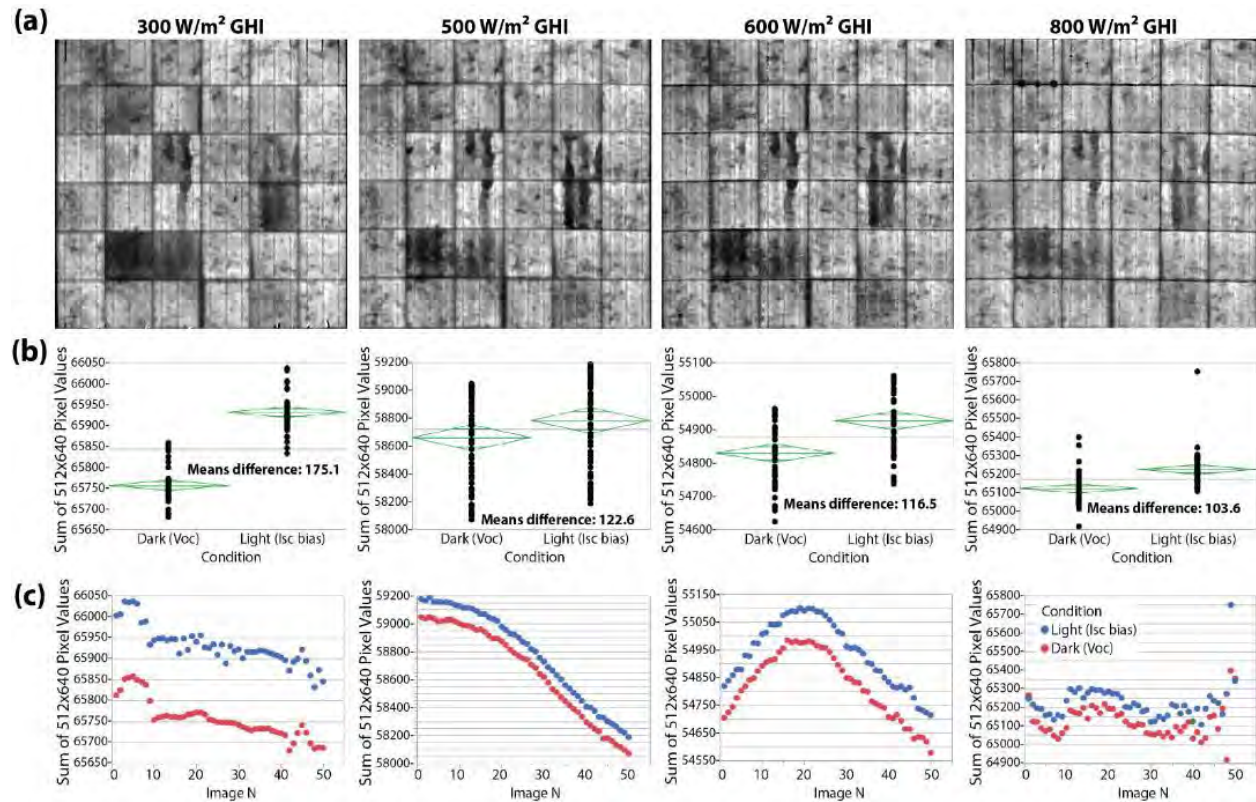


Figure 4: Outdoors image analysis from [28] © 2017 IEEE.

In addition optical power requirements for outdoor photoluminescence imaging on a drone is presented based on indoor lab measurement. Here it is concluded that laser linescans seem feasible for drone integration in terms of power requirements and signal strength.

In [29] the signal to noise ratio using the measurement principle described [28] were investigated. 50 light and dark images were used for averaging and the experiments showed that this strategy could be used for Outdoors EL imaging and with a signal to noise ratio of approximately 5 to 8 on average. The experiments further shows that the signal to noise ratio (SNR) decrease with increasing irradiance. In Figure 5 it can be seen that the irradiance decreases linearly as a function of time the SNR increases with approximately the same slope as a function of time. However at a global irradiance of almost 900 W/m<sup>2</sup> useful images that can be used for analysis and identify C-mode cracks, as defined in [30].

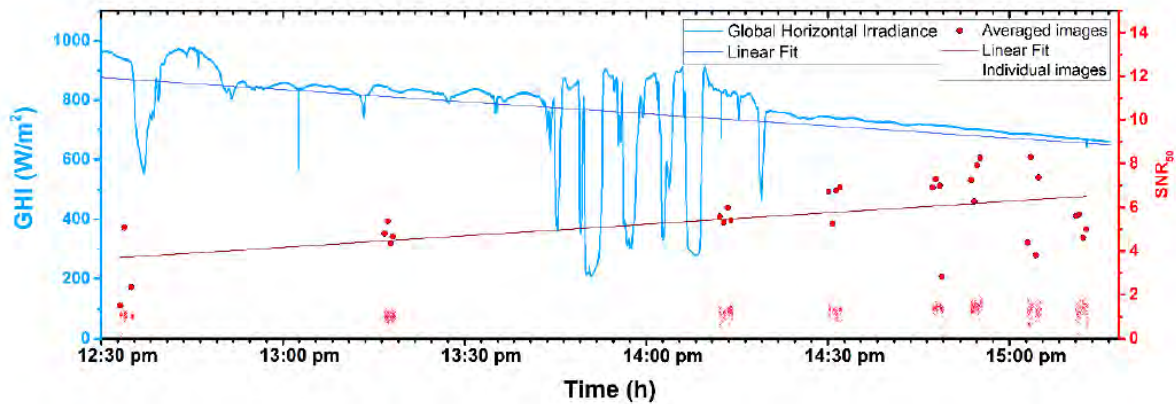


Figure 5: Global irradiance and signal to noise ratio of the averages images [29].

Further photoluminescence based on a laser line scan was proved feasible in the lab.

Photoluminescence is promising since it is a truly contact-less technique for automated inspection, however traditionally, large areas needs to be illuminated, and is practically impossible to implement on a drone. Laser line scans concentrate the light more and with the use of scanning methods, the work proves the feasibility of laser line scan PL. Here a 6 W laser was via optical components transferred into a line that was scanning the panel. Using this method, PL images were acquired for supplemental analysis.

After proving the feasibility of outdoors image acquisition in bright sun further steps were investigated to enable image acquisition in motion. A setup where the camera was put on a moveable dolly looking at a small string from a distance of 4 meters was created. This setup was used to develop image processing methods that correct for the motion and enable dark and light images subtraction. The details are described in [31], where successful methods were developed. Prior to the motion correction images the images were perspective corrected following the methods described in [32].

In [33] the InGaAs camera is put on the movable dolly, and EL images are taken using similar methods as in [29], where two modulation schemes are tested. The camera is moved, passing a faulty module with a speed of approximately 1 m/s, and the module was biased with a 60 Hz DC+AC signal not actively synchronized with the camera, where a frame rate of 120 frames per second (fps) was used. The average pixel values are used to determine the EL and the background signals. Image correction procedures were applied to ensure the averaging was done on pixels from the same spatial origin [31]. Image correction procedures were successfully implemented and EL images acquired with the camera in motion were successfully used to determine A, B and C mode cracks. The images are slightly blurred compared to the stationary outdoors ones.

In [34] the results from the previous works were used to implement the InGaAs camera on a drone combined with a PC recording the images. With an external power supply, the PV panels are biased but not synchronized with the image acquisition. Despite the lack of synchronization, advanced post processing algorithms detect the dark and light images after motion correction. The dark and light pictures were averaged for de-noising, light and dark images subtracted, and finally the pictures were perspective corrected, prior to EL picture analysis. The paper proofs that EL image from a drone are feasible and with a DC square wave biasing a signal to noise ratio of 4.6 is possible at a plane of array

(POA) irradiance of around  $970 \text{ W/m}^2$  - which can be considered as 1 sun. The achieved SNR is very close to the requirements from the EL-standard IEC TS 60904-13. For the outdoor images, 100 light and dark image pairs were required. DC+ AC biasing was also attempted and were acquired with a POA irradiance of  $856 \text{ W/m}^2$ . Here the SNR of the image was 1.6 favoring square wave DC biasing. A visual comparison of these two images reveals though that the DC + AC biasing appears to be of better quality and both pictures allow for identification of B and C mode cracks. The low SNR for the AC bias could be due to a smaller intensity differences between the dark and the light pictures.

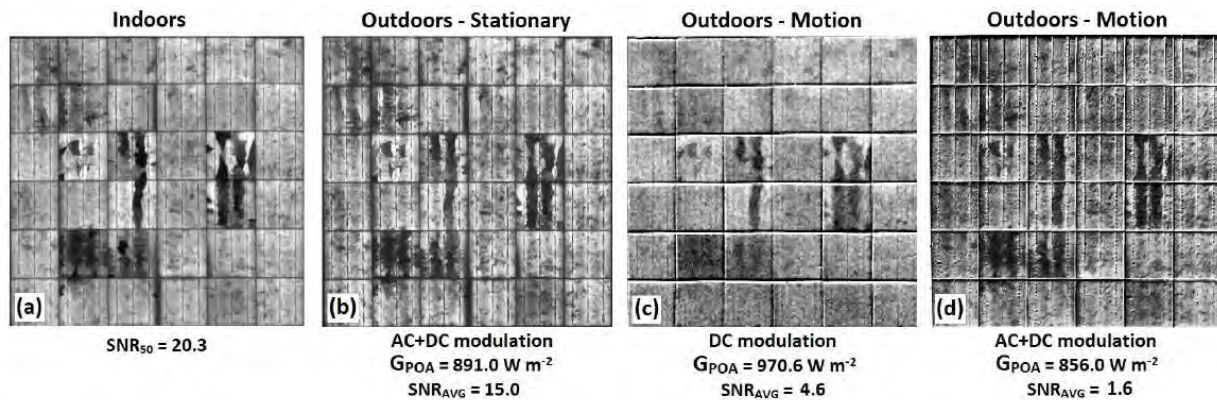


Figure 6: Pictures from [34] © 2020 IEEE

All in all the work shows that EL images might be feasible from a drone under the right biasing conditions, advanced post-processing of images and right application of filters.

The works on outdoor electroluminescence imaging proves the potential of the technique for automated field inspection and the technical proof of concept for string level outdoors electroluminescence is achieved. Further algorithm optimization and development are needed as well as inverter based biasing is required for widespread implementation. In addition, automated image analysis is required to handle the 1000s of EL pictures. The Laser line scanning PL/EL imaging has the potential of true contactless PL/EL-imaging and the feasibility of this approach is published in [35], [36].

### Part conclusion

The work on fault detection both using EIS and outdoor electroluminescence prove of principles are established for effective fault detection methods in the field. Both techniques require further work however, both techniques showed promising results towards the implementation stage. For both techniques string level control and excitation are needed which complicates use in the field. The Laser line-scan imaging offers the potential of being independent of biasing the modules and offers truly contactless inspection. More work to prove image acquisition is though ongoing [37].

## Optical characterization and development for PV applications

### Introduction

Optical characterization of PV modules are important for several reasons. First, this detailed knowledge can be used to optimize the light capture in the PV panels and thereby improving the nominal power and the yield. Reflection losses, which can be derived from this optical characterization, can, on an

annual basis, provide losses of up to 2.8 -3.6 % for systems reviewed in [38], suggesting that the reflection losses have greater impact than previously anticipated in the industry.

Optimization to minimize all the losses are important both in the product design as well as in the plant design phase, and here well characterized optical properties enable qualified decisions and serve as important validations for cell to module calculators, as SmartCalc.CTM, PV Lighthouse and Diadalos<sup>2</sup> and energy simulation tools as PVsyst, System Advisor Model, and PV-SOL<sup>3</sup>. Here PVsyst and PlantPredict offer detailed and customized modelling on the incidence angle modifier (IAM) [39]. Since the output of the energy yield simulation is used in the financial performance calculations, accurate and trusted energy yield simulations contribute to a lower financial risk.

For applications within building integrated photovoltaics (BIPV) and product integrated photovoltaics (PIPV), the products and installations are often placed in urban environments where aesthetical improvements needs to be considered to achieve public acceptance. In these applications efficiency can be sacrificed if it enables improved appearance, which e.g. could be a colored PV-panel [11] [40]. For most single-family houses, the roof and the façade areas are more than enough to cover the households annual electricity consumption, and further residential and commercial PV installations are in most western countries only financially attractive with a high degree of self-consumption. For appearance many optimization possibilities exist without severely sacrificing efficiency as long as the black appearance is accepted [11]. Technologies for coloration are available, however these are associated with an efficiency loss ranging between 10-50 % depending on technology, color and color saturation [11].

The work within this part of the thesis contributes to optimize and characterize the optical module parameters, as well as optimizing energy yield of a certain type of BIPV product.

### Optical Characterization

In [41] black silicon solar cells were fabricated based on previous work from the main author [42] and in a joint project electrochemical blackened ribbons were successfully made. Black silicon solar cells are useful since they have very low reflectance for all angles and can improve light absorption in the solar cell [42] and are also attractive for BIPV due the black appearance. The black silicon solar cells and the black ribbons served as important component for fabricating a complete black module. In [41] the interconnecting ribbons have a reflectance of less than 3 % and the black silicon reduces the total reflectivity of the multi crystalline solar cells from 8 % (measured on the raw cell) to well below 0.5 % for multi crystalline silicon. The produced black silicon cells had an efficiency of 16 % compared to the reference cell with an efficiency of 18 %. Despite the low reflectivity the black silicon solar cells is limited by high surface recombination velocity indicated by the EQE and IQE curves shown in [41] and is expected based on the first author's previous work.

---

<sup>2</sup> SmartCalc.CTM: [www.cell-to-module.com](http://www.cell-to-module.com) , PV Lighthouse: [www.pvlighthouse.com.au](http://www.pvlighthouse.com.au), Diadalos: [www.daidalos-cloud.de](http://www.daidalos-cloud.de)

<sup>3</sup> PVsyst: [www.pvsyst.com](http://www.pvsyst.com), System Advisor Model: [sam.nrel.gov](http://sam.nrel.gov), PV\*SOL: [valentin-software.com/en/products/pvsol-premium](http://valentin-software.com/en/products/pvsol-premium)

This work proves the feasibility of making complete black panels with low reflectivity, based on inorganic materials and potentially high efficiency, if good surface passivation for the black silicon can be developed.

The relative transmission to the PV cell as a function of angle is in the PV industry called the incidence angle modifier (IAM). The IAM is a quantification of the reflection and absorption in the front cover at different angles of incidence relative to normal incidence.

$$IAM = \frac{\tau(\theta)}{\tau(0)}, \theta = \text{angle of incidence}$$

The IAM is a module property that can be optimized via the module bill of materials, and in particular the choice of front cover. For most industrial applications, solar glass with an antireflective coating and in some cases a surface texture on the outer glass surface is used.

In [43] an indoor laboratory measurement setup for measuring the IAM is developed. A laser driven light source is illuminating the sample with a broad band collimated light with a spot size of 38 mm and a beam divergence of 0.1 degree. The relatively large spot size combined with the high intensity is advantageous for a high signal and ensuring representative signals from surface structures with lateral sizes of  $\mu\text{m}$ 's. The sample is mounted on an optical motor rotating the sample, and the short circuit current is measured for each angle via a Lab-View based transducer using a shunt resistor. An illustration of the measurement setup is shown in Figure 7.

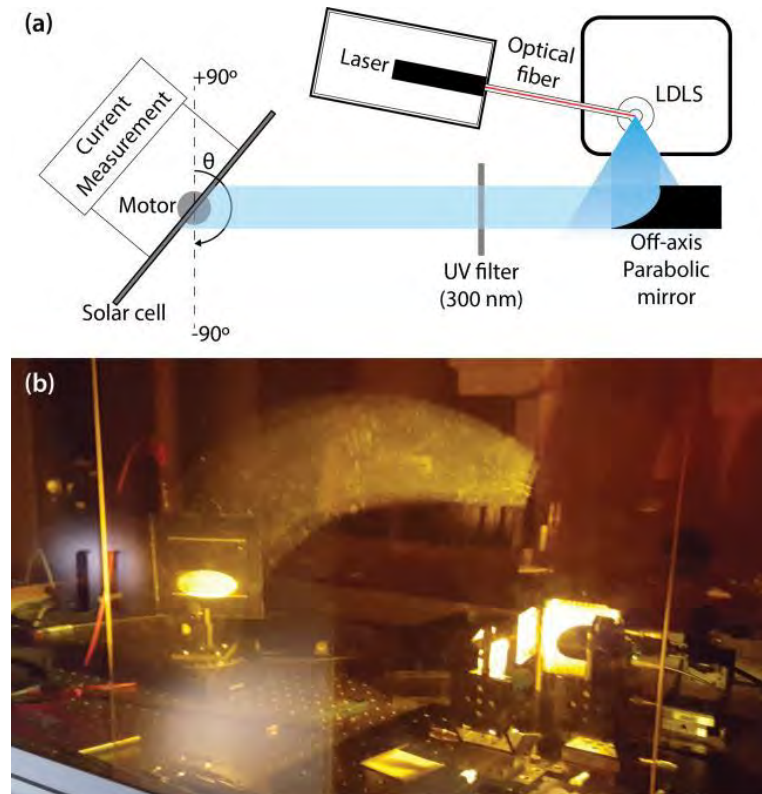


Figure 7: IAM measurement setup [43].

Six different glasses were characterized as well as a bare cell. Reproducible IAM measurements for all six samples were successfully acquired, and the IAM curves and the relative deviation from the raw cell is shown in Figure 8. The deep structured glass (sample 4) showed worse performance than the bare cell at angles of incidence between 0 and 45 degree, otherwise large differences between the glasses were only observed for angles of incidences larger than 45°. The measured IAM curves were used for PVsyst simulations where the monthly energy was simulated for 4 different locations at different latitudes using latitude tilt<sup>4</sup>. Overall, the diffuse glass gave the highest gain compared to the bare cell for all latitudes by 1.8 to 2.2 %. Certain structured glasses also outperformed the bare cell with 1.8 to 2 %. This conclusion is expected, as the diffuse glass have the highest IAM for most angles.

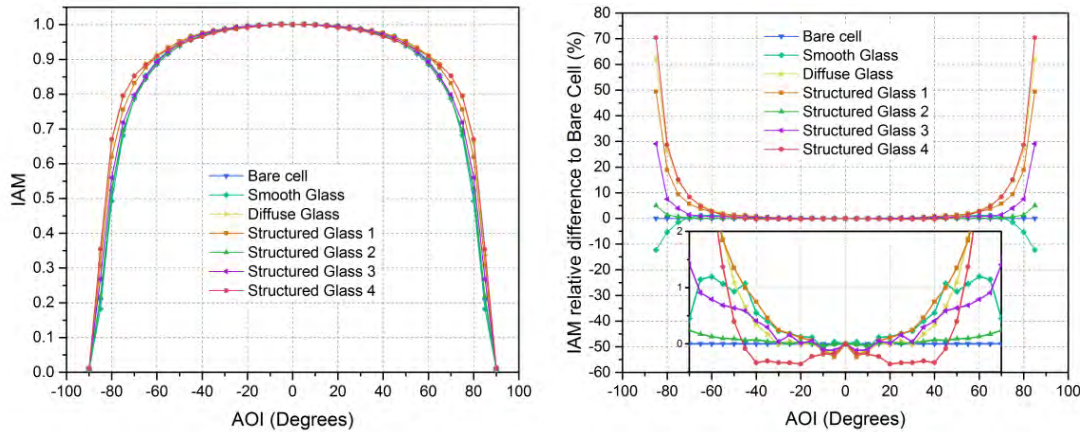


Figure 8: IAM curves (left) and IAM differences to the bare cell (right) [43].

In [44] the same setup is used to measure the IAM on encapsulated black silicon samples Figure 9. Low reflectance losses has been reported previously on raw cells with black silicon [42] however the optical environment changes when the cell is encapsulated. The cells were produced as described in [41], and repeatable measurements were performed on two different black silicon samples encapsulated in thermoplastic Poly Olefin and a standard window glass. Compared to the reference cell, IAM gains for the black silicon samples were observed for AOIs greater than 65° and gains of 32 % were reported at 85°, however at this angle the uncertainty is large.

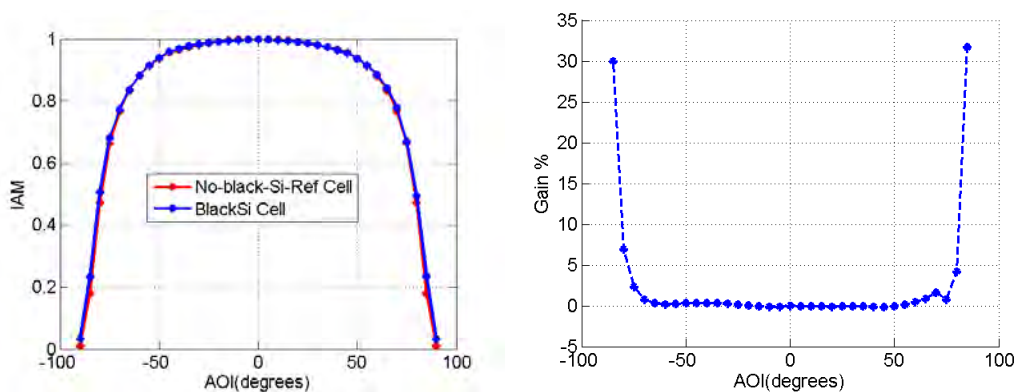


Figure 9: Black silicon IAM (left) and IAM gain (right) [44] © 2017 IEEE.

<sup>4</sup> Latitude tilt = tilt corresponding to the Latitude of location.

In [45] a round robin campaign with 8 different laboratories are executed. 4 different methods for acquiring IAM curves were available among the different labs, and the same 2 times 3 samples were characterized using each laboratory's standard procedure, though to ensure complete comparability the rotational angle was defined, enabling comparable measurements if anisotropies were present. For incidence angles with absolute values below  $40^\circ$  all the measurements of all laboratories were comparable when adjusted for uncertainties. Beyond AOI of  $40^\circ$  the deviations increased, however 5 labs including DTU were comparable within 2 % between for angles of  $-75^\circ$  to  $70^\circ$ . At AOI of  $85^\circ$  the uncertainty became large, and these measurements are problematic and difficult. The data also showed that a high degree of symmetry in the AOI measurements provide low uncertainty.

The results in [45] confirms that our AOI measurement capability works and provides accurate measurements, and further work on validation is ongoing [46].

Deploying photovoltaics in the urban environment on buildings adds new additional constraints on the appearance, and here photovoltaics with different colors has recently become available [11]. Since colored appearance requires a mix of specific wavelength in the visible region to be reflected these reflections causes a loss in the photocurrent that translates to a loss in energy production. Quantifying the colored appearance of a surface can be done following the CIE methodology [47], where the Tristimulus values are calculated based on the reflectance spectrum and the d 65 illuminant (reference spectrum) using the color matching functions. This color appearance is dependent on the light source used for color characterization, and in order to circumvent this light source dependence, the CIELAB color space compares the color appearance to a white sample measured under the same light source. For coloration, there is a metamerism, where multiple spectra can give the same color, and therefore coloration of photovoltaics opens a new field of engineering with optimizing coloration and photon economy. The aim is to achieve the highest color intensity of the desired color based on a reflection spectrum using as few photons as possible.

A few theoretical studies [48]–[50] have been published making progress in finding representative metrics quantifying the color efficiency in a useful way, however some disagreement between authors on this metric is evident and this work is still ongoing. Determination of the power production of the solar cell and the efficiency loss due to coloration are well established and can be done in many PV labs. However comparing the strength/saturation of the coloration across the full color spectrum is difficult. Despite the coloration efficiency metric is not well established [48]–[50], Peharz [48], creates synthetic idealized box spectra's and concludes that all RAL<sup>5</sup> colors matching the RAL color chart can be made with an efficiency loss of less than approximately 20 %, using two box like reflection spectra. As described in [11] many different methods for coloration are possible and especially the structural colors, based on constructive interference between thin dielectric layers shows a strong angular depended color appearance.

In [51] a single plane bidirectional reflectance distribution function (BRDF) measurement setup is described, where the laser driven light source used in previous publications [43] [44] [45], now with improved optical collimation, is used. A spectrometer, that can rotate independently mounted on a rotation stage, is added to measure the reflection. The measurement system enables acquisition of the

---

<sup>5</sup> RAL is a European color system with reference colors originating from Germany  
[https://en.wikipedia.org/wiki/RAL\\_colour\\_standard](https://en.wikipedia.org/wiki/RAL_colour_standard)

single plane BRDF function where both the angle of incidence and the angle of observation can be varied independently - within some limits see Figure 10.

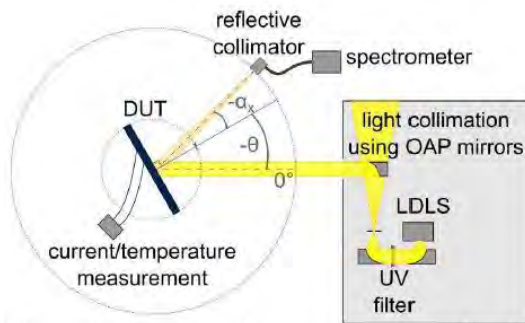


Figure 10: Sketch of the single plane BRDF measurement setup [51].

This data is used to calculate the tristimulus values and transfer the data into the CIELAB color space for each observation angle. 3 different sample types where multiple different colors within each sample type were tested and selected results presented. The sample types were Kromatix™, where dielectric thin-films create a selective optical filter on the inside of the glass, and the front surface of these glasses are satinated. The two remaining samples were inkjet-printed colored glass, where the coloration is based on ceramic pigments that absorbs different wavelengths, and colored interlayer foils that were also dyed.

The coloration appearance showed that the Kromatix™ sample group had a color appearance strongly angle dependent, with one group being iridescent and another group with a significant change in lightness, but this group also showed the least losses. For the other groups the color showed a good constancy with respect to angles, however interestingly one color of the inkjet printed samples showed a slight iridescence, where the Hue changes as a function of angle.

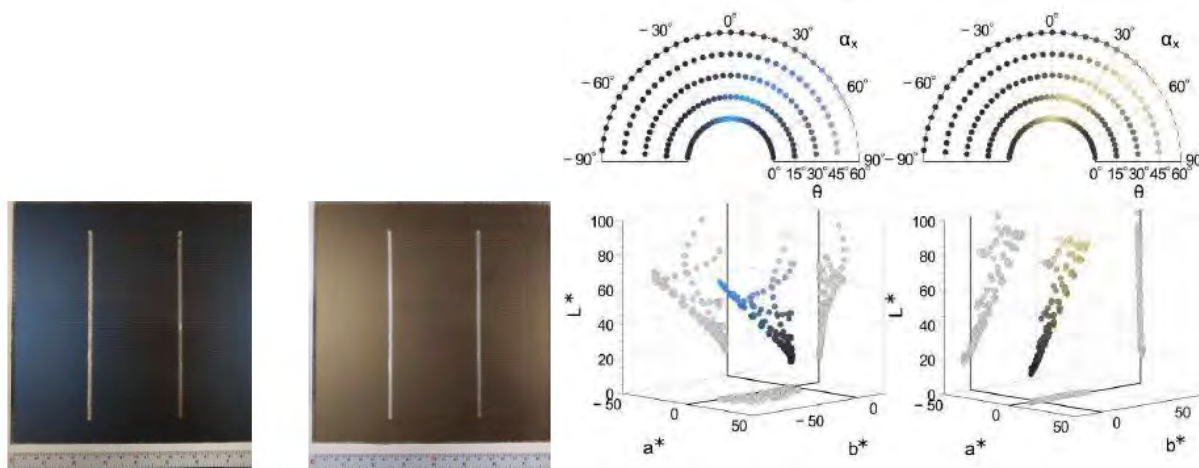


Figure 11 Samples and color appearance measurements for two selected Kromatix samples [51].

The efficiency loss for the inkjet printed colored samples was significantly ranging from 20- 40 %, compared to the same uncolored reference. For the other samples, it was not possible to have an

uncolored reference of the same type why comparable measurement determining the coloration loss cannot be concluded with a high degree of certainty, and therefore a direct comparison of sample groups is not possible. However, the colored interlayer samples seem to have a loss of 15-20 % and the losses for the structural colored samples seems to be 5 % referring to a non-identical reference.

IAM measurement on the samples were also performed. For all samples the IAM response were strongly dependent on color and showed increased angular losses compared to the uncolored references. The mechanisms behind this increase in angular loss are currently under investigation will be published when results are available in the near future.

This work plays an important role in making a qualified choice of architectural impressions when deploying BIPV solutions on building skins, and further provide documentation for stakeholders, that the BIPV product is compliant with local architectural restrictions. With the EU energy performance of buildings and Directive (EPBD) [52] demanding nearly zero energy buildings, deployment of PV on buildings is difficult to avoid for both new buildings and renovation projects.

### Reflector systems

Systems using Bifacial PV panels have also been developed for stand-alone purposes. The objective has been to improve light harvest at low sun heights during winter and at high latitudes and to reduce the costs. The hypothesis was that the retroreflector would improve winter performance, and in combination with the use of bifacial solar cells a reduction of the battery size and reduced size of the needed PV-panel could be possible. A sensor tower was developed for powering sensors in remote areas and the necessary retro reflector optics were developed, modeled and characterized.

In [53] a simple optical model for the retro reflector shown in Figure 12 is developed based on ray tracing, demonstrating an optimization tool. The reflector volume is in the model filled with a transparent material with refractive index of 1.5 corresponding to that of glass. The model uses 3 ray paths, and the optical absorption is modelled using solar angles for the different locations, assuming constant direct normal irradiance (DNI) and further the reflection losses at the glass surface of the panels is neglected. The absorber in the middle is a bifacial panel, and this absorption is compared to a south facing monofacial panel of the same area as a single side of the bifacial panel.

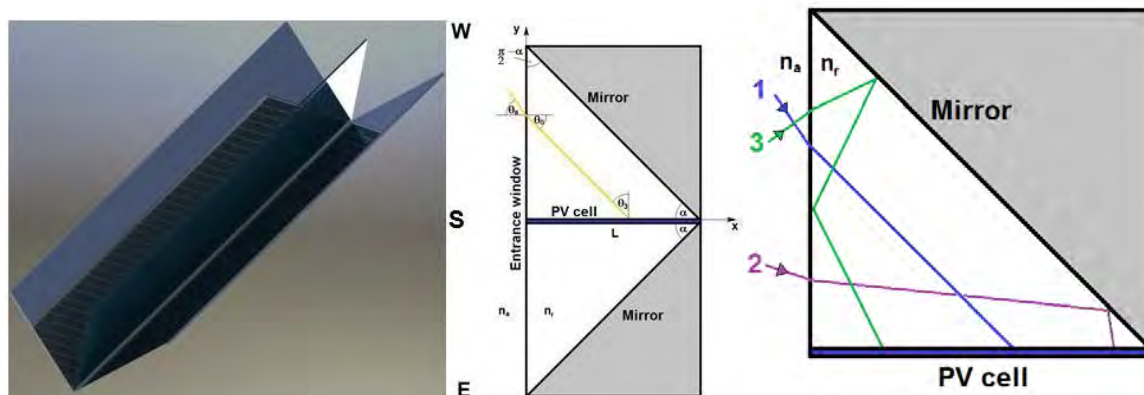


Figure 12: Model of the retro reflectors [53] © 2016 IEEE .

Four cities, being Rome, Munich, Copenhagen and Trondheim is simulated for the shortest and the longest day of the year, and the optical gain is shown to be between 33 % and 68 %, with the highest

gain being at the highest latitude at the shortest day of the year. For the longest day of the year the optical gain is almost similar for all locations.

In [54] the consequence of filling the reflector volume with an index matched transparent material as (acrylic or BK 7) is investigated. The simulations performed, show the light, that is reflected at the reflector and is escaping the PV-panel, contributes with around 30 % of the energy (ray path 3 on Figure 12). Filling the volume in the reflector with a material with a refractive index matched to glass ( $n_r = 1.5$ ) allow the system to harvest almost double as much energy compared to the monofacial reference for all locations simulated both for the longest and the shortest day of the year. Material absorption and reflection at the entrance surface is also investigated, and using realistic absorption coefficients the additional loss are found to be around 4% for both BK 7 and acrylic filled reflectors.

In [55] the reflector design is optimized by reducing the reflector making the PV absorber extends out of the reflector as shown in Figure 13. This enables the absorber to capture most of the escaped light. Simulation on this reflector is made with the reflector volume consisting of air using the same simplified assumptions as in previous works [53] [54]. The simulation shows that this retroreflector doubles the light harvest on the shortest day of the year and reduces the light harvest by approximately 25 % on the longest day of the year for Copenhagen. Simulations further shows that in April the reflector hardly makes any difference.

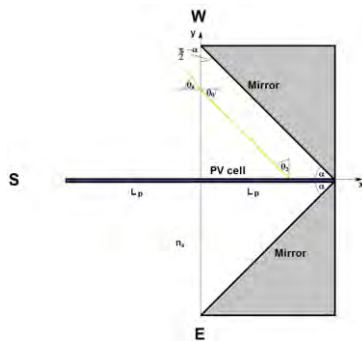


Figure 13: Modified reflector design. Reproduced from [55], with the permission of AIP Publishing.

A prototype, shown in Figure 14, was created for model validation. The validation of the model was done using nearby solar measurements direct (and diffuse) solar irradiation as well as equipping the prototype with a data logger measuring the short circuit current of the PV-panel. The model and the measured data shows some disagreement which could be caused by contributions from diffuse light, IAM losses and the fact that the cells do not fill out the complete area of the panel.



Figure 14: Picture of the system modeled and characterized. Reproduced from [55], with the permission of AIP Publishing .

## Part Conclusion

The work on the optical characterization proves a useful measurement system for characterizing optical properties of small PV panels, which can be used both to optimize and achieve further knowledge about the optical losses. It is also important for optimizing the energy yield and the power rating of PV panels and further improving the accuracy of the energy yield modelling. With the latest improvements, the system will also be a valuable tool for characterizing and developing new colored BIPV technologies and assist in assessing the color stability of colored PV panels, where data for publication is under preparation.

The development of the reflector systems proved the feasibility and the knowledge for further operation can be downscaled and used for other PIPV applications, however the rapid price decline of the PV panels has made the system less advantageous, since system savings are no longer evident.

## Development and Characterization of product integrated photovoltaic systems

### Introduction

Product integrated PV systems (PIPV) are according [56] defined as products with one or more integrated PV cells on the surface, that is powering the products functionally. Inclusion of a battery is optional and applications are solely terrestrial. Examples of products can be solar powered lighting products, PV driven phone chargers, sensors connected the internet of things and the most wide spread example is the solar powered calculators from the 80's. A history of PIPV developments from the 70's is illustrated in [57].

The general advantage of stationary PIPV products is that no cabling is required for the installation, which greatly reduces the installation costs- particularly in the urban environment where costs of new cable establishments can be up to 700 € pr. meter [58]. With these prices, standalone operation of e.g. park lights can be feasible as lighting after sunset. However, at Northern latitudes, powerful light for critical functions where frequent and reliable functionality is required through the winters are generally not possible.

The products are often placed in the urban environment with many obstructions for the direct sunlight and it is important to use all the incoming energy from the solar cells optimally. The performance of the subparts in these systems is dependent of the load point and therefore it is important to characterize and model the power converters, batteries etc. at the relevant load points to ensure and predict the performance. Further energy optimization can also be done using energy management where the systems are only using energy when it is needed for the receivers and is in deep standby mode the rest of the time to minimize the standby power consumption. An example could for instance be a small lighting bollard placed in an urban environment, which could be programmed to light during the dark evening hours from sunset to midnight, save the energy during the night and if there is enough energy, light for an hour or two in the morning. Advanced systems could have PIR-sensors detecting when there is audience, however our experience shows, that the standby consumption can easily exceed the saved energy.

### Product integrated photovoltaic development and characterization.

The contributions within this thesis focus on development and characterization of mostly high end lighting products, which are developed to also be able to provide light at high latitudes also during the dark winter months. The challenge for these products is to optimize the complete energy system in order to ensure that the photovoltaic energy harvested, is not lost in the systems internal voltage conversions etc. and optimize energy management strategies still keeping the standby consumption low.

In [58] a laboratory for characterization of all parts in a light to light (L2L) systems is established. Here the efficiency of the PV panel can be measured from irradiance levels of  $50 \text{ W/m}^2$  to  $1000 \text{ W/m}^2$  and further electronic emulation of the PV panel facilitates measurements of the total charging efficiency, which enables detailed knowledge about the utilization of the energy available at the PV panel. Standby consumption measurements, led- driver measurement efficiency and luminaire efficacy can be measured and is exemplified in a product. The establishment of this lab has been crucial for further developments within the PIPV research.

In [59] an organic-LED (OLED) based L2L system is developed and the OLED and the used power converter are characterized. The OLED showed acceptable performance and good light emission homogeneity. The power converter for this systems, managing and converting the electric power flows in the system, is a 3 port converter specially designed of PV L2L products. Since the product is working either in energy harvesting mode or in energy dissipation mode, not in both modes simultaneously, a topology reusing a switch and the inductor, was developed. The advantage is a potential price reduction of up to some percent's since especially the inductor is a price heavy component. The component selection and the switching frequencies were optimized for peak efficiency at low loads. Efficiency measurements of the power point tracking efficiency and the power conversion efficiency was mapped for the full operating range, using the lab described in [58]. The measurements for the 10 W power converter showed a peak efficiency of 97 % at 1.8 W and a total efficiency of 94 % at 0.5 W - see Figure 15 (right contour plot with the input current and voltage on the axis). These efficiencies at the low power operating points are crucial in order to maximize energy harvest since peak load operation of these products is in general very rare.

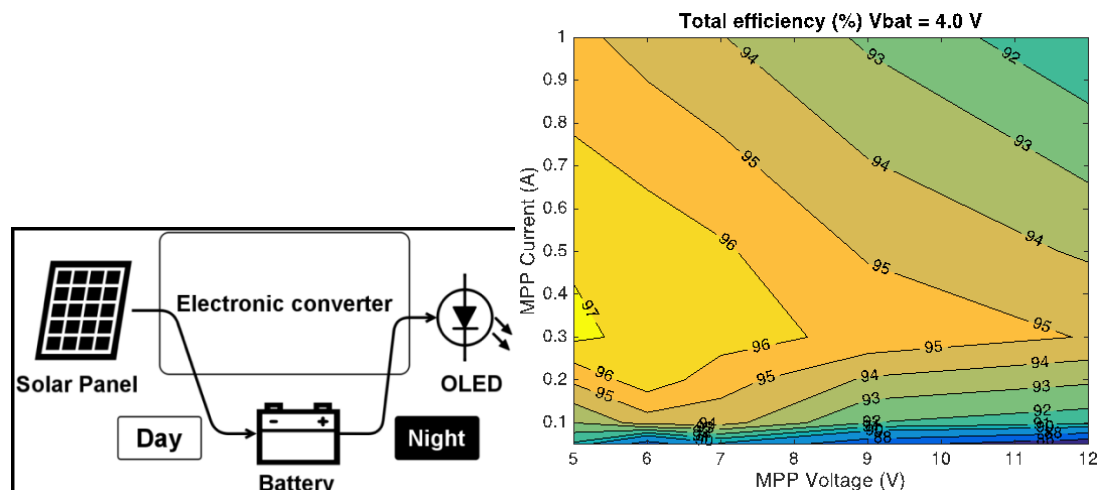


Figure 15: Converter principal diagram and measured charging efficiency for the converter at a battery voltage of 4 volts, with the input currents and voltages on the y and x-axis respectively [59].

The presented converter technology is commercialized in the private company Nordic Firefly A/S [60], where the author is CO-founder, but have exited the company.

In [61] additional details on the indoor laboratory developed in [58] is described, and characterized components are assembled in a L2L system. A first attempt to create a performance model of the (L2L) systems is described, and field measurements in a newly established living lab, where also the incoming radiation is measured, is used to validate the model. The modelled and measured power flows for the charging behavior are shown in Figure 16, and deviation compared to measured power flows at low sunlight and at the threshold where the battery close to being fully charged is observed. These deviations is in the proceeding claimed to be due to insufficient component characterization, however reviewing the findings the low light deviation could also likely coincide with low sun height on a horizontally installed panel, and therefore be due to lack of IAM loss corrections. Further the charging behavior around the voltages where the battery is fully charged, could likely be due to different charging methods, where constant current mode is used, when there is no power limitations and constant voltage mode or trickle charging is used when battery state of charge (SOC) is above ca. 70-80 %, and the power needs to be limited.

Overall the modelled and measured energies for a day deviates up to around 5 %. However the model cannot predict in great detail the exact power flows to the battery.

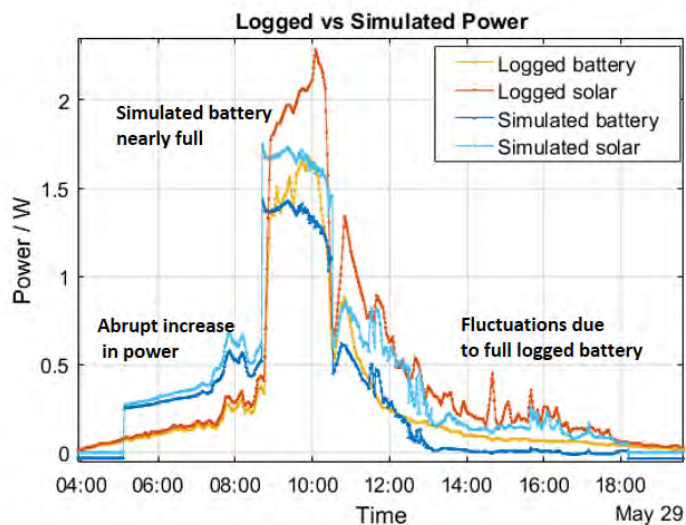


Figure 16: Model comparison from field data [61].

In [62] the previous work from [59] and [61] was applied on specific products in collaboration with several companies. This effort resulted in almost 300 pcs of a product, the Lighttube<sup>6</sup>, were deployed in Saudi Arabia at the King Abdulaziz Centre for World Culture in Dhahran, Saudi Arabia.



Figure 17: Left Image of the King Abdulaziz Centre for World Culture in Dhahran Saudi Arabia, Right image of the Lighttube product deployed [62] © 2016 IEEE.

In [63] a development procedure using the PIPV labs is described, with the aim of developing an add on for an outdoor table facilitating lighting, music streaming as well as laptop and phone charging.

<sup>6</sup> <https://out-sider.dk/da/product/lighttubes>

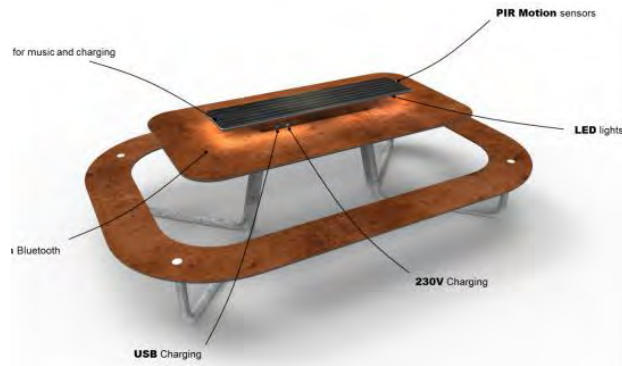


Figure 18: Illustration of the table and the Sun Hub add on [63].

The energy balances of the system was modelled using typical meteorological year (TMY) data for Denmark, and after space constraints were agreed in the design group the allowable area enabled the PV panel to be dimensioned, and afterwards the remaining components were dimensioned and chosen. Commercial components for the different functionalities were bought, characterized and implemented in the add on hub. A simple energy management system was also developed, where some functionalities were disabled when the battery were at a low state of charge (SOC), and thereby a prioritization of functionalities was made.

The table was field tested at Roskilde Festival 2017 where it survived and an anthropologic assessment was done. Two interesting results were found; the users accepted reduced functionality since that is the nature of the product, and secondly the users used the 230 Vac laptop outlet for phone charging rather than the USB outlet. This is undesirable since the power first needs to be converted from 12 volts to 230 Vac and then from 230 Vac to  $\sim 5$  V dc, and maybe up 30-50 % total conversion loss is associated with this use pattern.

In [64] time synchronization using open circuit voltage measurements is investigated. For producers of high-end solar driven lighting products, the luminaire is supposed to be activated at a desired time, and this can be achieved using an internal clock and a preprogrammed dimming scheme. Using this method the devices must be programmed with a time synchronization and a diming scheme matching the specific geographical position for the installation. This method complicates manufacturing procedures and requires reprogramming if the devices will be reinstalled a significant distance from the programmed position. A change in latitude will change the day length and a change in longitude will require local solar time adjustment.

Alternative methods is a self adjusting algorithm that learns the changes in day length duration, and using these inputs as learnings to the energy management algorithm. In [64] Open circuit voltage measurements are used to determine the day length, and deviations of up to 70 minutes from the astronomical sunset were observed, with this offset decreasing if the devices are placed under obstructions and on cloudy days. Development of setting the right thresholds was done and using a number of consecutive days for polynomial fitting the day length duration is determined with accuracy allowing synchronization within max 5 minutes, which is acceptable for most applications.

## Part Conclusion

The contributions and general work within PIPV have helped multiple companies in developing products, facilitated the creation of the spin-off company Nordic Firefly and provided scientific documentation of the products functionality required for the involving companies to successfully sell their products.

## Conclusion

The research presented in this thesis covers many fields within applied photovoltaics underlining that applied photovoltaics is a multidisciplinary and broad field. The fields are reflecting the work in which I have been involved and is addressing the need for the involved companies which has been a part of the projects. The description of the specific sections end with a part conclusion, summarizing the overall progress and contributions within the specific fields.

The first topic that was presented was fault finding of faulty panels in the field, where both work on electrical impedance spectroscopy and outdoors electroluminescence imaging was presented.

For the electrical impedance spectroscopy, it has been shown that impedance spectroscopy is a promising method for early detection of faults in the field, and this can be done during nighttime without compromising power production. Further work on correlating degradations states to characteristic impedance spectra is proposed, and further work on locating the faulty panel in the string is proposed as well.

Research correlating the impedance spectra with faults for single cells is done in [65], where some of the work presented here, is cited.

The outdoor electroluminescence proves that it is feasible to acquire electroluminescence images from a Drone, provided, that the string can be forward biased using a waveform and advanced image processing, correcting images and subtracting dark and light images, are done. Within this topic there is still ongoing research to mature the technology and also photoluminescence imaging for outdoor applications is under development.

For both methods excitation signals to the string is needed, which could be provided from the inverter or the combiner boxes, however development work here is required to reverse the power flow.

For the optical part the relative reflection loss has been characterized on single cell laminates and been validated through a round robin campaign. Further, the laboratory measurement system was expanded to facilitate single plane reflectance measurements allowing also color characterization of BIPV samples. The round robin campaign has gained attention within the community, and the measurement uncertainty for different IAM methods has been compared, which is useful for evaluating the variability for reflection losses.

The color characterization has already proved to be a very useful tool in the assessment of and development of colored BIPV solutions. Further, the tool is also useful for color stability measurements after accelerated aging, since the lifetime requirements of BIPV products is very high, 30-50 years as for conventional building materials. Future research also involves assessing glare from BIPV materials, which can help authorities in developing useful guidelines and legislation.

The development of the reflector concept showed development of a prototype, however the rapid price decline of solar cells and modules, made this solution less attractive.

The work presented within the product integrated photovoltaics, where a laboratory, a living lab and various performance models have been developed and used for product development, have enabled successful products for our collaborating companies and enabled the creation of the spin-off company

Nordic Firefly. Further research within this field is ongoing - especially for improving the performance models of the systems.

Overall this thesis presents progress in all fields and is contributing to improve the applications of photovoltaics within the specific fields.

## Bibliography

- [1] M. Schmela, A. Beauvais, L. Clark-Memler, M. Heisz, B. Ildefonso, and R. Rossi, "Global Market Outlook For Solar Power / 2020 - 2024," 2020.
- [2] IEA, "World Energy Outlook 2020," Paris, 2020.
- [3] B. Burger *et al.*, "Photovoltaics Report," 2020.
- [4] VDMA, "Update ITRPV 2020 Results 2019 including maturity report 2020." 2020.
- [5] R. Fu, D. Feldman, and R. Margolis, "U.S. Solar Photovoltaic System Cost Benchmark: Q1 2018," *Nrel*, no. November, pp. 1–47, 2018.
- [6] G. Di Lorenzo, R. Araneo, M. Mitolo, A. Niccolai, and F. Grimaccia, "Review of O&M Practices in PV Plants: Failures, Solutions, Remote Control, and Monitoring Tools," *IEEE J. Photovoltaics*, vol. 10, no. 4, pp. 914–926, 2020, doi: 10.1109/JPHOTOV.2020.2994531.
- [7] International Renewable Energy Agency - IRENA, *Future of solar photovoltaic*, vol. November. 2019.
- [8] IEA-PVPS Task 13, "PV Performance Modeling Methods and Practices Results from the 4th PV Performance Modeling Collaborative Workshop," 2017.
- [9] IEA-PVPS Task 13, "Uncertainty in Yield Assessments and PV LCOE," 2020.
- [10] SolarPower Europe. & ETIP PV, "Solar Skins : An opportunity for greener cities," 2019.
- [11] IEA PVPS Task 15, "Coloured BIPV-Market, Research and Development," 2019.
- [12] IEA PVPS Task 15, *Multifunctional Characterisation of BIPV Proposed Topics for Future International Standardisation Activities Task 15 Enabling Framework for BIPV acceleration*. 2020.
- [13] K. Mertens, *Photovoltaics: Fundamentals, Technology, and Practice*, 2nd ed. Wiley, 2018.
- [14] G. Apostolou, "Design Features of Product-Integrated PV An Evaluation of Various Factors under Indoor Irradiance Conditions," Delft University of Technology, 2016.
- [15] M. Köntges *et al.*, *Review of Failures of Photovoltaic Modules*. 2014.
- [16] Emazys, "EMAZYS." [Online]. Available: <https://emazys.com/>. [Accessed: 12-Nov-2020].
- [17] I. Mora-Seró, G. Garcia-Belmonte, P. P. Boix, M. A. Vázquez, and J. Bisquert, "Impedance spectroscopy characterisation of highly efficient silicon solar cells under different light illumination intensities," *Energy Environ. Sci.*, vol. 2, no. 6, pp. 678–686, 2009, doi: 10.1039/b812468j.
- [18] M. I. Oprea *et al.*, "Impedance Characterization of PV Modules in Outdoor Conditions," *32nd Eur. Photovolt. Sol. Energy Conf. Exhib.*, no. 64014, pp. 1849–1853, 2016.
- [19] M. I. Oprea *et al.*, "Detection of potential induced degradation in c-Si PV panels using electrical impedance spectroscopy," in *Conference Record of the IEEE Photovoltaic Specialists Conference*, 2016, vol. 2016-Novem, doi: 10.1109/PVSC.2016.7749885.
- [20] S. Thorsteinsson *et al.*, "Novel field test design for acquisition of DC and AC parameters during service,"

- Conf. Rec. IEEE Photovolt. Spec. Conf.*, vol. 2016-Novem, pp. 1608–1610, 2016, doi: 10.1109/PVSC.2016.7749892.
- [21] J. Symonowicz, N. Riedel, S. Thorsteinsson, D. Sera, and P. Behrendorff Poulsen, “New Method of Silicon Photovoltaic Panel Fault Detection Using Impedance Spectroscopy,” *33rd Eur. Photovolt. Sol. Energy Conf. Exhib.*, pp. 1831–1835, 1831.
- [22] Huawei, “*濟無*No Title No Title.” [Online]. Available: <https://solar.huawei.com/eu/Products/FusionSolar>. [Accessed: 20-Nov-2020].
- [23] Solarity, “Exclusive List of Top Trends for the PV industry (2020),” 2020. [Online]. Available: <https://solarity.cz/blog/trends-for-pv-industry-in-2020/>. [Accessed: 26-Jan-2021].
- [24] S. Spataru, P. Hacke, and D. Sera, “Automatic Detection of Inactive Solar Cell Cracks in Electroluminescence Images,” pp. 1421–1426, 2018, doi: 10.1109/pvsc.2017.8366106.
- [25] S. V Spataru *et al.*, “Method for Evaluating the Severity of Solar Cell Cracks in,” in *Proceedings of 37th European Photovoltaic Solar Energy Conference and Exhibition*, 2020, pp. 1130–1135, doi: <https://doi.org/10.4229>.
- [26] M. Köntges *et al.*, *Assessment of photovoltaic module failures in the field*. 2017.
- [27] C. Honsberg and S. Bowden, “Photovoltaics Education Website - Electroluminescence,” *Photovoltaics Education Website*, 2019. [Online]. Available: <https://www.pveducation.org/pvcdrom/characterisation/electroluminescence>. [Accessed: 12-Jan-2021].
- [28] G. A. D. R. Benatto *et al.*, “Development of outdoor luminescence imaging for drone-based PV array inspection,” in *Proceedings of the 44th IEEE Photovoltaic Specialists Conference, PVSC 2017*, 2017, pp. 2682–2687, doi: 10.1109/PVSC.2017.8366602.
- [29] G. Alves dos Reis Benatto *et al.*, “Luminescence Imaging Strategies for Drone-Based PV Array Inspection,” *33rd Eur. Photovolt. Sol. Energy Conf. Exhib.*, pp. 2016–2020, 2017.
- [30] M. Köntges, I. Kunze, S. Kajari-Schröder, X. Breitenmoser, and B. Bjørneklett, “The risk of power loss in crystalline silicon based photovoltaic modules due to micro-cracks,” *Sol. Energy Mater. Sol. Cells*, vol. 95, no. 4, pp. 1131–1137, 2011, doi: 10.1016/j.solmat.2010.10.034.
- [31] G. A. dos Reis Benatto *et al.*, “Image Processing for daylight Electroluminescence PV Imaging acquired in movement,” *35th Eur. Photovolt. Sol. Energy Conf. Exhib.*, vol. 1, no. September, pp. 2005–2009, 2018, doi: 10.4229/35thEUPVSEC20182018-6DV.1.19.
- [32] C. Mantel *et al.*, “Correcting for Perspective Distortion in Electroluminescence Images of Photovoltaic Panels,” in *2018 IEEE 7th World Conference on Photovoltaic Energy Conversion, WCPEC 2018 - A Joint Conference of 45th IEEE PVSC, 28th PVSEC and 34th EU PVSEC*, 2018, doi: 10.1109/PVSC.2018.8547724.
- [33] G. A. Dos Reis Benatto *et al.*, “Outdoor Electroluminescence Acquisition Using a Movable Testbed,” in *2018 IEEE 7th World Conference on Photovoltaic Energy Conversion, WCPEC 2018 - A Joint Conference of 45th IEEE PVSC, 28th PVSEC and 34th EU PVSEC*, 2018, doi: 10.1109/PVSC.2018.8547628.
- [34] G. Alves Dos Reis Benatto *et al.*, “Drone-Based Daylight Electroluminescence Imaging of PV Modules,” *IEEE J. Photovoltaics*, vol. 10, no. 3, pp. 872–877, 2020, doi: 10.1109/JPHOTOV.2020.2978068.
- [35] G. A. D. R. Benatto *et al.*, “Photoluminescence Imaging Induced by Laser Line Scan: Study for Outdoor Field Inspections,” in *2018 IEEE 7th World Conference on Photovoltaic Energy Conversion, WCPEC 2018 - A Joint Conference of 45th IEEE PVSC, 28th PVSEC and 34th EU PVSEC*, 2018, doi: 10.1109/PVSC.2018.8547416.
- [36] G. A. dos Reis Benatto *et al.*, “Scaling up Laser Line Photoluminescence Imaging for Outdoor Inspections,” *35th Eur. Photovolt. Sol. Energy Conf. Exhib.*, pp. 1352–1354, 2018, doi: 10.4229/35thEUPVSEC20182018-

5CV.3.41.

- [37] G. A. dos Reis Benatto, A. A. Santamaria Lancia, T. K. Hass, P. B. Poulsen, and S. V Spataru, "Detection of Solar Cell Cracks by Laser Line Induced Lateral Currents and Luminescence Imaging," *37th Eur. Photovolt. Sol. Energy Conf. Exhib.*, pp. 1053–1057, 2020, doi: 10.4229/EUPVSEC20202020-4AV.1.40.
- [38] International Energy Agency, *Technical Assumptions used in PV Financial Models*. 2017.
- [39] S. Boppana, K. Passow, J. Sorensen, B. H. King, and C. Robinson, "Impact of Uncertainty in IAM Measurement on Energy Predictions," *2018 IEEE 7th World Conf. Photovolt. Energy Conversion, WCPEC 2018 - A Jt. Conf. 45th IEEE PVSC, 28th PVSEC 34th EU PVSEC*, pp. 2276–2281, 2018, doi: 10.1109/PVSC.2018.8548024.
- [40] BIPVBOOST, "Update on BIPV market and stakeholder analysis," no. October 2018, 2019.
- [41] R. S. Davidsen *et al.*, "BLACK SILICON SOLAR CELLS WITH BLACK RIBBONS," in *32nd European Photovoltaic Solar Energy Conference and Exhibition*, 2016, pp. 631–634.
- [42] R. S. Davidsen, "Nanostructuring of Solar Cell Surfaces." DTU, Kgs. Lyngby, 2016.
- [43] M. Amdemeskel *et al.*, "Indoor Measurement of Angle Resolved Light Absorption by Antireflective Glass in Solar Panels," *33rd Eur. Photovolt. Sol. Energy Conf. Exhib.*, pp. 1723–1726, 2017, doi: 10.4229/EUPVSEC20172017-5BV.4.78.
- [44] M. W. Amdemeskel *et al.*, "Indoor Measurement of Angle Resolved Light Absorption by Black Silicon," no. i, pp. 2672–2676, 2018, doi: 10.1109/pvsc.2017.8366366.
- [45] N. Riedel-Lyngskær *et al.*, "Interlaboratory comparison of methodologies for measuring the angle of incidence dependence of solar cells," *35th Eur. Photovolt. Sol. Energy Conf. Exhib.*, no. i, pp. 1034–1039, 2018, doi: 10.4229/35thEUPVSEC20182018-5BO.10.4.
- [46] N. Riedel-Lyngskær *et al.*, "Interlaboratory comparison of angular-dependent photovoltaic device measurements: Results and impact on energy rating," *Prog. Photovoltaics Res. Appl.*, no. July, pp. 1–19, 2020, doi: 10.1002/pip.3365.
- [47] W. R. McCluney, *Introduction to Radiometry and Photometry, 2nd ed.* Artech House, 2014.
- [48] G. Peharz *et al.*, "Quantifying the influence of colors on the performance of c-Si photovoltaic devices," *J. Chem. Inf. Model.*, vol. 208, no. October, pp. 299–308, 2013, doi: 10.1016/j.enbuild.2019.109623.
- [49] J. Halme and P. Mäkinen, "Theoretical efficiency limits of ideal coloured opaque photovoltaics," *Energy Environ. Sci.*, vol. 12, no. 4, pp. 1274–1285, 2019, doi: 10.1039/c8ee03161d.
- [50] A. Røyset, T. Kolås, and B. P. Jelle, "Coloured building integrated photovoltaics: Influence on energy efficiency," *Energy Build.*, vol. 208, 2020, doi: 10.1016/j.enbuild.2019.109623.
- [51] M. Babin, A. Thorseth, A. A. S. Lancia, and S. Thorsteinsson, "CHARACTERISATION OF ANGULAR DEPENDENT OPTICAL PROPERTIES OF DIFFERENT COLORING TECHNOLOGIES EMPLOYED IN BIPV PRODUCTS," in *36th European Photovoltaic Solar Energy Conference and Exhibition*, 2020, pp. 1136–1142.
- [52] European Parliament, *Directive (EU) 2018/844 of the European Parliament and of the Council of 30 May 2018 amending Directive 2010/31/EU on the energy performance of buildings and Directive 2012/27/EU on energy efficiency*. European Union, 2018.
- [53] M. L. Jakobsen, S. Thorsteinsson, P. B. Poulsen, P. M. Rodder, and K. Rodder, "Vertical reflector for bifacial PV-panels," *2016 IEEE 44th Photovolt. Spec. Conf. PVSC 2016*, pp. 1–4, 2016, doi: 10.1109/PVSC.2017.8366625.
- [54] M. L. Jakobsen, S. Thorsteinsson, P. B. Poulsen, P. M. Rødder, and K. Rødder, "RAY TRACING MODELLING

- OF REFLECTOR FOR VERTICAL BIFACIAL PANEL,” in *32nd European Photovoltaic Solar Energy Conference and Exhibition*, 2016, pp. 1418–1420.
- [55] M. L. Jakobsen, S. Thorsteinsson, P. B. Poulsen, N. Riedel, P. M. Rødder, and K. Rødder, “Bifacial PV cell with reflector for stand-alone mast for sensor powering purposes,” in *AIP Conference Proceedings*, 2017, vol. 1881, doi: 10.1063/1.5001437.
- [56] A. Reinders, P. Verlinden, W. Van Sark, and A. Freundlich, *Photovoltaic Solar Energy*. Wiley, 2017.
- [57] W. Eggink and A. Reinders, “PRODUCT INTEGRATED PV: THE FUTURE IS DESIGN AND STYLING,” in *32nd European Photovoltaic Solar Energy Conference and Exhibition*, 2016, pp. 2823–2826.
- [58] S. Thorsteinsson *et al.*, “PV LED ENGINE CHARACTERIZATION LAB FOR STANDALONE LIGHT TO LIGHT SYSTEMS,” in *29th European Photovoltaic Solar Energy Conference and Exhibition PV*, 2014, pp. 3059–3061.
- [59] R. O. Ploug *et al.*, “DESIGNING HIGH EFFICIENT SOLAR POWERED OLED LIGHTING SYSTEMS,” in *32nd European Photovoltaic Solar Energy Conference and Exhibition*, 2016, pp. 2523–2527.
- [60] Nordic Firefly, “Nordic Firefly.” [Online]. Available: <http://www.nordicfirefly.com/>. [Accessed: 09-Dec-2020].
- [61] P. Nymann *et al.*, “DESIGN, CHARACTERIZATION AND MODELLING OF HIGH EFFICIENT SOLAR POWERED LIGHTING SYSTEMS,” in *32nd European Photovoltaic Solar Energy Conference and Exhibition*, 2016, pp. 2832–2836.
- [62] P. B. Poulsen *et al.*, “Designing high efficient solar powered lighting systems,” in *Conference Record of the IEEE Photovoltaic Specialists Conference*, 2016, vol. 2016-Novem, doi: 10.1109/PVSC.2016.7750143.
- [63] P. B. Poulsen *et al.*, “Sun Hub – Energy Hub for Outdoor Tables,” *33rd Eur. Photovolt. Sol. Energy Conf. Exhib.*, pp. 2771–2774, 2017, doi: 10.4229/EUPVSEC20172017-6BV.3.105.
- [64] A. Adrian Santamaria Lancia, N. Riedel, R. O. Ploug, S. Thorsteinsson, P. B. Poulsen, and A. Gisele Dos Reis Benatto, “Synchronization of Solar Stand-alone Devices and Autonomous Energy Management through Solar Time Measurements,” in *2018 IEEE 7th World Conference on Photovoltaic Energy Conversion, WCPEC 2018 - A Joint Conference of 45th IEEE PVSC, 28th PVSEC and 34th EU PVSEC*, 2018, doi: 10.1109/PVSC.2018.8548183.
- [65] N. Katayama, S. Osawa, S. Matsumoto, T. Nakano, and M. Sugiyama, “Solar Energy Materials and Solar Cells Degradation and fault diagnosis of photovoltaic cells using impedance spectroscopy,” *Sol. Energy Mater. Sol. Cells*, vol. 194, no. January, pp. 130–136, 2019, doi: 10.1016/j.solmat.2019.01.040.

## Total list of publications

### Journal articles

#### **Drone-Based Daylight Electroluminescence Imaging of PV Modules**

Benatto, G. A. D. R., Mantel, C., Spataru, S. V., Santamaria Lancia, A. A., Riedel, N., Thorsteinsson, S., Poulsen, P., Parikh, H. R., Forchhammer, S. & Séra, D., 2020, In : *IEEE Journal of Photovoltaics*. 10, 3, p. 872 - 877

Citation index: 3

#### **Bifacial PV cell with reflector for stand-alone mast for sensor powering purposes**

Jakobsen, M. L., Thorsteinsson, S., Poulsen, P. B., Riedel, N., Rødder, P. M. & Rødder, K., 2017, In : *Aip Conference Proceedings*. 1881, 8 p., 070004.

Citation index: 1

#### **Photovoltage versus microprobe sheet resistance measurements on ultrashallow structures**

Clarysse, T., Moussa, A., Parmentier, B., Bogdanowicz, J., Vandervorst, W., Bender, H., Pfeffer, M., Schellenberger, M., Nielsen, P. F., Thorsteinsson, S., Lin, R. & Petersen, D. H., 2010, In : *Journal of Vacuum Science and Technology. Part B. Microelectronics and Nanometer Structures*. 28, 1C, p. 8-14

Citation index: 5

#### **Accurate microfour-point probe sheet resistance measurements on small samples**

Thorsteinsson, S., Wang, F., Petersen, D. H., Hansen, T. M., Kjær, D., Lin, R., Kim, J-Y., Nielsen, P. F. & Hansen, O., 2009, In : *Review of Scientific Instruments*. 80, 5, p. 053902

Citation index: 43

#### **Parametric Investigation of Rate Enhancement during fast Temperature Cycling of CO Oxidation in Microreactors**

Jensen, S., Thorsteinsson, S., Hansen, O. & Quaade, U., 2008, In : *Chemical Engineering Journal*. 135, S1, p. S237-S241

Citation index: 3

#### **Forced thermal cycling of catalytic reactions: experiments and modelling**

Jensen, S., Olsen, J. L., Thorsteinsson, S., Hansen, O. & Quaade, U., 2007, In : *Catalysis Communications*. 8, p. 1985-1990

Citation index: 8

#### **Oxidation of methane over a Rh/Al<sub>2</sub>O<sub>3</sub> catalyst using microfabricated reactors with integrated heating**

Younes-Metzler, O., Johansen, J., Thorsteinsson, S., Jensen, S., Hansen, O. & Quaade, U., 2006, In : *Journal of Catalysis*. 241, 1, p. 74-82

### Conference proceedings:

#### **Characterisation of Angular Dependent Optical Properties of Different Coloring Technologies Employed in BIPV Products.**

Babin, M., Santamaria Lancia, A. A., Thorseth, A. & Thorsteinsson, S., 2020, *Proceedings of 37th European Photovoltaic Solar Energy Conference and Exhibition*. p. 1136-1142

### **Large-Scale Bifacial PV Test Field Performance Compared to Simulations Using Commercially Available Software, Research-Based and Open Source Tools**

Riedel, N., Berrian, D., Alvarez Mira, D., Aguilar Protti, A. C. D., Thorsteinsson, S., Poulsen, P. B., Libal, J. & Vedde, J., 2020, *Proceedings of 37th European Photovoltaic Solar Energy Conference and Exhibition*. p. 1324-1329

### **Method for Evaluating the Severity of Solar Cell Cracks in Electroluminescence Images**

Spataru, S., Benatto, G. A. D. R., Hass, T. K., Santamaria Lancia, A. A., Poulsen, P. B. & Thorsteinsson, S., 2020, *Proceedings of 37th European Photovoltaic Solar Energy Conference and Exhibition*. p. 1130-1135

### **Sunlight Variation Study for Drone-Based Daylight Electroluminescence Imaging of PV Modules**

Benatto, G. A. D. R., Mantel, C., Santamaria Lancia, A. A., Villebro, F., Riedel, N., Thorsteinsson, S., Poulsen, P., Forchhammer, S., Parikh, H. R., Spataru, S. V. & Séra, D., 2019, *Proceedings of 36th European Photovoltaic Solar Energy Conference and Exhibition*. p. 1651-1655 (36th European Photovoltaic Solar Energy Conference and Exhibition).

### **Correcting for Perspective Distortion in Electroluminescence Images of Photovoltaic Panels**

Mantel, C., Spataru, S., Parikh, H., Sera, D., Benatto, G. A. D. R., Riedel, N., Thorsteinsson, S., Poulsen, P. B. & Forchhammer, S., 2018, *Proceedings of 7th World Conference on Photovoltaic Energy Conversion*. IEEE.

### **Direct Beam and Diffuse Spectral Irradiance Measurements in a Nordic Country Analyzed With the Average Photon Energy Parameter**

Riedel, N., Thorseth, A., Santamaria Lancia, A. A., Thorsteinsson, S., Poulsen, P. B., Iandolo, B., Davidsen, R. S. & Benatto, G. A. D. R., 2018, *Proceedings of 7th World Conference on Photovoltaic Energy Conversion*. IEEE

### **Image Processing for daylight Electroluminescence PV Imaging acquired in movement**

Benatto, G. A. D. R., Mantel, C., Santamaria Lancia, A. A., Gravensen, M., Riedel, N., Thorsteinsson, S., Poulsen, P. B., Forchhammer, S., Parikh, H., Spataru, S. & Sera, D., 2018, *Proceedings of the 35th European Photovoltaic Solar Energy Conference and Exhibition*. p. 2005 - 2009 6DV.1.19

### **Interlaboratory comparison of methodologies for measuring the angle of incidence dependence of solar cells**

Riedel, N., Santamaria Lancia, A. A., Amdemeskel, M. W., Thorsteinsson, S., Poulsen, P. B., Plag, F., Kröger, I., Slooff, L. H., Jansen, M. J., Carr, A. J., Manshanden, P., Bliss, M., Betts, T., Jauregui, I. P., Mayo, M. E., Balenzategui, J. L., Roldan, R., Kräling, U., Baarah, G., Iandolo, B. & 4 others, , 2018, *Proceedings of the 35th European Photovoltaic Solar Energy Conference and Exhibition*.

### **Outdoor Electroluminescence Acquisition Using a Movable Testbed**

Benatto, G. A. D. R., Mantel, C., Riedel, N., Santamaria Lancia, A. A., Thorsteinsson, S., Poulsen, P. B., Forchhammer, S., Thorseth, A., Dam-Hansen, C., Kenn H. B., F., Vedde, J., Larsen, M., Voss, H., Parikh, H., Spataru, S. & Sera, D., 2018, *Proceedings of 7th World Conference on Photovoltaic Energy Conversion*. IEEE, p. 0400-0404

### **Photoluminescence Imaging Induced by Laser Line Scan: Study for Outdoor Field Inspections**

Benatto, G. A. D. R., Chi, M., Jensen, O. B., Santamaria Lancia, A. A., Riedel, N., Iandolo, B., Davidsen, R. S., Hansen, O., Thorsteinsson, S. & Poulsen, P. B., 2018, *Proceedings of 7th World Conference on Photovoltaic Energy Conversion*. IEEE, p. 0395-0399

### **Scaling up Laser Line Photoluminescence Imaging for Outdoor Inspections**

*Benatto, G. A. D. R., Chi, M., Santamaria Lancia, A. A., Riedel, N., Jensen, O. B., Thorseth, A., Dam-Hansen, C., Thorsteinsson, S. & Poulsen, P. B., 2018, Proceedings of the 35th European Photovoltaic Solar Energy Conference and Exhibition.*

### **SNR Study of Outdoor Electroluminescence Images under High Sun Irradiation**

*Mantel, C., Benatto, G. A. D. R., Riedel, N., Thorsteinsson, S., Poulsen, P. B., Parikh, H., Spataru, S., Sera, D. & Forchhammer, S., 2018, Proceedings of 7th World Conference on Photovoltaic Energy Conversion. IEEE, p. 3285-3289*

### **Synchronization of Solar Stand-alone Devices and Autonomous Energy Management through Solar Time Measurements**

*Santamaria Lancia, A. A., Riedel, N., Ploug, R. O., Thorsteinsson, S., Poulsen, P. B. & Benatto, G. A. D. R., 2018, Proceedings of 7th World Conference on Photovoltaic Energy Conversion. IEEE, p. 0632 -0637*

### **Black silicon solar cells with black bus-bar strings**

*Daidsen, R. S., Tang, P. T., Mizushima, I., Thorsteinsson, S., Poulsen, P. B., Frausig, J., Nordseth, O. & Hansen, O., 2017, 2016 IEEE 43rd Photovoltaic Specialists Conference (PVSC). IEEE, p. 2885-2888 4 p.*

### **Designing high efficient solar powered lighting systems**

*Poulsen, P. B., Thorsteinsson, S., Lindén, J., Ploug, R. O., Knott, A., Mira Albert, M. D. C., Mogensen, I. & Retoft, K., 2017, Proceedings of the 2017 IEEE 44th Photovoltaic Specialist Conference (PVSC). IEEE.*

### **Development of outdoor luminescence imaging for drone-based PV array inspection**

*Benatto, G. A. D. R., Riedel, N., Thorsteinsson, S., Poulsen, P. B., Thorseth, A., Dam-Hansen, C., Mantel, C., Forchhammer, S., H. B. Frederiksen, K., Vedde, J., Petersen, M., Voss, H., Messerschmidt, M., Parikh, H., Spataru, S. & Sera, D., 2017, Proceedings of the 44th IEEE Photovoltaic Specialists Conference, Ppsc 2017. IEEE, 2 p. (Proceedings of the 44th IEEE Photovoltaic Specialists Conference, Ppsc 2017).*

### **Indoor measurement of angle resolved light absorption by antireflective glass in solar panels**

*Amdemeskel, M. W., Benatto, G. A. D. R., Riedel, N., Iandolo, B., Davidsen, R. S., Hansen, O., Poulsen, P. B., Thorsteinsson, S., Thorseth, A. & Dam-Hansen, C., 2017, Proceedings of the 33rd European Photovoltaic Solar Energy Conference and Exhibition.*

### **Indoor Measurement of Angle Resolved Light Absorption by Black Silicon**

*Amdemeskel, M. W., Iandolo, B., Davidsen, R. S., Hansen, O., Benatto, G. A. D. R., Riedel, N., Poulsen, P. B., Thorsteinsson, S., Thorseth, A. & Dam-Hansen, C., 2017, Proceedings of the international 2017 IEEE Photovoltaic Specialists Conference. IEEE*

### **Luminescence Imaging Strategies for Drone-Based PV Array Inspection**

*Benatto, G. A. D. R., Riedel, N., Mantel, C., Thorsteinsson, S., Poulsen, P. B., Chi, M., Thorseth, A., Jensen, O. B., Dam-Hansen, C., Forchhammer, S., Kenn H. B., F., Vedde, J., Petersen, M., Voss, H., Messerschmidt, M., Messerschmidt, M., Parikh, H., Spataru, S. & Sera, D., 2017, Proceedings of 33rd European Photovoltaic Solar Energy Conference and Exhibition.*

### **New method of silicon photovoltaic panel fault detection using impedance spectroscopy**

*Symonowicz, J. K., Riedel, N., Thorsteinsson, S., Sera, D. & Poulsen, P. B., 2017, Proceedings of 33rd European Photovoltaic Solar Energy Conference and Exhibition. p. 1831-5*

### **SUN HUB – ENERGY HUB FOR OUTDOOR TABLES**

*Poulsen, P. B., Benatto, G. A. D. R., Riedel, N., Thorsteinsson, S., Santamaria Lancia, A. A., Symonowicz, J. K., Retoft, K. & Mogensen, I., 2017, Proceedings of 33rd European Photovoltaic Solar Energy Conference and Exhibition. p. 2771-2774*

### **Toward a drone-based EL and PL inspection tool for PV power plants**

*Riedel, N., Benatto, G. A. D. R., Thorsteinsson, S., Poulsen, P. B., Spataru, S. & Sera, D., 2017, PV Reliability Workshop.*

### **Angle Resolved Performance Measurements on PV Glass and Modules.**

*Juutilainen, L. T., Thorsteinsson, S., Poulsen, P. B., Thorseth, A., Amdemeskel, M. W., Canulescu, S., Rødder, P. M. & Rødder, K., 2016, Proceedings of the 2016 European Photovoltaic Solar Energy Conference and Exhibition 2016. p. 2235-8*

### **Black silicon solar cells with black bus-bar strings**

*Daidsen, R. S., Tang, P. T., Mizushima, I., Thorsteinsson, S., Poulsen, P. B., Frausig, J., Nordseth, Ø. & Hansen, O., 2016, Proceedings of 43rd IEEE Photovoltaic Specialists Conference. IEEE, p. 2885-2888*

### **Black Silicon Solar Cells with Black Ribbons.**

*Daidsen, R. S., Tang, P. T., Mizushima, I., Thorsteinsson, S., Poulsen, P. B., Frausig, J., Nordseth, Ø. & Hansen, O., 2016, Proceedings of the EU PVSEC 2016.*

### **Black silicon with black bus-bar strings**

*Daidsen, R. S., Tang, P. T., Mizushima, I., Thorsteinsson, S., Poulsen, P. B., Frausig, J., Nordseth, Ø. & Hansen, O., 2016, Proceedings of Norwegian Solar Cell Conference 2016.*

### **Design, Characterization and Modelling of High Efficient Solar Powered Lighting Systems**

*Nymann, P., Svane, F., Poulsen, P. B., Thorsteinsson, S., Lindén, J., Ploug, R. O., Mira Albert, M. D. C., Knott, A., Mogensen, I. & Retoft, K., 2016, Proceedings of the 2016 European Photovoltaic Solar Energy Conference and Exhibition 2016. p. 2827-31*

### **Designing high efficient solar powered lighting systems**

*Poulsen, P. B., Thorsteinsson, S., Lindén, J., Ploug, R. O., Knott, A., Mira Albert, M. D. C., Mogensen, I. & Retof, K., 2016, Proceedings of IEEE 43rd Photovoltaic Specialist Conference 2016. IEEE, p. 2712-2714*

### **Designing High Efficient Solar Powered OLED Lighting Systems.**

*Ploug, R. O., Poulsen, P. B., Thorsteinsson, S., Thorseth, A., Corell, D. D., Wolff, J., Dam-Hansen, C. & Knott, A., 2016, Proceedings of the 2016 European Photovoltaic Solar Energy Conference and Exhibition.*

### **Detection of Potential Induced Degradation in c-Si PV Panels Using Electrical Impedance Spectroscopy**

*Oprea, M., Spataru, S., Sera, D., Basu, R., Andersen, A., Poulsen, P. B. & Thorsteinsson, S., 2016, 43rd IEEE Photovoltaic Specialist Conference. IEEE, p. 1575-1579*

### **Impedance characterization of PV modules in outdoor conditions**

*Oprea, M., Thorsteinsson, S., Spataru, S., Sera, D., Poulsen, P. B., Andersen, A. & Basu, R., 2016, Proceedings of the 2016 European Photovoltaic Solar Energy Conference and Exhibition - 2016. p. 1849-53*

### **Novel field test design for acquisition of DC and AC parameters during service**

*Thorsteinsson, S., Poulsen, P. B., Schou, J., Andersen, A. R., Basu, R., Sera, D., Spataru, S. & Oprea, M-I., 2016, Proceedings of IEEE 43rd Photovoltaic Specialist Conference 2016. IEEE, p. 1608-1610*

### **Ray Tracing Modelling of Reflector for Vertical Bifacial Panel**

*Jakobsen, M. L., Thorsteinsson, S., Poulsen, P. B., Rødder, P. M. & Rødder, K., 2016, Proceedings of the 2016 European Photovoltaic Solar Energy Conference and Exhibition 2016.*

### **Vertical reflector for bifacial PV-panels**

*Jakobsen, M. L., Thorsteinsson, S., Poulsen, P. B., Rødder, P. M. & Rødder, K., 2016, IEEE 43rd Photovoltaic Specialist Conference 2016. IEEE, p. 2678-2681*

### **PV LED ENGINE characterization lab for stand alone light-to-light systems**

*Poulsen, P. B., Thorsteinsson, S. & Lindén, J., 2015, Proceedings of 4th Symposium Small PV-Applications.*

### **PV led engine characterization lab for standalone light to light systems**

*Thorsteinsson, S., Poulsen, P. B., Lindén, J., Hansen, S. S., Dam-Hansen, C., Mira Albert, M. D. C., Knott, A. & Norby, P., 2014, Proceedings of EU PVSEC 2014.*

### **CopenHybrid – Development of a CO2 Neutral Hybrid Street Lighting System for the Danish Municipalities' Illumination Classes**

*Poulsen, P. B., Dam-Hansen, C., Thorseth, A., Thorsteinsson, S., Lindén, J., Hansen, S. S., Ellermann, S., Bak, C., Skrzypinski, W. R., Beller, C., Kock, C. W., Bühler, F., Harboe, R. K., Boesgaard, P., Jensen, T., Søndergaard, O., Andresen, C., Fahlén, M., Maare, T., Prestegaard, H. & 2 others, , 2013, Proceedings of the 28th EU PVSEC. p. 5DO.13.1 6 p.*

### **Experimental investigation of small wind turbines on hybrid street lamps**

*Skrzypinski, W. R., Thorsteinsson, S., Bak, C., Poulsen, P. B., Thorseth, A., Beller, C., Bühler, F. & Andresen, C., 2013, Proceedings of 12th World Wind Energy Conference & Renewable Energy Exhibition (WVEC 2013). World Wind Energy Association (WWEA)*

### **Simulation Tool for Designing off-Grid PV Applications for the Urban Environments**

*Poulsen, P. B., Dam-Hansen, C., Thorseth, A., Thorsteinsson, S., Lindén, J., Petersen, P. M., Mira Albert, M. D. C., Knott, A., Norby, P., Jensen, A. K., Mogensen, I., Lyhne, M., Herbst, S. & Bay, A., 2013, Proceedings of the 28th EU PVSEC. p. 5CV.7.41 3 p.*

### **Microreactor for investigation of fast temperatur cycling of catalytic reactions**

*Jensen, S., Thorsteinsson, S., Hansen, O. & Quaade, U., 2006, 5th Unsteady-State Processes in Catalysis: USPC-5. Osaka, Japan: Elsevier*

### **Microreactor for investigation of fast temperature cycling of catalytic reactions**

*Jensen, S., Thorsteinsson, S., Hansen, O. & Quaade, U., 2006, 5th International Conference on Unsteady-State Processes in Catalysts (USPC-5). Osaka, Japan, November 22, p. 37-38*

**Nickel silicide thermal stability: effects of oxygen anneal and silicon microstructure**

*Thorsteinsson, S., Jensen, S., Quaade, U., Larsen, A. N., Hansen, J. L. & Hansen, O., 2006, Proceedings of the 20th European Conference on Solid-State Transducers, Eurosensors XX, Gothenburg, Sweden, September 17-20, 2006, paper #W2C-P3. Gothenburg, Sweden*

**Response surface modelling of rate enhancement during fast temperature cycling of catalytic reactions in microreactors**

*Jensen, S., Thorsteinsson, S., Hansen, O. & Quaade, U., 2006, IMRET9 Berlin. Berlin, Germany, p. 132-133*

**Integrated nickel disilicide thermometers for high-temperature applications**

*Thorsteinsson, S., Jensen, S., Younes-Metzler, O., Quaade, U. & Hansen, O., 2005, Proceedings of the 16th Micromechanics Europe Workshop (MME), September 4-6. Gothenburg, Sweden, p. 248-251*

## Contributions

## IMPEDANCE CHARACTERIZATION OF PV MODULES IN OUTDOOR CONDITIONS

Oprea Matei I.<sup>\*1</sup>, Spataru Sergiu V.<sup>1</sup>, Sera Dezso<sup>1</sup>, Thorsteinsson Sune<sup>2</sup>, Poulsen Peter B.<sup>2</sup>,  
Andersen Anders R.<sup>3</sup>, Basu Ronni<sup>3</sup>, Frederiksen Kenn H. B.<sup>4</sup>

<sup>\*</sup>mio@et.aau.dk, <sup>1</sup>Aalborg University, Department of Energy Technology  
Pontoppidanstraede 111, DK-9220 Aalborg, Denmark

<sup>2</sup>Technical University of Denmark, Department of Photonics Engineering  
Frederiksborgvej 399, DK-4000 Roskilde, Denmark

<sup>3</sup>EmaZys Technologies ApS  
Green Tech Center, Lysholt Alle 6, DK-7100 Vejle, Denmark

<sup>4</sup>Kenergy  
Grønningen 43, DK-8700 Horsens, Denmark

**ABSTRACT:** Impedance spectroscopy (IS) has been used for laboratory characterizations of photovoltaic (PV) technologies under well controlled conditions. This work applies IS for outdoor characterization of PV panels, in order to observe the effect of ambient conditions on the PV impedance spectrum, and further construct an impedance model that can link environmental changes to the model's parameters. To achieve this, a setup has been developed for long-term impedance spectra monitoring synchronized with accurate irradiance and temperature data. Preliminary results show clear correlation between the determined parameters and irradiance conditions.

**Keywords:** impedance spectroscopy, photovoltaic panel, photovoltaic string, outdoor characterization, AC model

### 1 INTRODUCTION

It has been shown before that impedance spectroscopy [1, 2] can be used as characterization technique [3-8] for solar cells and PV modules [9]. However, previous works typically focused on materials characterization in laboratory conditions (i.e. in dark or under controlled irradiance and temperature) and not performance or diagnostics. In this study, the focus is on identifying a correlation between environmental variations and equivalent PV module, or string, AC parameters.

Current-voltage (I-V) characterization is perhaps the most common diagnostic tool for both PV strings and modules, but IS methods may have the potential of detecting and locating additional faults and degradation from an early stage of development. The parameters extracted from the impedance model can be used in diagnostic methods, long term monitoring, or to identify arc faults and short-circuits in PV strings.

However, application of IS on operating PV strings, i.e. in outdoor conditions faces the challenge of uncontrolled environmental conditions. The actual irradiance and temperature will affect the overall impedance spectra of the PV string.

A straightforward effect of increased irradiance will be the reduction of the apparent parallel resistance, due to the forward characteristic of the parallel diode (see Fig 1).

On the other hand, the dependency of the parallel capacitance on the ambient conditions is less direct. The capacitance value varies with the operating conditions of the PV cells, meaning irradiance level as well as the operating point on the IV curve [6].

The purpose of this work is to investigate the effect of the ambient conditions on the impedance spectrum of PV modules. These results can be further used to detect system failures when these appear [10].

In a broader perspective, we aim to determine if IS can be an effective field test tool for detecting incipient degradation of the solar cells and modules, which can be difficult to detect outdoor by traditional characterization methods.

IS measurements have been performed outdoor on a crystalline silicon (c-Si) PV module and a string, using a commercial IS analyzer for PV modules and arrays [11].

In order to eliminate the effect of the load (operating point) on the measurement of the parallel capacitance and resistance, all our measurements have been performed in no load (open circuit) conditions.

The measurement procedure is an automated test-setup that is able to continuously monitor the impedance spectra of several standard sized PV modules. The measurement data is processed through fitting for extracting the equivalent circuit parameters (Fig. 1) that are correlated to the information provided by irradiance sensors available on the setup.

The paper is structured as follows: a short description of the AC model used will be discussed in section 2, together with the description of the setup and the parameters used to perform the IS measurements. Further on, in section 3, the measurement results will be presented. Together with the measurement, the parameter fitting results will be discussed. At the end, the study's findings are concluded to offer an overview of this work.

### 2 METHODOLOGY

#### 2.1 Modelling approach

The model considered for determining the parameters is a single diode one [12], as shown in Fig. 1 A). The corresponding AC model [13][6] is shown in Fig. 1 B), where the AC behavior of the diode in the equivalent circuit is modeled by two parallel capacitances ( $C_{diff}$  and  $C_{dep}$ ) and an equivalent resistance ( $R_d$ ). The two parallel capacitors and resistors can be represented by a single component of each type, ( $C_p$  and  $R_p$ ) resulting in the simple AC equivalent circuit in Fig. 1 C), based on which the parameters  $C_p$  and  $R_p$  will be determined [10]. Due to the variability of both  $C_{diff}$  and  $C_{dep}$ , as well as  $R_d$  with the current through the diode D (Fig 1 A), both  $C_p$  and  $R_p$  will be affected by irradiance conditions as well as the operating point of the PV panel or string.

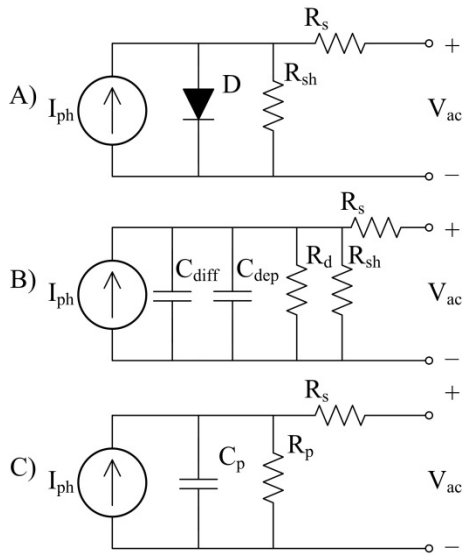


Fig. 1 The single diode model is considered for this study and is presented in A). This DC model can be translated into an AC model presented in B). The two capacitances are considered as a single parallel capacitance ( $C_p$ ). The same approach is applied for the two resistances in parallel ( $R_p$ ), resulting in C).

The series resistance ( $R_s$ ) is considered known and will not be further discussed in this study. On the other hand, the diode's equivalent parameters are dependent on its operating point:  $R_d$  is large when the diode is blocked, while its value decreases significantly with increasing forward current. The  $C_{diff}$  is dominant when the diode is in conduction state and the  $C_{dep}$  can be observed when the diode is blocking state.

The photo-generated current ( $I_{ph}$ ) is dependent on the irradiance and sets the operating point of the diode.

Eq. (1) describes how the parameters of the equivalent circuit (Fig. 1 C) are fitted from the actual measured data. In this study only the variation of the parameters with regard to the irradiance is considered.

The measurement of impedance is made under absolute (norm) and phase (angle) form. In order to apply the fitting, the results are transformed in real and imaginary values. The relations between the two forms of the impedance are presented in eq. (2) and (3). Fig. 3 is given as an example of such a measurement in two different irradiance conditions.

$$Z_{pv} = \left[ R_s + \frac{R_p}{1 + (\omega R_p C_p)^2} \right] - i \left[ \frac{\omega R_p^2 C_p}{1 + (\omega R_p C_p)^2} \right] \quad (1)$$

In eq. (1) the notations used are:  $Z_{pv}$  – PV panel impedance,  $R_s$  – series resistance,  $R_p$  – parallel resistance,  $C_p$  – parallel capacitance,  $\omega$  – angular frequency ( $\omega = 2\pi f$ ) and  $i$  – imaginary operator. The relation between the real and imaginary parts of the impedance and the norm – phase form is given by:

$$|Z_{pv}| = \sqrt{\{Z_{pv}\}_{Re}^2 + \{Z_{pv}\}_{Im}^2} \quad (2)$$

$$\theta = \text{atan2}(\{Z_{pv}\}_{Im}, \{Z_{pv}\}_{Re}) \quad (3)$$

## 2.2 Automatic test setup

Results have been achieved using a single c-Si module mounted on a rooftop installation, which is located in the proximity of an advanced solar irradiance measurement station. Furthermore a string of 12 PV panels composed by 60 c-Si cell has undergone the same routine, but in this case the environmental conditions have been recorded through the string inverter.

The measurements have been performed with a Z100 impedance analyzer that has been automated through software to perform and record impedance spectra at every 9 minutes, meaning around 6 measurements per hour.

The frequency range used for these measurements is from 200 Hz to 100kHz. The lower limit is motivated by hardware limitations. The upper limit is imposed by the increasing effect of the wires inductance as discussed in section 3.

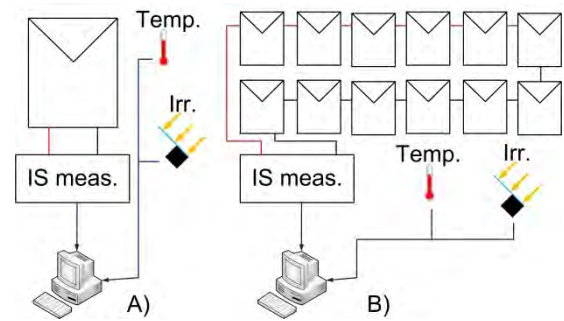


Fig. 2 Principle diagram for module (A) and for string (B) characterization. The measurements are performed over 24 hours using a Z100 impedance analyzer. Both the single panel and string's panels are c-Si modules.

## 3 RESULTS

Performing the measurements as stated at point 2.2 results in a multitude of curves as the ones presented in Fig. 3. Using the model depicted in Fig. 1 C) and characterized by eq. (1) the equivalent parameters of the PV module, or string, are determined. The focus is on the parallel elements of the circuit,  $R_p$  and  $C_p$ , thus the  $R_s$  will not be presented.

The variation of absolute value is similar in both cases, for the panel and for the string. The results are shown in Fig. 4 in the case of the single panel respectively Fig. 8 for the string. The maximum absolute value is greater in the case of the sting, but this was to be expected as there are more panels connected together. In the case of phase, the measurements also yield similar result. The panel's measurements are shown in Fig. 5, while the string's measurements are presented in Fig. 9. Although the general trend is similar, there is a strong inductive influence that can be observed in the case of the sting. This influence can be accounted by the more interconnecting cables used in the string's case. Electromagnetic interference can be observed in both phase measurements in the region of low impedance (around midday).

The fitting results show a change of the operation point of the PV characteristic that is documented in the literature. The parallel resistance, dominated in some cases by the diode's dynamical resistance, is decreasing with regard to irradiance values. Fig. 6 and Fig. 10

present the results for the panel and string.

The opposite can be said about the capacitance. As the PV starts generating current the capacitance grows in direct relation with the irradiance. This can be interpreted considering the model from Fig. 1 B). The capacitance of the depletion region of the diode diminishes as the diffusion capacitance grows, exceeding the value of the first. The direct relation of the  $C_p$  with regard to irradiance is shown in Fig. 7 for the panel and in Fig. 11 in the case of the string.

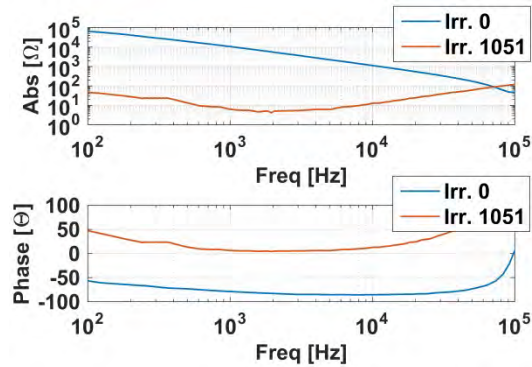


Fig. 3 Impedance spectrum measurement of a PV string, composed by absolute value and phase. Two cases are presented for comparison, and to further ease the understanding of next figures. The first measurement is performed in dark ( $0 \text{ W/m}^2$ ), during the night at 23:53 hours. The second case is a measurement made during high irradiance ( $1051 \text{ W/m}^2$ ), during mid-day at 11:58 hours.

The difference is visible for both, absolute and phase values. The norm decreases almost four orders of size, while the phase's characteristic changes from a capacitive one to more resistive one. It is worth mentioning that over a frequency of 50kHz the inductance of the circuit becomes dominant in relation with the capacitance of the PV modules, and the characteristic becomes strongly inductive. Thus one can conclude that the characteristic of the PV's changes significantly with the irradiance variation. In Fig. 4, Fig. 5, Fig. 8 and Fig. 9 will be shown measurements of impedance spectra over one day, creating a more complex 3D representation of absolute value and phase.

### 3.1 Panel characterization

The results of the IS measurement are presented in Fig. 4 and Fig. 5 for absolute value and phase. The figures show the change in the operating characteristic of the PV panel that goes from dark conditions to light conditions in the open voltage point.

The fitted parameters  $C_p$  and  $R_p$  reflect very well this transition. The resistance is shown in Fig. 6, while the capacitance is shown in Fig. 7. Both the capacitance as well as the resistance experiences a change of a few order of size, even though their changes are not the same. The capacitance is direct proportional with the irradiance, while the resistance is inverse proportional.

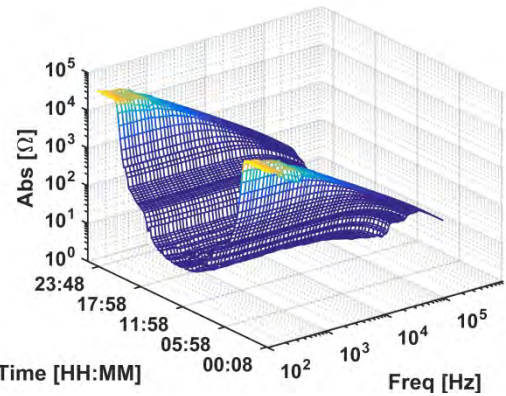


Fig. 4 Panel norm variation during one day. The x axis represents the measurement frequency range. The y axis shows the time point when the measurement has been performed. The z axis represents the absolute value. The shape of the impedance spectra corresponds with the expected variation since the PV panels is entering conduction, thus reducing its impedance. The values can be considered characteristic for a c-Si.

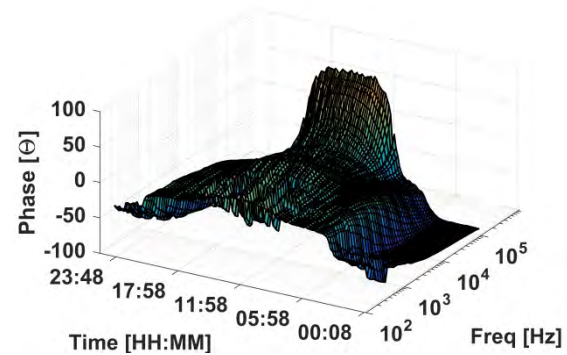


Fig. 5 Panel phase variation during one day. The x axis represents the measurement frequency range. The y axis shows the time point when the measurement has been performed. The z axis represents the phase value. The phase transformation during the day is significant, changing from a capacitive one, in the dark (early hours of the morning and night), to a more resistive-inductive during the day. A strong inductive influence can be observed at measurements during light conditions over the 50kHz threshold. Noise from EMI can be observed in the low impedance region, during midday at low frequency measurements.

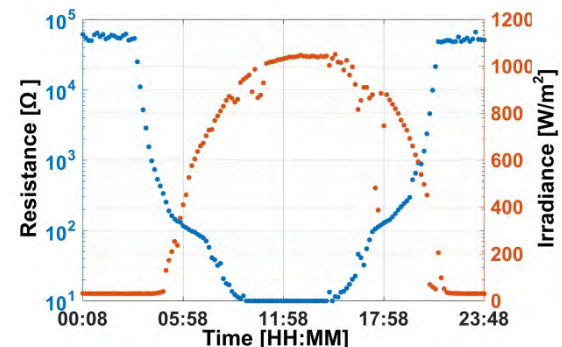


Fig. 6 Parallel resistance of panel. The fitted values of the IS measurements are presented on the left y axis, while the right y axis shows the irradiance variation during the day. The x axis presets the time point when the

measurement used to determine the parameter has been performed. The  $R_p$  varies inverse proportional with the irradiance. The lower value of saturation around  $10\Omega$  is set by the fitting algorithm used for the determination.

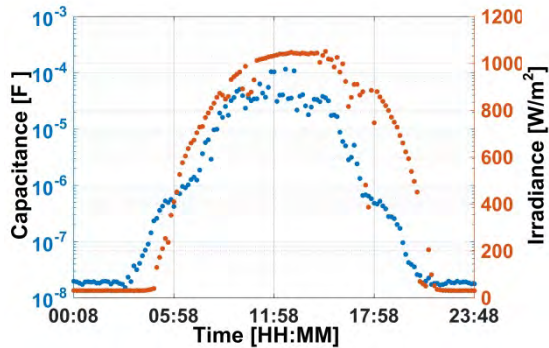


Fig. 7 Parallel capacitance of panel. The fitted values of the IS measurements are presented on the left y axis, while the right y axis shows the irradiance variation during the day. The x axis presets the time point when the measurement used to determine the parameter has been performed. The  $C_p$  parameter is direct proportional to the irradiance variation.

### 3.2 String Characterization

String measurements yield similar results as in the case of the panel. These are shown in Fig. 8, for the absolute value, and in Fig. 9 for the phase. For the string measurements, the absolute value tends to have higher values in the low frequency area. This can be explained as a result of having more panels connected together.

The phase also experiences a much more inductive character due to the interconnecting cables. As in the case of the panel, there is some EMI present in the low frequency area in the region of low impedance.

The fitted results for  $C_p$  and  $R_p$  show the same general trend as in the case of the panel determination. These are presented in Fig. 10 for the resistance and Fig. 11 for the capacitance. The values differ though from the ones seen in the case of the panel. The parallel capacitance is higher, while the parallel resistance is lower.

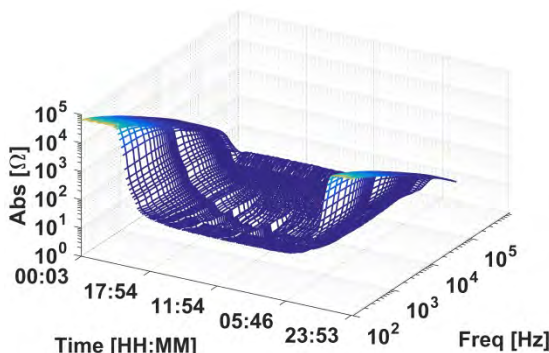


Fig. 8 String norm variation during one day. The x axis represents the measurement frequency range. The y axis shows the time point when the measurement has been performed. The z axis represents the absolute value. The measurement is consistent with the panel measurement presented in Fig. 4.

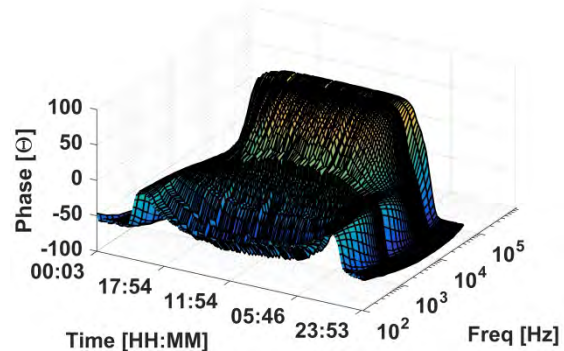


Fig. 9 String phase variation during one day. The x axis represents the measurement frequency range. The y axis shows the time point when the measurement has been performed. The z axis represents the phase value. The variation follows the same trend as the panel's phase in Fig. 5. But the more inductive values of the cables used for connection has a visible effect at a frequency higher than 10kHz in low impedance conditions.

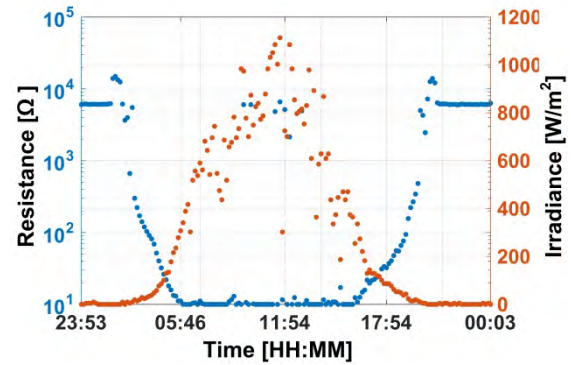


Fig. 10 Parallel resistance of string. The fitted values of the IS measurements are presented on the left y axis, while the right y axis shows the irradiance variation during the day. The x axis presets the time point when the measurement used to determine the parameter has been performed. Once again the string determination is consistent with the panel's determination. The trend is similar, although the lower values of  $R_p$  in dark conditions can be caused by the different characteristics of each of the panels in the string.

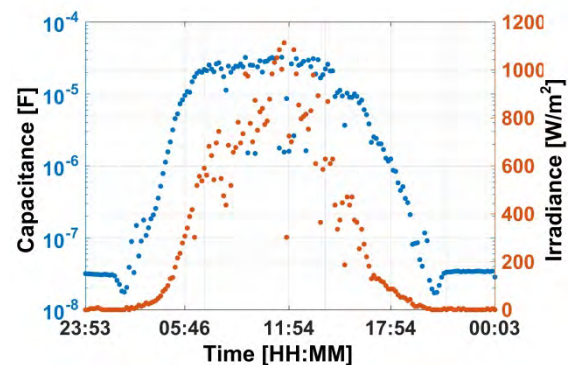


Fig. 11 Parallel capacitance of string. The fitted values of the IS measurements are presented on the left y axis, while the right y axis shows the irradiance variation during the day. The x axis presets the time point when the measurement used to determine the parameter has been

performed. In the case of the sting measurement, a greater value of the capacitance can be observed.

The IS measurements are consistent with the laboratory results simulating different irradiance conditions [4, 9]. Furthermore the parameters variation, both in the case of the parallel resistance as well as in the case of parallel capacitance is as expected from the previous studies [6].

Both the parallel capacitance and the parallel resistance show a very strong variation with irradiance. In both cases the change is around 3-4 orders of magnitude, therefore this significant variation needs to be accounted when AC impedance test are performed in outdoor conditions.

#### 4 CONCLUSION

The results show that IS can be applied to extract equivalent circuit parameters of PV panels and strings in the field, however environmental conditions strongly affect the extracted key parameters, which must be taken into account when drawing conclusion about the state of the panel or string. It is the aim that this analysis can give basis to a dynamical model that can use environmental measurements to account for the PV panel's parameters variation, to be further used for diagnostics.

#### Acknowledgement

This research was partially funded by the Danish Energy Agency within the EUDP program with the project journal number 64014-0507 "New technology for localization and characterization of faults in solar panels".

#### 5 REFERENCES

- [1] J. R. Macdonald, "Impedance spectroscopy," *Annals of Biomedical Engineering*, vol. 20, pp. 289-305, 1992.
- [2] E. Barsoukov and J. R. Macdonald, *Impedance Spectroscopy*: Wiley, 2005.
- [3] L. a. Mallette and R. L. Phillips, "Modeling solar cells for use as optical detectors: background illumination effects.," *Applied optics*, vol. 17, pp. 1786-1788, 1978.
- [4] R. L. Mueller, M. T. Wallace, and P. Iles, "Scaling nominal solar cell impedances for array design," in *Photovoltaic Energy Conversion, 1994., Conference Record of the Twenty Fourth. IEEE Photovoltaic Specialists Conference - 1994, 1994 IEEE First World Conference on* vol. 2, ed, 1994, pp. 2034-2037 vol.2.
- [5] R. Anil Kumar, M. S. Suresh, and J. Nagaraju, "GaAs/Ge solar cell AC parameters under illumination," *Solar Energy*, vol. 76, pp. 417-421, 2004.
- [6] I. Mora-Seró, G. Garcia-Belmonte, P. P. Boix, M. a. Vázquez, and J. Bisquert, "Impedance spectroscopy characterisation of highly efficient silicon solar cells under different light illumination intensities," *Energy & Environmental Science*, vol. 2, p. 678, 2009.
- [7] Y. Y. Proskuryakov, K. Durose, M. K. Al Turkestani, I. Mora-Seró, G. Garcia-Belmonte, F. Fabregat-Santiago, *et al.*, "Impedance spectroscopy of thin-film CdTe/CdS solar cells under varied illumination," *Journal of Applied Physics*, vol. 106, pp. 1-9, 2009.
- [8] D. Chenvidhya, K. Kirtikara, and C. Jivacate, "A new characterization method for solar cell dynamic impedance," *Solar Energy Materials and Solar Cells*, vol. 80, pp. 459-464, 2003.
- [9] D. Chenvidhya, K. Kirtikara, and C. Jivacate, "PV module dynamic impedance and its voltage and frequency dependencies," *Solar Energy Materials and Solar Cells*, vol. 86, pp. 243-251, 2005.
- [10] J. Johnson, D. Schoenwald, S. Kuszmaul, J. Strauch, and W. Bower, "Creating dynamic equivalent PV circuit models with impedance spectroscopy for arc fault modeling," *Conference Record of the IEEE Photovoltaic Specialists Conference*, pp. 002328-002333, 2011.
- [11] (2016). *EmaZys Z100 □□ PV Test Instrument*. Available: <http://emazys.com/z100-pv-test-instrument/>
- [12] T. Markvart and L. Castañer, *Practical Handbook of Photovoltaics: Fundamentals and Applications: Fundamentals and Applications*: Elsevier, 2003.
- [13] S. M. Sze and K. K. Ng, *Physics of Semiconductor Devices*: Wiley, 2006.

# Detection of Potential Induced Degradation in c-Si PV Panels Using Electrical Impedance Spectroscopy

Matei I. Oprea<sup>1</sup>, Sergiu V. Spataru<sup>1</sup>, Dezso Sera<sup>1</sup>, Peter B. Poulsen<sup>2</sup>, Sune Thorsteinsson<sup>2</sup>, Ronni Basu<sup>3</sup>, Anders R. Andersen<sup>3</sup>, Kenn H.B. Frederiksen<sup>4</sup>

<sup>1</sup>Department of Energy Technology, Aalborg University, Aalborg, DK-9220, Denmark

<sup>2</sup>Department of Photonics Engineering, Technical University of Denmark, Roskilde, DK-4000, Denmark

<sup>3</sup>EmaZys Technologies ApS, Vejle, DK-7100, Denmark

<sup>4</sup>Kenergy, Horsens, DK-8700, Denmark

**Abstract** — Impedance spectroscopy (IS) is an established characterization and diagnostic method for different electrical and chemical research areas such as batteries and fuel cells, but not yet widely adopted for photovoltaics (PV). This work, for the first time, investigates an IS based method for detecting potential-induced degradation (PID) in c-Si PV panels. The method has been experimentally tested on a set of panels that were confirmed to be affected by PID by using traditional current-voltage (I-V) characterization methods, as well as electroluminescence (EL) imaging. The results confirm the effectiveness of the new approach to identify PID in PV panels.

**Index Terms** — c-Si PV panel, Impedance spectroscopy, Potential induced degradation, AC modelling, Parameter fitting, Current-voltage characterization, Electroluminescence imaging

## I. INTRODUCTION

Potential-induced degradation (PID) is a failure mode in solar cells caused by voltage stress on the photovoltaic (PV) module. PID can affect both crystalline and thin film modules, to an extent depending on material and environmental factors. In this work only the shunting type PID (PID-s) will be considered. PID-s is a common degradation that can develop rapidly and can cause significant reductions in module performance [1], due to the decreased parallel (shunt) resistance ( $R_p$ ) and a reduction of fill factor (FF). PID can be reversed to some extent if detected in time [2].

In previous related studies [3-11], impedance spectroscopy (IS) has been used to characterize new solar cells or small PV modules primarily for extracting the dynamic parameters. For the first time in this work, this method is applied to degrading modules, for fault diagnosis. Since IS enables the measurement of the panels equivalent parallel capacitance, it may provide an extra indicator over DC current-voltage (I-V) characterisation methods that can be used for fault diagnosis.

IS has some potential advantages over current commercially available I-V characterization methods when it comes to outdoor measurements. First, it is more economically efficient, as it does not require a high power circuit. Second, IS measurements can be performed during the night, without interrupting the power production of the PV system.

In this work, a residential PV system experiencing a considerable decrease in performance due to PID was analysed. The best and worst performing modules have been

selected for detailed laboratory testing. By employing I-V and electroluminescence (EL) measurements, the degradation of the modules has been confirmed as PID.

The IS tests confirmed the degradation of the PV panels observed from the I-V and EL laboratory measurements, and showed similarly decreased shunt resistance. Furthermore, the IS measurements have shown that the capacitance of the panels has also increased due to PID of the PV panels.

The results support the hypothesis that IS can be a suitable diagnostic method for PV panels. These findings open new possibilities in faults and degradations studies through AC characterization means.

In the next section the AC modelling is briefly presented. Section III describes the characterization means utilized to observe the severity of the degradation. The findings of this research are shown in section IV. The last section contains the discussion and final remarks.

## II. AC MODELLING

Commonly, the AC behaviour of solar cell and PV modules is modelled using lumped electrical circuits, for both light [11, 12] and dark solar cell operation conditions [9, 11, 13]. In this work we focus on dark IS characterization of PV modules, and consequently we use the AC solar cell model shown Fig. 1, to analyse the PV module degradation.

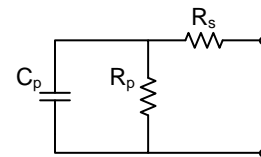


Fig. 1 The equivalent circuit model used for the parameter fitting. In this case the emphasis is on the parallel components  $C_p$  and  $R_p$ .

Derivations of this model have been done in [3, 6, 9] together with parameter extraction [14]. However, to determine the parameters of equivalent circuit the equation (1) is derived in real (2) and imaginary (3) parts. The two corresponding models are fitted to the IS measurements. Typically in c-Si PV panels the series resistance ( $R_s$ ) is three

orders of magnitude smaller than the shunt resistance ( $R_p$ ). Although  $R_s$  is included in the fitting equation, the results of the fitting for this parameter are neglected and will not be presented.

The IS measurements consist of norm (absolute value) and phase (angle) of the PV panel impedance. To determine the lumped circuit model parameters we need to convert the norm and phase measurements to their real and imaginary counterparts, using Euler's formula.

$$Z \cong R_s \cdot \frac{R_p}{1 + j\zeta C_p R} \quad (1)$$

$$\text{Re}\{Z\} \cong R_s \cdot \frac{R_p}{1 + \zeta^2 C_p^2 R^2} \quad (2)$$

$$\text{Im}\{Z\} \cong 0 \frac{\zeta C_p R^2}{1 + \zeta^2 C_p^2 R^2} \quad (3)$$

Where  $Z$  represents the impedance of the circuit,  $j$  is the imaginary unit and  $\omega$  is the angular frequency defined as:

$$\zeta \cong 2\sigma f \quad (4)$$

### III. EXPERIMENT SETUP

The I-V characterization is performed in light as well as in dark conditions using a Spi-Sun 5600SLP sun simulator [15]. The flasher is an A+A+A+ rated device.

The EL images are taken with a Photonic Science short wave infrared (SWIR) camera [16]. The test is executed in a dark chamber with the PV module forward biased. The current is set at 10% of the rated short circuit current ( $I_{sc}$ ) as this value is recommended for observing PID [17].

IS characterization is performed using a HP 4284A Precision LCR meter [18]. The frequency range employed is 20 Hz – 100 kHz. Above this frequency range, the impedance of the connection circuit (lead wires, connectors) becomes dominant and the assumptions made for fitting are no longer valid. The excitation signal is a sinusoidal voltage with  $2V_{\text{peak}}$ . A DC forward bias of equivalent value is used to keep the bypass diodes of the module blocked. The IS measurements are executed in dark conditions.

### IV. STUDY CASE

A residential PV plant located in southern Denmark, with a total installed capacity of 9.36 kW, was inspected for faults, since the plant experienced a dramatic loss in power generation compared to the installed power, as shown in Fig. 2.

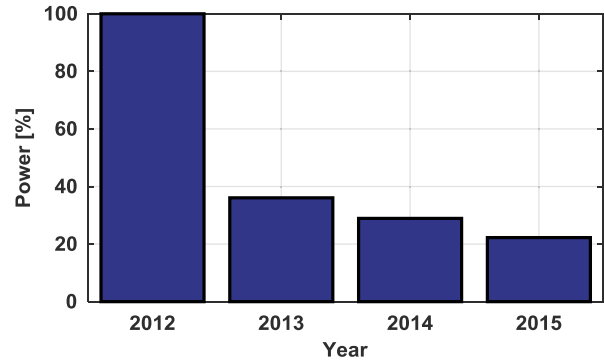


Fig. 2 Plant recorded yearly production from installation, normalized to the first year. The pattern shows a fault rather than a natural degradation, since the power drops in one year to less than 40% of the initial output.

The plant consists of a total of 36 c-Si panels connected in 3 strings with each having 12 modules in series. The strings are connected to a SMA inverter [19], limited to 6 kW due to grid connectivity rules. The converter has two maximum power point tracker (MPPT) inputs, thus one string is connected to MPPT2 while the other two are paralleled at MPPT1 as it can be seen in Fig. 3.

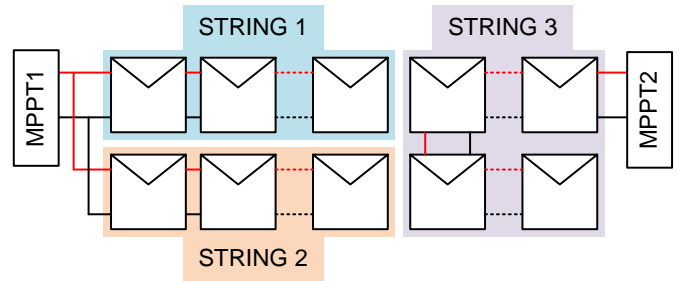


Fig. 3 Plant setup is composed by 36 PV panels connected in 3 equal strings to a SMA converter. The inverter has 2 MPPT channels hence two of the string are parallel on one input while the third string is connected to the second channel.

Field tests with the Z100 PV analyzer, an IS based diagnostic tool for PV arrays [20], have reflected the state of the panels. The best one and worst five performing modules have been selected for laboratory testing with the purpose to evaluate the overall performance and confirm the degradation type, which at the time was suspected to be PID.

The laboratory EL imaging and I-V characterization tests confirm that this is a case of PID of shunting type. The maximum power has dropped from the datasheet rating, as well as the fill factor. Fig. 7 shows EL measurements, confirming the suspected degradation in this case. The pattern is consistent with PID [21].

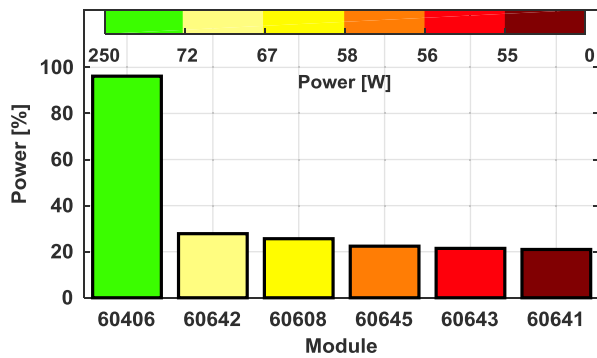


Fig. 4 Decrease of STC  $P_{max}$  of the modules relative to their datasheet value. It can be observed that the best performing module has an expected loss in power of around 1% per year from the rated value, while the other worst performing modules have an indisputable degradation problem.

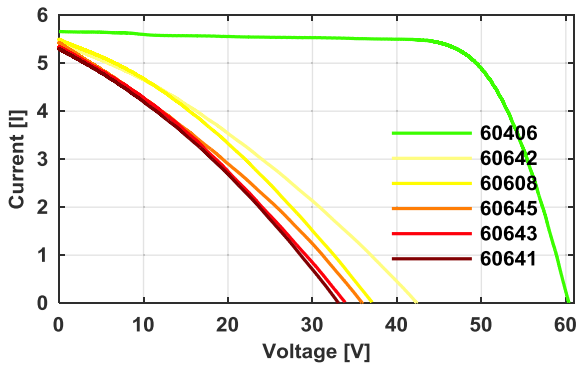


Fig. 5 Modules light I-V characteristic accentuate the advanced state of degradation of the PV panels.

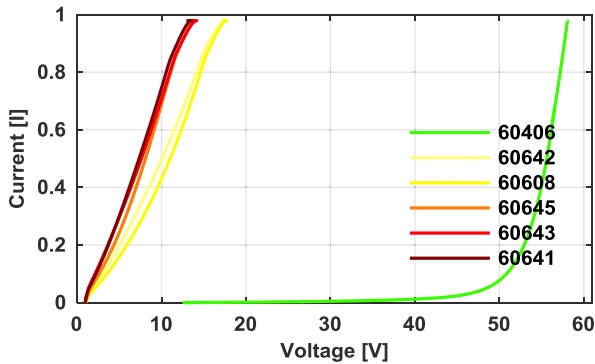


Fig. 6 Dark I-V characteristics of the PV modules correlated with the EL results point out the degradation to be PID. The shunt resistance had dropped considerably.

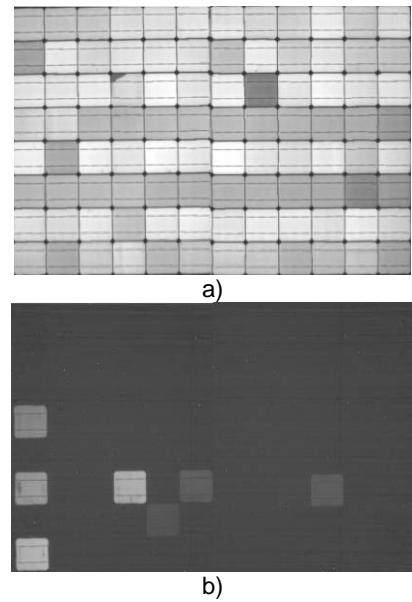


Fig. 7 EL image of a good panel, a) module 60406, versus a degraded panel, b) module 60608, taken in low current bias conditions.

The results obtained using I-V characterization and EL imaging demonstrate the severity of PID [21]. The drop in FF can be observed from the light I-V characteristic presented in Fig. 5. The accentuated slope in the region denotes a drop in shunt resistance, visible also in dark I-V (Fig. 6). The EL images support these results by revealing an overall cell degradation in the affected modules as shown in Fig. 7 b).

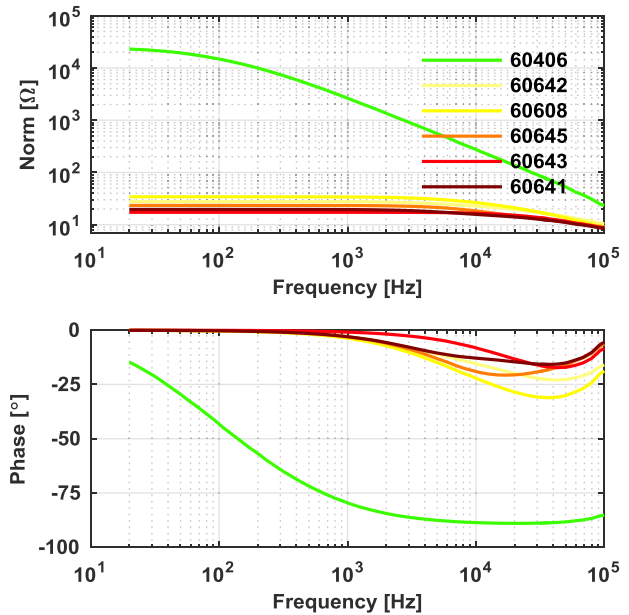


Fig. 8 Impedance spectra of the six PV modules, measured in dark condition in a frequency range from 20Hz to 100 kHz. The difference is evident between the best performing module (60406) and the others.

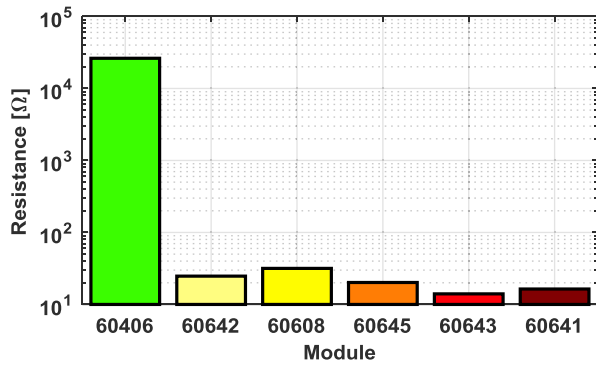


Fig. 9 Shunt resistance values determined from the IS measurements illustrate the same picture as the other characterizations. The PID modules have an  $R_p$  much lower than the typical value for c-Si PV panels, which is around few k $\Omega$ .

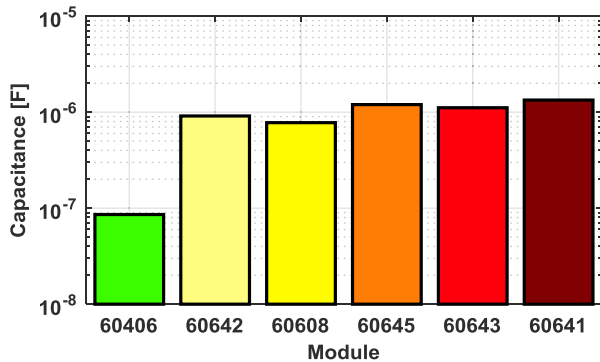


Fig. 10 The parallel capacitance shows one order of magnitude increase in value for the degraded modules in comparison to the well performing module. The change is significant and supports the hypothesis that the AC parameters can be used to observe changes in the PV panel state.

The shunt resistance determined by IS in Fig. 9 shows good correlation with the light and dark I-V measurement results. Furthermore, the panels' parallel capacitance in Fig. 10 show a strong increase in the degraded panels, consistent with the trends in shunt resistance and fill factor decrease.

## V. CONCLUSIONS

In this work a case study of c-Si PV panels that experienced PID in the field has been investigated. It has been shown that PID can affect the capacitance of PV panels, and simple IS methods can be used to detect the change in the parallel capacitance of commercial PV panels. In the study case a significant increase in capacitance has been detected in the presence of extensive PID. The results confirm the potential of IS as a diagnostic method for PV modules also in the field, however further controlled degradation tests are needed to better assess the dependency of the parallel capacitance on

PID in the early stages of degradation. It should be noted that other types of faults may have a similar effect on the parallel capacitance, therefore further research is needed for assessing the value of this parameter in presence of various faults.

## REFERENCES

- [1] P. Hacke, S. Spataru, K. Terwilliger, G. Perrin, S. Glick, S. Kurtz, *et al.*, "Accelerated Testing and Modeling of Potential-Induced Degradation as a Function of Temperature and Relative Humidity," *IEEE JOURNAL OF PHOTOVOLTAICS*, vol. 5, pp. 1549-1553, 2015.
- [2] S. Pingel, S. Janke, and O. Frank, "Recovery methods for modules affected by potential induced degradation (PID)," in *27th European Photovoltaic Solar Energy Conference and Exhibition (Frankfurt)*, 2012, pp. 3379-3383.
- [3] R. L. Mueller, M. T. Wallace, and P. Iles, "Scaling nominal solar cell impedances for array design," in *Photovoltaic Energy Conversion, 1994., Conference Record of the Twenty Fourth. IEEE Photovoltaic Specialists Conference - 1994, 1994 IEEE First World Conference on* vol. 2, ed, 1994, pp. 2034-2037 vol.2.
- [4] J. H. Scofield and O. College, "Admittance measurements on Cu(In,Ga)Se<sub>2</sub> polycrystalline thin-film solar cells," *Renewable Energy*, pp. 291-294, 1995.
- [5] M. S. Suresh, "Measurement of solar cell parameters using impedance spectroscopy," *Elsevier*, vol. 43, pp. 21-28, 1996.
- [6] R. Anil Kumar, M. S. Suresh, and J. Nagaraju, "Measurement and comparison of AC parameters of silicon (BSR and BSFR) and gallium arsenide (GaAs/Ge) solar cells used in space applications," *Solar Energy Materials and Solar Cells*, vol. 60, pp. 155-166, 2000.
- [7] R. A. Kumar, M. S. Suresh, and J. Nagaraju, "Facility to measure solar cell ac parameters using an impedance spectroscopy technique," *Review of Scientific Instruments*, vol. 72, pp. 3422-3426, 2001.
- [8] R. Anil Kumar, M. S. Suresh, and J. Nagaraju, "GaAs/Ge solar cell AC parameters under illumination," *Solar Energy*, vol. 76, pp. 417-421, 2004.
- [9] D. Chenvidhya, K. Kirtikara, and C. Jivacate, "PV module dynamic impedance and its voltage and frequency dependencies," *Solar Energy Materials and Solar Cells*, vol. 86, pp. 243-251, 2005.
- [10] L. Raniero, E. Fortunato, I. Ferreira, and R. Martins, "Study of nanostructured/amorphous silicon solar cell by impedance spectroscopy technique," *Journal of Non-Crystalline Solids*, vol. 352, pp. 1880-1883, 2006.
- [11] I. Mora-Seró, G. Garcia-Belmonte, P. P. Boix, M. a. Vázquez, and J. Bisquert, "Impedance spectroscopy characterisation of highly efficient silicon solar cells under different light illumination intensities," *Energy & Environmental Science*, vol. 2, p. 678, 2009.
- [12] L. a. Mallette and R. L. Phillips, "Modeling solar cells for use as optical detectors: background illumination effects.," *Applied optics*, vol. 17, pp. 1786-1788, 1978.
- [13] D. Chenvidhya, K. Kirtikara, and C. Jivacate, "A new characterization method for solar cell dynamic impedance," *Solar Energy Materials and Solar Cells*, vol. 80, pp. 459-464, 2003.
- [14] E. Barsoukov and J. R. Macdonald, "Impedance Spectroscopy," *Impedance Spectroscopy: Theory, Experiment, and Applications*, pp. 1-595, 2005.
- [15] (2016). *Spi-Sun Simulator 5600SLP*. Available: <http://www.spirecorp.com/products/class-a-sun-simulation.cfm>

- [16] (2016). *SWIR camera - NIR camera - InGaAs camera*. Available: <http://www.photonic-science.com/products/swir-ingaas-cameras.html>
- [17] P. Hacke, K. Terwilliger, R. Smith, S. Glick, J. Pankow, M. Kempe, *et al.*, "System voltage potential-induced degradation mechanisms in PV modules and methods for test," in *Photovoltaic Specialists Conference (PVSC), 2011 37th IEEE*, 2011, pp. 000814-000820.
- [18] "Model 4284A Precision LCR Meter," in *Operation Manual (Dec. 1991) pp*, ed: Hewlett-Packard, 1991, pp. 2-1.
- [19] "SUNNY TRIPOWER 5000TL - 12000TL Three-Phase Inverter datasheet," ed: SMA Solar Technology AG, 2014.
- [20] (2016). *Emazys Z100 PV Test Instrument*. Available: <http://emazys.com/z100-pv-test-instrument/>
- [21] S. Pingel, O. Frank, M. Winkler, S. Daryan, T. Geipel, H. Hoehne, *et al.*, "Potential Induced Degradation of solar cells and panels," in *Photovoltaic Specialists Conference (PVSC), 2010 35th IEEE*, 2010, pp. 002817-002822.



## Novel field test design for acquisition of DC and AC parameters during service

Thorsteinsson, Sune; Poulsen, Peter Behrendorff; Schou, Jørgen; Andersen, Anders Rand; Basu, Ronni; Sera, Dezso; Spataru, Sergiu; Oprea, Matei-Ion

*Published in:*  
Proceedings of IEEE 43rd Photovoltaic Specialist Conference 2016

*Link to article, DOI:*  
[10.1109/PVSC.2016.7749892](https://doi.org/10.1109/PVSC.2016.7749892)

*Publication date:*  
2016

*Document Version*  
Publisher's PDF, also known as Version of record

[Link back to DTU Orbit](#)

*Citation (APA):*  
Thorsteinsson, S., Poulsen, P. B., Schou, J., Andersen, A. R., Basu, R., Sera, D., Spataru, S., & Oprea, M-I. (2016). Novel field test design for acquisition of DC and AC parameters during service. In *Proceedings of IEEE 43rd Photovoltaic Specialist Conference 2016* (pp. 1608-1610). IEEE.  
<https://doi.org/10.1109/PVSC.2016.7749892>

---

### General rights

Copyright and moral rights for the publications made accessible in the public portal are retained by the authors and/or other copyright owners and it is a condition of accessing publications that users recognise and abide by the legal requirements associated with these rights.

- Users may download and print one copy of any publication from the public portal for the purpose of private study or research.
- You may not further distribute the material or use it for any profit-making activity or commercial gain
- You may freely distribute the URL identifying the publication in the public portal

If you believe that this document breaches copyright please contact us providing details, and we will remove access to the work immediately and investigate your claim.

# Novel field test design for acquisition of DC and AC parameters during service

Sune Thorsteinsson<sup>a</sup>, Peter Behrendorff Poulsen<sup>a</sup>, Jørgen Schou<sup>a</sup>, Anders Rand Andersen<sup>b</sup>, Ronni Basu<sup>b</sup>,  
Dezso Sera<sup>c</sup>, Sergiu Spataru<sup>c</sup>, Matei-Ion Oprea<sup>c</sup>

<sup>a</sup>Department of Photonics Engineering, Technical University of Denmark, Frederiksborgvej 399, Building 130, 4000 Roskilde, Denmark, \*sunth@fotonik.dtu.dk, phone: +45 46774521

<sup>b</sup>Emazys Technologies Aps, Lysholdt Allé 6, 7100 Vejle, Denmark

<sup>c</sup>Aalborg University, Department of Energy Technology, Pontoppidanstraede 101, 9220 Aalborg, Denmark

**Abstract** — Being able to monitor early signs of PV module degradation, is needed to ensure stable power production throughout the service life of a PV installation. Recently, impedance spectroscopy is proven to be a useful tool for detection of the presence and location of significant errors, and may have potential for more. In this work we describe a field test design where the modules are operating at their maximum power point, and via relays is switched out one by one for acquisition of an IV curve and an impedance spectrum. Some of the modules involved will undergo stimuli to accelerate certain degradation mechanisms, and fitting parameters extracted from the field test will be correlated with irradiance and compared to similar parameters of virgin modules of same kind, and conventional laboratory measurements on the same modules. The proposed method will provide data for exploration of early degradation signs using impedance measurements.

## I. INTRODUCTION

Despite manufacture guarantee of 25 years, many defect and failure mechanisms occur on PV-modules in the field [1], [2]. For most non-solar farm installations the performance ratio is not monitored carefully [3]. Thus defects and failures are not discovered until they have developed significantly, a significant visual defect occurs or the power production from the installation decreases 10's of % from one year to another. For residential installations, inspections and error searching are also associated with significant costs, almost comparable to the value of the installation.

Time domain reflectometry has been proposed and proved to be able to locate faults on a single PV string [4]. Recently, a new method has become commercially available for detecting the location of significant faults as open circuits, shorts, failing bypass diodes and earth faults [5]. This technique is based on advanced analysis of impedance measurements. Impedance spectroscopy has been widely used for DSC cells (Dye Sensitized Solar Cells) and thin-film technologies for decades. However, recent research shows promising results also applied on PV modules. This work will describe a measurement setup and preliminary results for a further investigation of which information about the PV modules health can be extracted from impedance analysis.

## II. THEORY

Interpretation of impedance spectra's using AC equivalent circuits for one specific spectra is fairly well described in the literature [6]-[8] and from [8] the simplified equivalent circuit model shown in Fig. 1. is found.

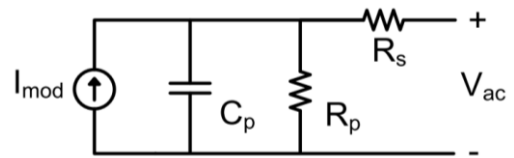


Fig. 1. Simplified equivalent AC circuit model of a PV-module

In the model the corresponding complex impedance is given by  $Z_{PV}$

$$Z_{PV} = \left[ R_s + \frac{R_p}{(\omega R_p C_p)^2 + 1} \right] - j \left[ \frac{\omega R_p^2 C_p}{(\omega R_p C_p)^2 + 1} \right] \quad (1)$$

which can be fitted to measured data, and from there values of for  $R_s$ ,  $R_p$  and  $C_p$  can be found. However, it is well known from the literature that these parameters change with illumination, and the bias.[6], [7], [9].

## III. FIELD TEST

The overall objective of this work is to establish a field test that enables to investigate how the faults on PV modules develop during normal operation. Of particular interest is to monitor and compare the impedance spectra recorded in the open circuit bias with the IV-curves. The recorded panel data will then be correlated with irradiance data and module temperature data.

The objective described above will be achieved by connecting the modules to commercially available load electronics for grid connection. A relay system will be created which can switch the modules into a “measurement bus” facilitating a measurement of an IV-curve and acquisition of an impedance spectrum. The modules mounted on the field test will all be of the same kind and batch from the producer.

However, some will be new, and some will have been exposed to accelerated aging to stimulate specific degradation mechanisms.

The overall principle is shown in Fig. 2. and the load system is designed with the aim to maximize the time each module is operating in its maximum power point.

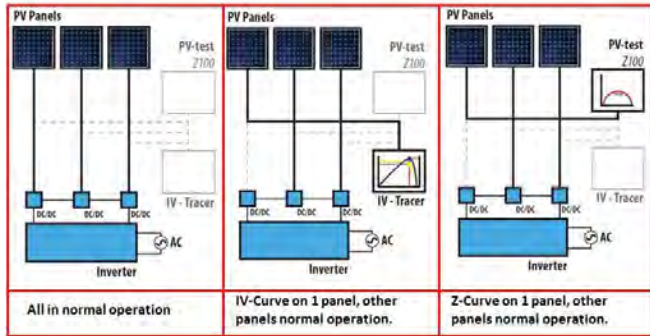


Fig. 2. Conceptual sketch of the field test.

SolarEdge power optimizers (OP 250-LV) will be connected to the modules, allowing independent module operation for module voltages above 5 volts. The output of the power optimizers is connected in series to a Solar Edge 3 KVA inverter. The serial architecture of the power optimizer system allows tracking at low voltages, which increases the module choice, to better match physical limitations of e.g. chambers for accelerated ageing. However, a minimum number of panels are required to insure sufficient input voltage to the inverter. The first type of PV modules to be mounted on the testing rack are multi crystalline panels with 36 cells. The modules have a peak power of 150 W, and a maximum power point voltage of 18 Volts. In the field test, 18 panels of these will be mounted resulting in 2.55 kWp since one module will always be switched out for measurements and thus the inverter is oversized to avoid power limitations of the inverter.

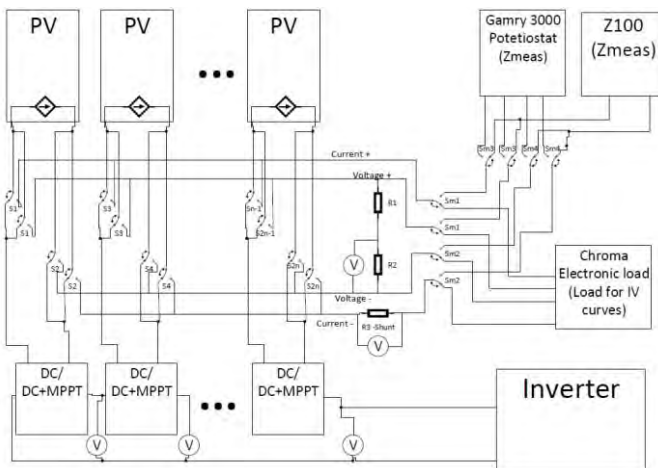


Fig 3. Wiring concept of the field test

The wiring diagram is shown in Fig. 3, it consists of a module part switching the individual modules in to a measurement bus, consisting of both sense and current wires, and a measurement part directing the other end of the measurement bus to the desired characterization equipment.

The relays and measurement system is controlled via LabVIEW using the FPGA based Compact Rio technology where fast data acquisition is possible, and safety checks in the measurement routines allows only one panel at a time to be switched to the measurement bus.

Out of the 18 panels, 8 will be characterized in a cyclic routine with IV-curves and impedance spectra. 17 modules give a total nominal DC voltage on the module side of 306 V. This is chosen in order to give power optimizers a relatively low boost ratio of approximately 15 %, and thereby maximizing their operating range.

For the IV-tracing an electronic load will load the module to obtain 1. quadrant IV curves, with the voltages and current being measured by an external data logger capable of simultaneous sampling with a rate of 50 ks/sec. For impedance measurement a Z100 device from EmaZys Technologies Aps and a Gamry 3000 AE potentiostat will be used. The impedance of the cables will be measured with the cable shorted and used to correct the impedance measurements on the modules. An outdoor reference cell and a pyranometer will be mounted in plane of array (POA), with the first being able to detect fast changes in radiation and the latter being able to measure the POA irradiation precisely. The fast response time of the reference cell combined with the fast logging using the FPGA allows for point irradiance corrections of the IV curves. The temperature on the back of each module will also be logged using thermocouples.

### III. EXPERIMENTAL PLAN

The aim of the field test is to search for signs of early degradation of modules, of particular interest is:

- ≠ By pass diode failures
- ≠ Potential induced degradation (PID)
- ≠ Micro cracks
- ≠ Ribbon damage
- ≠ Delamination

To obtain the best possible starting point 32 modules, fabricated in the same batch, will be used for the investigation.

- ≠ 2 modules will be flashed and stored in darkness to be used as reference
- ≠ 5 modules will be mounted outside and used as outdoor reference to monitor natural degradation
- ≠ 10 modules will be exposed to mechanical loads introducing micro cracks
- ≠ 5 modules will be exposed to high voltage to stimulate PID degradation
- ≠ 10 modules will be reserved for thermal aging

## ACKNOWLEDGEMENT

This research is funded by the Danish Energy Agency within the EUDP programme with the project journal number 64014-0507 “New technology for localization and characterization of faults in solar panels”.

## REFERENCES

- [1] M. Köntges, S. Kurtz, C. Packard, U. Jahn, K. A. Berger, K. Kato, T. Friesen, H. Lui, and M. Van Iseghem, “Review of Failures of Photovoltaic Modules,” 2014.
- [2] D. Degraaff, R. Lacerda, and Z. Campeau, “Degradation Mechanisms in Si Module Technologies Observed in the Field; Their Analysis and Statistics,” *PV Modul. Reliab. Work. Golden, CO*, no. February, 2011.
- [3] J. Leloux, J. Taylor, R. Moretón, L. Narvarte, D. Trebosc, A. Desportes, and S. Solar, “Monitoring 30 , 000 PV systems in Europe: Performance , Faults , and State of the Art,” no. September, 2015.
- [4] T. Takashima, J. Yamaguchi, and M. Ishida, “Fault detection by signal response in PV module strings,” *Conf. Rec. IEEE Photovolt. Spec. Conf.*, no. 1, pp. 8–12, 2008.
- [5] Emazys, “Z 100 PV analyzer.” Emazys, 2015.
- [6] D. Chenvidhya, K. Kirtikara, and C. Jivacate, “PV module dynamic impedance and its voltage and frequency dependencies,” *Sol. Energy Mater. Sol. Cells*, vol. 86, pp. 243–251, 2005.
- [7] M. P. Deshmukh, R. A. Kumar, and J. Nagaraju, “Measurement of solar cell ac parameters using the time domain technique,” *Rev. Sci. Instrum.*, vol. 75, no. 2004, pp. 2732–2735, 2004.
- [8] J. Johnson, D. Schoenwald, S. Kuszmaul, J. Strauch, and W. Bower, “Creating dynamic equivalent PV circuit models with impedance spectroscopy for arc fault modeling,” *2011 37th IEEE Photovolt. Spec. Conf.*, pp. 002328–002333, 2011.
- [9] T. Pongklang, D. Chenvidhya, and K. Kirtikara, “Voltage and frequency dependent impedances of dye-sensitized solar cell,” *Energy Procedia*, vol. 52, pp. 536–540, 2014.

Prior to any stimuli, flash curves, impedance spectra and electroluminescence (EL) test are performed on the modules. The outdoor reference modules together with a selection of modules that has received degradation stimuli will be mounted on the field. Prior to mounting on the field test, flash tests, EL-test and laboratory impedance spectra’s will be record as references.

The fitted values for the AC parameters being the parallel resistance, the series resistance and the parallel capacitance will be correlated with irradiation and temperature, and their development will be monitored and compared with flashing results and EL imaging. It is the expectation from the authors, that these experiments will guide the way for using impedance spectroscopy on installations to detect early signs of module degradation.

## IV. SUMMARY

In this work we have described a field test design with the purpose of getting more knowledge of PV module degradation by investigation by impedance spectroscopy alongside IV characterization. The modules are operating at their maximum power point, and are switched out one by one via relays for acquisition of an IV curve and an impedance spectrum. Some of the modules involved will undergo stimuli to accelerate certain degradation mechanisms, and fitting parameters extracted from the field test will be correlated with irradiance and compared to similar parameters of virgin modules of same kind, and conventional laboratory measurements on the same modules. The proposed method will provide data for exploration of early degradation signs using impedance measurements. The field test is in the moment in its final state of preparation and the software is close to being finished enabling a commissioning during the summer of 2016.

## NEW METHOD OF SILICON PHOTOVOLTAIC PANEL FAULT DETECTION USING IMPEDANCE SPECTROSCOPY

Joanna Symonowicz<sup>1,\*</sup>, Nicholas Riedel<sup>1,a</sup>, Sune Thorsteinsson<sup>1,b</sup>, D. Sera<sup>2,c</sup>, and Peter Behrendorff Poulsen<sup>1,d</sup>

<sup>1</sup> Department of Photonics Engineering, Technical University of Denmark  
Frederiksborgvej 399, 4000 Roskilde, Denmark

<sup>2</sup> Department of Energy Technology, Aalborg University, 9220 Aalborg, Denmark

<sup>a</sup> nrie@fotonik.dtu.dk, <sup>b</sup> sunth@fotonik.dtu.dk, <sup>c</sup> des@et.aau.dk, <sup>d</sup> ppou@fotonik.dtu.dk

\* jokas@fotonik.dtu.dk / +48 517 611 149

**ABSTRACT:** The aim of our project is to develop a new method for photovoltaic (PV) panel fault detection based on analysing its impedance spectra (IS). Although this technique was successful in assessing the state of degradation of fuel cells and batteries [1, 2], it has never been applied to PV cells on a wide scale. In this paper, we show that, unlike current-voltage (I-V) tests, the IS method is capable of early detection of changes in PV panel parameters due to microcracks and potential-induced degradation (PID). Although our measurements are only successful under dark conditions, the results are similar for both laboratory environment and for outdoor tests in various weather conditions. A fully developed IS technique, accounting for all kinds of most common PV panel degradation types, would surpass the existing PV fault detection methods then it comes to cost and accuracy [3,4].

**Keywords:** c-Si, Degradation, Impedance, Experimental Methods

### 1 INTRODUCTION

The IS technique is based on applying a small sinusoidal signal ( $E$ ) to a measured device over a span of a few decades of frequency ( $\omega$ ). The current response ( $I$ ) to a sinusoidal potential ( $E$ ) is a sinusoid at the same frequency but shifted in phase. An expression analogous to Ohm's Law allows us to calculate the complex system impedance [5-7] (see (1)).

$$(1) Z = \frac{E}{I} = \frac{E_0 \sin(\omega t)}{I_0 \sin(\omega t + \varphi)} = Z_0 \frac{\sin(\omega t)}{\sin(\omega t + \varphi)}$$

Furthermore, with Euler's relationship, it is possible to express impedance as a complex function [6] (see (2)).

$$(2) Z_0 \frac{\sin(\omega t)}{\sin(\omega t + \varphi)} = Z_0 \exp(i\varphi) = Z_0 (\cos\varphi + i\sin\varphi)$$

A solar cell's behaviour can be described by an equivalent electrical circuit [8-11]. Such a circuit consists of common electrical elements that have a basis in the physical electrochemistry of the system. Each element contributes to the overall impedance response. Using a fitting method on measured data, it is possible to extract parameters of the equivalent circuit's individual parts [3,4, 8-11].

In this work we use the simplified dynamical equivalent model for a PV cell [11-13] which is presented in fig. 1 along with the corresponding impedance equation and its Nyquist plot. Although the model is derived for dark IS characterization, it should be a good approximation also for light characterization [3, 11-15].

Any changes in the equivalent electrical circuit parameters ought to indicate distortion in a PV module's performance [3,9]. The first use of AC measurements in fault detection was an investigation on how hot spots affect PV panel capacitance [16]. Next, it has been proven that potential-induced degradation (PID) in c-Si PV panels results in a significant decrease in  $R_p$  and an increase in  $C_p$  values [3,9]. No other forms of degradation has been described by the IS method yet.

The focus of our experiment is PV module microcracks. This is a very common fault of PV panels, often seen in the field, which can easily be inflicted by a bad installation or any mechanical action that affects the integrity of the solar cells. After inflicting microcracks on silicon PV panels, we would like to spot changes in their  $R_p$ ,  $R_s$  and  $C_p$  parameters in both indoor and outdoor experiments [17]. This would verify that the IS analysis is an accurate tool for field fault detection.

$$Z_{PV} = \left[ R_s + \frac{R_p}{(\omega R_p C_p)^2 + 1} \right] - i \left[ \frac{\omega R_p^2 C_p}{(\omega R_p C_p)^2 + 1} \right]$$

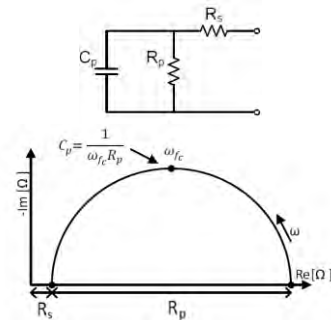


**Figure 1:** The simplified dynamical equivalent model for a PV cell - complex impedance equation  $Z_{PV}$  (top), its equivalent circuit model (middle), and its Nyquist plot visualizing how the parameters can be extracted by the fitting routine (bottom) [3,4, 8-11].

### 2 EXPERIMENTAL DETAILS

#### 2.1 Stresses on modules

In our experiment we are considering ten silicon PV modules (see fig. 2). Three of them serve as a reference. Six panels, called the uCrack group, underwent mechanical stresses at the Department of Energy Technology at Aalborg University. The total weight used for the degradation was 400 kg (sand bags). The overall pressure put on panels was, thus, 3.9 kPa. The weights were distributed uniformly twice on panels' front surface

and once on its back. The one remaining module (PID\_05) received a PID test.

The degradation quantification was carried out by the I-V (current-voltage) and electroluminescence (EL) characterization. I-V measurements were performed in light using a Spi-Sun 5600SLP sun simulator. The EL photos were taken with a Photonic Science short wave infrared (SWIR) camera in a dark chamber with the PV module forward biased at 90% standard test condition (STC) short circuit current ( $I_{sc}$ ). The result of the stresses was a  $P_{loss}$  of 4% in five of PV modules (uC\_05 to uC\_09) and a  $P_{loss}$  of 30% in the uC\_04 panel. PID\_05 did not display any performance reduction ( $P_{loss}$  of 0%). Figure 2 includes a visual image of the test modules along with their corresponding EL images and  $P_{loss}$  values.

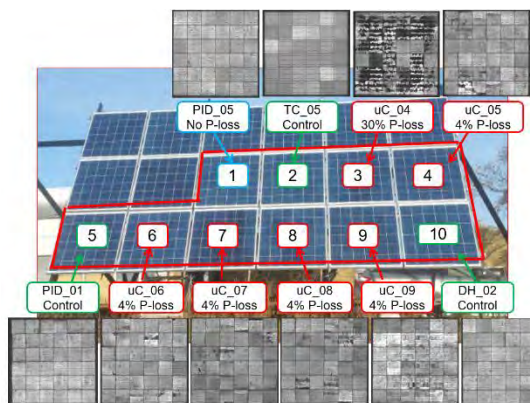


**Figure 2:** Field station for the I-V, IS and weather conditions measurements built at DTU, Risø Campus.

## 2.2 Indoor measurements

All ten panels were tested once again at Danmarks Tekniske Universitet (DTU) Institut for Fotonik. We performed multi-irradiation I-V investigations using EcoSun 10L Ecoprogetti to recheck the  $P_{loss}$  values of 0%, 4%, and 30%. We then used a Gamry Reference 3000 Potentiostat [18] ( $AC=0.01V$ ) for the IS tests in dark conditions at  $T=25^{\circ}C$ . The IS test on irradiated samples ( $G \neq 0 W/m^2$ ) was impossible due to equipment overloads [18]. The IS data was fit to the  $Z_{PV}$  equation using the Levenberg-Marquadt method.

## 2.3 Outdoor measurements

The outdoor measurements required the construction of a field station (see fig. 2). The block scheme of the station is presented in figure 3. Test samples are grid-tied via a string inverter when not measured. Each module has a DC-DC power optimizer. The modules are individually taken out of the energy production circuit and into the measurement circuit using relays. I-V and IS are measured on an individual panel before switching the next panel from energy production to measurement. The parameter extraction routine based on a simple RC circuit fitting method [3] runs automatically after the whole day of data collection. The IS curves are obtained by Emazys Z100 PV Analyzer ( $AC = 2V$ ) [19] while I-V tests are performed by a Chroma single quadrant load.

The field station has been operating since November 2016 in various weather conditions. It possesses two pyrometers and a thermocouple on the back sheet of each module. Back sheet temperatures varied from  $-10^{\circ}C$  up to  $60^{\circ}C$  while an irradiation was 1 to  $1200 W/m^2$ .

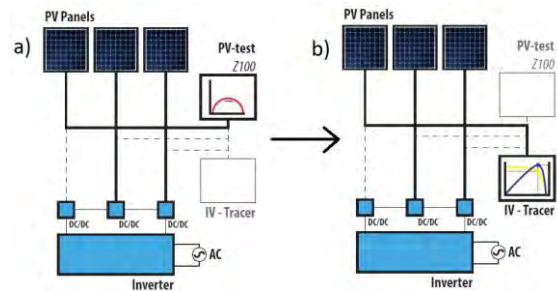


**Figure 3:** The block diagram of the field station. IS (a) followed by I-V (b) are measured on one panel at the time.

## 3 RESULTS

### 3.1 I-V measurements

Figure 4 shows the comparison between the DTU indoor and outdoor I-V measurements for similar irradiation conditions ( $200-800 W/m^2$ ) and temperature of about  $25^{\circ}C$ . The values of maximum power points (Pmp) for our tests (EcoSun indoors and Chroma single quadrant load outdoors) correspond to the  $P_{loss}$  values detected by Spi-Sun 5600SLP sun simulator during the panel damage preparation.

Indoor measurements are usually higher by circa 5W. This may be due to variations in temperature throughout the outdoor measurements. The deviation can also be caused by different equipment sets used for I-V detection as well as long wires implemented in the field station. Since the deviation is constant, we assume that outdoor I-V measurements reflect indoor ones and that the field station operates correctly. This information is essential to ensure the good performance of the innovative IS tests.

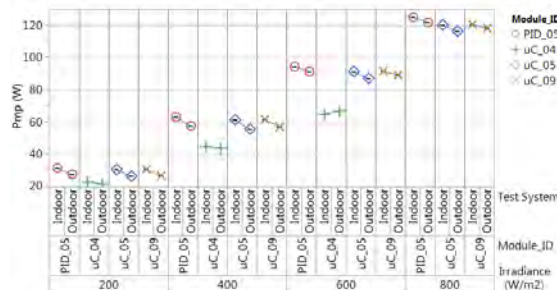


**Figure 4:** The comparison between indoor and outdoor I-V measurements at multi irradiance ( $200-800 W/m^2$ ). The Pmp values of individual modules are very similar for indoor and outdoor test and confirm the correct functioning of our field station.

Figure 5 demonstrates that traditional I-V method fails in early detection of changes in AC circuit parameters due to microcracks and PID. The PID module ought to experience rise in  $C_p$  [3]. The uCrack group should exhibit lower  $R_p$  values and higher  $R_s$  values than the Control group [16]. Such performance was only detected for the uCrack panel with 30%  $P_{loss}$  which is a large scope of damage. It is well-known that I-V curve is insufficient to detect important parameters, such as interfacial diffusion, transition capacitance followed by resistive and capacitive components of p-p+ interface of a silicon solar cell [20]. Since these mechanisms regulate the values of AC circuit parameters, the extracted  $R_s$ ,  $R_p$ ,  $C_p$  are not exact [20].

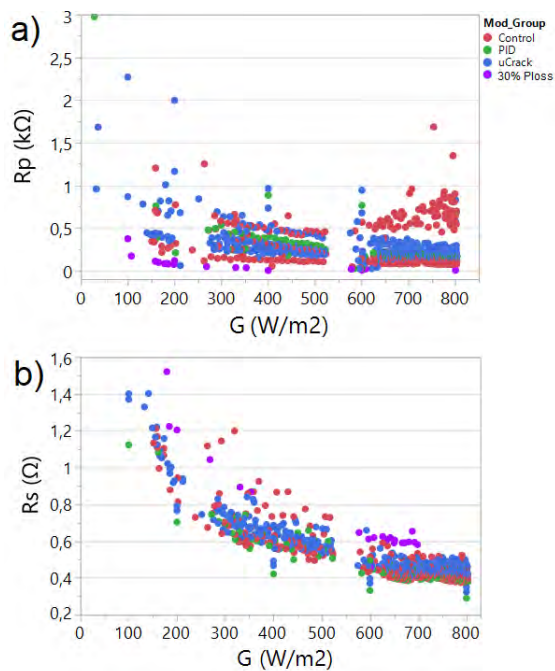


**Figure 5:**  $R_p$  (a) and  $R_s$  (b) extracted for indoor and outdoor I-V tests. The traditional I-V method is incapable of detecting changes in AC circuit parameters unless PID and microcrack damages are prominent.

### 3.2 IS Measurements

So far, our IS method has been only successful for the measurements in dark conditions (fig. 6a,b). Once  $G \neq 0 \text{ W/m}^2$  the IS curves are the same for all degradation groups and, thus, the values of extracted parameters do not differ, either (see fig. 6c). The plateau observed at high  $\text{Im}Z$  values for  $G \neq 0 \text{ W/m}^2$  (fig. 6c) is due to a limited frequency resolution of Emazys Z100 PV Analyzer [19], which goes down only to 100 Hz. Currently, we are updating the test bed so it can reach frequencies down to 1 Hz.

Similar shapes of IS curves for all degradation groups at high  $G$  might be caused by limitations of our equipment. However, it is equally possible that the changes due to microcracks are dimmed during solar cell operation. This explains the failure of multi-irradiance IV technique. Nonetheless, the IS tests performed in total darkness seem to be the best option for two reasons. First, most of the previous research involving extraction of parameters from this AC circuit has been performed in total darkness [3, 8-12]. Hence, the model has been proven reliable numerous times for PV panels under no illumination. Second, once the PV modules performance is only tested at night, no power production time is wasted during the day.

From November 2016 until September 2017 the field station was operating only during the day. Hence, no dark condition data was collected during this period. In September 2017 we decided to take the night time data into account. That is why indoor data (fig. 7) was extracted in December 2016 while the outdoor data in fig. 8 was extracted in September 2017. The dissimilarities in their values are due to divergence in equipment and weather conditions. Nevertheless, in this work the focus is on how the parameters differ between module stress groups (uCrack, PID, and Control) and that information is clearly indicated in our data.

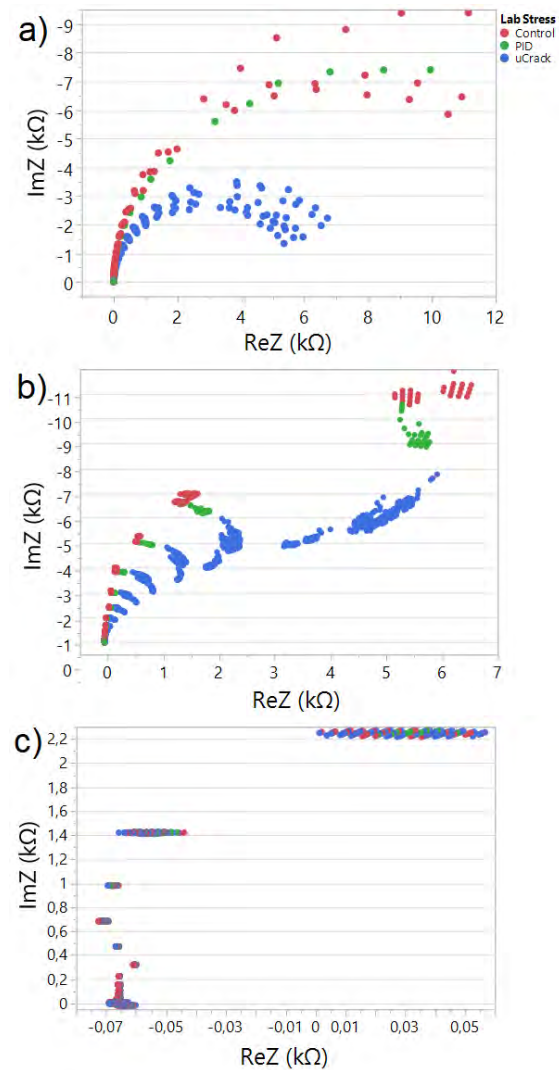


**Figure 6:** Overlay of IS spectra Nyquist plots at  $G=0 \text{ W/m}^2$  for indoor (a) and outdoor tests (b), and at  $G=700\text{-}800 \text{ W/m}^2$  for outdoor tests (c). The IS curves for individual degradation groups are distinguishable only at  $G=0 \text{ W/m}^2$ .

For both indoor and outdoor tests at  $G = 0 \text{ W/m}^2$  we were able to observe that  $R_p$  values of control modules are higher than uCrack group (fig. 7a, 8a). The lower  $R_p$  values illustrate a bigger leakage current in PV cells [3,9] and explain the 4-30%  $P_{\text{loss}}$  we saw in the I-V data. The PID module exhibits a much smaller  $R_p$  value after 9 months of field station performance (fig. 8a). Simultaneously, its  $C_p$  and  $R_s$  values have increased. These are the symptoms of PID described in [3,9]. It is possible that the damage was minor at first (during indoor tests) and grew during PV panel functioning in altering weather conditions.  $C_p$  remains the same for uCrack and Control groups. The divergence of  $C_p$  behaviour for PID and microcracks (fig. 7c, 8c) is very convenient as it shows the proficiency of the IS method to distinguish between various kinds of faults.

Behaviour of  $R_s$  is problematic (fig. 7b, 8b). For indoor tests, uC\_04 module with 30%  $P_{\text{loss}}$  exhibits 2,5 times higher  $R_s$  value than the rest of panels for indoor tests (fig. 7b). The remaining modules from uCrack group have the same  $R_s$  values as Control group. This is not the case for outdoor measurements were all uCrack

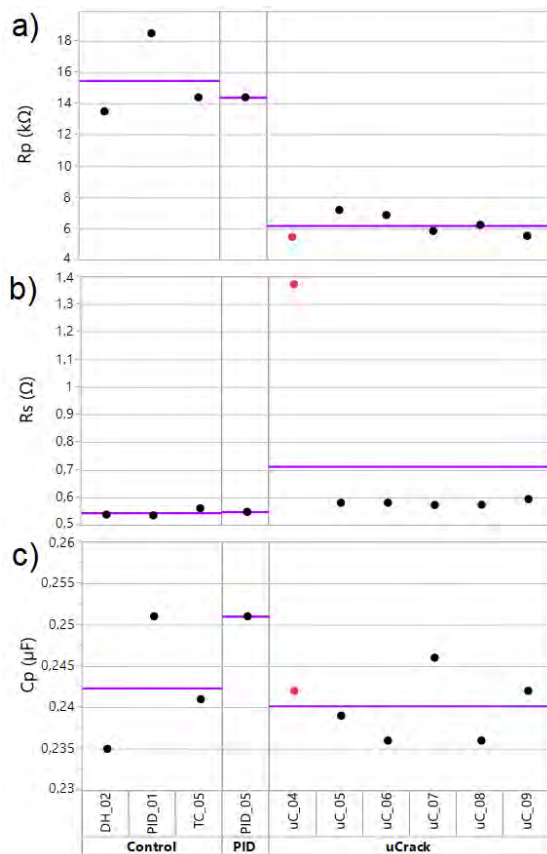


**Figure 7:**  $R_p$  (a),  $R_s$  (b), and  $C_p$  (c) parameters extracted from IS curves for indoor measurements in dark conditions at  $T=25^\circ\text{C}$ .

modules display increase in  $R_s$  by  $\times 2.5$ . In general, the upsurge in  $R_s$  indicates less current flow through the PV junction [3,9]. This might be due to mechanical surface damages [16]. We made sure that the  $P_{mp}$  values for individual modules are the same in September 2017 as in December 2016 using the outdoor I-V data. It is possible that signal  $AC=0,01$  V of indoor potentiostat is not enough to expose higher  $R_s$  for minor microcracks [3]. Accordingly, indoor tests must be repeated for  $AC=2$  V.

We must bear in mind that the changes of  $R_s$ ,  $R_p$  and  $C_p$  may account for various PV panel faults [14-15]. Therefore, at this point we are only able to detect a deviation in module performance which should be further investigated by a plant manager with I-V measurements. Nonetheless, once IS spectra are scrupulously tested for all the most common PV defects, it might be possible to specify a kind of fault based only on the IS parameters change rate.

#### 4 CONCLUSIONS

So far, we were able to detect alterations in PV panel parameters due their faults only in the dark conditions. However, the implantation of IS method exclusively at night does not interfere with solar power production, which is a huge advantage. We proved that the parameters are extracted more accurately than in case of I-V tests.

Our results confirm previous studies on how PID changes AC circuit parameters values [3]. The alterations in  $R_p$  and  $R_s$  after infliction of microcracks also

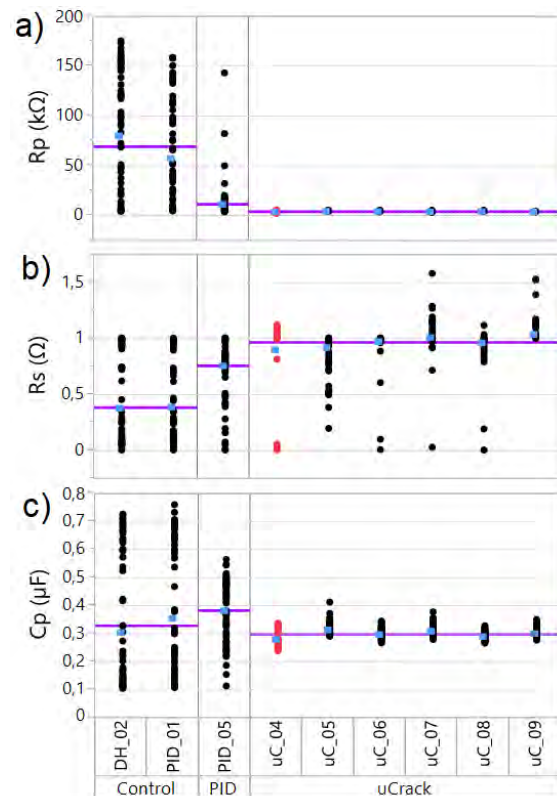


**Figure 8:**  $R_p$  (a),  $R_s$  (b), and  $C_p$  (c) parameters extracted from IS curves for field station tests in dark conditions at  $T=25^\circ\text{C}$ . Blue dots indicate the mean values of distributions.

agree with theory [16]. The latter results are different from the ones caused by PID. Therefore, the IS method has the potential to distinguish between various types of faults.

The observed differences indicate that the IS method has the potential to be a successful tool for solar panel fault detection. However, at the moment, the identified changes in  $R_p$ ,  $R_s$ , and  $C_p$  only indicate a possible PV module performance failure, which should be further investigated by other detection techniques. In the future, we hope to be able to assess the  $P_{loss}$  value only through the field IS measurements. In order to achieve our goal, we first need to perform more indoor tests based on various defect types as a reference for the future outdoor data.

#### 5 ACKNOWLEDGEMENTS

The work on the present study was funded by the Energy Technology Development and Demonstration Program (EUDP) through the project *New technology for localization and characterization of faults in solar panels*. We would also like to thank Matei-Ion Oprea from the Department of Energy Technology at Aalborg University for laying the foundations for our work.

#### 6 REFERENCES

- [1] D. Stroe et al., IECON Proceedings (Industrial Electron. Conf.), (2013) 6734–6739.
- [2] I.F. Grigoras, Master thesis (Aalborg Univ.), (2013).

- [3] M.I. Oprea, Master thesis (Aalborg Univ.), (2013).
- [4] R.A. Kumar, M.S. Suresh, J. Nagaraju, Review of Scientific Instruments, Vol. 72 (2001) 3422-3426.
- [5] E. Barsoukov, J.R. Macdonald, Wiley Interscience Publications, (2005).
- [6] A.J. Bard, L.R. Faulkner, Wiley Interscience Publications, (2000).
- [7] J.R. Scully, D.C. Silverman, M.W. Kendig, ASTM, (1993).
- [8] R.A. Kumar, M.S. Suresh, J. Nagaraju, Solar Energy Materials and Solar Cells, Vol. 60 (2000) 155-166.
- [9] M.I. Oprea et al., Proceedings of the IEEE 43rd PVSC, (2016).
- [10] R.L. Mueller, M.T. Wallace, P. Iles, Proceedings of the IEEE 24th PVSC, Vol. 2 (1994), pp. 2034-2037.
- [11] D. Chenvidhya, K. Kirtikara, C. Jivacate, Solar Energy Materials and Solar Cells, Vol. 86 (2005) 243-251.
- [12] D. Chenvidhya, K. Kirtikara, C. Jivacate, Solar Energy Materials and Solar Cells, Vol. 80 (2003) 459-464.
- [13] I. Mora-Sero, G. Garcia-Belmonte, P.P. Boix, M. Vazquez, J. Bisquert, Energy Environ. Sci., Vol. 2 (2009) 678.
- [14] D.C. Jordan and S.R. Kurtz, Prog. Photovoltaics Res. Appl., Vol. 21 (2013) 12-29.
- [15] M. Quintana, D.L. King, T.J. McMahon, and C.R. Osterwald, Proceedings of the IEEE 29th PVSC, (2002) 1436-1439.
- [16] K.A. Kim, G.-S. Seo, B.-H. Cho, Fellow, P.T. Krein, IEEE Trans. On Power Electr., Vol. 31(2) (2016).
- [17] J.I. van Mülken, U.A. Yusufoglu, A. Safiei, H. Windgassen, R. Khandelwal, T.M. Pletzer, H. Kurza, Energy Procedia, Vol. 27 ( 2012 ) 167 – 172 .
- [18] [www.gamry.com/potentiostats/reference-3000/](http://www.gamry.com/potentiostats/reference-3000/), [22.08.2017].
- [19] [emazys.com/z100-pv-analyzer](http://emazys.com/z100-pv-analyzer), [22.08.2017].
- [20] P. Yadav, K. Pandey, V. Bhatt, M. Kumar, J. Kim, Renewable and Sustainable Energy Reviews, Vol. 76 (2017) 1562-1578.



Aalborg Universitet

AALBORG UNIVERSITY  
DENMARK

## Development of outdoor luminescence imaging for drone-based PV array inspection

Benatto, Gisele Alves dos Reis; Riedel, Nicholas; Thorsteinsson, Sune; Poulsen, Peter; Thorseth, Anders; Dam-Hansen, Carsten; Mantel, Claire; Forchhammer, Søren; H. B. Frederiksen, Kenn; Vedde, Jan; Petersen, Michael; Voss, Henrik; Messerschmidt, Michael; Parikh, Harsh; Spataru, Sergiu; Sera, Dezso

*Published in:*

Proceedings of the 44th IEEE Photovoltaic Specialists Conference, PVSC 2017

*DOI (link to publication from Publisher):*

[10.1109/PVSC.2017.8366602](https://doi.org/10.1109/PVSC.2017.8366602)

*Publication date:*

2017

*Document Version*

Accepted author manuscript, peer reviewed version

[Link to publication from Aalborg University](#)

*Citation for published version (APA):*

Benatto, G. A. D. R., Riedel, N., Thorsteinsson, S., Poulsen, P., Thorseth, A., Dam-Hansen, C., Mantel, C., Forchhammer, S., H. B. Frederiksen, K., Vedde, J., Petersen, M., Voss, H., Messerschmidt, M., Parikh, H., Spataru, S., & Sera, D. (2017). Development of outdoor luminescence imaging for drone-based PV array inspection. In *Proceedings of the 44th IEEE Photovoltaic Specialists Conference, PVSC 2017* IEEE Press. I E E E Photovoltaic Specialists Conference. Conference Record <https://doi.org/10.1109/PVSC.2017.8366602>

### General rights

Copyright and moral rights for the publications made accessible in the public portal are retained by the authors and/or other copyright owners and it is a condition of accessing publications that users recognise and abide by the legal requirements associated with these rights.

- ? Users may download and print one copy of any publication from the public portal for the purpose of private study or research.
- ? You may not further distribute the material or use it for any profit-making activity or commercial gain
- ? You may freely distribute the URL identifying the publication in the public portal ?

# Development of outdoor luminescence imaging for drone-based PV array inspection

Gisele A. dos Reis Benatto<sup>1</sup>, Nicholas Riedel<sup>1</sup>, Sune Thorsteinsson<sup>1</sup>, Peter B. Poulsen<sup>1</sup>, Anders Thorseth<sup>1</sup>, Carsten Dam-Hansen<sup>1</sup>, Claire Mantel<sup>1</sup>, Søren Forchhammer<sup>1</sup>, Kenn H. B. Frederiksen<sup>2</sup>, Jan Vedde<sup>3</sup>, Michael Petersen<sup>4</sup>, Henrik Voss<sup>5</sup>, Michael Messerschmidt<sup>5</sup>, Harsh Parikh<sup>6</sup>, Sergiu Spataru<sup>6</sup> and Dezso Sera<sup>6</sup>

<sup>1</sup>Department of Photonics Engineering, Technical University of Denmark, Frederiksborgvej 399, 4000, Roskilde, Denmark

<sup>2</sup>Kenergy, Grønningen 43, 8700, Horsens, Denmark

<sup>3</sup>SiCon Silicon & PV consulting, J N Vinthersvej 5, 3460, Birkerød, Denmark

<sup>4</sup>Skive Kommune, Torvegade 10, 7800 Skive, Denmark

<sup>5</sup>Sky-Watch A/S, Østre Alle 6 Støvring, Nordjylland, 9530, Denmark

<sup>6</sup>Aalborg University, Aalborg, 9220, Denmark

**Abstract** — In this work we investigate and present preliminary results for two methods for luminescence imaging of photovoltaic (PV) modules in outdoor conditions, with the aim of choosing the most suitable method for implementation on a drone PV plant inspection system. We examined experimentally both electroluminescence (EL) and photoluminescence (PL) PV module imaging methods under natural light conditions, and determined that fast pulsed EL imaging with InGaAs detector cameras can yield reasonably accurate results under daylight conditions. Moreover, we formulated the necessary requirement for a PL light source, which would allow PL imaging of modules under daylight conditions.

**Index Terms** — drone-based PV inspection, electroluminescence imaging, image processing, outdoor defect detection, photoluminescence imaging.

## I. INTRODUCTION

In order to ensure expected return on investment (ROI) of small and large-scale photovoltaic (PV) installations, regular fault detection for effective maintenance, is highly important. Present day PV panels are designed to operate for 25-30 years, however field experience shows that after 11-12 years of operation 2% or more of all PV panels fail [1]. However, the failure rate is even higher for older installations, especially those manufactured before the year 2000 [2].

In practice, the frequency and inspection detail level is often limited by manpower and cost. Presently, drone-based infrared (IR) thermography inspection of solar plants is a reality, and the technology is expected to develop further into automated solar plant inspection [3]–[5]. The accuracy of thermographic fault detection though, presents limitations – primarily related to deconvoluting the failure signature into failure type and severity, which can be overcome when performed in combination to electro-(EL) or photo-(PL) luminescence imaging of the panels. The combination of defect detection techniques has been already tested in laboratory [1], [6], although many limitations still need to be addressed in order to obtain image acquisition outdoors and integrate, automatize and optimize the imaging system in a drone.

In this work, we investigate and present preliminary results for two methods for luminescence imaging of PV modules in outdoor conditions, with the aim of choosing the most suitable method for implementation on a drone PV plant luminescence inspection system. First, we investigate a pulsed EL imaging method under daylight conditions, to determine the necessary camera and measurement parameters. In the second part, we examine a PL imaging method under natural low light conditions, to determine if PL imaging would be feasible for outdoor PL imaging, along with the necessary light source requirements. The concept of PL/EL in a drone is illustrated in Fig. 1.



Fig. 1. Sketch of the concept of automatized drone inspection.

## II. EXPERIMENT AND METHODOLOGY

The experimental tests performed in this work are focused on investigating EL and PL imaging techniques that are suitable for implementation into a drone-based inspection system. The PL technique avoids the need for electrical contact into the solar panels, which is a time limiting factor for drone-based inspection, especially in large-scale solar plants.

The luminescence emission peak for silicon-based solar cells at ambient temperature is at 1150 nm [7], near a water absorption band in the solar spectrum (AM 1.5), as illustrated in Fig. 2. In the same figure, the quantum efficiencies of two camera detectors: i) a cooled Si charge-coupled device (CCD) ii) and short-wave infrared (SWIR) InGaAs, able to detect the emission peak, are plotted. Comparing the curves with the peak positions it is clear that a CCD camera can acquire only a small portion of the emission peak. At the same time, the SWIR InGaAs can detect the emission entirely, providing fast integration times, ideal for drone operation. Additionally, the InGaAs detector avoids the most intense section of the solar spectrum. Even though, to avoid the relatively intense sunlight, a sharp optical band-pass filter is used, with the transmission wavelength illustrated as the white area in Fig. 2.

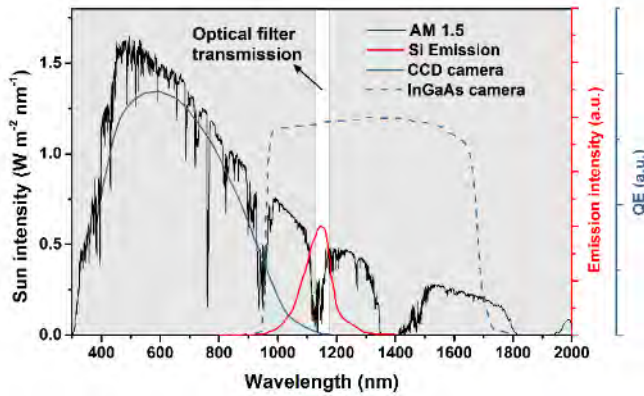


Fig. 2. AM 1.5 sun spectrum (black line), CCD (solid blue line) and InGaAs (dashed blue line) camera QE curves, and silicon emission peak (red line). The grey areas show wavelengths that are cut off with the use of an optical filter in order to avoid detection of the sunlight.

### A. Electroluminescence

The EL images shown in this paper are acquired from a mechanically stressed 36 cell multicrystalline silicon solar panel with 1 x 1 meter dimension. An InGaAs camera from Hamamatsu model C12741-03, and an OD>4.0 1150nm band-pass filter with 50nm FWHM was used to obtain all EL images.

A sequential image acquisition system was implemented in order to enhance the quality of the images obtained at high noise level during the day. Such system synchronizes the image acquisition with an electrical forward bias applied by a DC power supply. Fig. 3 illustrates the synchronizing circuit, driven by an Arduino logic controller, and the pulse width modulated (PWM) waveforms applied to the PV panel and camera. The exposure time is established separately in the camera software.

To estimate the effect of the sun on the imaging process and to better understand the noise characteristics towards an InGaAs detector and develop image processing strategies, we acquired sequences of 100 images (50 under forward bias (signal) and 50 as background images for subtraction) at 6 Hz with 20 ms exposure time, under 300, 500, 600, and 800 W/m<sup>2</sup>

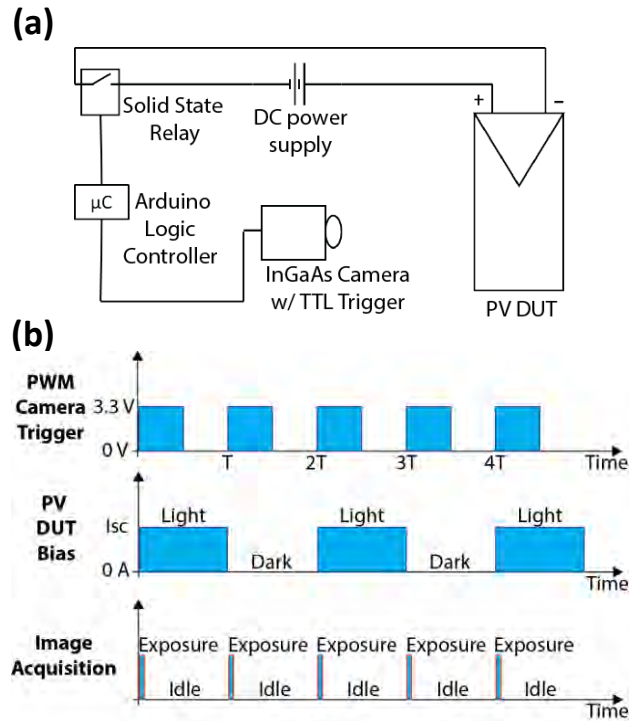


Fig. 3. Basic trigger circuit that synchronizes the imaging and forward bias from a DC power supply (a); and the PWM waveforms driven by the Arduino logic controller (b).

global horizontal irradiance (GHI). The solar irradiance was acquired by a weather station [8] located just few meters from the imaging position. The iris aperture was f4 for 300 W/m<sup>2</sup> and f8 for the remaining. The images were acquired at around 2.6 meters from the panel.

As averaging several pictures is the most common way the minimize noise from images, we perform it the enhance image quality. The image processing included taking the difference between the average of light and dark images, automatic stretching of the initial dynamic range (the source images are 16bits) to 8 bits for display and cropping of the whole image to the region of interest. T-tests of the images pixel values were performed for better understanding of signal the noise ratio (SNR).

### B. Photoluminescence

PL images indoors were acquired using a laser diode at 800 nm with capacity of 13 W maximum optical power, while the camera and the laser were circa 0.5 meter far from the sample. The sample consisted of a multicrystalline silicon cracked PV cell. The same camera and filter used for EL was used to obtain PL images. The images were acquired at 700 ms exposure time for 54, 71, 87, 104 and 120 W/m<sup>2</sup> light intensity on the plan of the cell, which corresponded respectively to 3, 4, 5, 6 and 7 W of optical power from the laser.

### III. RESULTS AND DISCUSSION

#### A. Electroluminescence

EL imaging during the night is comparable to indoors EL imaging, where normally there is no significant ambient light noise levels. For comparison, Fig. 4 shows the indoors EL image of the mechanically stressed module. However, during the day such images are surrounded by high, and very often variable, light noise levels, primarily from the sunlight itself.

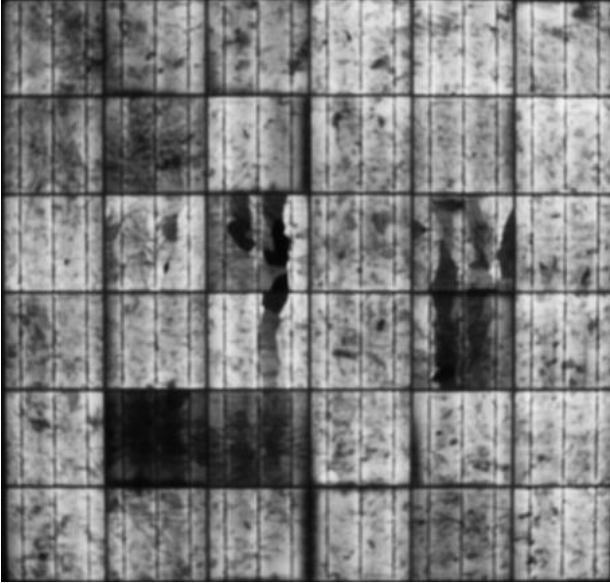


Fig. 4. Indoors EL image of mechanically stressed PV module, showing cracks and disconnected cell areas.

Fig 5a shows the EL images acquired under different sun irradiation levels, after averaging, subtracting, and image processing. The irradiance on the plane of the module array (POA) was 117.6, 332.3, 467.8, and 714.5 W/m<sup>2</sup> respectively; using the Hay Davie's model for diffuse irradiance on a tilted surface [9]. At 800 W/m<sup>2</sup> for example, there was a strong direct beam irradiance when the image was taken, which did not limit the EL image quality after processing. All the final images present roughly similar information for broken cells and shunt defects present in the module and detected in Fig. 4.

The plots in Fig. 5b show the two sample t-tests that compare the image pixel values under dark (0 current bias) and light (I<sub>SC</sub>

bias) conditions for each test irradiance. The y-axis show the summation of pixel values in the InGaAs detector (512x640), where the value of each pixel is a value between 0.0 (i.e. completely dark) and 1.0 (i.e. completely saturated).

Each t-test shows data from 50 light and 50 dark images at a given irradiance. The green diamonds show the 95% confidence interval of the mean wherein the horizontal green line shows the mean and the top and bottom corners show the confidence interval. The dark and light pixel distributions are considered significantly different when the confidence intervals do not overlap. The t-tests show that the dark and light pixel distributions are significantly different ( $p < 0.05$ ) for all irradiances except for 500 W/m<sup>2</sup> ( $p = 0.06$ ). The difference between dark (background) and light (I<sub>SC</sub> bias) image means illustrates how it was possible to obtain the images in Fig. 5a. As the difference decreases with the irradiation level, the SNR was lower, yet with significant difference.

The sun intensity though constantly varies during the image acquisition, dependent on to the time of the day and cloud cover. Fig. 5c show the time series of light and dark images sequences, as their pixel values changed during the circa 17 seconds that sequence took to acquire. Such variation is directly related to the ambient illumination (sun intensity) variation as it equally affects both the light and background reference (dark) images. Even though irradiance fluctuations bring challenges in particular situations, such variations did not impose visual limitations in the daylight outdoor EL imaging after processing. Nevertheless, automatic aperture adjustment will be required to avoid image saturation during drone inspection.

Averaging several pictures is the most common way the minimize noise from images. Although, to take several pictures of the same scene, if the system camera-power supply is not fast enough, it can be limiting for the drone movement. Fig. 6 shows the resulting averaged and subtracted images when different amounts of light and dark images are used under. All images in Fig. 6 were taken under 300 W/m<sup>2</sup> illumination in natural sunlight. The average of 8 light and dark images (16 in total images), show a good level of noise removal. For this, it is required that the drone keeps position for 0.32s, with a power supply as fast as the camera triggering for 20ms exposure time. This is achievable if the drone is equipped with an appropriate camera stabilization gimbal, in addition to performing digital imaging stabilization on the acquired images. However, fewer averaged pictures does allow the detection of major defects in this example.

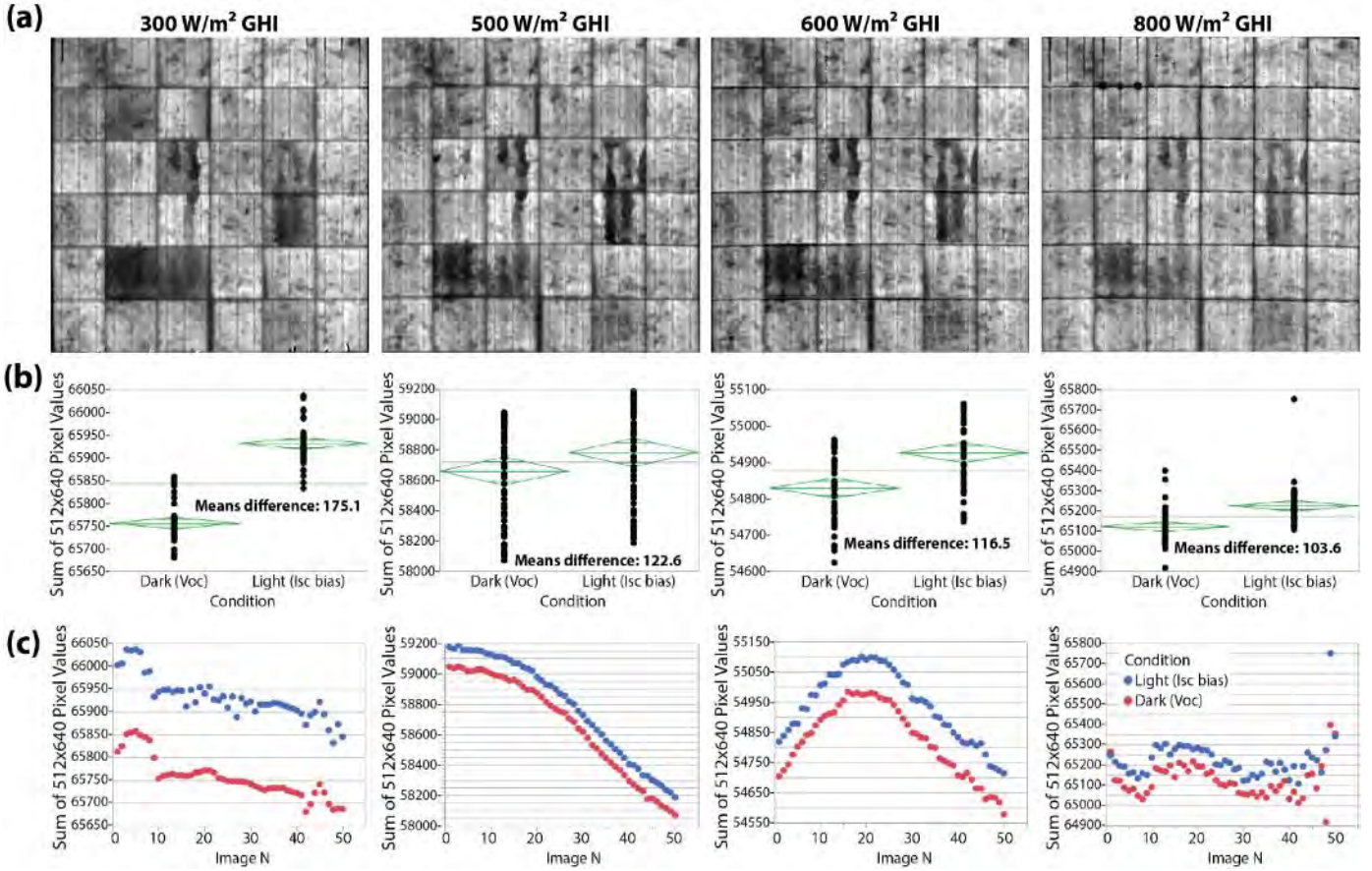


Fig. 5. EL images obtained under different sun irradiation levels, after image processing, automatic cropping and contrast correction (a); sum of pixel values of dark and light images of the correspondent image above, with the mean and 95% confidence interval shown as green diamonds (b); correspondent time series of light (blue dots) and dark (red dots) images, showing variations of light intensity during the acquisition of the sequence of images (c).

### B. Photoluminescence

In addition to the outdoors EL imaging tests, laboratory PL tests were performed. Fig. 7 show the images acquired at 700 ms exposure time for 54, 71, 87, 104 and 120 W/m<sup>2</sup> light intensity on the plan of the cell. Therefore, long exposure times were required for such low illumination rates. As the intensity of a light source complies with the inverse-square law, even a powerful light source will have limited maximum distance from the panels. At the same time, such powerful light source will require cooling, which poses size and weight challenges for the drone.

For the development of the best strategy of minimum weight and best light source for PL outdoor imaging, a measurement modeling was developed, in order to correlate the relevant variables of the system. Such model for the PL image signal generated by an artificial light source ( $S$ ) in arbitrary units can be expressed as the equation below:

$$S = \frac{1}{D^2} \frac{P_{optical}}{A} \tau \eta_{PL}(\lambda_{Light}) \rho_{Camera}(\lambda_{PL}) \quad (1)$$

Where  $D$  is the distance from sample (panel) to the light source;  $P_{optical}$  is the optical power output of the light source which is related to the electrical power input and device

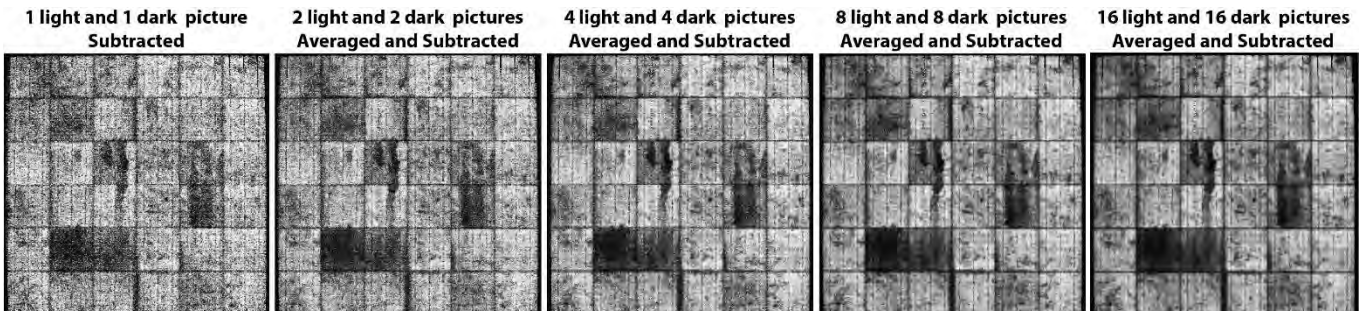


Fig. 6. Averaged and subtracted EL pictures of a solar panel acquired outdoors under 300 W/m<sup>2</sup> sun illumination.

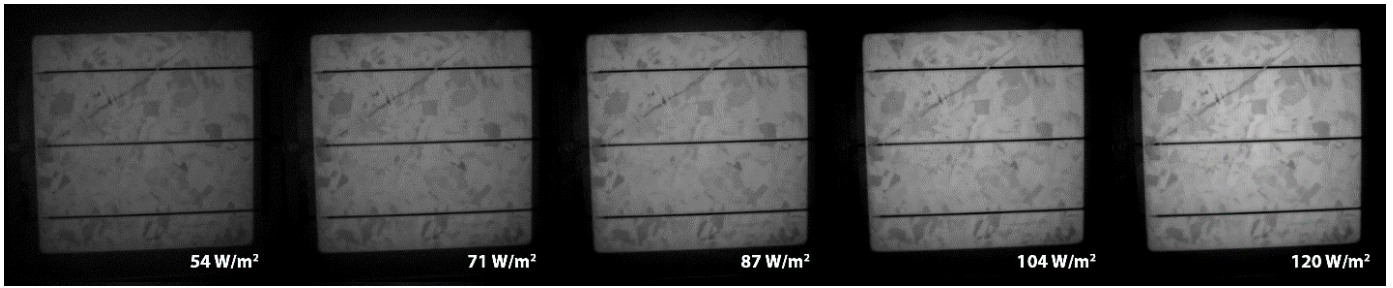


Fig. 7. PL images taken using 800nm laser diode, under 700ms exposure time, from a polycrystalline silicon wafer under different illumination.

efficiency, leading to known heating and consequentially the need for certain cooling.  $A$  is the area to be illuminated, contained by designed optics in order to avoid light loss.  $\tau$  is the exposure time or the time required for the light to be on, here correspondent also to the camera exposure time.  $\eta_{PL}(\lambda_{Light})$  is the PL quantum yield, related to the absorbed photons in the PV module (PV/silicon quantum efficiency) at the given wavelength of the light source and reemitted in the same direction as the incident light.  $\rho_{Camera}(\lambda_{PL})$  is the camera acquisition factor that correlates quantum efficiency, dynamic range, among other sensor and camera designed features, at a certain wavelength, in this case correspondent to the luminescence signal wavelength (centred at 1150 nm).

With such vision of the system, it was possible to correlate the signal response measured in the laboratory with the needed requirements to build a drone integrated light source that will allow outdoor PL imaging. Taking into consideration the available technologies, a laser line scan following the drone movement is the one that complies sufficiently with optical power and current image acquisition requirements. In this case, the area needed to be illuminated is smaller, making the  $\frac{P_{optical}}{A}$  factor lower. Fig. 8 illustrates the above described approach.

According to (1), the laser line scan approach with current available technology will be able to acquire the similar signal presented in Fig. 7 ( $71 \text{ W/m}^2$ ) at three meters distance of a full size module with 20 ms exposure time. Another example would

be a fast pulsing high power laser, supplied by capacitors. The approaches as pulsing laser and LEDs so far presented too low signal intensity for the current setup, but as the whole system is in development, they are not discarded.

## V. CONCLUSION

The EL imaging performed for PV inspection during the day under high sun intensity address the possibility of performing EL imaging inspection with more freedom, during more hours of the day, and simultaneous IR and EL. In a drone system, the compatibility will remain the same for either daylight or nighttime EL. In future work the forward bias and camera triggering will be carried out via wireless communication. In addition, we will focus efforts on improving imaging processing, which can be done automatically and without losing flight time.

The next step for this analysis is to develop a controllable test bed with a moving camera and check the limit of frames from a video taken at certain speeds. The camera used in this work has the maximum frame rate of 60 fps, which is relatively low for this application. Consequently, a faster camera will allow more pictures to be taken in a shorter period, and the future tests will define how fast the drone can move while it takes different amounts of pictures for the image processing.

The PL indoor measurement parameters permitted the measurement modeling for the light source development, which indicates a line laser scan as the most promising light source for outdoor PL and drone integration.

## ACKNOWLEDGEMENT

The authors acknowledge the financial support from Innovation Fund Denmark for the project 6154-00012B DronEL – Fast and accurate inspection of large photovoltaic plants using aerial drone imaging.

## REFERENCES

- [1] M. Köntges *et al.*, “Review of Failures of Photovoltaic Modules,” 2014.
- [2] D. C. Jordan and S. R. Kurtz, “Photovoltaic degradation rates - An Analytical Review,” *Prog. Photovoltaics Res. Appl.*, vol.

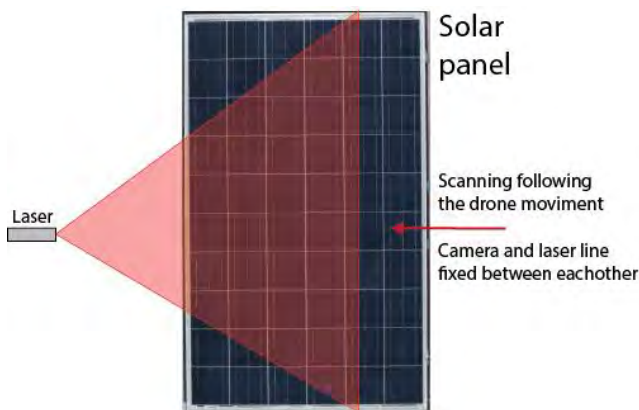


Fig. 8. Laser line scan PL approach.

- 21, no. 1, pp. 12–29, 2013.
- [3] S. Dotenco *et al.*, “Automatic detection and analysis of photovoltaic modules in aerial infrared imagery,” *2016 IEEE Winter Conf. Appl. Comput. Vis.*, pp. 1–9, 2016.
- [4] “The drones that inspect and maintain photovoltaic power plants,” *sUAS News - The Business of Drones*. [Online]. Available: <https://www.suasnews.com/2015/04/the-drones-that-inspect-and-maintain-photovoltaic-power-plants/>. [Accessed: 25-Jan-2017].
- [5] “Drones to cut plant inspection costs as South Africa eyes quality,” *PV Insider*. [Online]. Available: <http://analysis.pv-insider.com/drones-cut-plant-inspection-costs-south-africa-eyes-quality>. [Accessed: 25-Jan-2017].
- [6] S. Johnston and T. Silverman, “Photoluminescence and Electroluminescence Imaging Workstation,” *NREL*, 2015.
- [7] W. S. Yoo, K. Kang, G. Murai, and M. Yoshimoto, “Temperature Dependence of Photoluminescence Spectra from Crystalline Silicon,” *ECS J. Solid State Sci. Technol.*, vol. 4, no. 12, pp. P456–P461, 2015.
- [8] DTU Fotonik, “DTU Risø PV Weather Data.” [Online]. Available: [http://ftnk-psolmaal.win.dtu.dk/B130\\_PV\\_Weather/index.html](http://ftnk-psolmaal.win.dtu.dk/B130_PV_Weather/index.html). [Accessed: 18-May-2017].
- [9] J. E. Hay and J. A. Davies, “Calculations of the solar radiation incident on an inclined surface,” in *Proc. of First Canadian Solar Radiation Data Workshop*, 1980, p. 59.

## LUMINESCENCE IMAGING STRATEGIES FOR DRONE-BASED PV ARRAY INSPECTION

Gisele A. dos Reis Benatto<sup>1</sup>, Nicholas Riedel<sup>1</sup>, Claire Mantel<sup>1</sup>, Sune Thorsteinsson<sup>1</sup>, Peter B. Poulsen<sup>1</sup>, Mingjun Chi<sup>1</sup>, Anders Thorseth<sup>1</sup>, Ole Bjarlin Jensen<sup>1</sup>, Carsten Dam-Hansen<sup>1</sup>, Søren Forchhammer<sup>1</sup>, Kenn H. B. Frederiksen<sup>2</sup>, Jan Vedde<sup>3</sup>, Michael Petersen<sup>4</sup>, Henrik Voss<sup>5</sup>, Michael Messerschmidt<sup>5</sup>, Harsh Parikh<sup>6</sup>, Sergiu Spataru<sup>6</sup> and Dezso Sera<sup>6</sup>

<sup>1</sup>Department of Photonics Engineering, Technical University of Denmark, Frederiksborgvej 399, 4000, Roskilde, Denmark, garb@fotonik.dtu.dk

<sup>2</sup>Kenergy, Grønningen 43, 8700, Horsens, Denmark

<sup>3</sup>SiCon Silicon & PV consulting, J N Vinthersvej 5, 3460, Birkerød, Denmark

<sup>4</sup>Skive Kommune, Torvegade 10, 7800, Skive, Denmark

<sup>5</sup>Sky-Watch A/S, Østre Alle 6 Støvring, 9530, Nordjylland, Denmark

<sup>6</sup>Aalborg University, Pontoppidanstraede 101, 9220, Aalborg, Denmark

**ABSTRACT:** The goal of this work is to develop outdoor defect detection imaging and understand fully its challenges and limitations. The imaging is based on luminescence strategies that will be used for fast and accurate UAV-based inspection system for PV power plants. We studied electroluminescence (EL) acquisition under natural light conditions during several times of the day, under high sun irradiation, to unveil the sunlight noise characteristics towards an InGaAs detector. In order to bring more freedom to a drone-based inspection, we also show the preliminary results of a laser-line based photoluminescence (PL) strategy as a viable method for an outdoor module PL imaging system.

**Keywords:** Electroluminescence, Photoluminescence, Defects, Inspections

## 1 INTRODUCTION

Regular fault detection is highly important to ensure the expected return on investment (ROI) of both small and large-scale PV installations. Field experience shows that after 11-12 years of operation 2% or more of all PV panels fail, despite the fact that they are designed for lasting 25-30 years [1]. PV system inspections are even more necessary for older installations (installed before 2000), since modules manufactured before the 2000 are known to have more significant reliability issues [2]. Furthermore, a number of external factors such as transportation, wind and snow loads, and daily thermal stresses can cause critical damage to the PV panels, which are not always visually detectable. The frequency and detail level of an inspection is often limited by manpower and cost. Drone-based IR thermography surveys of solar plants are a reality today, and are expected to become an automated solar plant inspection method in the near future [3]–[5]. The accuracy of thermographic fault detection though, presents limitations, which can be surpassed when performed in combination to EL and/or PL imaging of the panels. In the laboratory, the combination of these defect detection techniques has already been tested [1], [6], however many challenges still need to be addressed in order to optimize, integrate and automatize the imaging system on a drone.

In this work, we present the results related to the development of the optimization of the outdoor luminescence techniques. First, we show the progress in the understanding and overcoming of the sunlight noise in EL imaging, using optical filters, lock-in signal and image processing. In the following, we present the first results using a laser-line approach under natural low light conditions, as a viable method for an outdoor module PL imaging, since it requires relative low optical power. The outdoor PL imaging enables a drone-based contactless inspection system that does not require hardware connections, as in the case for EL or PL using the sunlight as the light source.

## 2 METHODOLOGY

The luminescence emission peak for silicon-based solar cells at ambient temperature is centred at 1150 nm [7], near a water absorption band in the solar spectrum (AM 1.5) [8]. Two camera detectors are commonly used to detect such emission: i) cooled Si charge-coupled devices (CCD) ii) and short-wave infrared (SWIR) InGaAs sensors. Nevertheless, only the second allows a short enough integration times for non-stationary luminescence image acquisition; therefore, it is ideal for drone operation [9]. The InGaAs detector has a second advantage in that its quantum efficiency (QE) is not active in the most intense wavelengths of the solar spectrum, which is the main source of noise for daylight luminescence imaging. In the following described experiments, an InGaAs camera from Hamamatsu model C12741-03, and an OD>4.0 1150nm band-pass filter with 50nm FWHM was used. The sample was a mechanically stressed module consisting of 36 multicrystalline silicon 156 mm x 156 mm cells.

### 2.1 Electroluminescence

Figure 1a illustrates the outdoor EL setup which consists of a DC power supply unit (PSU), a PV module and an InGaAs camera connected to a modulating box. Such system synchronizes the image acquisition with an electrical forward bias applied by the DC power supply. Figure 1b shows the synchronizing circuit, driven by an Arduino logic controller, and Figure 1c shows the pulse width modulated (PWM) waveforms applied to the PV panel and camera. A PC connected to the camera was required for image data acquisition and settings control. The exposure time was established separately in the camera software.

One of the strategies to enhance the quality of the images obtained at high noise level during the day was sequential image acquisition. We acquired sequences of 100 images (50 under forward bias (EL signal) and 50 as background images for subtraction) at 6 Hz with 20 ms exposure time, while global horizontal irradiance (GHI) was observed through a fast response Si photodiode sensor in a weather station located few meters from the imaging position [10]. The complete image sequence took circa 17 seconds to acquire. Such strategy was used in order to

estimate the effect of the sun irradiation on the imaging process and to better understand and overcome the noise characteristics towards the InGaAs detector. The iris aperture was f8 for all outdoor image acquisitions. A 25 mm fixed focus lens was used, and in order to photograph the whole panel, the camera was positioned at 2.6 meters from the solar module.

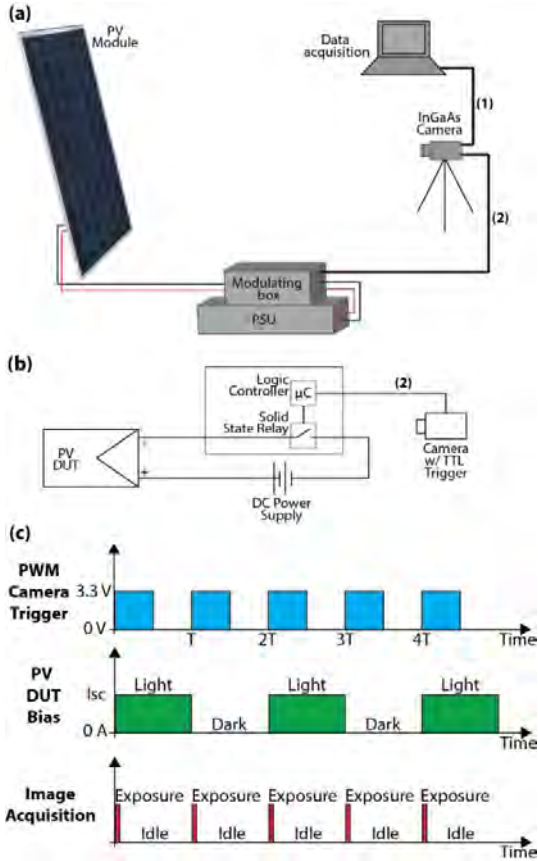


**Figure 1:** Outdoor EL imaging setup (a); correspondent basic trigger circuit that synchronizes the imaging and forward bias from a DC power supply (b); and PWM waveforms driven by the logic controller. Connection path (1) can be replaced with the frame grabber integrated to the drone CPU board, and (2) by radio connection to the modulating box.

As averaging several pictures is a very common method to denoising images, we averaged several EL images per scene to enhance image quality. The image processing included taking the difference between the average of light and dark images, linear scaling of the pixel values, automatic stretching of the initial dynamic range (the source images are 16 bits) to 8 bits for display and cropping of the whole image to the region of interest.

The signal to noise ratio averaged for the imaged scene ( $SNR_{50}$ ) was calculated following the guidelines established in the EL technical standard (IEC TS 60904-13 [11]) using the equation (1), where noise level is obtained from the average absolute deviation of two EL images:

$$SNR_{50} = \frac{\sum_k (0.5 \cdot (EL_1(k) + EL_2(k)) - BG(k))}{\sum_k (|EL_1(k) - EL_2(k)| \cdot \sqrt{0.5 \cdot (\frac{2}{\pi})^{0.5}})} \quad (1)$$

In (1),  $EL_1$  and  $EL_2$  are EL images from the same scene,  $BG$  is the background image of the same scene, and

all the operations are made pixel-by-pixel ( $k$ ). We called “ $SNR_{50}$  of individual images” when the  $SNR_{50}$  is calculated with regular computation, i.e. using two single EL images and one single BG image. When  $SNR_{50}$  is calculated to averaged images,  $EL_1$  and  $EL_2$  correspond to two averaged images from 25 EL images (as we acquired 50 images with EL signal in each sequence), and  $BG$  correspond to the averaged image from 50 background images, all from the same scene/sequence. For this  $SNR_{50}$  value, we refer as “ $SNR_{50}$  of averaged images”.

## 2.2 Photoluminescence

PL images under low natural light were acquired using an 800 nm laser diode at 6 W, while the camera and the laser were circa 0.7 meter from the sample. The laser beam coming from a fibre was shaped into a 4 mm thick line with <5% of optical power loss. The line beam was manually scanned over the area of interest. The sample consisted of the same module used for electroluminescence, with focus in the three cells from row 3, columns B, C and D (see Figure 2). The images were acquired with a 30 ms exposure time.

## 3 RESULTS AND DISCUSSION

### 3.1 Electroluminescence

The EL outdoor imaging experiments in this work were performed on a special testbed, designed for developing outdoor and drone based EL imaging. Here we used several strategies to perform the EL imaging at any time of the day and evaluate possible challenges. For guidance and qualitative comparison, Figure 2 shows the indoors EL image of the mechanically stressed module sample used in the work, which complies with the minimum SNR for EL laboratory measurements:  $SNR_{50} \geq 45$ . However, during the day such images are compromised by high and very often variable light noise levels, primarily from the sunlight itself. For such reasons, the signal to noise ratio requirement for outdoor EL is considerably lower:  $SNR_{50} \geq 5$ .

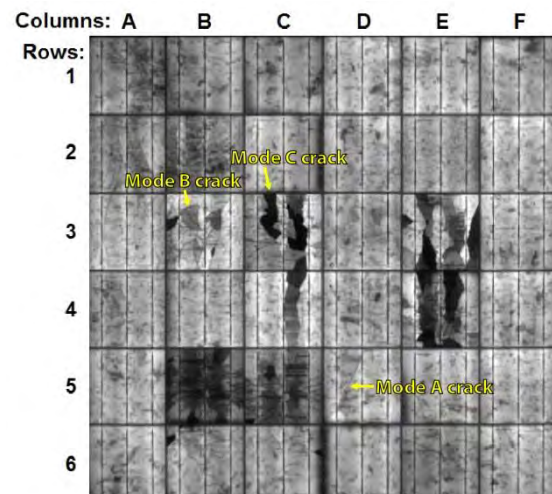


**Figure 2:** Indoors EL image of mechanically stressed PV module, showing mode A, B and C cracks.  $SNR_{50} = 46.20$ .

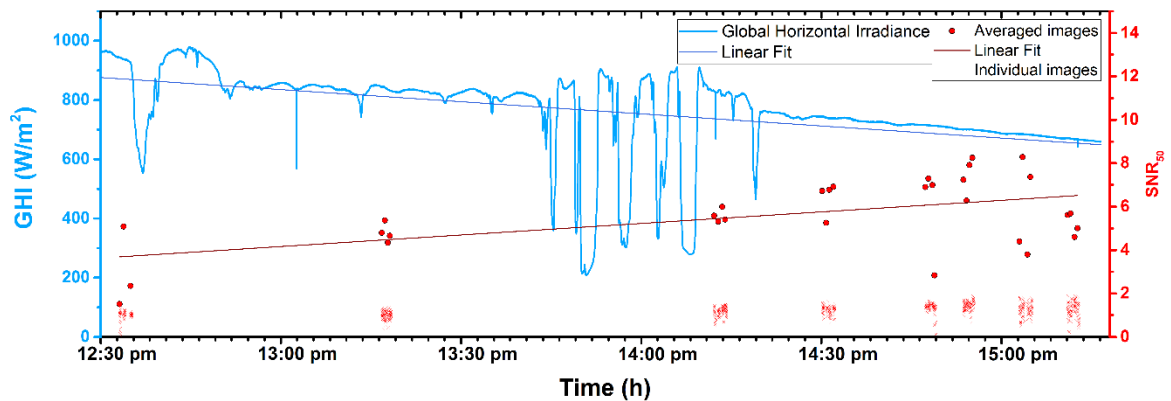
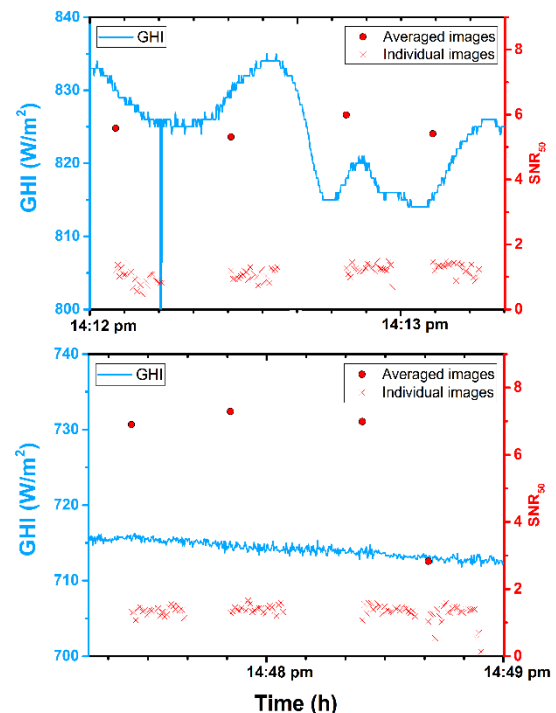


**Figure 3:** SNR<sub>50</sub> of averaged (red dots) and individual (red crosses) EL images, from sequences acquired under the correspondent GHI (light blue line). The linear fit of the GHI (dark blue line) and the SNR<sub>50</sub> of averaged images (dark red line) are also shown.

The sun intensity constantly varies, depending on the time of the day and cloud cover, while the InGaAs sensor is highly sensitive to variations in the light intensity. For this matter, we need to understand what the requirements are for EL imaging in a system including camera, EL signal and sun irradiation, in order to obtain the highest SNR. To obtain images as close as possible to the real field inspection condition, we performed the experiments in a bright, but partially cloudy day, with the panel was 75° tilted from the horizontal facing south. We acquired sequences of images in groups of at least three sequences.

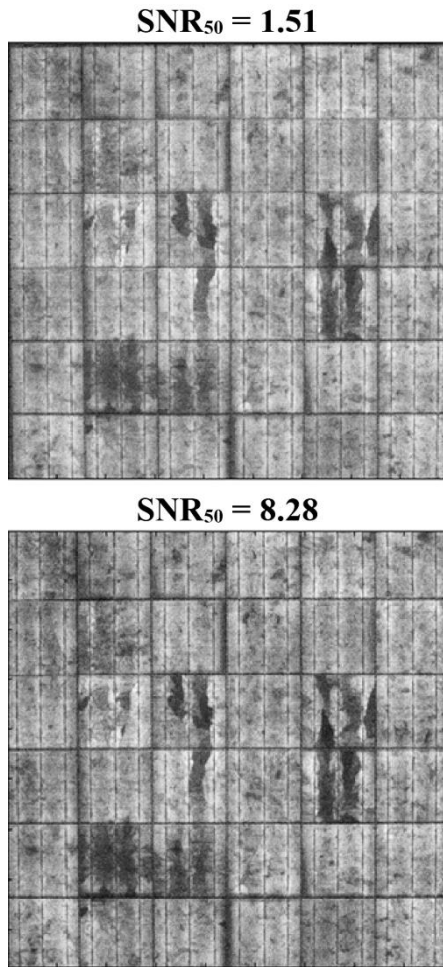
In Figure 3, the SNR<sub>50</sub> of the EL image sequences were plotted with correspondent global horizontal irradiation (GHI) in the moment of the image acquisition. In total, 31 image sequences were taken in a period of 3 hours. This measurement was performed under very high irradiation (~700-850 W/m<sup>2</sup>) and as such, the iris aperture was very small (f8) to avoid saturation on the detector. Both SNR<sub>50</sub> of individual (red crosses) and averaged (red dots) images were plotted in the graph of Figure 3. At first, we verified the substantial improvement in SNR<sub>50</sub> of averaged images in relation to the individual images, with general improvement due to the denoising by averaging. At the same time, we observe that the average of SNR<sub>50</sub> values of individual images remained constant along the GHI decrease during the day, while the linear fit SNR<sub>50</sub> of the averaged images (dark red line) rose with very similar inclination as the linear fit (dark blue line) of the GHI throughout the day.

Figure 4 shows the zoomed in values for two periods of the graph from Figure 3, one with high variation of sun irradiation (Figure 4 top) and the other with high variation of SNR<sub>50</sub> values of averaged images (Figure 4 bottom). The SNR<sub>50</sub> of the individual images is not directly affected by the GHI variations. Figure 4 bottom show sequences taken in a relatively stable GHI period, however, the last sequence presents a high variation SNR<sub>50</sub> of individual images, which may be caused by internal factors, such as the PSU electrical bias. At Figure 4 bottom, one of the SNR<sub>50</sub> of the averaged images presented very low SNR<sub>50</sub> value, which might be related to individual SNR<sub>50</sub> variations between sets of images. One reason to this low value could be that the method chosen to denoise, the averaging, is not optimal due to varying acquisition conditions. For such cases, advanced denoising process could be applied.



**Figure 4:** SNR<sub>50</sub> of averaged (red dots) and individual (red crosses) EL images, from sequences acquired under the correspondent GHI (light blue line). Two sections zoomed in from Figure 3

The images corresponding to the lowest and the highest SNR<sub>50</sub>, after the application of the image processing routine, are shown in Figure 5. Even though the lowest SNR<sub>50</sub> does not comply with the minimum requirements of the standard (SNR<sub>50</sub> ≥ 5), the image presented similar qualitative information and is able to show clearly mode C cracks present in the module (see Figure 2). Automatic defect detection methods such as EL intensity distributions (ELID) of mode C crack could be applied here, using the relative EL signal from the unbroken cells [12].



**Figure 5:** Outdoor EL images of the lowest (top) and highest (bottom) SNR<sub>50</sub> obtained under high sun irradiation levels, after image processing, automatic cropping, and contrast correction.

### 3.2 Photoluminescence

Photoluminescence is a very challenging technique to be applied outdoors, due to the need for powerful light sources. At the same time, such technique could provide full freedom for a drone to execute luminescence imaging throughout strings in large-scale PV farms, independent of time demanding changes in electrical contacts. As a strategy toward PL outdoor imaging, we used a line shaped laser beam, with the aim to enhance the optical power per area and lower the required exposure time. Such PL strategy also brings up the possibility of using additional optical filtering (lenses and polarizers) which can be important alternatives for daylight luminescence inspection.

Figure 6 shows the comparison of EL and PL imaging using laser-line scan of cells B3, C3 and D3 of the module shown in Figure 2. PL emission induced by laser-line scan provided different information than EL. The broken and isolated regions of the cell (darker in EL) appear brighter than the unbroken or the still connected regions. As such regions have high series resistance, the probability of charge carriers generated by the laser to recombine radiatively is high, as they do not have proper electric connection to disperse [13], [14]. This method can be used either for complementary information to improve automatic assessment or for accurate contactless defect detection. Comparing the PL imaging induced by a

homogeneous laser beam over a single cell illuminated area, the exposure time decreased from 700 ms to 30 ms from laser-area to laser-line beam respectively.

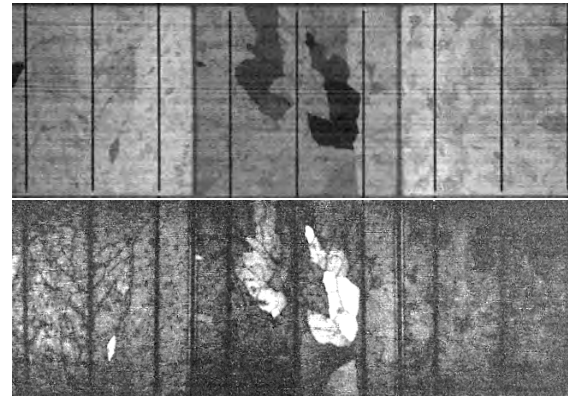


**Figure 6:** EL (top) and PL (bottom) PL image using laser-line scan of cells B3, C3 and D3 of the module from Figure 2.

## 4 DRONE INTEGRATION

For the integration of the EL setup into a drone, the connections 1 and 2 shown in Figure 1a need to be replaced with wireless connections. The modulation box is adapted to have radio communication to camera triggering. The synchronisation between imaging on the drone and the bias current needs to be accurate, therefore precise timestamping will be performed on an electronic board embedded on the drone. The final drone-based EL concept is shown in the top of Figure 7.

For non-stationary images, and therefore for drone applications, several images have to be acquired fast. At the current stage of this work, EL images for qualitative analysis can be acquired with eight EL images averaged and subtracted by eight background images. With a PSU capable to be as fast as the camera triggering for 20 ms exposure time, this amount of images can be obtained with a drone, equipped with an appropriate camera stabilization gimbal, keeping its position for 0.32 s. A faster camera could reduce the images acquisition time to 0.15 s. Moreover, further strategies can be used in terms of image processing in cases image displacements of few centimetres. Regarding the saturation of the detector due to high sun irradiation, which in this work needed to be controlled manually by the iris aperture, it will not be the case using an InGaAs camera adaptive to natural light variations.

As EL imaging is a technique that requires electrical contacting, it will be a time limiting factor for drone-based inspection, especially in large-scale solar plants. A PL imaging induced by a laser-line scan following the drone movement is a promising technique towards a contactless luminescence technique. As the laser-line concentrates the optical power in a small area, the total optical power acquired can comply with the weight and cooling requirements for a drone payload. An illustration of the scan orientation is shown in the bottom of Figure 7.

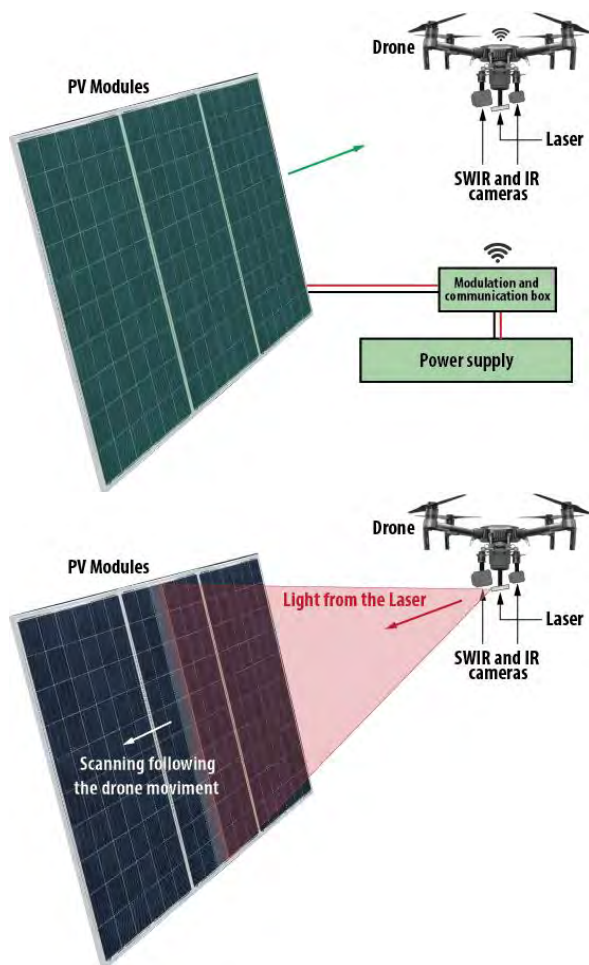


**Figure 7:** Drone-based inspection concept for EL (top) and PL laser-line scan (bottom).

## 5 CONCLUSIONS

In this work, EL imaging was performed successfully under high GHI, using the EL signal modulation and image processing. The averaging of the images from the modulation sequence lead to denoising by averaging, and the improvement of  $SNR_{50}$  was observed. We observed also that the  $SNR_{50}$  of the averaged images increases with linear decrease in GHI.

At the same time, the  $SNR_{50}$  of individual images was not directly affected by GHI variations, and  $SNR_{50}$  of averaged images was low when individual  $SNR_{50}$  presented high variation between sets of images, making denoising by averaging not optimal in such conditions. However, the lowest  $SNR_{50}$  image presented similar qualitative information and showing mode C cracks clearly.

The PL image using a laser-line scan excitation allowed covering a larger module area than a beam over an area, and at the same time lowered the exposure time for the technique from 700 to 30 ms.

The next steps of this work includes: forward bias and camera triggering carried out via wireless communication; controllable testbed with a moving camera to determine the limits of modulating EL image acquisition; scaling up laser-line scan for outdoor PL inspections.

## 6 ACKNOWLEDGEMENTS

The authors acknowledge the financial support from Innovation Fund Denmark for the project 6154-00012B DronEL – Fast and accurate inspection of large photovoltaic plants using aerial drone imaging.

## 7 REFERENCES

- [1] M. Köntges *et al.*, “Review of Failures of Photovoltaic Modules,” 2014.
- [2] D. C. Jordan and S. R. Kurtz, “Photovoltaic degradation rates - An Analytical Review,” *Prog. Photovoltaics Res. Appl.*, vol. 21, no. 1, pp. 12–29, 2013.
- [3] S. Dotenco *et al.*, “Automatic detection and analysis of photovoltaic modules in aerial infrared imagery,” *2016 IEEE Winter Conf. Appl. Comput. Vis.*, pp. 1–9, 2016.
- [4] “The drones that inspect and maintain photovoltaic power plants,” *sUAS News - The Business of Drones*. [Online]. Available: <https://www.suasnews.com/2015/04/the-drones-that-inspect-and-maintain-photovoltaic-power-plants/>. [Accessed: 25-Jan-2017].
- [5] “Drones to cut plant inspection costs as South Africa eyes quality,” *PV Insider*. [Online]. Available: <http://analysis.pv-insider.com/drones-cut-plant-inspection-costs-south-africa-eyes-quality>. [Accessed: 25-Jan-2017].
- [6] S. Johnston and T. Silverman, “Photoluminescence and Electroluminescence Imaging Workstation,” *NREL*, 2015.
- [7] W. S. Yoo, K. Kang, G. Murai, and M. Yoshimoto, “Temperature Dependence of Photoluminescence Spectra from Crystalline Silicon,” *ECS J. Solid State Sci. Technol.*, vol. 4, no. 12, pp. P456–P461, 2015.
- [8] G. dos Reis Benatto *et al.*, “Development of outdoor luminescence imaging for drone-based PV array inspection,” *IEEE Photovolt. Spec. Conf.*, 2017.
- [9] J. Adams *et al.*, “Non-Stationary Outdoor EL-Measurements with a Fast and Highly Sensitive InGaAs Camera,” *32nd Eur. Photovolt. Sol. Energy Conf. Exhib.*, 2016.
- [10] DTU Fotonik, “DTU Risø PV Weather Data.” [Online]. Available: [http://ftnk-psolmaal.win.dtu.dk/B130\\_PV\\_Weather/index.html](http://ftnk-psolmaal.win.dtu.dk/B130_PV_Weather/index.html). [Accessed: 18-May-2017].
- [11] I.E.C., “PNW/TS 82-901 Ed. 1.0 Photovoltaic devices - Part 13: Electroluminescence of photovoltaic modules (proposed future IEC TS 60904-13).” <http://www.iec.ch/>.
- [12] S. Spataru, P. Hacke, and D. Sera, “Automatic Detection of Inactive Solar Cell Cracks in Electroluminescence Images,” *44rd IEEE Photovolt. Spec. Conf.*, 2017.
- [13] T. J. Silverman, M. G. Deceglie, K. Vansant, S. Johnston, and I. Repins, “Illuminated outdoor luminescence imaging of photovoltaic modules,” in *IEEE Photovoltaic Specialists Conference*, 2017.
- [14] I. Zafirovska, M. K. Juhl, J. W. Weber, O. Kunz, and T. Trupke, “Module inspection using line scanning photoluminescence imaging,” *32nd Eur. Photovolt. Sol. Energy Conf. Exhib.*, 2016.



## Outdoor Electroluminescence Acquisition Using a Movable Testbed

**Benatto, Gisele Alves dos Reis; Mantel, Claire; Riedel, Nicholas; Santamaria Lancia, Adrian Alejo; Thorsteinsson, Sune; Poulsen, Peter Behrendorff; Forchhammer, Søren; Thorseth, Anders; Dam-Hansen, Carsten; Kenn H. B., Frederiksen**

*Total number of authors:*  
16

*Published in:*  
Proceedings of 7th World Conference on Photovoltaic Energy Conversion

*Link to article, DOI:*  
[10.1109/PVSC.2018.8547628](https://doi.org/10.1109/PVSC.2018.8547628)

*Publication date:*  
2018

*Document Version*  
Peer reviewed version

[Link back to DTU Orbit](#)

### *Citation (APA):*

Benatto, G. A. D. R., Mantel, C., Riedel, N., Santamaria Lancia, A. A., Thorsteinsson, S., Poulsen, P. B., Forchhammer, S., Thorseth, A., Dam-Hansen, C., Kenn H. B., F., Vedde, J., Larsen, M., Voss, H., Parikh, H., Spataru, S., & Sera, D. (2018). Outdoor Electroluminescence Acquisition Using a Movable Testbed. In *Proceedings of 7th World Conference on Photovoltaic Energy Conversion* (pp. 0400-0404). IEEE. <https://doi.org/10.1109/PVSC.2018.8547628>

---

### General rights

Copyright and moral rights for the publications made accessible in the public portal are retained by the authors and/or other copyright owners and it is a condition of accessing publications that users recognise and abide by the legal requirements associated with these rights.

- Users may download and print one copy of any publication from the public portal for the purpose of private study or research.
- You may not further distribute the material or use it for any profit-making activity or commercial gain
- You may freely distribute the URL identifying the publication in the public portal

If you believe that this document breaches copyright please contact us providing details, and we will remove access to the work immediately and investigate your claim.

# Outdoor Electroluminescence Acquisition Using a Movable Testbed

Gisele A. dos Reis Benatto<sup>1</sup>, Claire Mantel<sup>1</sup>, Nicholas Riedel<sup>1</sup>, Adrian A. Santamaria Lancia<sup>1</sup>, Sune Thorsteinsson<sup>1</sup>, Peter B. Poulsen<sup>1</sup>, Søren Forchhammer<sup>1</sup>, Anders Thorseth<sup>1</sup>, Carsten Dam-Hansen<sup>1</sup>, Kenn H. B. Frederiksen<sup>2</sup>, Jan Vedde<sup>3</sup>, Michael Larsen<sup>4</sup>, Henrik Voss<sup>4</sup>, Harsh Parikh<sup>5</sup>, Sergiu Spataru<sup>5</sup> and Dezso Sera<sup>5</sup>

<sup>1</sup>Department of Photonics Engineering, Technical University of Denmark, Frederiksborgvej 399, 4000, Roskilde, Denmark,

<sup>2</sup>Kenergy, Grønningen 43, 8700, Horsens, Denmark

<sup>3</sup>SiCon Silicon & PV consulting, J N Vinthersvej 5, 3460, Birkerød, Denmark

<sup>4</sup>Sky-Watch A/S, Østre Alle 6 Støvring, 9530, Nordjylland, Denmark

<sup>5</sup>Aalborg University, Pontoppidanstraede 101, 9220, Aalborg, Denmark

**Abstract** — The experimentation with a movable outdoor electroluminescence (EL) testbed is performed in this work. For EL inspections of PV power plants, the fastest scenario will include the use of unmanned aerial vehicle (UAV) performing image acquisition in continuous motion. With this motivation, we investigate the EL image quality of an acquisition in motion and the extent of image processing required to correct scene displacement. The results show processed EL images with a high level of information even when acquired at 1 m/s camera speed and at frame rate of 120 fps.

**Index Terms** — Electroluminescence, PV inspections, PV reliability.

## I. INTRODUCTION

The addition of 74 GW of photovoltaics capacity occurred around the world only in 2016, overcoming the growth of any other energy producing fuel for the first time [1]. Such elevate number of power implies that a very high number of modules have been installed and are subjected to many failure sources provoked by material aging, unnoticed manufacture defects and extreme weather conditions. For this reason, regular fault detection is highly desirable to ensure the return on investment (ROI) of both small and utility scale PV installations. However, frequency and the level of detail of an inspection is often limited by available work force and cost. Electroluminescence (EL) imaging can be used to rapidly and accurately detect a large range of major and minor faults in PV modules such as cell cracks, broken interconnections, PID among others [2], [3]. In other words, EL imaging can reveal many faults often not detectable by current field inspection methods such as infrared thermography or electrical characterization. State-of-the-art EL image acquisition however faces crucial technical limitations, including long exposure times and low signal-to-noise ratio (SNR) under sun irradiation.

The most commonly used cameras for EL imaging have silicon-based detectors (such as a CCD), which present a weak spectral sensitivity in the EL emission range of crystalline silicon solar cells. Although a high resolution can easily be

achieved with these detectors, their long image exposure times (on the order of seconds) limit inspection time and their application in non-stationary systems such as in UAV. In contrast, cameras with InGaAs-based detectors have a good spectral response to the silicon luminescence emission and therefore shorter integration times, which can be even shorter 1 ms [4].

Background (BG) images are often necessary to correct for ambient light noise, and are strictly necessary when performing daylight EL. The capability to acquire many images per scene, with high frame rates, allows outdoor daylight EL acquisition to be performed in very short intervals or even in motion with proper image processing, such as motion estimation and compensation.

Research efforts are ongoing to develop a fully automated solar plant inspection method including UAV based EL imaging [2], [4]–[6]. To support this effort, the objective of this paper is to perform the image processing required to obtain a final EL image from an original EL video acquisition in motion, in a system that includes lock-in EL for daylight measurements. Such technical development requires fast image acquisition and extensive image processing, i.e. module recognition and segmentation allowing for motion compensation, for posterior averaging and background removal to enhance the SNR of the final EL images.

## II. EXPERIMENTAL DETAILS AND METHODOLOGY

### A. Test string and electrical contact

For this experiment, one PV module was mounted in a test string, which was highly damaged by potential-induced degradation (PID) and cell cracks. The module consisted of 72 mono-crystalline 12.7 cm cells, arranged in a 6 x 12 matrix. Although the experiment was performed in a test string, only one module is analysed in this work concerning motion compensation and image processing. The experiment was performed outdoors, under natural light during a mostly

cloudy day when the diffuse light contribution was roughly 80% of the total global irradiance. The modules were installed facing south at 60 degrees inclination.

The outdoor EL setup, which consisted of a DC power supply unit (PSU), a PV module connected to a modulating (lock-in) box (Fig. 1). Such system synchronizes the image acquisition with an electrical forward bias applied by the DC power supply. The camera triggering was synchronized remotely via a 2.4 GHz Arduino Nano radio frequency module located in the EL lock-in modulation box. This wireless communication was designed for UAV applications, where the camera will be controlled by an embedded PC and powered by the UAV battery. The modulation frequency is programmable and driven by an Arduino logic controller. The pulse width modulated (PWM) waveforms applied to the PV panels in two different scenarios concerning the control of the camera can be seen in Fig. 2. Scenario 1 corresponds to the camera trigger in synchronization with the PV device under test (DUT) bias signal, while Scenario 2 corresponds to an unsynchronized signal, so the camera was able to acquire as many images as possible (in practice 4-5 per EL/BG state of the of the DUT bias) during the motion.

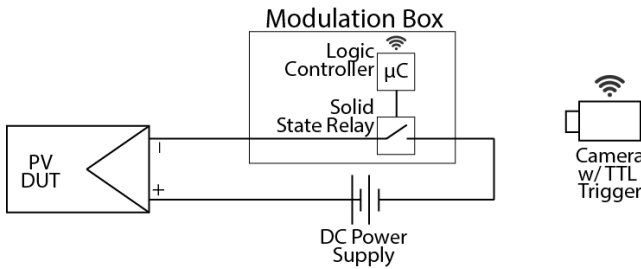


Fig. 1. Panels and modulation box connection circuit. The camera synchronization was performed via radio communication with the logic controller.

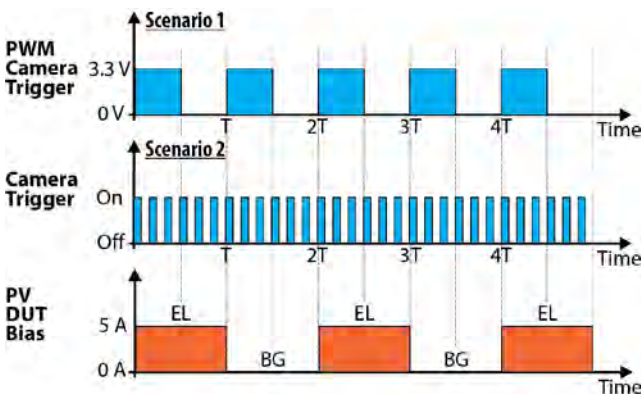


Fig. 2. PWM waveforms driven by the logic controller. The rising edges in the camera trigger waveforms correspond to when the image acquisition begins. Scenario 2 has the camera controlled by the internal trigger (see text for details).

### B. Camera and motion setup

An InGaAs camera with 640 x 512 resolution and 14 bits dynamic range from Raptor Photonics model Owl640 is used for the experiment. A PC connected to the camera was required for image data acquisition and settings control. The EL images were acquired at 25 Hz PWM trigger frequency, which corresponds to a PSU frequency of 12.5 Hz. The exposure time was fixed for both scenarios (1 ms) and frame rate were 25 fps in Scenario 1 (controlled by the PWM camera trigger) and 120 fps in Scenario 2 (settled at the camera software – see Fig. 2). Note that the rising edges in the camera trigger waveforms correspond to when the image acquisition begins.

The luminescence emission peak for silicon-based solar cells at ambient temperature is centred at 1150 nm [7], therefore, to avoid detecting light from the sun and surroundings, an OD>4.0 1150nm band-pass filter with 50nm FWHM was used. A 25 mm fixed focus sapphire lens, without aperture control, was used, and in order to photograph the whole panels in vertical position, the camera was placed at approximately five meters from the test string, so a full module in portrait position could fit in the field of view.

The camera was fixed to a dolly equipped with wheels and placed on rails (Fig. 3). This mount allowed the acquisition of EL images at fixed distance from the PV modules, while the camera was moved in parallel along the length of the string. The camera was moved manually during images sequence acquisition at a speed of approximately 1 m/s, controlled with a stopwatch.

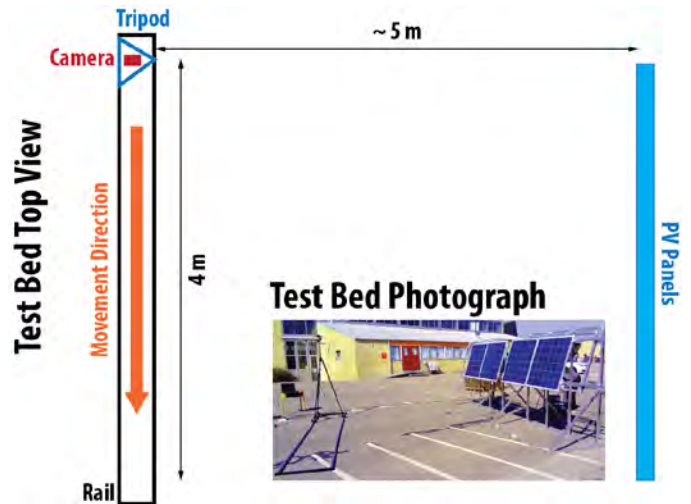


Fig. 3. Outdoor EL movable test bed. Top view diagram and photograph in the inset.

### C. Image processing for motion compensation

To increase the quality of images for better failure diagnostic, EL and BG images are often averaged separately and the resulting  $EL_{AVG}$  and  $BG_{AVG}$  and then subtracted. A

priori to those averaging and subtracting operations, due to the non-stationary acquisition, numerous image-processing steps are required, and the automation of this process is ongoing. The programming steps to process the EL and BG images developed for this work include:

- i. Identification of images containing the complete module
- ii. Module edges and corner recognition;
- iii. Module segmentation and cropping to region of interest;
- iv. Split of EL and BG images;
- v. Motion estimation and compensation;
- vi. Averaging for denoising;

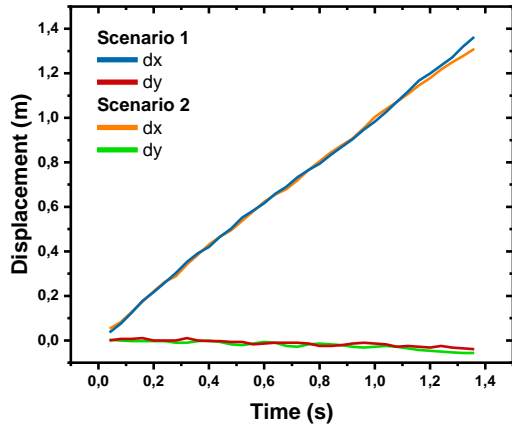


Fig. 4. Computed motion compensation for the image sequence acquired with the test bed illustrated in Fig.3.

- vii. EL and BG subtraction
- viii. Mapping to 8 bits and contrast correction for visualization.

From the image sequence (or video) acquired, the actual speed of the camera could be calculated from the computed motion shown in graph of Fig. 4. Even though the motion was manually induced, the speed is shown to be adequately constant throughout the image acquisition. Displacement on the y-axis along the image sequence was due to vibrations during the motion on the x-axis and it was also compensated for. On average, the images in motion analyzed in this work were captured at 0.97 m/s, here on referred as  $\sim 1$  m/s for simplification.

#### IV. RESULTS AND DISCUSSION

The EL images acquired in motion outdoors, after image processing are shown in Fig. 5, together with its stationary EL image taken indoors with a high-resolution DSLR camera. The Scenario 1 represents the situation when the BG image is taken sequentially right after the EL image, minimizing alterations in the final image quality that might occur with ambient light variations, i.e. sun irradiance variation, what has been shown to have influence in EL daylight image acquisition [8]. Scenario 2 in the other hand represent the fast image acquisition up to the camera image acquisition limit, therefore acquiring the highest amount of images possible at the given speed. The camera motion speed ( $\sim 1$  m/s) and the DUT lock-in frequency (25 Hz) was kept the same for both scenarios. In

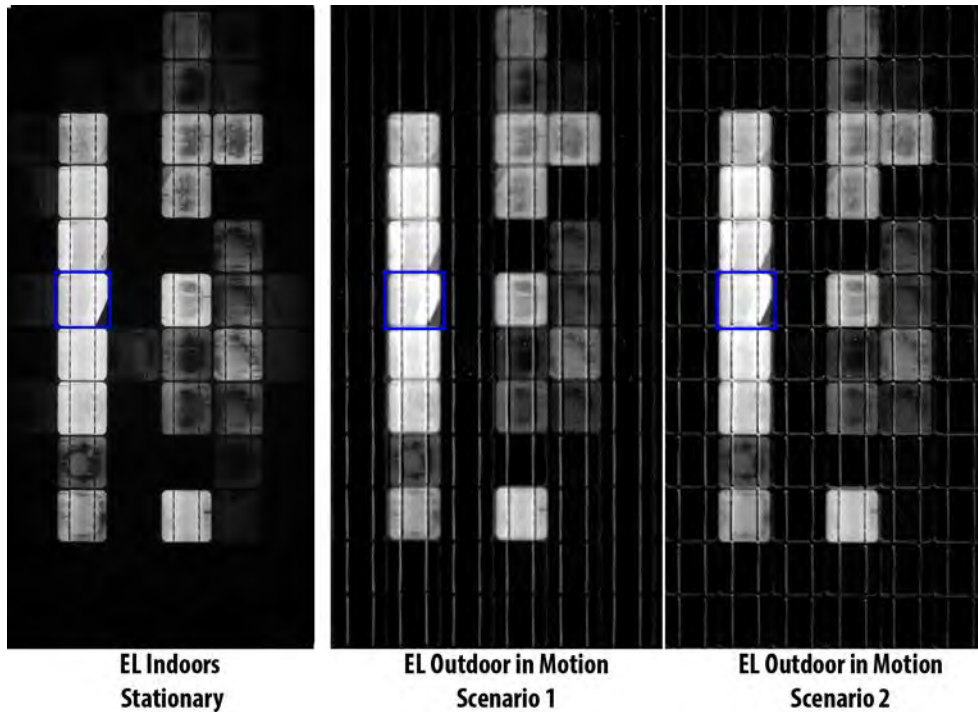


Fig. 5. EL image acquired indoors at stationary conditions compared with outdoor EL images acquired in motion ( $\sim 1$  m/s) using synchronized (Scenario 1) and unsynchronized (Scenario 2) lock-in and camera triggering after image processing (see text for further details).

the Scenario 1, the amount of images available for averaging were 34, i.e. 17 EL and 17 BG images. In the Scenario 2, the amount of images available were 162, or 81 EL and 81 BG images. While 34 images may be limiting for EL imaging at high sun irradiance, 162 images offers more than enough images for averaging and SNR enhancement to obtain EL images at  $>900 \text{ W/m}^2$  GHI and strong direct beam [8]. Even though the indoors EL is performed with a much higher resolution camera, the outdoors EL final images acquired in motion show very similar level of details. For the sun irradiance and weather conditions at the moment of the test (overcast), the higher amount of images available in Scenario 2 did not add on the obtained visual quality than the images available in Scenario 1, therefore not all available images from Scenario 2 were used to obtain the resulting image Fig. 5. The  $\text{SNR}_{50}$  calculated for the resulting images (following the guidelines from [9] and the extension proposed on [10]) was 7.9 for Scenario 1 using 34 images and 6.7 for Scenario 2 using 44 images. These values tend to change considerably with the measurement conditions, combined with camera settings and bias, what suggests further investigation concerning specific factors in the future. We can discern the shunted cells typically in the edges of a module affected by PID, and cracks in several of the not completely shunted cells.

The resulting images still present a certain level of pixel mismatch after the motion compensation, easily verified by observing the ribbon and interconnection that would not appear after subtraction if the pixel displacement were accurate over the whole module. The motion compensation was more accurate on the top of the module than on the bottom (in the x-axis). Independent of the scenario characteristics itself, but possibly due to the higher amount of images used, the Scenario 2 EL image exhibited a mismatch also in the y-axis after the applied correction detected as shown in the graph of Fig. 4. Those mismatches are due to perspective distortion and can be compensated for after the module segmentation and motion compensation steps [11].

An important challenge for fast acquisition of outdoors EL is to detect minor failures using low resolution cameras, and for lock-in EL in motion, this play a decisive role to the obtainment of final EL image. We verified that the main information level provided by outdoors non-stationary EL is preserved even with minor displacements; however, it may compromise the detection of faults of little dimensions such as micro-cracks. In Fig. 6, the detail of the cracked cell 6B (coordinate defined following the guidelines at [9], indicated in Fig. 5 with a blue square) is shown for the same three EL images in Fig. 5. Cell 6B present a mode C crack in the bottom left corner, finger interruption in the top left and a mode A crack (or micro-crack) between the busbars. Even though some of the finger interruptions may be unclear in the outdoor EL images taken in motion, the micro-crack is observable as an apparent difference in shade when zoomed in for the automatic contrast correction applied.

In order to evaluate how the micro-crack appears in the final outdoor EL images taken in motion, in Fig. 7, the gray value profile from the corresponding red lines drawn in Fig. 6 are presented. The EL Indoors stationary image had pixel resolution reduced to match the EL Outdoor camera resolution for comparison. Using the indoors stationary EL as guide (as the acquisition conditions, i.e. stationary, indoors, camera resolution and sharpness enhance considerable the image properties), we verify that the micro-crack is not well defined as a trough in the profile for the outdoor EL in motion as in the EL stationary. Instead, the gray value arises smoothly (from the right to the left), a better defined trough for Scenario 1, possibly due to its better pixel match. However, in the full module appearance, the micro-crack can be easily confirmed. This example shows that the final non-stationary EL image, due to its image quality, may be more challenging for automatic defect detection based on histogram analysis and/or gray value signature, and may require machine-learning tools for the task.

Finally, no blur effect from the individual non-stationary EL images were observed with acquisition made at 25 (Scenario 1) or 120 fps (Scenario 2) at the speed tested ( $\sim 1 \text{ m/s}$ ).

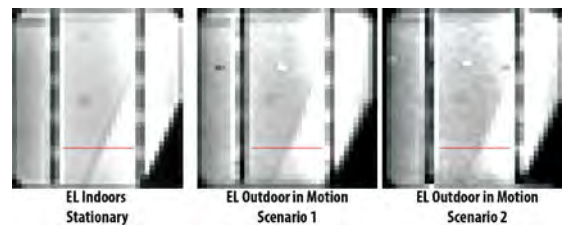


Fig. 6. Detail from cell 6B from the modules EL images shown in Fig. 5. EL Indoors stationary had pixel resolution reduced to match the EL Outdoor camera resolution for comparison.

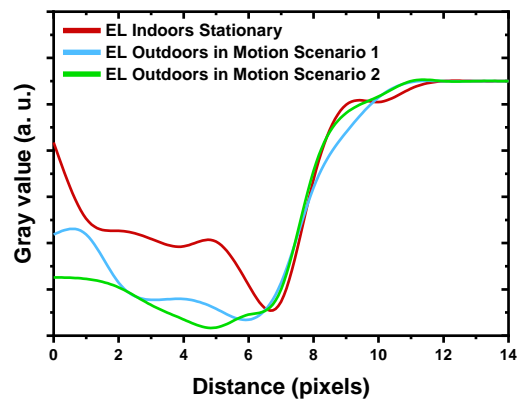


Fig. 7. Gray value profile over a micro-crack corresponding to the horizontal red line drawn in the EL images at Fig. 6.

## V. CONCLUSION

In this work, we performed the experiment and the image processing steps to obtain outdoor lock-in EL images acquired in motion. The critical information regarding the state of the

active area of the PV modules was not only preserved in the processed non-stationary EL images, but very little dimension faults such as micro-cracks and finger interruptions were possible to be recognized. These results confirm the application of outdoor measurement of lock-in EL in motion suggested by Adams et al. [4] and is a step further towards fast EL acquisition in the field. The current speed recorded here would allow the lock-in EL image acquisition for 1 PV module per second, which corresponds to a minimum of 100 kW of PV modules inspected per hour, depending on the installation configuration.

While two different image acquisition scenarios have been performed here, the ideal scenario in daylight conditions will be the combination of both Scenarios 1 and 2, where ambient light interference can be avoided and the highest amount of images acquired. To allow efficient use of these resources, two image processing steps, i.e. module segmentation and perspective correction, should take place along with motion compensation.

The continuation of this work will further address the image processing and perform lock-in EL image acquisition with a movable test bed at different sun irradiance levels and faster speeds.

#### ACKNOWLEDGEMENTS

The authors acknowledge the financial support from Innovation Fund Denmark for the project 6154-00012B DronEL – Fast and accurate inspection of large photovoltaic plants using aerial drone imaging.

#### REFERENCES

- [1] OCDE & IEA, “Market Report Series: Renewables 2017, analysis and forecasts to 2022,” *J. Qual. Particip.*, vol. 104, no. 42, pp. 20142–20142, 2017.
- [2] J. B. S. Koch, T. Weber, C. Sobottka, A. Fladung, P. Clemens, “Outdoor Electroluminescence Imaging of Crystalline Photovoltaic Modules: Comparative Study between Manual Ground-Level Inspections and Drone-Based Aerial Surveys,” *32nd Eur. Photovolt. Sol. Energy Conf. Exhib.*, pp. 1736–1740, 2016.
- [3] M. Köntges et al., “Review of Failures of Photovoltaic Modules,” *IEA-Photovoltaic Power Syst. Program.*, pp. 1–140, 2014.
- [4] J. Adams et al., “Non-Stationary Outdoor EL-Measurements with a Fast and Highly Sensitive InGaAs Camera,” *32nd Eur. Photovolt. Sol. Energy Conf. Exhib.*, 2016.
- [5] C. Buerhop and H. Scheuerpflug, “Field inspection of PV-modules using aerial, drone-mounted thermography,” *29th Eur. Photovolt. Sol. Energy Conf. Exhib.*, pp. 2975–2979, 2013.
- [6] G. A. dos Reis Benatto et al., “Development of outdoor luminescence imaging for drone-based PV array inspection,” *IEEE Photovolt. Spec. Conf.*, 2017.
- [7] T. Fuyuki, H. Kondo, T. Yamazaki, Y. Takahashi, and Y. Uraoka, “Photographic surveying of minority carrier diffusion length in polycrystalline silicon solar cells by electroluminescence,” *Appl. Phys. Lett.*, vol. 86, no. 26, pp. 1–3, 2005.
- [8] G. A. dos Reis Benatto et al., “Luminescence imaging strategies for drone-based PV array inspection,” *33rd Eur. Photovolt. Sol. Energy Conf. Exhib.*, pp. 2016–2020, 2017.
- [9] IEC, “PNW/TS 82-901 Ed. 1.0 Photovoltaic devices - Part 13: Electroluminescence of photovoltaic modules (proposed future IEC TS 60904-13).” <http://www.iec.ch/>.
- [10] C. Mantel et al., “SNR Study of Outdoor Electroluminescence Images under High Sun Irradiation,” *IEEE 7th World Conf. Photovolt. Energy Convers.*, pp. 2–4, 2018.
- [11] C. Mantel et al., “Correcting for Perspective Distortion in Electroluminescence Images of Photovoltaic Panels,” *IEEE 7th World Conf. Photovolt. Energy Convers.*, 2018.



## Drone-Based Daylight Electroluminescence Imaging of PV Modules

**Benatto, Gisele Alves dos Reis; Mantel, Claire; Spataru, Sergiu Viorel; Santamaria Lancia, Adrian Alejo; Riedel, Nicholas; Thorsteinsson, Sune; Poulsen, Peter; Parikh, Harsh Rajesh; Forchhammer, Søren; Séra, Dezso**

*Published in:*  
IEEE Journal of Photovoltaics

*Link to article, DOI:*  
[10.1109/JPHOTOV.2020.2978068](https://doi.org/10.1109/JPHOTOV.2020.2978068)

*Publication date:*  
2020

*Document Version*  
Peer reviewed version

[Link back to DTU Orbit](#)

*Citation (APA):*  
Benatto, G. A. D. R., Mantel, C., Spataru, S. V., Santamaria Lancia, A. A., Riedel, N., Thorsteinsson, S., Poulsen, P., Parikh, H. R., Forchhammer, S., & Séra, D. (2020). Drone-Based Daylight Electroluminescence Imaging of PV Modules. *IEEE Journal of Photovoltaics*, 10(3), 872 - 877.  
<https://doi.org/10.1109/JPHOTOV.2020.2978068>

---

### General rights

Copyright and moral rights for the publications made accessible in the public portal are retained by the authors and/or other copyright owners and it is a condition of accessing publications that users recognise and abide by the legal requirements associated with these rights.

- Users may download and print one copy of any publication from the public portal for the purpose of private study or research.
- You may not further distribute the material or use it for any profit-making activity or commercial gain
- You may freely distribute the URL identifying the publication in the public portal

If you believe that this document breaches copyright please contact us providing details, and we will remove access to the work immediately and investigate your claim.

# Drone-Based Daylight Electroluminescence Imaging of PV Modules

Gisele A. dos Reis Benatto<sup>1</sup>, Claire Mantel<sup>1</sup>, Sergiu Spataru<sup>1</sup>, Adrian A. Santamaria Lancia<sup>1</sup>, Nicholas Riedel<sup>1</sup>, Sune Thorsteinsson<sup>1</sup>, Peter B. Poulsen<sup>1</sup>, Harsh Parikh<sup>2</sup>, Søren Forchhammer<sup>1</sup>, Dezso Sera<sup>3</sup>

<sup>1</sup>Department of Photonics Engineering, Technical University of Denmark, Frederiksborgvej 399, 4000, Roskilde, Denmark.

<sup>2</sup>Department of Energy Technology, Aalborg University, Pontoppidanstraede 101, 9220, Aalborg, Denmark.

<sup>3</sup>Science and Engineering Faculty, Queensland University of Technology, Gardens Point Campus, 2 George Street, QLD 4000, Brisbane, Australia.

**Abstract**—Electroluminescence (EL) imaging is a PV module characterization technique, which provides high accuracy in detecting defects and faults such as cracks, broken cells interconnections, shunts, among many others; furthermore, the EL technique is used extensively due to a high level of detail and direct relationship to injected carrier density. However, this technique is commonly practiced only indoors – or outdoors from dusk to dawn – because the crystalline silicon luminescence signal is several orders of magnitude lower than sunlight. This limits the potential of such a powerful technique to be used in utility scale inspections, and therefore the interest in the development of electrical biasing tools to make outdoor EL imaging truly fast and efficient. With the focus of quickly acquiring EL images in daylight, we present in this article a drone-based system capable of acquiring EL images at a framerate of 120 frames per second. In a single second during high irradiance conditions, this system can capture enough EL and background image pairs to create an EL PV module image that has sufficient diagnostic information to identify faults associated with power loss. The final EL images shown in this work reached representative quality  $SNR_{AVG}$  of 4.6, obtained with algorithms developed in previous works. These drone-based EL images were acquired with global horizontal solar irradiance close to one sun in the plane of the array.

**Index Terms**—Electroluminescence, Imaging, Photovoltaic cells, Crystalline Silicon PV, Characterization of Defects in PV.

## I. INTRODUCTION

In 2017, the worldwide photovoltaic electricity production was of 460 TWh, with a cumulative capacity of almost 400 GWp [1]. This growth represents a significant investment in the energy sector, in the order of a hundred billion dollars or euros. Approximately 60% of the world's PV capacity corresponds to utility-scale projects and this share has only increased in the last years. This trend points out the need for fast and effective PV inspections to assure the expected solar energy harvest.

The accuracy in identifying module faults in a PV plant is usually proportional to the time dedicated to the inspection. Fast inspections can be performed with Unmanned Aerial Vehicles (UAV, or drones) using visual and thermographic cameras, which provide information on glass breakage, soiling, bird dropping, disconnected strings, hotspots, among other major defects. However, disconnected PV modules or

strings, PID shunted cells, and faulty bypass diodes are all failures that are not detectable by visual inspection and cause only a slight temperature increase between active and inactive module parts, making them more difficult or even impossible to detect under low irradiance conditions [2]. Electroluminescence (EL) is inherently more accurate than infrared thermography in identification of faults because EL images offer resolution in the semiconductor material level. Furthermore, the availability of EL is significantly higher than infrared, considering weather conditions vary greatly with location and latitude [3]. The limitations of EL imaging mainly occur due to the sensitivity of the camera detector in the wavelength of interest and the presence of intense stray light, essentially sunlight.

The recently published IEC technical specification for EL and field experience require EL measurements to be acquired under  $<100 \text{ W m}^{-2}$  outdoor light intensity [2], [4]. Such a constraint not only limits inspection time, but also can create additional drawbacks, for instance restrictions to site access, UAV flight time restrictions, and safety concerns when making the electrical connections in a dark and sometimes humid environment, among others.

It is of high importance to develop a system that can perform daylight EL with UAV image acquisition. Under bright sunlight (i.e. global horizontal irradiance - GHI  $> 100$



Fig. 1. Drone-based daylight EL acquisition system.

$W m^{-2}$ ) it is usually not sufficient to use daylight filters and subtract (calculate the difference of each pixel) a single background (BG) image to obtain a clear EL image. The intensity of the EL signal is several orders of magnitude lower than sunlight, which lead to a very low signal-to-noise ratio (SNR) [5], [6]. However, by acquiring many EL/BG image pairs taken at the same fixed position and adding post processing steps – which consist on the average and subtraction of the BG for each pair – the SNR can be increased to an acceptable level. For outdoor EL, the accepted  $SNR_{50}$  (the simplified quantification of image quality) should be higher than 5 [4]. In addition, an extension of the  $SNR_{50}$  equation was proposed for the specific case when averaging is required [7], where  $SNR_{AVG}$  should also be higher than 5 to obtain an outdoor EL image with satisfactory quality.

The primary requirement for daylight EL imaging is that images have to be acquired fast and with short exposure times to avoid motion blur and saturation due to sunlight; this requirement can be met with the use of cameras with InGaAs based detectors [8]. Even with the appropriate hardware, there are several further challenges to enhance the SNR of images taken from a UAV system: i) each PV panel has to be segmented with high accuracy; ii) the motion of the UAV must be compensated for the images to be averaged without loss in quality; iii) the true EL/BG difference – that can be translated in a delta of the mean pixel values – must remain stable and substantial in magnitude.

Here we present an acquisition system installed in a drone (Fig. 1) able to acquire 120 EL/BG modulated images per second (i.e. 60 image pairs), allowing bright daylight EL imaging of PV modules. The modulation approach (sequential acquisition of EL/BG image pairs) was adopted instead of a batch approach (sequential acquisition of EL images and then sequential acquisition of BG images), as modulation was a more robust approach during high solar irradiance variability, which is often the case in Denmark where the test flights were performed. The modulated electrical waveform was applied using two separate approaches: DC square waveform and AC+DC sinusoidal waveform. The final drone-based EL images shown in this work presented lower quality compared to those obtained indoors and stationary in daylight, but still having sufficient quality to identify the main features related to the module power loss.

## II. METHODOLOGY

In the following subsections, the details of the image acquisition system, device under test (DUT), electrical modulation and image post processing are presented. These steps were employed for the obtainment of the final EL images from a drone.

### A. Image acquisition

The EL/BG image pair acquisition apparatus is comprised of a hexacopter drone equipped with an InGaAs camera (640 x 512 pixels sensor) and an embedded PC for camera control, live image feedback and image storage. Fig. 2 shows an overlay of the solar spectrum, filter transmission and sensor sensitivity, which are the elements present in a typical daylight EL acquisition. The EL signal corresponds to the crystalline silicon (c-Si) luminescence spectrum. The camera, lens and filter details have been presented previously [9]. The acquired image consisted in the luminescence spectra from c-Si (red line) and sunlight (here the AM 1.5 spectrum – black line) which for this case is considered as noise. The spatial EL acquisition was made by an InGaAs sensor with quantum efficiency (QE) at around 80% in the region of the c-Si peak luminescence. To avoid the acquisition of the sun irradiance in most of the sensor QE region and favor the c-Si acquisition, a bandpass (BP) filter was used and its transmittance is also represented in Fig. 2. During the sequence acquisition, the exposure time must be kept fixed and chosen at the measurement to avoid saturation due to the sunlight.

Fig. 3 shows the main controls and hardware involved in the flight and image acquisition, as well as the post processing steps performed after flight. The drone and camera control were connected to a computer via two different Wi-Fi channels for better signal stability. The drone controller software allowed semi-autonomous flights, according to regulations on safety. The images are all stored locally in the

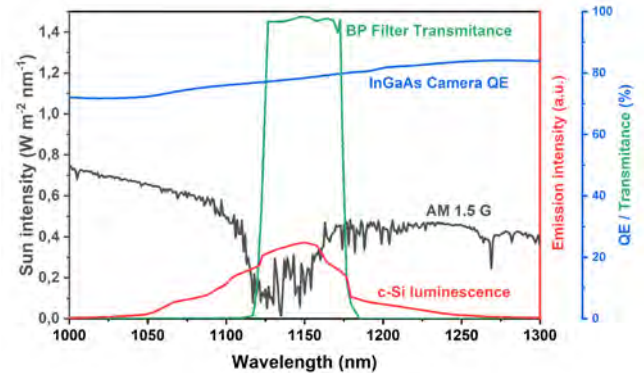


Fig. 2. Signal and sensor involved in daylight EL imaging. See text for further details.

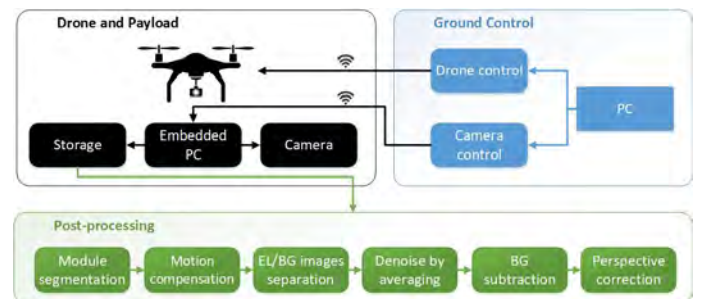


Fig. 3. Components of the drone-based EL/BG image acquisition system and post processing steps.

embedded PC (Apalis TK1 from Toradex) [10] and used for post image processing afterwards.

### B. DUT and electrical modulation

A mechanically stressed PV module with 36 multi-crystalline 15.6 x 15.6 cm cells arranged in a 6 x 6 cells matrix is used as the DUT in this work. Every two columns of the DUT were connect to a bypass diode, therefore the device had 3 bypass diodes in total. As informed by the manufacturer,  $V_{OC}$  and  $I_{SC}$  under STC conditions of this particular module was 22.6 V and 8.4 A respectively. The stressed module contained cells with several electrically connected cracks (A cracks), partially (B cracks) and completely isolated regions (C cracks) [11].

In order to witness the waveform shape and frequency flowing through the DUT during the EL image sequence acquisition, the measurement circuit illustrated in Fig. 4 was arranged to monitor the electrical signal in the PV module. The measurement setup consisted of a power supply unit (PSU) and a Keysight DSO-X2004A, 4-channel oscilloscope. The power supply was connected directly to the terminals of the DUT, and a 10 mΩ shunt resistor was placed at the negative terminal. The DUT voltage  $V_{PV}$  was measured at the terminals of the DUT and the current was measured as the voltage drop  $V_{Rsh}$  across the shunt resistor. Both voltages were measured in differential mode and the absolute value was calculated out of the subtraction of the positive and negative values for each  $V_{Rsh}$  and  $V_{PV}$ .

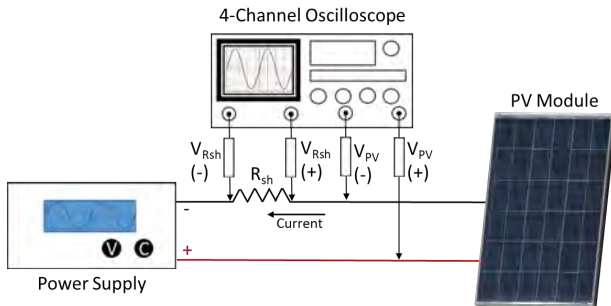


Fig. 4. Measurement circuit for the PSU waveforms running in the PV module.

#### a. DC electrical modulation

A bidirectional DC power supply unit (PSU) SM 1500-CP-30 from Delta Elektronika [12] was used to generate a modulated voltage bias for the PV panels, with a period chosen as a multiple of the camera acquisition period. Fig. 5 shows the measured voltage and current waveform programmed at 60 Hz when the connected PV panel was indoors at low light conditions and outdoors under 970 W m<sup>-2</sup> global irradiance measured in the plane of the array ( $G_{POA}$ ); the secondary y-axis shows the mean pixel values of the PV

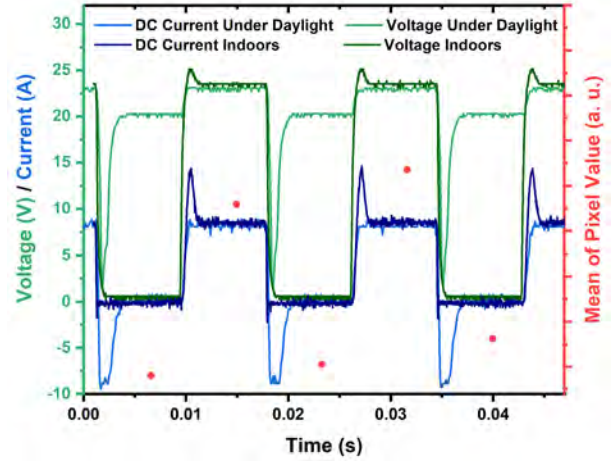


Fig. 5. DC current waveform at 60 Hz flowing through a PV panel indoors under low light and outdoors under 970 W m<sup>-2</sup> in the plane of the array.

panel EL/BG image pairs acquired at 120 fps outdoors at the same time.

The PSU was programmed to be controlled by voltage, corresponding current limits were set to 0 A and STC  $I_{SC}$ . The DC square wave signal was programmed with a period of 16.67 milliseconds, i.e. frequency of 60 Hz. The forward bias applied to the PV consisted of a programmed square wave DC voltage signal, pulsing between 0 V and 25 V. During the current and voltage modulation, it can be seen that indoors (no sun irradiance), the voltage goes to zero and tries to go the 25 V, but switches automatically to current control (CC) mode in  $\sim I_{SC}$  and correspondent voltage (slightly higher than  $V_{OC}$ ). This can be seen as a brief (app. 1 ms) transient overshoot in the current square wave measured indoor. Note that the panel voltage at the same injected current is slight lower than in the indoors case as the solar panel temperature was few degrees higher during the daylight. When the bias is performed outdoors, the programmed period for the voltage goes to 0 V results in a brief overshoot to  $-I_{SC}$ , as expected due to the sun irradiation on the device. Shortly after, the PSU switches automatically to CC mode, keeps the voltage at  $V_{OC}$  and the current closely to 0 A following the programmed waveform. When the voltage goes to 25 V, the PSU holds it in CC mode, avoiding the voltage provoked overshoot and maintaining the current at forward bias  $I_{SC}$  and correspondent voltage close to  $V_{OC}$ . Such effects can be explained by the PSU programming be performed based on voltage control, current limits driven by the PV module IV characteristics and capacitive effects of the cells in the module.

From the luminescence signal point of view and in general terms in module level in the purpose of this work, the luminescence intensity is directly proportional to the (internally and externally) injected carrier density in the PV device [13], [14]. Considering this, the mean pixel value of the PV panel images is higher when the injected current is higher, and lower when current is zero. However, the luminescence

signal is not zero when the injected current is zero under daylight conditions, as photoluminescence (PL) occurs between  $V_{OC}$  and  $V_{MPP}$ , with virtually zero PL signal at  $-I_{SC}$  [13], [15], [16]. Here we consider that “PL only” image acquisition would occur if images taken at  $V_{OC}$  were subtracted by images obtained at the  $-I_{SC}$  current overshoot, but the probability of the images to be acquired under the former condition was low and not observed during our tests in the form of abnormally lower mean pixel values. The collection of EL/BG images performed in the DC modulation condition was correspondent of the electrical signal in the DUT being  $+I_{SC}$  and zero current respectively. Therefore, PL signal is taken out by the subtraction, as the “low pixel value” images – considered here BG images – contain most of the PL signal that is not accounted for in the final version of the image. Thus, the BG images here are not as typically used for EL imaging background images during nighttime or indoors (no luminescence signal), as for daylight conditions the BG images do contain PL information. In the future, the consideration of the valuable characterization information contained in PL images and its potential to increase the overall luminescence signal should be considered for the DC modulation scenario. Here, only the EL image type of information was chosen to be considered, especially for the final image qualitative interpretation.

The frequencies of the electrical bias and framerate result in collecting an EL/BG image pair one after the other. This approach minimizes the interference of rapid fluctuations in solar irradiance during the measurements due to different levels of cloud cover. The apparent rise of the pixel values over time in Fig. 5 is an example of the effect of such interference, already noticeable in such short time period. The fast framerate allows acquiring many images of the same PV panel with the drone in movement, thus permitting the acquisition of several sequences of images (or video with several scenes) without the need for brief stops in front of each module. As the camera was not actively synchronized with the bias signal, an additional step separating EL from BG images by post-processing was necessary. This post-processing uses the average pixel value within the panel (higher for EL than BG images). The absence of synchronization between the camera and PSU implies that the phase between image acquisition and bias signal is not guaranteed and the post-processing also had to verify that the average pixel value between EL and BG was large enough to create a useful difference image. EL image repeatability without synchronization with the modulation signal can be achieved by EL image oversampling, analysis of the high and low states, and discarding the transient states. For the DC electrical signal, the measured frequency showed to be lower than expected compared to the programmed modulation period ( $\sim 58$  Hz) due to limitations of the DC power supply control. This lower frequency leads to a mismatch with the camera acquisition frequency. Consequently, a significant

amount of images acquired in the sequence are discarded as transient states by the EL/BG separation algorithm, leaving less images available for averaging and quality enhancement.

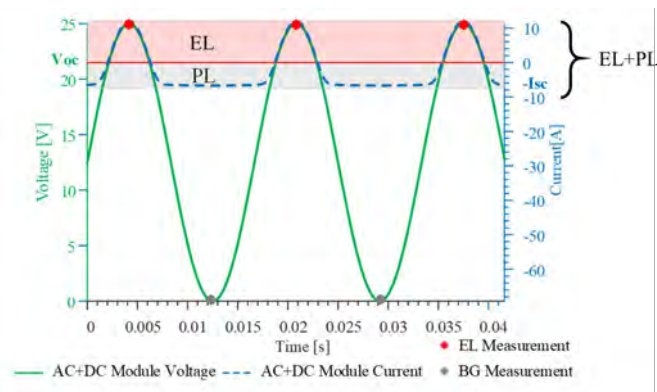


Fig. 6. Simulated AC+DC current and voltage waveform at 60 Hz under  $850 \text{ W m}^{-2}$  and  $48 \text{ }^\circ\text{C}$  cell temperature, depicting the PL (gray), EL (red) operation regions, and time instances when EL signal and BG images are acquired.

#### b. AC+DC electrical modulation

An AC PSU model AC6804A from Keysight was also used for modulated bias to avoid strong sun irradiance interferences in the bias signal. The forward bias applied to the PV consisted of an AC+DC coupling signal (sinusoidal AC signal with a DC offset). As in the DC case, the AC+DC sinusoidal signal frequency was 60 Hz, while image acquisition was performed with a framerate of 120 Hz. A simulation of the voltage and current waveform under sunlight ( $850 \text{ W m}^{-2}$  and  $48 \text{ }^\circ\text{C}$  cell temperature), is shown in Fig. 6. Here we can observe in gray the  $I_{SC}$  to  $V_{OC}$  operation region of the module, where the solar cell emit PL due to sunlight excitation only. The PL intensity is minimal at the  $(0\text{V}, -I_{SC})$  operation point, since most of the excess carriers are extracted [13], [14].

As in the previous case described in section B.a, the absence of synchronization between the camera and PSU implies that the phase between image acquisition and the waveform shown in Fig. 6 is arbitrary and verified by image post-processing. For this waveform, the delta can vary between acquisition sequences and is not necessarily dependent of the sun irradiation. A delta indicated by post-processing assures that the EL/BG difference is enough to acquire EL images correspondent to high (EL) and no/low bias (BG) states. The AC+DC modulation signal is smoother and frequency stable compared to the DC modulation, so as soon as the image acquisition starts close to a maximum or minimum bias, all the images in the sequence are available for image enhancement. More image sequences might be required to reach repeatability of EL imaging using AC+DC modulation, as the start point of the acquisition is arbitrary.

Between  $V_{OC}$  (21.5 V) and  $V_{MAX}$  (25 V), depicted in red in Fig. 6, the module is forward biased, and current is injected in the solar cells, causing EL radiation in addition to PL, as in this case the BG image does contain PL signal. The maximum EL radiation is reached at the maximum injected current (shown in the example of Fig. 6). As the acquisition for each operation point is arbitrary, the luminescence signal captured is EL+PL or can even be PL only, but for the sake of the comparison in this paper, we will call it “EL image”.

### C. Post processing

After drone flights, the images are transferred from the embedded PC internal storage and post processed using algorithms developed in MATLAB. The image processing steps for stationary daylight EL include EL/BG image separation, averaging, BG subtraction, perspective correction of the obtained image following the procedure detailed in [17], and quality control, i.e.  $SNR_{AVG}$  calculation following the formula detailed in [7]. For EL/BG images acquired in movement, as it is the case with drone acquisition, the following additional steps must be performed: i) PV panel edge detection and segmentation in each image of the sequence; ii) motion compensation of the whole image sequence. These two steps are performed before the EL/BG image separation, which is the first step for stationary daylight EL.

These additional steps require a very high degree of accuracy and robustness of the image processing algorithms, adding a much higher level of complexity. Moreover, EL/BG separation needs also to be improved to overcome variations not only from occasional cloud cover, but also from changes of angle of acquisition.

In each frame, the panel is firstly detected and segmented from the rest of the image content. That allows compensating the motion between different frames and registering across all images of the sequence with a full search block matching algorithm. After the denoising is performed by the averaging and BG subtraction steps, the perspective deformation is corrected to obtain a perfectly square panel. The complete set of steps taken by the post processing of drone-based EL images can be seen in the green box of Fig. 3.

The amount of images needed to improve the SNR until the recommended quality depends of many empirical factors, such as sun irradiance and EL/BG difference, but the main and the most decisive factor for image improvement is spatial match [7]. When spatial match is not a problem (in the case of stationary daylight EL), 16 image pairs are enough for visually acceptable EL image for cracks diagnosis [6]. In this work, we are dealing with two extreme scenarios, which are high sun irradiances and motion acquisition. Sequences acquired under high irradiances tend to provide smaller EL/BG deltas, however a considerable number of images (around 50 image pairs) well spatially matched overcomes this drawback and provides a good quality image to detect cell cracks. Detailed study correlating the concurrent factors for in daylight EL image quality are still under development.

## III. RESULTS AND DISCUSSION

Fig. 7 shows the EL images from the cracked PV panel acquired in four different conditions: indoors under low light (Fig. 7a), outdoors under bright daylight with stationary sequential image acquisition and AC+DC electrical modulation (Fig. 7b); outdoors under bright daylight with sequential image acquisition in motion from the drone system and DC electrical modulation (Fig. 7c); and outdoors under bright daylight with sequential images acquired in motion from the drone system and AC+DC electrical modulation (Fig. 7d). All outdoor sequences had 100 image pairs acquired and the resulting images required the post processing described in Section II.C, where the motion compensation took part only when the sequences were obtained in motion from the drone.

The drone acquisition of the DC modulated image occurred in a clear sky morning, with GHI varying from 839.9 to 845.7  $W m^{-2}$  during the course of the data acquisition. The module was positioned facing the sun and had approximately 970.6  $W m^{-2}$  in the POA. The drone acquisition of the AC+DC modulated image occurred in a partially cloudy afternoon with GHI varying from 226.4 to 768.6  $W m^{-2}$  and with PV panel  $G_{POA}$  measured 856.0  $W m^{-2}$  just before image acquisition. The exposure times in these irradiance situations were 0.37 ms for Fig.7b, 0.30 ms for Fig.7c and 0.26 ms for Fig 7d.

Stationary indoor and outdoor EL images (Figs. 7a and 7b

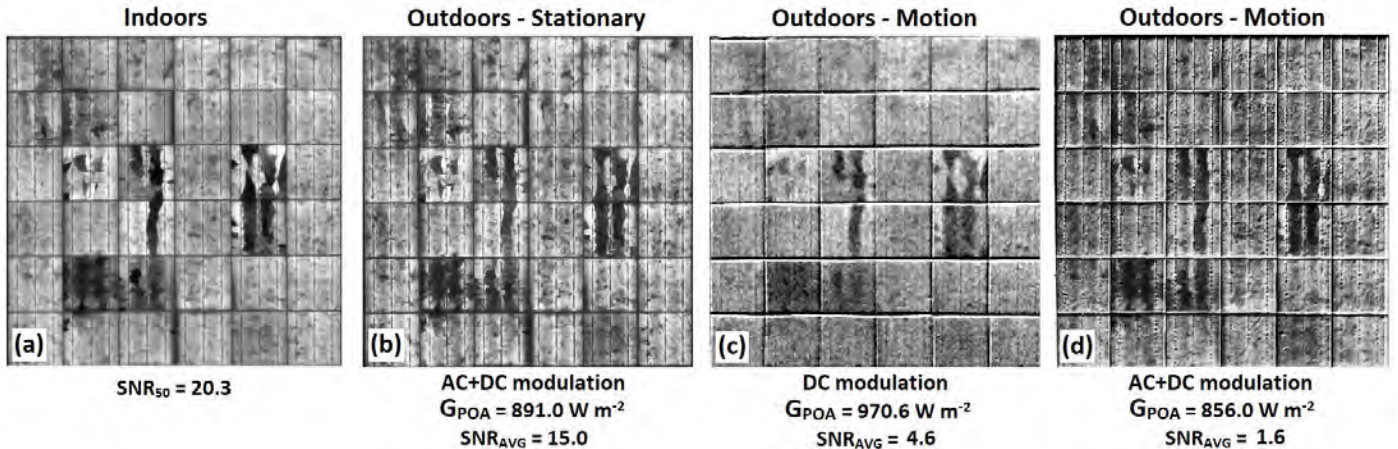


Fig. 7. Mechanically stressed PV panel EL images acquired in different conditions (see text for further details).

respectively) presented comparable visual quality. The calculated  $SNR_{50}$  and  $SNR_{AVG}$  were 20.3 for indoor and 15.0 for outdoor stationary respectively. For indoor, this value is relatively low, as it is expected to be higher than 45 for such conditions [4], however, the laboratory conditions was not similar to a dark room environment and the images were acquired with the drone system stationary, where slight motion and shaking may apply and reduce the quality. Here, the indoor image is shown for visual comparison with outdoor images, as the SNR calculations can present visual inconsistencies. The stationary outdoor image is presented for the same reason, as it was acquired in similar  $G_{POA}$  as the images acquired by the drone system.

The EL images obtained in motion from the drone had  $SNR_{AVG}$  of 4.6 for DC modulation signal and 1.6 for AC+DC modulation signal. These values are lower than the minimum requested quality for outdoor EL imaging ( $SNR_{50} = 5$ ) [4], while for the DC modulated one is very close. Visually, only B and C mode cracks were well identified for both images and the quality of the DC modulated image seems lower than the AC+DC modulated, even though the quantified quality tells the contrary. Spatial misalignment can be observed in the cell edges in the form of extra bright or dark edges. This occurred due to the segmentation registration occurring only at pixel level, as sub-pixel would imply interpolation and therefore create other types of uncertainties/mismatches. In Fig. 7c, instabilities in the DC modulation signal summed with the drone motion effected considerably the delta between EL and BG images, causing several images from the sequence to be discarded and there were fewer images available to improve quality. The visually low quality level presented by Fig. 7c compromises the identification of A cracks. Also, disconnected regions smaller than crystallographic defects cannot be visually identified as cracks. However, disconnected regions that are considerably larger than crystallographic defects are still well distinguishable. These faults are the ones that affect the most the power of this mechanically stressed module and can be segmented for power loss estimation.

In Fig. 7d, the AC+DC modulation signal presented more stability and after motion compensation, the delta between EL and BG images was well preserved and most of the images in the sequence could be used for quality enhancement. The lower quality here, compared with the outdoor stationary, is mainly due to mismatch in positioning the image pairs acquired in motion. We observed that positioning mismatch in sub-pixel level is enough to prevent optimal quality improvement in terms of the  $SNR_{AVG}$  quantification. Moreover, the magnitude of the delta between EL and BG images was considerably smaller in Fig. 7d than in Fig. 7c, what could be the reason for the low calculated  $SNR_{AVG}$ . As well as for Fig. 7c, the A cracks were barely identified in Fig. 7d, but crystallographic defects and disconnected cracks with similar dimensions are better differentiable than in Fig. 7c.

Improving quality of sequences acquired in motion proved to be a challenge, even with reproducible module segmentation and EL/BG image selection. The main reason we found so far for not reaching visual quality similar to the outdoor stationary was the large area where sub-pixel level matching of images is crucial. Before these results and observations found during the process of reaching them, stable modulation signals under sunlight and improved algorithms to active a higher level of match between the EL/BG image pairs are highly recommended to obtain daylight EL images from drones successfully. Additionally, the method suggested by the EL technical specification [4] to quantify the quality of the EL images presented inconsistencies between the calculation and visual identification of cell cracks.

#### IV. CONCLUSION

The drone-based daylight EL system presented in this paper is able to accomplish EL imaging of PV modules during high solar irradiance. The final resulting EL images presented lower quality compared with indoors and stationary daylight EL and enough quality to identify disconnected cell regions larger than crystallographic defects of multicrystalline Si cells. To the best of our knowledge, this was the first time reporting on EL images, which have been acquired from a drone with global horizontal solar irradiance higher than  $100 \text{ W m}^{-2}$ .

We also quantified the EL images quality following the recently published technical specification [4]. For the drone acquired images, the  $SNR_{AVG}$  presented a clear discrepancy between the number obtained and the visual quality of the EL images, with crack details possible to be identified in the image with an  $SNR_{AVG}$  of 1.6 were not possible to be distinguished in the image with  $SNR_{AVG}$  of 4.6. This indicates that a review of the method, especially for daylight EL, should take place in the future.

AC+DC electrical modulation offered a more reproducible mean pixel value delta between EL and BG images than DC electrical modulation and DC modulation presented higher delta magnitude than AC+DC modulation. The positioning mismatch was still the main issue for low quality in the drone-based EL.

We presented a look into the technical methods implemented so far, with the acquisition of individual module EL images during the day from a drone system. The algorithms demand further programming steps for a drone-based EL acquisition system to work efficiently in a utility scale environment.

#### ACKNOWLEDGMENTS

The authors acknowledge the financial support from Innovation Fund Denmark for the project 6154-00012B DronEL – Fast and accurate inspection of large photovoltaic plants using aerial drone imaging.

## REFERENCES

- [1] IEA, "Renewables 2018," 2018. [Online]. Available: <https://www.iea.org/media/presentations/Renewables2018-Launch-Presentation.pdf>. [Accessed: 18-Aug-2019].
- [2] M. Köntges *et al.*, "Review on Infrared and Electroluminescence Imaging for PV Field Applications - IEA-PVPS, Report," 2017.
- [3] S. Koch, T. Weber, T. Sobottka, A. Fladung, P. Clemens, and J. Berghold, "Outdoor Electroluminescence Imaging of Crystalline Photovoltaic Modules: Comparative Study between Manual Ground-Level Inspections and Drone-Based Aerial Surveys," in *32nd European Photovoltaic Solar Energy Conference and Exhibition*, 2016, pp. 1736–1740.
- [4] IEC, "IEC TS 60904-13 Photovoltaic Devices - Part 13: Electroluminescence of Photovoltaic Modules," <http://www.iec.ch/>.
- [5] L. Stoicescu, M. Reuter, and J. . Werner, "Daysy: Luminescence Imaging of PV Modules in Daylight," *29th Eur. Photovoltaics Sol. Energy Conf. Exhib. Amsterdam, Netherlands*, pp. 2553–2554, 2014.
- [6] G. A. dos Reis Benatto *et al.*, "Development of outdoor luminescence imaging for drone-based PV array inspection," *44th IEEE Photovolt. Spec. Conf.*, 2017.
- [7] C. Mantel *et al.*, "SNR Study of Outdoor Electroluminescence Images under High Sun Irradiation," in *2018 IEEE 7th World Conference on Photovoltaic Energy Conversion (WCPEC) (A Joint Conference of 45th IEEE PVSC, 28th PVSEC & 34th EU PVSEC)*, 2018, pp. 3285–3289.
- [8] J. Adams *et al.*, "Non-Stationary Outdoor EL-Measurements with a Fast and Highly Sensitive InGaAs Camera," *32nd Eur. Photovolt. Sol. Energy Conf. Exhib.*, 2016.
- [9] G. A. dos Reis Benatto *et al.*, "Image Processing for daylight Electroluminescence PV Imaging acquired in movement," *35th EU PVSEC 2018*, pp. 2005–2009, 2018.
- [10] Datasheet, "Apalis TK1." [Online]. Available: <https://docs.toradex.com/103129-apalis-tk1-datasheet.pdf>. [Accessed: 18-Aug-2019].
- [11] M. Köntges *et al.*, *Review of Failures of Photovoltaic Modules*. 2014.
- [12] Datasheet, "SM 15K - Series 15kW DC POWER SUPPLIES." [Online]. Available: [https://www.deltaelektronika.nl/upload/DATA\\_SHEET\\_SM15K\\_V201905.pdf](https://www.deltaelektronika.nl/upload/DATA_SHEET_SM15K_V201905.pdf). [Accessed: 18-Aug-2019].
- [13] T. Kropp, M. Berner, L. Stoicescu, and J. H. Werner, "Self-Sourced Daylight Electroluminescence from Photovoltaic Modules," *IEEE J. Photovoltaics*, vol. 7, no. 5, pp. 1184–1189, 2017.
- [14] U. Rau, "Reciprocity relation between photovoltaic quantum efficiency and electroluminescent emission of solar cells," *Phys. Rev. B - Condens. Matter Mater. Phys.*, vol. 76, no. 8, pp. 1–8, 2007.
- [15] T. J. Silverman, M. G. Deceglie, K. Vansant, S. Johnston, and I. Repins, "Illuminated outdoor luminescence imaging of photovoltaic modules," in *IEEE Photovoltaic Specialists Conference*, 2017.
- [16] R. Bhoopathy, O. Kunz, M. Juhl, T. Trupke, and Z. Hameiri, "Outdoor photoluminescence imaging of photovoltaic modules with sunlight excitation," *Prog. Photovoltaics Res. Appl.*, no. July, pp. 14–16, 2017.
- [17] C. Mantel *et al.*, "Correcting for Perspective Distortion in Electroluminescence Images of Photovoltaic Panels," *IEEE 7th World Conf. Photovolt. Energy Convers.*, 2018.

## BLACK SILICON SOLAR CELLS WITH BLACK RIBBONS

Rasmus Schmidt Davidsen<sup>\*,a</sup>, Peter Torben Tang<sup>b</sup>, Io Mizushima<sup>b</sup>, Sune Thorsteinsson<sup>c</sup>, Peter Behrendorff Poulsen<sup>c</sup>, Jesper Frausig<sup>d</sup>, Ørnulf Nordseth<sup>e</sup>, Ole Hansen<sup>a</sup>

<sup>a</sup> Department of Micro- and Nanotechnology, Technical University of Denmark, Ørsteds Plads building 345East, DK-2800 Kgs. Lyngby, Denmark,

<sup>b</sup> IPU, Nils Koppels Allé, Building 404, 2nd floor, DK-2800 Kgs. Lyngby, Denmark

<sup>c</sup> Department of Photonics, Technical University of Denmark, Frederiksborgvej 399 building 128, DK-4000 Roskilde, Denmark

<sup>d</sup> Gaia Solar A/S, Hammerholmen 9, DK-2650 Hvidovre, Denmark

<sup>e</sup> Institute for Energy Technology (IFE), Instituttveien 18, NO-2007 Kjeller, Norway

\*rasda@nanotech.dtu.dk, phone: +45 45255848

**ABSTRACT:** We present the combination of mask-less reactive ion etch (RIE) texturing and blackened interconnecting ribbons as a method for obtaining all-black solar panels, while using conventional, front-contacted solar cells. Black silicon made by mask-less reactive ion etching has total, average reflectance below 0.5% across a 156x156 mm<sup>2</sup> silicon (Si) wafer. Black interconnecting ribbons were realized by oxidizing copper resulting in reflectance below 3% in the visible wavelength range. Screen-printed Si solar cells were realized on 156x156 mm<sup>2</sup> black Si substrates with resulting efficiencies in the range 15.7-16.3%. The KOH-textured reference cell had an efficiency of 17.9%. The combination of black Si and black interconnecting ribbons may result in aesthetic, all-black panels based on conventional, front-contacted silicon solar cells.

**Keywords:** Black Silicon, Nanostructuring, BIPV, Aesthetics, Inorganic Black Ribbons

### 1 INTRODUCTION

Nanoscale texturing of Si surfaces has been shown [1,2] to reduce the total optical reflectance to well below 1% averaged over a broad range of wavelengths. Compared to typical reflectance of ~2 and ~8% from conventionally textured mono- [3] and multi-crystalline [4] Si solar cells, respectively, nanoscale texturing may potentially improve the power conversion efficiency of Si solar cells due to reduced reflectance loss. Nanostructured Si surfaces suppress the reflectance of light from the surface due to the resulting graded refractive index at the Si-air interface. We use mask-less reactive ion etching (RIE) to produce nanostructured Si, also known as 'black silicon' [5-7], as texturing for front-contacted Si solar cells. In addition, there is commercial interest in obtaining aesthetic and building-integrated solar cells and panels. We propose to achieve this by combining black silicon texturing with blackened interconnection ribbons strings in order to obtain an all-black panel, while using conventional, front-contacted Si cells.

### 2 BLACK SILICON SOLAR CELLS

#### 2.1 Black Silicon

Black silicon was realized on 156x156 mm<sup>2</sup> Czochralski (CZ) mono-crystalline Si wafers by mask-less reactive ion etching (RIE) in SF<sub>6</sub> and O<sub>2</sub> plasma at room temperature. Figure 1 shows a scanning electron microscope (SEM) image of the resulting nanostructure topology. The nanostructure topology consists of conical-like hillocks with average height of 300 nm and average spacing of 300 nm.

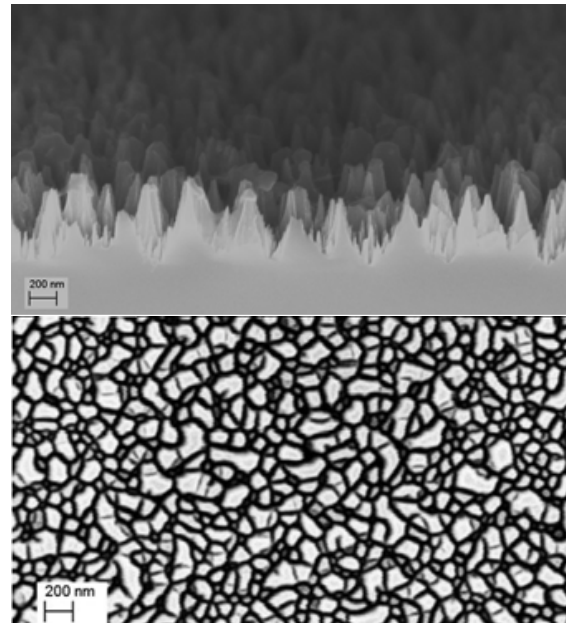


**Figure 1:** Scanning electron microscope image at 40 degrees (left) and 0 degrees tilt (right) of the nanostructure topology resulting from mask-less reactive ion etching.

Normal incidence reflectance measurements of the RIE-textured Si surfaces were performed using a broadband light source (Mikropack DH-2000), an integrating sphere (Mikropack ISP-30-6-R), and a spectrometer (Ocean Optics QE65000, 300-1000 nm).

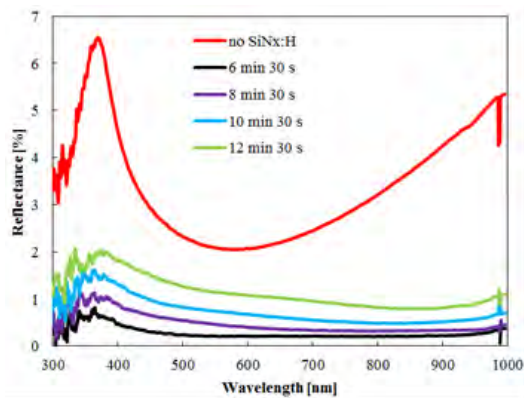


**Figure 2:** Measured total (diffuse+specular) reflectance of black Si with SiN<sub>x</sub>:H AR-coating as a function of wavelength in the range 300-1000 nm for four different PECVD SiN<sub>x</sub>:H deposition times representing four different SiN<sub>x</sub>:H thicknesses.

For the reflectance measurements hydrogenated silicon nitride (SiN<sub>x</sub>:H) deposited by plasma-enhanced chemical vapor deposition (PECVD) was applied. An n<sup>+</sup> emitter was formed on the RIE-textured Si using POCl<sub>3</sub> as dopant source prior to the deposition of SiN<sub>x</sub>:H. Since the refractive index profile of black Si is fundamentally different from that of conventionally textured or planar Si, the optimal SiN<sub>x</sub>:H thickness for black Si was investigated. The deposition time of the PECVD process was varied in steps of 2 minutes from the 'standard' time of 6 min and 30 s to 12 min and 30 s. The reflectance was then measured for the different SiN<sub>x</sub>:H thicknesses on RIE-textured Si wafers. The result is shown in Figure 2 which shows that a PECVD process time of 6 min and 30 s minimizes the reflectance of black Si. In general SiN<sub>x</sub>:H AR-coating reduces the reflectance of black Si. Deposition times are stated instead of SiN<sub>x</sub>:H thicknesses, since the exact thickness on black Si is not fully known due to the complicated surface morphology. On conventionally textured Si a 6 min and 30 s deposition yields a SiN<sub>x</sub>:H thickness of ~ 60 nm. Due to the broadband anti-reflective properties of black Si the SiN<sub>x</sub>:H thickness does not need to be optimized in terms of minimized reflectance at a certain wavelength. It seems from Figure 2 that the reflectance increases monotonically with SiN<sub>x</sub>:H thickness in the thickness range investigated.

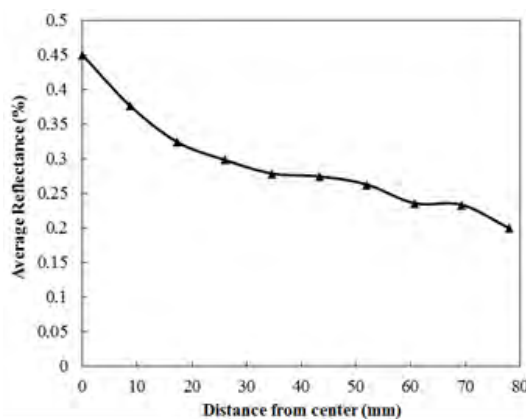


**Figure 3:** Measured total (diffuse + specular) reflectance of RIE-textured Si with SiN<sub>x</sub>:H averaged over the wavelength range 300-1000 nm as function of the distance from the center of a 156x156 mm<sup>2</sup> CZ wafer.

In order to quantify the spatial uniformity of RIE-texturing, the reflectance was measured at different positions across a 156x156 mm<sup>2</sup> CZ wafer textured by mask-less RIE after POCl<sub>3</sub> emitter diffusion and PECVD of SiN<sub>x</sub>:H (6 min and 30 s). The total (diffuse + specular) reflectance was measured in the wavelength range 300-1000 nm and the integrated average reflectance is plotted as function of distance from the wafer center in Figure 3. Figure 3 shows that the integrated average reflectance is below 0.5% across the entire 156x156 mm<sup>2</sup> wafer. The average reflectance decreases towards the edge of the wafer, but even though the relative difference from center to edge is significant, the absolute difference is ~ 0.2%. The deviation in reflectance across the wafer is probably due to the plasma chamber and wafer geometry.

## 2.2 Cell processing

Solar cells were fabricated from 156x156 mm<sup>2</sup> p-type CZ Si wafers using the following process steps:

1. Saw damage removal using an HF:HNO<sub>3</sub>:CH<sub>3</sub>COOH etchant mixture
2. Maskless RIE texturing
3. Diffusion of n-type emitter in a tube furnace using a POCl<sub>3</sub> source to obtain a sheet resistance of ~120 Ω/sq.
4. Deposition of anti-reflection coating on the front surface by plasma enhanced chemical vapour deposition (PECVD)
5. Screen-printing and firing of metal contacts
6. Laser edge isolation

The formation of an n-type emitter, using POCl<sub>3</sub> as the phosphorous doping source, was carried out using a Tempress TS-8603 tube furnace at a temperature of 836-838 °C for 37 minutes, followed by a 10 minutes drive-in. Hydrogenated amorphous silicon nitride (a-SiN<sub>x</sub>:H) was deposited using an Oxford Instruments PlasmaLab System133 PECVD tool with silane, ammonia and nitrogen at a temperature of 400 °C and a pressure of 800 mTorr for 6 minutes and 30 seconds. For the contact formation, an EKRA X5-ST5 semi-automatic screen printing machine was used. The contacts were printed using Ag paste (DuPont PV18A) on the front and Al paste (Monocrystal PASE-1207) on the rear. The contacted cells were subsequently dried and co-fired in a belt furnace with temperatures in the range of 780-945°C and a belt speed of 520 cm/min. Edge isolation was performed by laser ablation using a J-1030-515-343 FS System from Oxford Lasers. A wavelength of 515 nm and a repetition rate of 50 kHz were used for the laser scribing.

## 2.3 Characterization methods

Emitter sheet resistance was measured using a CMT-SR2000-PV unit from Advanced Instrument Technology. I-V curves were measured using a solar simulator (WACOM) to illuminate the solar cell (100 mW/cm<sup>2</sup>) with the AM1.5 spectrum while varying the bias voltage from -1V to +1V. Electro- and photo-luminescence (EL, PL) images were measured using a LIS-R1 unit from BTImaging. The reported lifetime values are average lifetimes across the wafers at an injection level of about 10<sup>15</sup> cm<sup>-3</sup>.

Internal quantum efficiency (IQE) measurements using an IQE-SCAN tool from pytools.

## 2.4 Results

A total of 24 full-area (156x156 mm<sup>2</sup>) black Si solar cells were fabricated and compared with known data for KOH-textured cells. Due to reduced adhesion of screen-printed metal fingers at the edges of some of the black Si cells, the final cells were cut in 100x100 mm<sup>2</sup> squares in the edge isolation. The adhesion issues on RIE-textured Si will be investigated further in future studies.

Figure 4 shows the current density-voltage characteristic for 3 different black Si solar cells and the KOH-textured reference cell and quantum efficiency for one black Si cell compared to the reference cell.

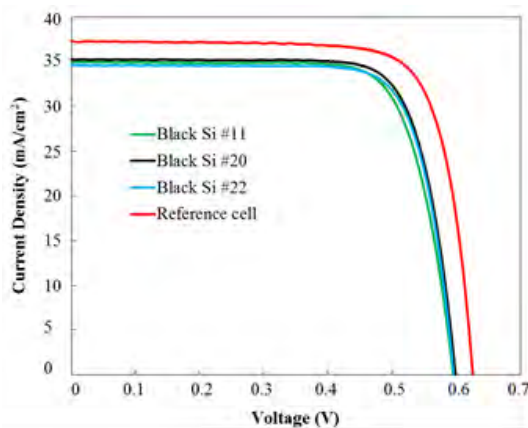


**Figure 4:** Current-density voltage (J-V) characteristic for 3 different black Si cells and a KOH-textured reference cell.

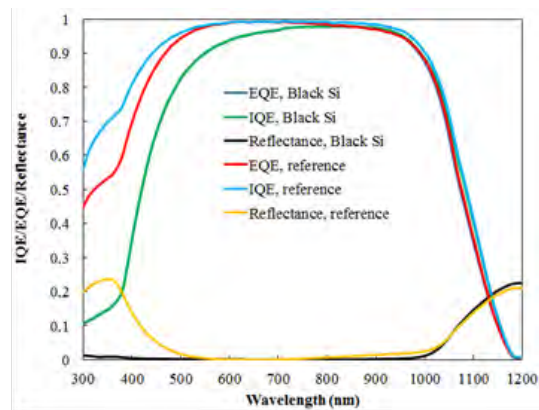


**Figure 5:** Internal (IQE) and External (EQE) Quantum Efficiency and reflectance as function of wavelength for the black Si cell (#11) and the KOH-textured reference cell.

**Table 1:** Short-circuit current ( $J_{sc}$ ), open-circuit voltage ( $V_{oc}$ ), fill factor (FF), power conversion efficiency and series resistance ( $R_s$ ) of 3 different black Si solar cells and a KOH-textured reference. The series resistance was extracted from EL and PL images.

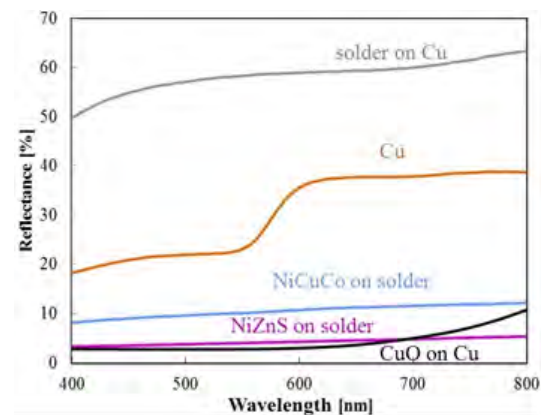
Cell	$J_{sc}$ (mA/cm <sup>2</sup> )	$V_{oc}$ (V)	FF (%)	Eff. (%)	$R_s$ ( $\Omega$ cm <sup>2</sup> )
BS #11	34.93	595	75.67	15.73	1.07
BS #20	35.25	598	76.91	16.22	1.03
BS #22	34.62	596	77.32	15.95	1.04
Ref cell	37.31	625	77.09	17.99	0.88

Figure 4 and Table 1 show that the black Si cells have power conversion efficiencies in the range of 15.7-

16.3%. The 3 cells shown in Figure 4 and Table 1 represent the best, worst and mean of the 24 fabricated cells. The efficiency of the black Si cells is lower than that of the KOH-textured reference cell. Table 1 show that the lower efficiency is primarily due to lower  $J_{sc}$  and  $V_{oc}$ . Furthermore, the IQE measurement in Figure 5 shows that the lower efficiency of black Si cells is primarily due to increased carrier loss at wavelengths below 600 nm probably due to increased surface and emitter recombination. This was expected since previous studies [8] show similar results and since no further attempt of optimization was made in terms of improved passivation or emitter quality.

## 3 BLACK RIBBONS

In order to obtain an all-black appearance of cells and panels, black Si may be combined with black interconnecting ribbons. The cell results reported in this work did not involve these strings. Three different processes for blackening the ribbons were investigated. NiZnS and NiCuCo alloys, respectively, were deposited directly on Cu ribbons with soldering coating. Cu ribbons with a black oxidized surface were realized by a chemical oxidation process. Electroplating was conducted in a beaker with electrolytes containing sulfate salts and a nickel anode. Reflection measurements on the bare and coated surfaces were performed using a spectrophotometer (Shimadzu 2600).



**Figure 6:** Measured reflectance as function of wavelength of interconnecting ribbons without (bare Cu, and Cu with solder) and with (NiCuCo, NiZnS, and CuO) black coatings.

Figure 6 shows the measured reflectance of the different ribbons. Reflectance of the strings with solder is high due to the bright metal surface, while the copper surface has a lower reflectance which increases for wavelengths above 600 nm. All of the blackened ribbons have significantly reduced reflectance. NiCuCo appears gray and has a higher reflectance compared with the other blackened ribbons, also, the reflectance of NiCuCo increases slightly towards longer wavelengths. The reflectance curve for NiZnS is quite flat and has a dark grey appearance. Oxidized Cu has the lowest reflectance, which increases slightly at longer wavelengths; indicating that the surface color has a red element due to Cu presence in the coating or due to the Cu substrate. In summary, Cu ribbons strings with CuO is the best match for black silicon with respect to the all-black appearance,

because of the comparatively low reflectance.

Energy Materials and Solar Cells, 140, 134-140, (2015).

#### 4 CONCLUSIONS

We have presented the combination of black silicon texturing realized by mask-less RIE and blackened interconnecting ribbons as a potential method for obtaining all-black solar panels, while using conventional, front-contacted silicon solar cells. Black silicon has a total, average reflectance below 0.5% in the wavelength range 300-1000 nm across a 156x156 mm<sup>2</sup> silicon wafer. The absolute difference in reflectance from center to edge of the 156x156 mm<sup>2</sup> silicon wafer was ~ 0.2%. Black ribbons were realized by oxidized Cu resulting in reflectance below 3% in the visible wavelength range. Screen-printed Si solar cells were realized on 156x156 mm<sup>2</sup> black Si substrates with resulting efficiencies in the range 15.7-16.3%. The KOH-textured reference cell had an efficiency of 17.9%. The combination of black Si and black ribbons may result in aesthetic, all-black panels based on conventional, front-contacted silicon solar cells.

#### 5 REFERENCES

- [1] Priolo, F., Gregorkiewicz, T., Galli, M., Krauss, T.F., "Silicon nanostructures for photonics and photovoltaics", *Nature Nanotechnology*, vol. 9, pp. 19-32, (2014). DOI: 10.1038/NNANO.2013.271.
- [2] Zhu, J., Yu, Z., Fan, S., Cui, Y., "Nanostructured photon management for high performance solar cells", *Materials Science and Engineering R*, vol. 70, pp. 330-340, (2010).
- [3] Zhao, L., Zuo, Y.H., Zhou, C.L., Li, H.L., Diao, H.W., Wang, W.J., "Theoretical investigation on the absorption enhancement of the crystalline silicon solar cells by pyramid texture coated with SiNx:H layer", *Solar Energy*, vol. 85, pp. 530-537, (2011).
- [4] Macdonald, D., Cuevas, A., Kerr, M., Samundsett, C., Ruby, D., Winderbaum, S., Leo, A., "Texturing Industrial Multicrystalline Silicon Solar Cells", *Solar Energy*, vol. 76, No.1, pp. 277-283, (2004).
- [5] Rahman, A., Ashraf, A., Xin, H., Tong, X., Sutter, P., Eisaman, M.D., Black, C.T., "Sub-50-nm self-assembled nanotextures for enhanced broadband antireflection in silicon solar cells", *Nature Communications*, vol. 6, pp. 59-63, (2015). DOI: 10.1038/ncomms6963
- [6] Liu, X., Coxon, P.R., Peters, M., Hoex, B., Cole, J.M., Fray, D.J., "Black Silicon: Fabrication methods, properties, and solar energy applications", Review Article, *Energy & Environmental Science*, Royal Society of Chemistry, vol. 7, pp. 3223-3263, (2014).
- [7] Allen, T., Bullock, J., Cuevas, A., Baker-Finch, S., Karouta, F. "Reactive ion etched black silicon texturing: A comparative study", In 40th Photovoltaic Specialist Conference (PVSC), IEEE, pp. 0562-0566, IEEE, (2014). doi:10.1109/PVSC.2014.6924983
- [8] Davidsen, R. S., Ormstrup, J., Ommen, M. L., Larsen, P. E., Schmidt, M. S., Boisen, A., Nordseth, Ø., Hansen, O., "Angle resolved characterization of nanostructured and conventionally textured silicon solar cells.", *Solar*

## INDOOR MEASUREMENT OF ANGLE RESOLVED LIGHT ABSORPTION BY ANTIREFLECTIVE GLASS IN SOLAR PANELS

Mekbib W. Amdemeskel<sup>1</sup>, Gisele A. dos Reis Benatto<sup>1</sup>, Nicholas Riedel<sup>1</sup>, Beniamino Iandolo<sup>2</sup>, Rasmus S. Davidsen<sup>2</sup>, Ole Hansen<sup>2</sup>, Peter B. Poulsen<sup>1</sup>, Sune Thorsteinsson<sup>1</sup>, Anders Thorseth<sup>1</sup>, Carsten Dam-Hansen<sup>1</sup>

<sup>1</sup> Department of Photonics Engineering, Technical University of Denmark, Frederiksborgvej 399, 4000 Roskilde, Denmark, mekwub@fotonik.dtu.dk

<sup>2</sup> Department of Micro- and Nanotechnology, Technical University of Denmark, Ørsteds Pl., 2800 Kongens Lyngby, Denmark

**ABSTRACT:** In this work, we present measurements of angle resolved light absorption of antireflective (AR) glass of PV samples, performed indoors using a collimated high radiance broadband light source. This indoor method proved to be viable and offered a significant simplification compared to outdoor measurements with trackers. The experimental results showed optical responses that are stable and suitable for indoor characterization of solar cells. We find the characteristic optical response of six different antireflective glasses, and based on such measurements, we perform PVsyst simulations and present the monthly DC energy production estimates across four distinct latitudinal locations with six different glass types. The results indicated that the AR glasses present different optical effects at the angles intervals between 0 – 45° and 60 – 90° and that the Diffuse AR glass can improve monthly yields by as much as 2% relatively to a bare cell.

**Keywords:** Antireflective glass, Angle of Incidence, Incidence Angle Modifier, Simulation.

### 1 INTRODUCTION

A solar cell output under working conditions is affected by several factors, such as the temperature of the cell, the intensity and incidence angle of the sunlight, which vary between different geographical locations and throughout the duration of a day in the year. In particular, the effect of the angle of incidence (AOI) on the optical properties of the cell – including the AR glass – is considerable for AOI larger than 45° and needs to be taken into account when assessing performance of solar cells. For instance, the effect of optical characteristics of various front glasses in PV modules was recently studied and the annual specific energy yields computed by Herrmann et al.[1]. Martin et.al investigated the angular reflection losses as function of tilt angle of solar cells at 79 sites under real conditions [2]. The effect of the presence of dust on the current output of the PV modules was also studied by exposing the front surface glass of the modules to dust [3]. Furthermore, the Centre for Renewable Energy Systems Technology in the UK has run a project to study optical loss reduction in PV modules with textured and AR coatings glasses, both via indoor and long term outdoor exposure [4]. Measurements of light transmissions on structured glasses using a solar simulator indicated that the current output increased with angle of incidence by increasing light transmission and decreasing temperature as compared to flat glasses [5]. In our work, we characterize six different glass types packaged into coupons using standard c-Si wafers. A bare c-Si cell without glass is included for reference. Our method is carried out by measuring short circuit current as function of incidence angle. In particular, we have built a set-up that allows automated, reliable measurements of the short circuit current as function of incidence angle with collimated, simulated sunlight. This indoor set-up has several advantages over measuring the AOI effect outdoors on a tracker: (i) the measurements are not compromised by the effects of atmospheric diffuse or ground reflected light; (ii) the spectrum and intensity of the light source remain constant throughout the test; and (iii) the rotation stage can move easily and accurately between -90° and + 90° AOI. Furthermore, indoor measurements using light sources such as flashlights are highly affected by the divergence of the beam. In contrast,

the light source used here provides bright illumination across the UV-VIS-NIR range together with high spatial and power stability. In addition, the light source is well collimated by collection optics to give a stable and reliable power measurement, with max. 0.1° beam divergence with a beam diameter of 38mm. We have calculated the maximum divergence by measuring the beam diameter at different distances along the beam propagation direction using Equation 1.

$$\theta = 2 \tan^{-1} \left( \frac{D_2 - D_1}{2l} \right) \quad (1)$$

Where  $\theta$  is the divergence angle,  $D_2$  is the beam diameter at distance “2” and  $D_1$  the beam diameter at distance “1”.

In this work, we normalize the relative short circuit current to a cosine response thereby isolating the optical effect of the glass-air interface. This form of data presentation is frequently described as the “incidence angle modifier” (IAM) and is used in PV modelling programs such as PVsyst. In addition, we perform PVsyst simulations based on the measured IAM data and share monthly DC energy production estimates with six different glass types across four distinct latitudinal locations.

### 2 EXPERIMENTAL METHOD

Angle resolved absorption measurements of PV modules with AR glass were performed using the set-up sketched in Figure 1. The following components were used: a laser driven light source (LDLS) EQ-99FXC (Energetiq Technology, Inc.) with spectral emission between 190 and 2100 nm, an off-axis parabolic mirror for light collimation, a UV filter, a sample holder stepper motor (Thorlabs - NR360S) and a LabVIEW controlled short circuit current ( $I_{sc}$ ) measuring transducer. The UV filter was positioned immediately after the light source in order to remove the UV-C part. The lab environment was kept at a temperature of 21°C using an air conditioning system.

The AOI ( $= \theta$ ) was varied by rotating the solar cells using a stepper motor around a vertical axis. The AOI are indicated with respect to normal incidence. The electrical transducer together with the LabVIEW controller was used

to measure the  $I_{sc}$  for AOI between  $90^\circ$  to  $-90^\circ$  with a  $5^\circ$  step size. Before starting all the measurements, we have aligned the samples normal to the collimated beam of diameter 38mm. For AOI larger than  $\pm 75^\circ$ , not all the light beam hits the solar cell. Therefore, we have computed an area, i.e. power correction factor, for the partial beam spot to recalculate the actual reduced power reaching the cell from the total power (full spot area). This area correction for large angles is similar to the standard cosine correction for measurements setups where the spot size is larger than the cell. In order to have track of the setup reproducibility, a stable reference cell was characterized before every new measurement. This setup has proven to be a viable method for determining the IAM for the study of optical losses [6]. Importantly, repeatability on the AOI was very high with a maximum relative standard deviation of 0.75%.

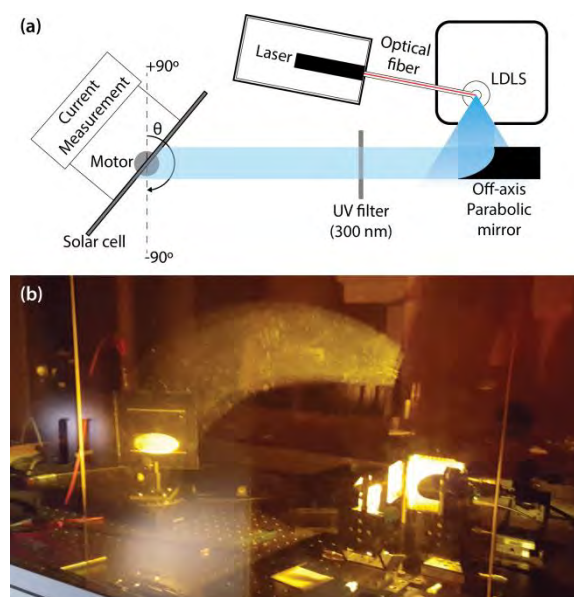


**Figure 1:** Top view Schematic (a) and photograph (b) of the setup for measuring angle resolved absorption.

Samples with the following commercially available AR glasses were used for the measurement, as well as a Bare Cell for comparison: Smooth Glass, Diffuse Glass, Structured Glass 1, Structured Glass 2, Structured Glass 3, and Structured Glass 4; where Structured Glass 1 had the smallest AR structure, 2 and 3 had intermediate structuring sizes, and Structured Glass 4 had the biggest (deep pyramidal structure). All seven samples are packaged with

the same c-Si wafer type (multicrystalline Si 156 x 156 mm), with the 6 encapsulated samples using standard EVA encapsulation) and have the same quantum efficiency (QE).

The electroluminescence (EL) images of all samples were taken in order to evaluate the samples integrity. A modified DSLR Nikon camera, from Brightspot, was used for the images acquisition.

### 3 RESULTS AND DISCUSSION

We show in Figure 2 the photographs (top) and EL images (bottom) of the seven different samples studied in this work. The EL images indicated that the samples had good integrity and present no cracks or shunts, with the only exception of the Prismatic glass sample. As the AOI experiment required a small cell area, the cracked region was avoided, as well as the bus bars, shown in the EL images.

#### 3.1 Angle of Incidence

We measured short circuit current versus angle of incidence ( $I_{sc}$ -AOI, or  $I_{sc}$ - $\theta$ ) for the different PV samples. Once we corrected  $I_{sc}$  by the area factor, the area at which the beam misses the solar cell for angles greater than  $\pm 75^\circ$ , we normalized it with respect to the value at the normal angle of incidence, i.e. for AOI =  $0^\circ$ . Since we used a collimated light source, we neglected the diffuse component. It is worth mentioning that, for this setup, the normalized and area corrected current is in fact the same as the Incident Angle Modifier (IAM) used in e.g. PVsyst. We characterized seven solar cells, and the IAM plots for these samples are shown in Figure 3. The graphs look very similar, overlapping each other. Therefore, Figure 4 shows the difference of the IAM values relative to the Bare Cell. The Structured Glass 4 sample displayed the highest output for IAM between  $80^\circ$  and  $85^\circ$ , followed by the samples Diffuse Glass, Structured Glass 1, Structured Glass 3, Structured Glass 2 and Smooth Glass respectively, with that last sample underperforming the Bare Cell sample in this angle interval. For the angles between  $70^\circ$  to  $0^\circ$ , Structured Glass 4 was the only sample that present IAM lower than the Bare Cell from  $0^\circ$  until  $45^\circ$ . Results for the sample Diffuse Glass were very close to Structured Glass 3 between  $0^\circ$  and  $45^\circ$ , while Structured Glass 1 and 2 are the better performing samples in this angle interval.

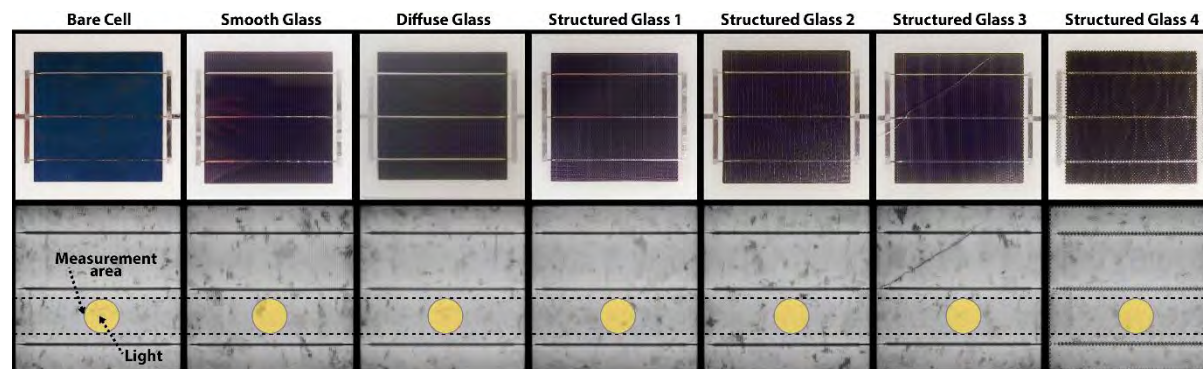


**Figure 2:** Photograph showing solar cells (top) and Electroluminescence image (bottom). The yellow spot show the approximate area illuminated by the LDLS at AOI =  $0^\circ$ .

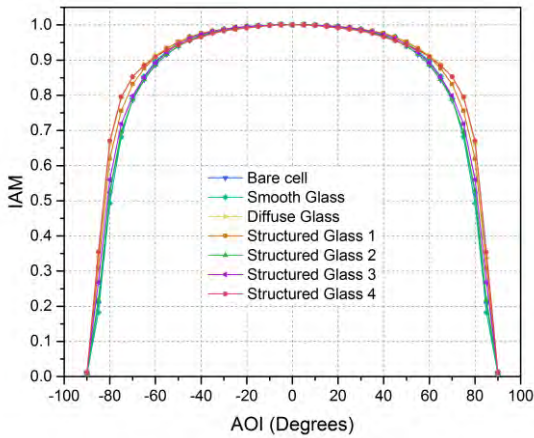


**Figure 3:** IAM-AOI plot for the Bare Cell sample and for the cells with different AR glass.

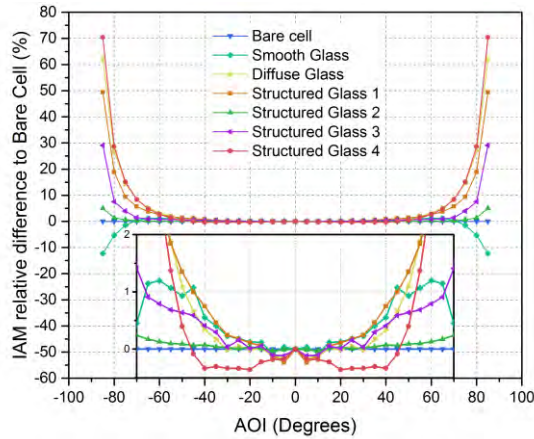


**Figure 4:** Difference of IAM values of the solar cells with different AR glass relative to the Bare Cell. The inset present the same graph with smaller y-scale for better view of the details.

3.3 Simulations

The measured IAM data shown in Figure 3 were used to create unique PV module files in PVsyst (.pan files). The seven unique modules were used to simulate the energy production of a 10 kW<sub>peak</sub> grid-tied system in four locations. The locations were selected so as to span a variety of latitudes. The locations modelled are: Copenhagen, Denmark (55.7°N, 12.4°S), Rome, Italy (41.8°N, 12.6°E), Miami, United States (25.9°N, 80.3°W) and Nairobi, Kenya (1.3°S, 36.8°E). With the exception of the glass surface, the PV module bill of materials (BOM) was kept constant in all simulations. The PV balance of system (BOS) was also kept constant in all simulations. A fixed-tilt rack was used and the tilt relative to a horizontal plane was equivalent to the location’s latitude. The monthly DC energy estimates relative to the Bare Cell are shown in Figure 5.

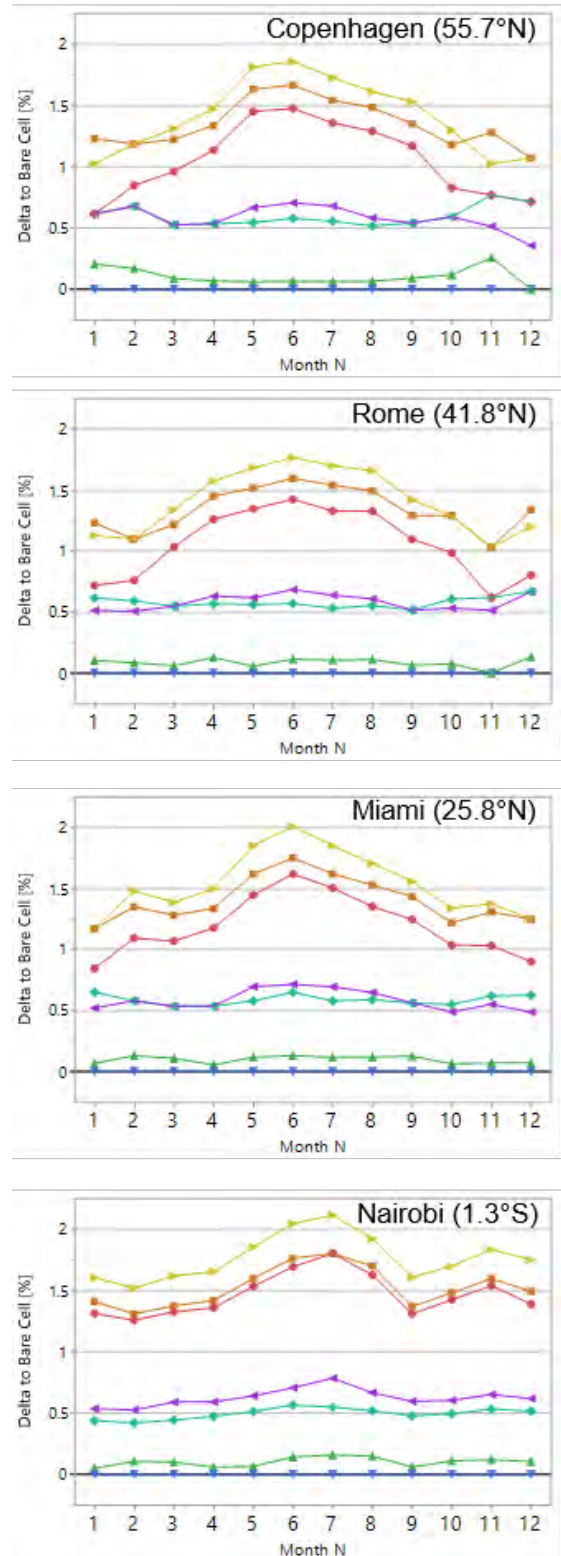


**Figure 5:** Summary of monthly DC energy production estimates when the seven glass types are used across four locations. Legend can be seen in Figure 4.

The PV system using Diffuse Glass is the top performer across all locations. On the summer solstice, the Diffuse Glass outperforms the Bare Cell by 1.8 to 2.2%. The Diffuse Glass sample outperformed Structured Glass 2 sample by as much as 1.8 – 2.0% depending on location. This result is not surprising given that Diffuse Glass sample IAM was higher than almost all samples between 60 – 85° AOI. The only sample that the Diffuse Glass did not outperform was Structured Glass 4, which underperformed even the Bare Cell from 0 – 45° AOI. The second highest performing PV system is the one using Structured Glass 1 followed by the system using Structured Glass 4 sample. This result is explained by the relatively low IAM performance of Structured Glass 4 at angles of 10 – 25° (Figure 4 inset) in spite of having high IAM performance between 60 – 85°.

The PV systems both in this simulation and typically in the field are oriented such that the AOI is minimized mid-day when solar irradiance is highest. For example, the worst case AOI at solar noon at the Copenhagen site is 25° (Winter Solstice). At AOI less than 25°, there is less than 0.5% difference in the IAM response between all glass types, as shown in Figure 4. Therefore, all the glass types provide nearly the same energy yield during the most irradiance-rich periods. Since the tilt angle of each modelled PV system was optimized for the respective latitude, the relative energy gains shown in Figure 5 are essentially the same irrespective of location.

#### 4 CONCLUSIONS

In this work, we presented an indoor study on the effect of the angle of incidences on the short circuit current of solar cells with and without AR glass, using a broadband, collimated light source. The established setup allowed automated and repeatable measurements of short circuit current for AOI between +90° and -90°, viable for determining the IAM for the study of optical losses. The results indicated that the different AR glasses present diverse optical effects from angles intervals between 0 – 45° and 60 – 90°.

PVsyst simulations showed that Diffuse Glass sample can improve monthly yields by as much as 2% relative to

Structured Glass 2 sample. The simulations assume a constant soiling loss for all glasses and locations, which likely will not hold true in the field. However, the intent was to study the effect on optical gains using various glass-air interfaces.

Based on the PVsyst simulations, we consider the setup presented a valuable tool for indoor measurements of the IAM i.e. the angular performance on solar cells and mini modules. Future work includes a Round Robin between other laboratories with AOI cell testing indoors and outdoors, for a comprehensive setup validation; and the modelling of different glass types on BIPV systems, where the installed tilt angle does not allow for receiving the optimal amount of solar irradiance.

#### 6 REFERENCES

- [1] W. Herrmann, L. Rimmelpacher, and M. Reuter, "Optical characteristics of PV module front glasses," pp. 4809–4814, 1801.
- [2] N. Martín and J. M. Ruiz, "Annual angular reflection losses in PV modules," *Prog. Photovoltaics Res. Appl.*, vol. 13, no. 1, pp. 75–84, 2005.
- [3] B. P. Rand, J. Genoe, P. Heremans, and J. Poortmans, "Solar Cells Utilizing Small Molecular Weight Organic Semiconductors," *Prog. Photovolt. Res. Appl.*, vol. 15, no. February 2013, pp. 659–676, 2007.
- [4] A. N. S. R. Williams, T. R. Betts, R. Gottschalg, D. Neumann, M. O. Prast, "Evaluating the Outdoor Performance of PV Modules with Different Glass Textures," *26th Eur. Photovolt. Sol. Energy Conf. Exhib.*, pp. 3152–3156, 2011.
- [5] M. Duell *et al.*, "Impact of Structured Glass on Light Transmission, Temperature and Power of PV Modules," *25th Eur. Photovolt. Sol. Energy Conf. Exhib. / 5th World Conf. Photovolt. Energy Conversion, 6-10 Sept. 2010, Val. Spain*, no. Figure 2, pp. 3867–3872, 2010.
- [6] M. W. Amdemeskel *et al.*, "Indoor Measurement of Angle Resolved Light Absorption by Black Silicon," *IEEE 44th Photovolt. Spec. Conf.*, 2017.

# Indoor Measurement of Angle Resolved Light Absorption by Black Silicon

Mekbib W. Amdemeskel<sup>1</sup>, Beniamino Iandolo<sup>2</sup>, Rasmus S. Davidsen<sup>2</sup>, Ole Hansen<sup>2</sup>, Gisele A. dos Reis Benatto<sup>1</sup>, Nicholas Riedel<sup>1</sup>, Peter B. Poulsen<sup>1</sup>, Sune Thorsteinsson<sup>1</sup>, Anders Thorseth<sup>1</sup>, Carsten Dam-Hansen<sup>1</sup>

<sup>1</sup> Department of Photonics Engineering, Technical University of Denmark, Frederiksborgvej 399, 4000 Roskilde, Denmark, mekwub@fotonik.dtu.dk

<sup>2</sup> Department of Micro- and Nanotechnology, Technical University of Denmark, Ørstedes Pl., 2800 Kongens Lyngby, Denmark

**Abstract** — Angle resolved optical spectroscopy of photovoltaic (PV) samples gives crucial information on PV panels under realistic working conditions. Here, we introduce measurements of angle resolved light absorption by PV cells, performed indoors using a collimated high radiance broadband light source. Our indoor method offers a significant simplification as compared to measurements by solar trackers. As a proof-of-concept demonstration, we show characterization of black silicon solar cells. The experimental results showed stable and reliable optical responses that makes our setup suitable for indoor, angle resolved characterization of solar cells.

## I. INTRODUCTION

The short circuit current output of solar cells under working conditions is affected by several factors. In particular, the effect of angle of incidence (AOI) on the optical properties, and therefore on the short circuit current, is considerable for AOI beyond 45° and needs to be taken into account when assessing performance of solar cells. Reindl et al. investigated the effect of diffuse irradiation as function of irradiation angle using four different models [1]. The effect of angle of incidence (AOI) on performance of crystalline silicon (c-Si) solar cells was studied as a function of irradiation angle by King et al. [2]. A comparison of angle resolved optical characterization of black Si solar cells with conventionally textured Si solar cells was recently presented by Davidsen et al. [3], however this work presented data on raw cells. In this work, we take a further step towards characterizing black Si based PV panels in working conditions by measuring short circuit current as function of incidence angle on encapsulated, one cell mini modules, black Si multi crystalline solar cell and a reference cell without black Si. In a more general perspective, we have built a set-up that allows automatized, reliable measurements of the short circuit current of solar cells as function of incidence angle with collimated (with an angular divergence of about 0.1°), simulated sunlight. This indoor set-up has several advantages over measuring the AOI effect outdoors on a tracker: (i) the measurements are not compromised by the effects of atmospheric diffuse or ground reflected light; (ii) the spectrum and intensity of the light source remain constant throughout the test; and (iii) the

rotation stage can move easily and accurately within -90° and + 90° AOI. Furthermore, indoor measurements using light sources such as flash lights are highly affected by the divergence of the beam. In contrast, the light source used here provides bright illumination across the UV-VIS-NIR range together with high spatial and power stability. In addition the light source is well collimated by collection optics to give a stable and reliable power measurement. PV simulation tools such as the familiar PVsyst describe the optical losses from increased AOI as an “incidence angle modifier” (IAM). It is also possible to use our set up to measure IAM data and use it in PVsyst simulations and estimate energy production solar cells across different locations.

## II. EXPERIMENTAL METHOD

Black Si based solar cells were fabricated on p-type wafers as previously described [3], using a maskless reactive ion etch (RIE) process to texture the Si surface. In brief, the following steps were followed: (1) saw damage removal by etching in 30 % KOH at 75 °C for 2 min followed by cleaning in 20 % HCl at room temperature for 5 min and rinsing using deionized water; (2) Maskless RIE at room temperature in a plasma with O<sub>2</sub> : SF<sub>6</sub> ≈ 1:1 gas flow ratio, chamber pressure of 28 mTorr, 13.56 MHz radio-frequency and platen power of 30 W, (STS RIE); (3) Emitter formation using a tube furnace (Tempress Systems) with liquid POCl<sub>3</sub> as dopant source and N<sub>2</sub> as carrier gas at 840 °C and atmospheric pressure for 50 min, followed by removal of phosphor-silicate glass (PSG) in 5% hydrofluoric acid (HF); (4) Plasma enhanced chemical vapor deposition (PECVD) of 60 nm hydrogenated amorphous silicon nitride (SiNx:H) anti-reflective coating at 400 °C using a PlasmaLab System 133 (Oxford Instruments); (5) Screen-printing of Ag front and Al rear contacts with standard Ag and Al pastes using an EkraX5-STs screen printer, followed by co-firing of the front and rear contacts at 800 °C using a RTC Model LA-309 belt furnace; (6) Edge isolation by laser ablation using a J-1030-515-343FS System (Oxford Lasers Ltd). For the encapsulation, ribbons were soldered on the solar cell and a standard lamination procedure was performed at 140 °C following the encapsulants

manufacturer's recommendations, with a stack consisting of 4 mm window glass, 450  $\mu\text{m}$  TPO (Thermo Plastic Poly olefin), the cell, 450  $\mu\text{m}$  TPT (Tedlar Polyster Tedlar) backsheet, and a black colored TPT back-sheet.

Angle resolved absorption measurements of the black silicon cells were performed using the set-up sketched in Fig. 1(a). A laser driven light source (LDLS) EQ-99FXC (Energetiq Technology, Inc.) with spectral emission between 190 and 2100 nm, collimated using an off-axis parabolic mirror, was used together with a UV filter, a sample holder stepper motor (THORLABS-NR360S) and a LABVIEW controlled short circuit current ( $I_{sc}$ ) measuring transducer with an impedance of 0.670 ohms. The UV filter was positioned immediately after the light source in order to remove the UV-C part. The spectrum of the LDLS with and without filter in comparison with the solar spectrum is shown in Fig. 2. The measurement room was kept at a temperature of 21°C using an air conditioning system.

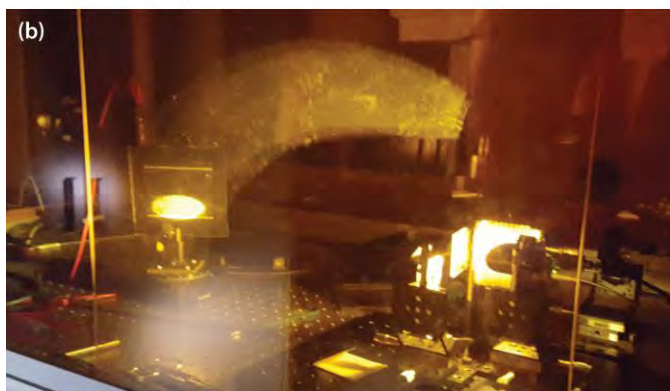
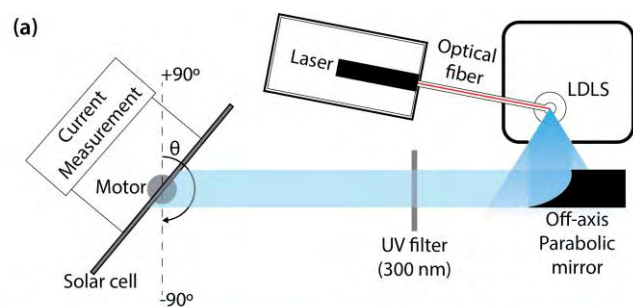


Fig. 1 Top view Schematic (a) and photograph (b) of the setup for measuring angle resolved absorption.

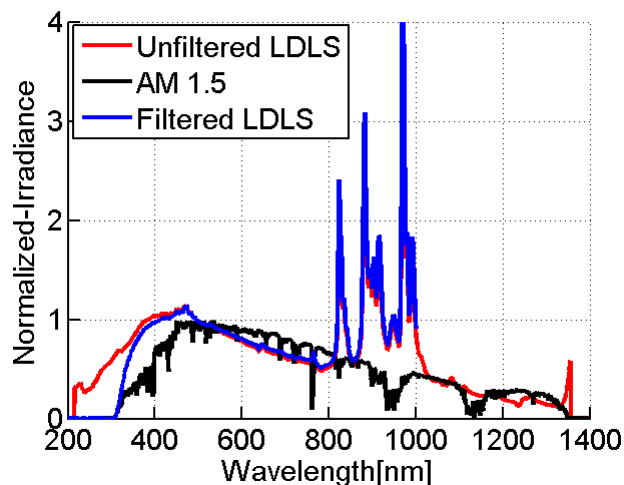


Fig. 2 The sun, filtered and unfiltered LDLS spectrum normalized to sun peak wavelength.

The AOI was changed by rotating the solar cells using a stepper motor around the vertical axis. The AOI are indicated with respect to normal incidence. The electrical transducer together with LABVIEW station was used to measure the  $I_{sc}$  for AOI between 90° to -90° with a 5° step size.

### III. RESULTS AND DISCUSSION

Short circuit current versus angle of incidence ( $I_{sc}$ -AOI, or  $I_{sc}$ - $\theta$ ) curves were obtained for two different TPO encapsulated black Si based samples, black Si multi crystalline solar cell and a reference cell without black Si Fig. 5 (a). We have performed an initial repeatability test by acquiring  $I_{sc}$ -AOI curves 10 times for the same samples. This repeatability of the set up was checked by calculating the error- $I_{sc}$  and relative standard deviation (RSD) of the individual angular measurements. Results are summarized in Fig. 3 and Fig. 4. In particular, we determined the highest relative standard deviation of  $I_{sc}$  to be 0.75 % for AOI larger than + 80°. Hence, for all of our calculations we have used the average of the measurements at a given angle. From these calculations we can conclude that our measurement set up is highly repeatable.

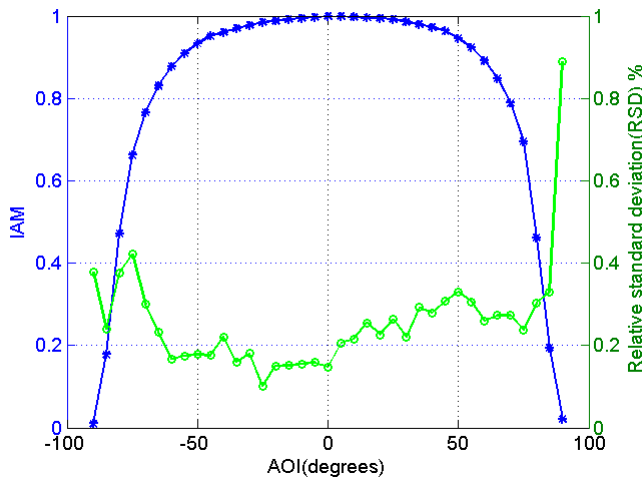


Fig. 3 AOI-IAM and AOI –RSD plot for reproducibility of our measurement setup.

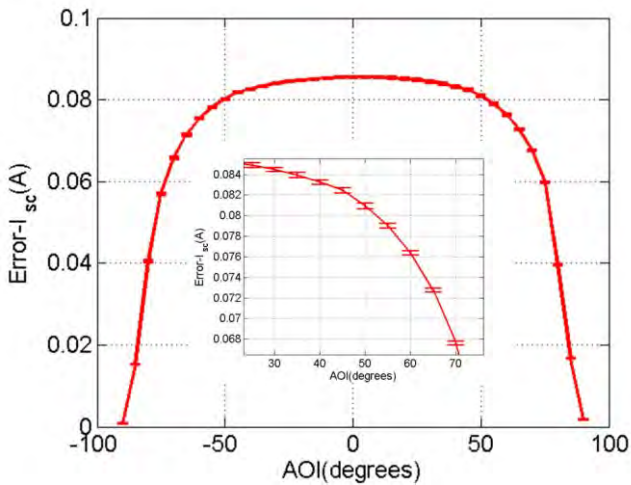


Fig. 4 AOI-Isc error plot for reproducibility of our measurement setup.

It is worth mentioning that, for AOI larger than  $\pm 75^\circ$ , not all the light beam hits the solar cell, as can be seen in Fig. 5(b) and (c). Therefore, we have computed an area i.e. power correction factor (it is calculated by dividing the partial area of the beam on the cell by the full elliptical area of the beam as shown in Fig. 5 (b) and (c)) for the partial beam spot to recalculate the actual reduced power reaching the cell from the total power (full spot area). This area correction for large angles is similar to the standard cosine correction for measurements setups where the spot size is larger than the cell.

Once corrected by the area factor,  $I_{sc}$  was normalized to the value at the normal angle incidence, i.e. for  $AOI = 0^\circ$ . Since we are using a collimated light source, we have neglected the diffuse component. Thus for this setup the normalized and area corrected current is in fact the Incident Angle Modifier (IAM) used in e.g. PV-syst. We characterized two black

silicon cells, and the IAM for these samples is shown in Fig. 6. The graphs look very similar, with only a very slightly faster decay at larger AOI for sample 1. Furthermore, for a better comparison, we have compared two other samples, named black Si multi crystalline solar cell and a reference cell without black Si. In the same way as for the two black silicon measurements, we have carried out  $I_{sc}$  versus AOI measurement. After area correction, the IAM was computed and plotted for these samples as shown in Fig. 7.

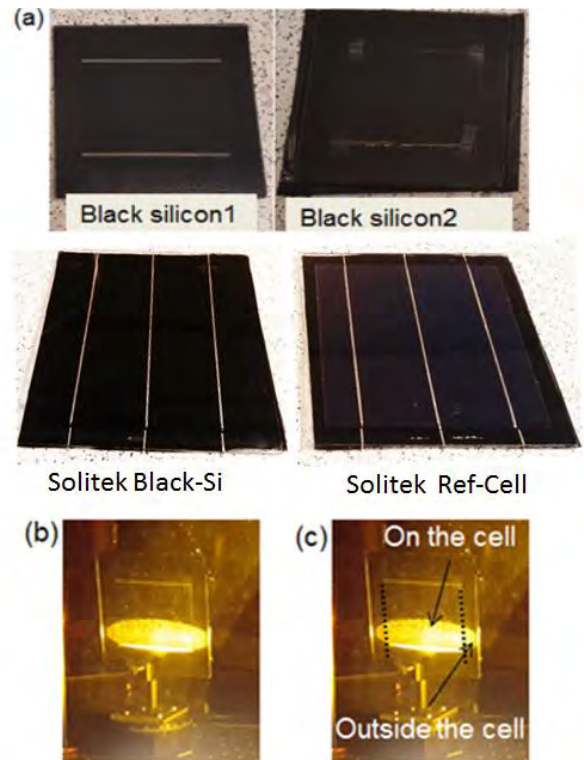


Fig. 5 Photograph showing the three black silicon solar cells and reference cell without black Si (a) and illustration of portion of the beam missing the solar cell for AOI larger than  $\pm 75^\circ$ .

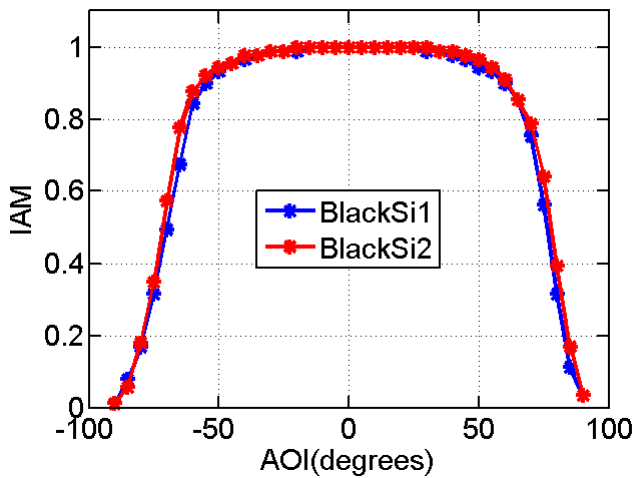


Fig. 6 IAM-AOI plot for the two black silicon solar cells.

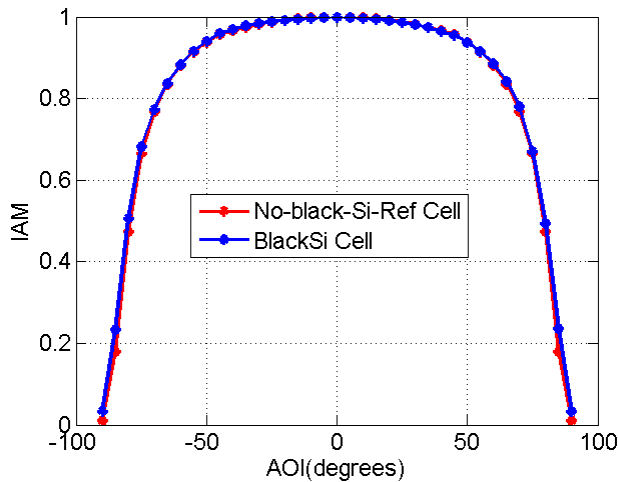


Fig. 7 AOI-IAM plot for black Si multi crystalline solar cell and a reference cell without black Si.

From the measurement between black Si multi crystalline solar cell and a reference cell without black Si, we have calculated the gain obtained by black Si in comparison with the reference cell without black Si. The AOI versus gain plot is shown in the Fig. 8

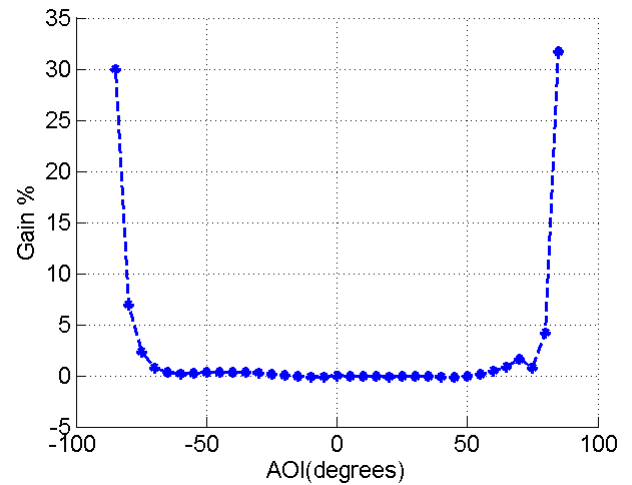


Fig. 8 A plot showing the gain of the black silicon solar cell over a reference cell without black silicon.

#### IV. CONCLUSIONS

In conclusion, we presented here an indoor study on the effect of the angle of incidence on the short circuit current of encapsulated, black silicon based solar cells, using a broadband, collimated light source. In a wider perspective, our setup allows for automatized, reliable measurements of short circuit current for AOI between  $+90^\circ$  and  $-90^\circ$  and is not restricted to measurements on black silicon. Results indicate the setup to be a viable method for determining the IAM. Importantly, reproducibility on the AOI was very high with a maximum average relative standard deviation of 0.75%. Moreover, from our measurement of black Si and reference cell without black cell; we have shown that the black silicon yields more significant gain in the output than the latter standard cell at a higher angle from the normal angle of incidence (which is 32% for  $85^\circ$ ). In the future we have planned to do more measurements on standard cells for validation of the method and systematic tests allowing for determination of the angular performance for black silicon with EVA encapsulated cells in combination with different types of glasses (ARC coated and structured). The setup presented here is a valuable tool for indoor measuring of the IAM i.e. the angular performance on solar cells and mini modules.

## REFERENCES

- [1] D. T. Reindl, W. A. Beckman, and J. A. Duffie, "Evaluation of hourly tilted surface radiation models," *Sol. Energy*, vol. 45, no. 1, pp. 9–17, 1990.
- [2] D. L. King, J. A. Kratochvil, and W. E. Boyson, "Measuring solar spectral and angle-of-incidence effects on photovoltaic modules and solar irradiance sensors," *Conf. Rec. Twenty Sixth IEEE Photovolt. Spec. Conf. - 1997*, no. September, pp. 1113–1116, 1997.
- [3] R. S. Davidsen, J. Ormstrup, M. L. Ommen, P. E. Larsen, M. S. Schmidt, A. Boisen, Ø. Nordseth, and O. Hansen, "Angle resolved characterization of nanostructured and conventionally textured silicon solar cells," *Sol. Energy Mater. Sol. Cells*, vol. 140, pp. 134–140, 2015.

## INTERLABORATORY COMPARISON OF METHODOLOGIES FOR MEASURING THE ANGLE OF INCIDENCE DEPENDENCE OF SOLAR CELLS

Nicholas Riedel<sup>1</sup>, Adrián A. Santamaría Lancia<sup>1</sup>, Mekbib Amdemeskel<sup>1</sup>, Sune Thorsteinsson<sup>1</sup>, Peter B. Poulsen<sup>1</sup>, Fabian Plag<sup>2</sup>, Ingo Kröger<sup>2</sup>, Lenneke H. Slooff<sup>3</sup>, Mark J. Jansen<sup>3</sup>, Anna J. Carr<sup>3</sup>, Petra Manshanden<sup>3</sup>, Martin Bliss<sup>4</sup>, Tom Betts<sup>4</sup>, Iñigo Petrina Jauregui<sup>5</sup>, Mikel Ezquer Mayo<sup>5</sup>, Jose L. Balenzategui<sup>6</sup>, Ruben Roldan<sup>7</sup>, Ulli Kräling<sup>8</sup>, Ghassan Baarah<sup>8</sup>, Beniamino Iandolo<sup>9</sup>, Rasmus S. Davidsen<sup>9</sup>, Anders Thorseth<sup>1</sup>, Carsten Dam-Hansen<sup>1</sup>, Gisele A. dos Reis Benatto<sup>1</sup>

<sup>1</sup>Department of Photonics Engineering, Technical University of Denmark, Frederiksborgvej 399, 4000, Roskilde, Denmark

<sup>2</sup>Physikalisch Technische Bundesanstalt (PTB), Bundesallee 100, D-38116 Braunschweig, Germany

<sup>3</sup>Energy Research Centre of the Netherlands (ECN>TNO), P.O. Box 1, 1755 ZG Petten, The Netherlands

<sup>4</sup>Centre for Renewable Energy Systems Technology (CREST), Loughborough University, Loughborough, Leicestershire, LE11 3TU, UK

<sup>5</sup>Spanish National Renewable Energy Centre (CENER), C/Ciudad de la Innovación 7, 31621 Sarriguren (Navarra), Spain

<sup>6</sup>CIEMAT, Department of Energy, Avda. Complutense 40, 28040 Madrid, Spain

<sup>7</sup>University of Applied Sciences and Arts of Southern Switzerland, Institute for Applied Sustainability to the Built Environment (SUPSI - ISAAC), Campus Trevano, CH-6952 Canobbio, Switzerland

<sup>8</sup>Fraunhofer Institute for Solar Energy Systems ISE, CaLab PV Modules, Heidenhofstrasse 2, 79110 Freiburg, Germany

<sup>9</sup>Department of Micro- and Nanotechnology, Technical University of Denmark, Ørsteds Pl., 2800 Kongens Lyngby, Denmark

**ABSTRACT** — The aim of this work is to compare angle of incidence (AOI) measurement setups for solar cells between laboratories with such capability. For the first time, we compare relative light transmission measurements among eight laboratories, whose measurement techniques include indoor and outdoor methods. We present the relative transmission measurements on three 156 mm x 156 mm crystalline-Si (c-Si) samples with different surface textures. The measurements are compared using the expanded uncertainties provided by each laboratory. Five of the eight labs showed an agreement better than  $\pm 2\%$  to the weighted mean between AOIs from  $-75^\circ$  to  $70^\circ$ . At AOIs of  $\pm 80^\circ$  and  $\pm 85^\circ$ , the same five labs showed a worst case deviation to the weighted mean of  $-3\%$  to  $5\%$  and  $0\%$  to  $18\%$ , respectively. When measurement uncertainty is considered, the results show that measurements at the highest incidence angle of  $\pm 85^\circ$  are problematic, as measurements from four out of the six labs reporting uncertainty were found non-comparable within their stated uncertainties. At  $85^\circ$  AOI a high to low range of up to  $75\%$  was observed between all eight laboratories.

### 1 INTRODUCTION

Intercomparisons between laboratories are important to ensure reliable and accurate measurements to the highest level of confidence. Laboratories have different methods, equipment setups and procedures, and it is of great value to assess the comparability of their results. Moreover, the IEC 61853-2 standard, which provides procedures on how to conduct AOI measurements on PV devices was recently published [1]. Thus, a round-robin on AOI measurements will allow us to validate the newly adopted standard, provide feedback to standardization bodies, and establish a baseline that future round-robin campaigns can improve upon. The results from this intercomparison will provide data which will be used in a future study to investigate the impact of measurement deviation on modelling and energy prediction.

The core objective of this work is to determine the level of agreement in the relative transmissivity measurements performed at eight laboratories for each angle of incidence  $\theta$ . The relative transmissivity is commonly referred to in other works as the incidence angle modifier (IAM). The range of angles extends from  $-85^\circ$  to  $+85^\circ$  in steps of  $5^\circ$ . The results are analyzed using the  $E_n$  number statistical method as outlined in ISO 17043:2010 [2]. This approach is commonly used in proficiency testing and it provides insight to the equivalence of the participating laboratories' test results. The data obtained from the participating laboratories is analyzed with the following objectives: (i) evaluate whether the measurement deviations from the weighted mean are within each partner laboratory's stated uncertainties; (ii) validate if the procedures stipulated by

the existing IEC 61853-2 result in comparable measurements when different measurement techniques are used; and (iii) determine the main sources of uncertainty that contribute to non-agreement of measured values between partners.

Although numerous round-robin programs have been conducted for PV measurements at Standard Test Conditions (STC) [3-5], the literature shows comparatively few works on round-robins or laboratory comparisons of angular dependent measurements. The intercomparisons of AOI measurements to date have compared a limited number of laboratories and methods. For example, the authors in [6] compared outdoor measurements performed in real-time at Sandia National Laboratories (SNL) and CFV Solar Test Lab, which lay roughly 10 km apart from each other. These two labs used unique methods to measure the AOI response of full-sized PV modules and found an acceptable level of agreement between their measurements. The authors in [7] compared AOI measurements again performed at SNL on full-sized PV modules to the IAM data for the same modules in PVsyst's database, or to measurements performed at an unnamed third party lab. The authors found that these three sources often had significant deviations for the same module type, up to a 14% difference in relative transmissivity at large AOIs. In this work, we present the AOI measurements made on three unique single cell (156 x 156 mm) laminates by eight European laboratories. The measurement systems encompass five different light sources including one lab that performed the measurements outdoors.

TABLE I: Description of participating laboratory measurement systems [8-11].

Laboratory	Test condition	Rotation stage	Description of light source
CENER	Outdoor	1-axis, 0° to 90°, Automated	Natural sunlight. Diffuse directly measured
CIEMAT	Indoor	1-axis, +90° to -90°, Automated	Continuous collimated broadband halogen lamp (1kW DXW)
CREST	Indoor	1-axis, +90° to -90°, Automated	Pasan 3b flasher with broadband Xe arc lamp (class AAA)
DTU	Indoor	1-axis, +90° to -90°, Automated	Energetiq (EQ-99FCX) broadband laser driven light source
ECN>TNO	Indoor	1-axis, +90° to -90°, Manual	Pasan flasher with broadband Xe arc lamp (class AAA)
Fraunhofer ISE	Indoor	1-axis, +90° to -90°, Manual	Pasan flasher with broadband Xe arc lamp (class AAA)
PTB	Indoor	2-axis, +90° to -90°, Automated	Tuneable laser system with broadband bias lamps
SUPSI	Indoor	1-axis, +90° to -90°, Automated	Pasan flasher with broadband Xe arc lamp (class AAA)

## 2 EXPERIMENTAL DETAILS

### 2.1 Partner laboratories and procedures

Eight scientific institutions from six European countries are involved in the measurement comparison. These include the Department of Photonics Engineering at the Technical University of Denmark (DTU Fotonik), Physikalisch Technische Bundesanstalt (PTB), the Energy Research Centre of the Netherlands (ECN>TNO), the Centre for Renewable Energy Systems Technology (CREST) at Loughborough University, the Spanish National Renewable Energy Centre (CENER), the Laboratory of Photovoltaic Solar Energy PVLab at CIEMAT, the University of Applied Sciences and Arts of Southern Switzerland (SUPSI), and Fraunhofer Institute for Solar Energy Systems (ISE). A brief description of each laboratory's measurement setup is described in Table I [8-11].

The measurement systems used at CREST, ECN>TNO, Fraunhofer ISE and SUPSI are based on a flash system used for full-sized modules. However, each one of these labs used a different approach to build the rotation stage. The rotation stage at ECN>TNO, for example is only capable of holding small laminates (roughly 20 x 20 cm), while the CREST, Fraunhofer ISE, and SUPSI rotation stages can accommodate small laminates up to full-sized modules. The CIEMAT and DTU systems are only capable of testing single cell laminates and the PTB system can accommodate mini-modules with up to four 156 x 156 mm cells. DTU was the only laboratory that performed the test with a light source that did not cover the full active cell area (i.e. the diameter of the collimated light beam in the DTU system was 12 mm). The two-axis tracker at CENER can accommodate full-sized module and since single cell laminates were used as the devices under test (DUTs) in this round-robin, they utilized the tracker's area to perform the test on all DUTs at once.

All the participant laboratories were asked to use their standard techniques for AOI measurements. The axis of rotation was predefined in order to allow the results from the different partners to be directly comparable. The definition for which angular direction was positive and negative was made explicitly clear in a memorandum document that all partners received. The document also specified the location of the rotational axis and tolerances for the precise location of the front of the PV cell surface within the laminate. The samples made for this round-robin have an offset of approximately 1.5 mm  $\pm$  0.5 mm from the rear side (back sheet) to the front surface of the PV cell. The participant laboratories were encouraged to use this tolerance when mounting the samples in their measurement system, although larger

deviations from the rotational axis to the center of the PV cell would be acceptable for the outdoor measurement system.

The physical quantity measured by the partner labs is the short circuit current ( $I_{SC}$ ) of each DUT over the specified angular range. The data of ultimate interest, however, are the relative transmissivity  $\tau(\theta)$  values. The relative transmissivity  $\tau(\theta)$  - sometimes referred to as the IAM - represents the percentage of in-plane direct beam irradiance available to the PV cell for conversion to electricity. The  $\tau(\theta)$  is calculated by normalizing the  $I_{SC}$  measured at each angle to the  $I_{SC}$  value measured at normal incidence. No procedures were provided to the partner labs as to how to correct for fluctuations in the test environment during the measurement (e.g. spectrum, irradiance or temperature) and instead it was left up to each partner to use their standard correction approach. A common temperature coefficient for  $I_{SC}$  was provided to the partner labs in the case temperature corrections were necessary.

### 2.2 Devices under test (DUT)

The round-robin includes measurements of three different PV devices in duplicate (i.e. each lab measures six DUTs in the total). Redundant samples were used so there would always be a backup in the case that any one sample became damaged. Electroluminescence (EL) images were taken before each laboratory started testing to ensure that no damage occurred during transportation. The analysis of EL images taken before the first lab's measurement and after the final lab's measurement showed that no cell damage had occurred during transportation. However, the glass of one sample was damaged about halfway through the campaign, which highlights the necessity of duplicate samples in round-robin campaigns. The measurements made on the damaged sample are not published here.

All DUTs have the following specifications: (i) An active cell area of 156 mm x 156 mm; (ii) full area dimensions of 200 mm x 200 mm; (iii) 3.2 mm thick finely textured PV glass substrate; (iv) ethylene-vinyl acetate (EVA) encapsulant; (v) two tabs as metal contacts; and (vi) a flat polymeric backsheets with slight curvature around the cell edges. The differences between the DUTs are the cell types and cell texturing. Two DUTs are mono-crystalline standard silicon; two DUTs are multi-crystalline black silicon textured under reactive ion etch (RIE) treatment (referred to as 'Black-Si A' hereafter) [12]; and two DUTs are multi-crystalline black silicon textured under atmospheric pressure dry etching (ADE) treatment (referred to as 'Black-Si B' hereafter) [13]. The edges of samples were covered with non-transparent tape to prevent measurement artifacts at large

incident angles.

IEC 61853-2 specifies that three measurements shall be taken at each angle. Six DUTs and 38 angles per sample would mean that each laboratory needs perform 684 measurements. In most cases, this was not possible due to time constraints and therefore only one measurement per angle, per sample was provided by most laboratories.

### 2.3 Uncertainty and Analysis of Results

Six of the eight labs provided the expanded uncertainty ( $k = 2$ ) for the value of relative transmissivity  $\tau(\theta)$  at each measured angle  $\theta$ . Two of these labs provided DUT specific uncertainty while the other four provided an uncertainty estimate that covered all samples in this round-robin.

The uncertainty of each lab's measurement is critical for establishing comparability through the  $E_n$  number calculation (1). The two labs that were not able to provide measurement uncertainty were assumed to have the worst case uncertainty. That is for every angle measured, the highest uncertainty submitted by any lab is used as the measurement uncertainty for the labs without uncertainty.

For every sample and every angle, an  $E_n$  number is calculated per (1).

$$E_n = \frac{x_i - X_{ref,i}}{\sqrt{UC_i^2 + UC_{ref,i}^2}} \quad (1)$$

Wherein  $x_i$  is the individual laboratory's measured relative transmissivity  $\tau(\theta)$  and  $UC_i$  is the expanded ( $k = 2$ ) uncertainty of the lab's measurement of  $\tau(\theta)$ . The reference value  $X_{ref,i}$  is the weighted mean of all partner's measured  $\tau(\theta)$  values for a given sample at a given angle. Here the measurements are weighted by the uncertainty provided by each partner. Weighting the results in this manner has the consequence of shifting the  $X_{ref}$  value towards the measured values ( $x_i$ ) of the laboratories with lower uncertainty. For every sample and every angle, the  $X_{ref,i}$  value is calculated using equation (2).

$$X_{ref,i} = \frac{\sum_{i=1}^N \frac{x_i}{\sigma_i^2}}{\sum_{i=1}^N \frac{1}{\sigma_i^2}} \quad (2)$$

Wherein  $\sigma_i$  is the  $k = 1$  uncertainty of the lab's measurement. The value  $\sigma_i$  is squared in (2) to arrive at the variance, which is additive by nature, whereas the standard deviation is not. Finally,  $UC_{ref,i}$  is the expanded ( $k = 2$ ) combined uncertainty of  $X_{ref,i}$  and is calculated per (3). Calculating  $UC_{ref}$  in this way yields a value that is always lower than any of the participating labs' declared uncertainties.

$$UC_{ref,i} = \frac{2}{\sqrt{\sum_{i=1}^N \frac{1}{\sigma_i^2}}} \quad (3)$$

The relative transmission measurements from each laboratory are said to be coherently within their declared uncertainty when  $-1 \leq E_n \leq 1$ . In other words, the condition  $-1 \leq E_n \leq 1$  is met when the difference between a lab's measurement ( $x_i$ ) and the reference value ( $X_{ref,i}$ ) is less than or equal to the root sum of squares (RSS) of the lab's declared uncertainty ( $UC_i$ ) and the reference

uncertainty ( $UC_{ref,i}$ ). The sign of  $E_n$  provides a convenient way of discerning whether a lab's measurement is high ( $E_n = +$ ) or low ( $E_n = -$ ) relative to the weighted group mean.

## 3 RESULTS

The expanded uncertainty provided from each partner laboratory is shown as a function of AOI in Figure 1. Since there were three unique DUTs in the campaign, some labs accordingly reported an expanded uncertainty for each of the three DUTs. The uncertainty from partners who did provide DUT specific uncertainty (CREST and PTB) is represented by range bars and a dot symbol. The range bars show the maximum and minimum uncertainty reported by the laboratory while the dot in the middle represents their median uncertainty. The same convention is used to represent  $UC_{ref}$ . Note how  $UC_{ref}$  is less than the uncertainty of all laboratories at each angle. The uncertainty provided by partners with non-DUT specific uncertainty is represented with 'x' symbols. Figure 1 shows a trend of increasing uncertainty with increasing AOI, wherein a range of 0.1% to 3% at normal incidence and a range of 2.5% to 9.3% at 85° AOI is observed. The specific reasons for this increasing trend will be unique to a given measurement system (e.g. increasing non-uniformity or uncertainty of the measured angle  $\theta$ ). In the DTU measurement system, for example, the increase of uncertainty at large angles is primarily due to an increased contribution of uncertainty from the measured angle  $\theta$ .

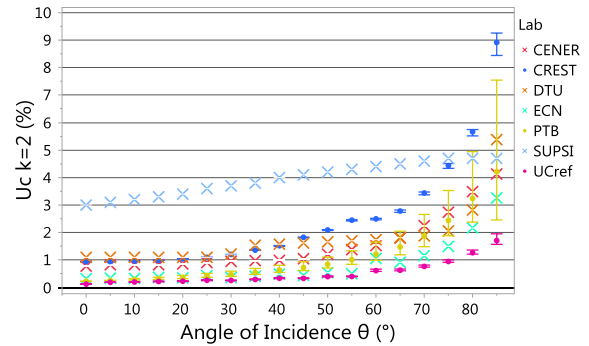


**Figure 1:** Expanded uncertainty from six laboratories as a function of AOI. The expanded uncertainty of the reference ( $UC_{ref}$ ) is also shown. Labs providing a single uncertainty value at each angle are noted with an 'x' whereas labs with uncertainty specific to each DUT are noted with dots and range bars.

The measurements on sample Black-Si A performed by the eight partner laboratories are shown in Figure 2. We show the high-level results from this sample only because the measurement differences between the labs showed a consistent trend and because sample Black-Si A showed the worst case range (max-min) among the eight labs. Figure 2 shows an increasing measurement range between the labs with an increasing AOI. This result follows the same trend of increasing uncertainty with increasing AOI purported by the partner laboratories. In the positive direction, the measurement range is less than 0.1 (10%) up to a +60° AOI, while in the negative direction the range is less than 0.1 up to a -70° AOI. We attribute the difference between measurements at positive and negative angles to an

artifact in some participant's results, not because of an inherent non-symmetry in the DUT itself. The maximum disagreement of 0.69 (69%) and 0.75 (75%) is observed at  $+85^\circ$  and  $-85^\circ$  AOI, respectively. This large disagreement is mostly driven by the outdoor measurement performed by CENER. If this measurement is removed, the range at  $85^\circ$  AOI is decreased to 0.23 (23%) in the positive direction and 0.36 (36%) in the negative direction.

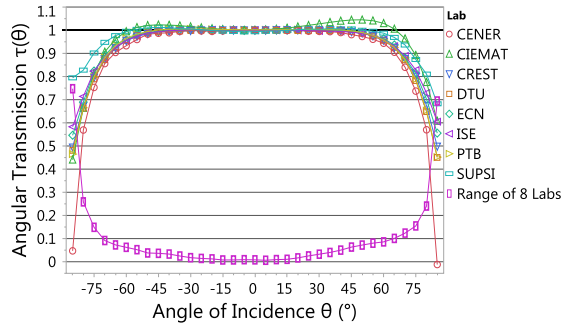


**Figure 2:** Overlay of transmission as a function of AOI  $\theta$  as measured by eight laboratories on sample Black-Si A. The range of all measurements is also shown.

In Figure 3 we show the difference between each lab's angular transmission measurement  $\tau(\theta)$  and the reference value  $X_{ref}$ . Recall that there are three DUTs, and thus three  $X_{ref}$  values at each AOI. The error bars drawn around each data point represent the maximum and minimum difference to the reference value; the center of the data point between the bars represents the median difference. Note that the deltas of -33% to -45% at  $\pm 85^\circ$  reported by CENER have been removed from the plot in order to create a finer view of the y-axis.

Figure 3 shows that the agreement between all labs relative to the weighted mean is better than  $\pm 2\%$  in the limited range of AOIs from  $-30^\circ$  to  $25^\circ$ . However, it is only the measurements from CIEMAT and SUPSI that show dispersion from the group at low angles. If CIEMAT and SUPSI's data are excluded, then the agreement between the six remaining labs is better than  $\pm 2\%$  for AOIs  $-50^\circ$  to  $50^\circ$ . Beyond  $-50^\circ$  to  $50^\circ$ , CENER's measurements become increasingly lower relative to the other labs'. If CENER's measurements are also excluded, five of the eight labs have an agreement of better than  $\pm 2\%$  from the weighted mean on all samples between  $-75^\circ$  to  $70^\circ$ . At  $\pm 80^\circ$  these same five labs show worst case agreement of -3% to 5% relative to the weighted mean (Black-Si A), and a best case agreement of -1% to 0.5% relative to the weighted mean (Mono-Si). And finally, at  $\pm 85^\circ$  the five labs show worst case agreement of 0% to 18% relative to the weighted mean (Black-Si B) and a best case agreement of 0.5% to 8.5% (Mono-Si). The worse agreement on the Black-Si as compared to Mono-Si sample could be due to the difference in surface structures or differences in low-light behavior.

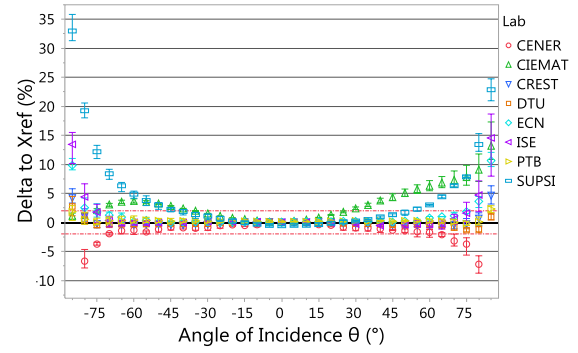


**Figure 3:** Plot showing the difference between each lab's measurement and the reference value  $X_{ref}$ . The error bars show each lab's max and min difference to  $X_{ref}$ . The red dashed reference lines are drawn at  $\pm 2\%$ .

In Figure 4 we present the results from the  $E_n$  number calculation as a function of AOI for the Black-Si A sample. The profile observed in Figure 4 is similar to that in Figure 3 because the data in Figure 3 are the numerator used in the  $E_n$  calculation. Figure 4 shows 39 (of 280 total) measurements where the results are not comparable within the stated or assumed uncertainties. In other words, 14% of the time  $E_n$  is greater than 1 or less than -1, wherein all instances occur at AOIs  $\geq |\pm 40|^\circ$ . PTB and CREST are the only two labs whose measurements result in  $-1 \leq E_n \leq 1$  for all AOIs. Thus, we can say that their measurements agree to the weighted mean within the stated uncertainties for all measurement angles.

The CIEMAT data show 10 instances of non-comparability. Therefore the worst case uncertainty assumed for the CIEMAT measurements is clearly too conservative to make them comparable to the rest of the partners. Interestingly, CIEMAT shows several instances of non-comparability in the positive angular direction, but none in the negative direction. This is due to the non-symmetrical measurements they obtained (Figure 2). The reason behind the non-symmetry is still uncertain, but we believe it is likely due to an offset in the vertical axis of rotation from the middle of the PV cell. In addition, it is also possible that the optics unique to the CIEMAT measurement system result in the partial polarization of light from the halogen lamp, which in return would alter the reflection and transmission properties.

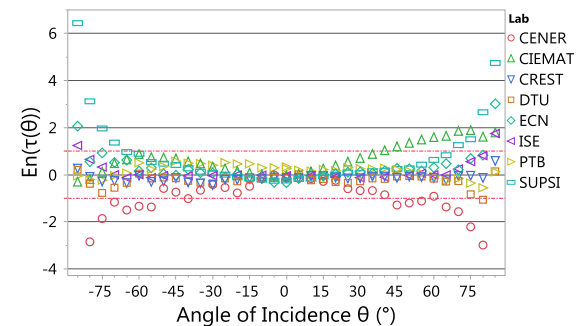


**Figure 4:**  $E_n$  number as a function of AOI  $\theta$  for the measurements from eight laboratories.

The CENER data show 16 instances of measurements that deviate from the weighted mean beyond their reported uncertainty level. The CENER measurements are consistently lower than the measurements from the other seven partners and this difference increases at

higher AOIs. The CENER measurements were the only measurements in this round-robin performed outdoors. However, we do not conclude that the low results are attributable to the outdoor approach itself. To better understand the differences that can occur indoors versus outdoors, we propose to extend the measurement campaign to additional laboratories performing the AOI test outdoors.

The SUPSI data show 8 instances where their measurements do not agree within the stated uncertainty and all 8 instances occur at AOIs  $\geq |\pm 70^\circ|$ . Although the SUPSI measurements are consistently higher than most of the labs at every AOI (Figure 2 and Figure 3), they are also the lab with the most conservative uncertainty. However, the stated uncertainty of 4.6% to 4.7% at AOI  $\geq 70^\circ$  is not conservative enough for comparability. The reason(s) for SUPSI's higher than average angular transmission measurements are still under investigation. At the time of writing the high measurements are believed to be due to unwanted reflections within the test bed. These reflections are more pronounced in the negative direction than in the positive direction. The SUPSI data show that establishing comparability is not dependent on the light source used. CREST, ECN>TNO, ISE and SUPSI all used Xe flash lamps to measure the samples and yet SUPSI shows significant deviations from the other three labs.

DTU, ECN>TNO and ISE all show generally good agreement to the weighted mean; each lab shows one or two instances where their measurements are not comparable within the stated or assumed uncertainties. For DTU this occurs at AOI of  $80^\circ$  while for ECN>TNO and ISE it occurs at the extreme angles of  $\pm 85^\circ$ . In actuality the measurements from ECN>TNO are closer to the weighted mean than ISE's at these high AOIs, since the uncertainties provided by ECN>TNO are more conservative than the maximum uncertainty assigned to the ISE measurements.

To understand the uncertainty level necessary for CIEMAT and ISE to be comparable to the weighted mean, we solve (1) for  $UC_i$  while leaving  $E_n = 1$  and  $X_{ref,i}$  and  $UC_{ref,i}$  constant based on results from the other six labs. The results are shown in Figure 5 for the Black-Si A sample. The maximum uncertainty at each AOI reported by any of the other six labs is also shown. Since the expanded uncertainty limit for ISE is less than 1% out to  $\pm 65^\circ$ , we can conclude that their measurements agree well to the weighted mean within that range. However, an uncertainty between 11.7% and 17.7% at the highest angles of  $\pm 85^\circ$  would be required for comparability.

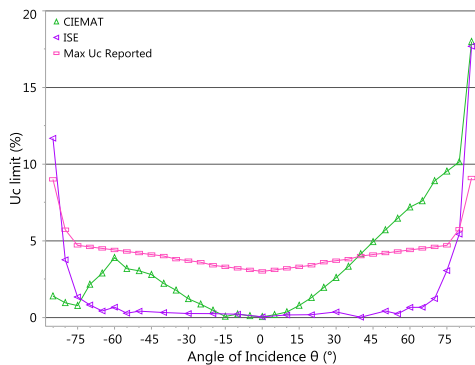


**Figure 5:** Minimum uncertainties required in order for CIEMAT's and ISE's measurements to be comparable to the weighted mean of the other six labs.

As mentioned, the measurement differences between labs showed the same trend across all three samples. Nevertheless we wish to give a full perspective of how the  $E_n$  number varied across samples and angles. In Figure 6, we show the number of labs that had an  $E_n$  number outside the limit of comparability. Figure 6 shows that at the extreme AOIs half or more of the labs have deviations that are not fully covered by their uncertainty budgets. This result highlights the difficulty of performing accurate measurements at high AOIs. Figure 6 includes all eight laboratories and assumes the worst case uncertainty for the ISE and CIEMAT data.

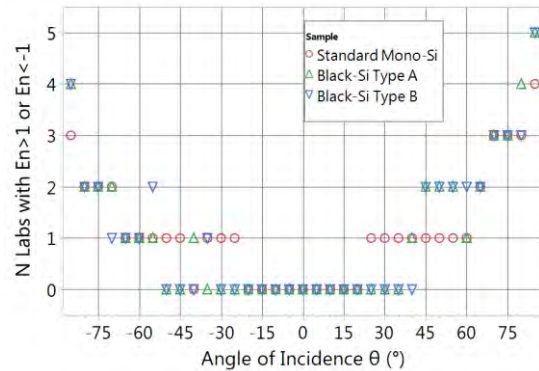


**Figure 6:** Plot showing the number of labs that do not comply to the condition  $-1 \leq E_n \leq 1$  as a function of AOI.

IEC 61853-2 states that the rotational symmetry of the test system shall be verified at  $-80^\circ$  and  $80^\circ$  AOI. It further states that the deviation in the relative transmissivity at these two angles shall not deviate by more than 2%. We performed this check for all eight laboratories and the results for the Black-Si A sample are shown in Figure 7. The limits of  $\pm 2\%$  are indicated by the dashed red reference lines. It can be seen in Figure 7 that the labs who were the most comparable always meet the IEC requirement for symmetry. On the contrary, the labs with the lowest comparability and largest deviations from the weighted mean, showed symmetry that did not comply with the standard. This result suggests that it is a good practice to verify the symmetrical performance of a test system for measurement of the angular dependency of PV devices.

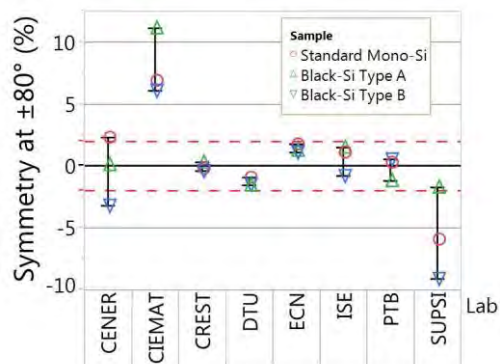


**Figure 7:** Variability plot showing the symmetry of the relative transmissivity measurements at  $\pm 80^\circ$ . Three data points are shown for each lab, one for each sample.

## 4 SUMMARY

The results from an international round-robin between eight laboratories performing angular dependent measurements have been presented. Five of the eight labs showed an agreement better than  $\pm 2\%$  between AOIs from  $-75^\circ$  to  $70^\circ$ . At AOIs of  $\pm 80^\circ$  and  $\pm 85^\circ$ , the same five labs showed a worst case deviation to the weighted mean of  $-3\%$  to  $5\%$  and  $0\%$  to  $18\%$ , respectively. These worst cases were observed on the 'Black-Si A' and 'Black-Si B' samples. The results showed that measurements at the highest incidence angle of  $\pm 85^\circ$  are problematic, where a high to low range of up to  $75\%$  was observed among the eight labs.

The results provided by CREST and PTB agreed to the weighted average within their stated uncertainties for all angles. Similarly, the results from DTU and ECN>TNO agreed to the weighted average within their uncertainties, for all angles except  $85^\circ$ . At high angles of incidence ( $\geq 70^\circ$ ) the measurements from three to five labs were found not comparable within their stated or assumed uncertainties. The more frequent non-comparability observed at high angles of incidence suggests that labs may need to reconsider a more conservative uncertainty budget at angles  $\geq 70^\circ$ .

In a future work we will investigate the influence of the measurement deviations observed in this round-robin on modelled energy production. Furthermore, we plan to extend the round-robin to obtain more data from laboratories performing the AOI test outdoors.

## 5 ACKNOWLEDGEMENTS

We would like to thank all the partner laboratories for all their time and work performing the measurements. The facility and part of the work at DTU has been made possible by the grant "LEDMET - Center for LED metrology" from Innovation Fund Denmark.

## 6 REFERENCES

- [1] "IEC 61853-2, Photovoltaic (PV) module performance testing and energy rating - Part 2: Spectral responsivity, incidence angle and module operating temperature measurements." 2016.
- [2] "ISO/IEC 17043:2010 Conformity Assessment – General Requirements for Proficiency Testing International Organization for Standardization." 2010
- [3] B. Mihaylov *et al.*, "Results of the SOPHIA intercomparison Part-1: STC, low-irradiance conditions and temperature coefficient measurements of C-Si technologies" in *29th Eur. Photovolt. Sol. Energy Conf. Exhib.*, 2014
- [4] D. Dirnberger *et al.*, "Progress in photovoltaic module calibration: Results of a worldwide intercomparison between four reference laboratories" *Meas. Science and Tech.*, vol. 25, no. 10, 2014.
- [5] E. Salis *et al.*, "Improvements in world-wide intercomparison of PV module calibration," *Solar Energy*, Volume 155, October 2017, Pages 1451-1461
- [6] B. H. King *et al.*, "Recent advancements in outdoor measurement techniques for angle of incidence effects," in *IEEE 42<sup>nd</sup> Photovoltaic Specialist Conference (PVSC)*, 2015
- [7] S. Boppana *et al.*, "Impact of uncertainty in IAM measurement on energy predictions," *7th World Conference on Photovoltaic Energy Conversion (WCPEC-7) 2018*
- [8] M. W. Amdemeskel *et al.*, "Indoor measurement of Angle resolved light absorption by antireflective glass in solar panels", *34th Eur. Photovolt. Sol. Energy Conf. Exhib.*, 2017
- [9] J.L. Balenzategui and F. Chenlo, "Measurement and analysis of angular response of bare and encapsulated silicon solar cells," *Sol. Energy Materials & Sol. Cells*, vol. 86, pp. 53–83, 2005.
- [10] F. Plag, I. Kröger, T. Fey, F. Witt, & S. Winter "Angular-dependent spectral responsivity - Traceable measurements on optical losses in PV devices" *Prog. Photovoltaics Res. Appl.*, Special Issue Paper, pp. 1–14, 2017.
- [11] L.H. Sloof *et al.*, "Looking at the annual yield from various angles: Optical model verification for structured glass" in *33rd Eur. Photovolt. Sol. Energy Conf. Exhib.*, 2016
- [12] R. S. Davidsen *et al.*, "Black silicon laser-doped selective emitter solar cell with 18.1% efficiency," *Sol. Energy Materials & Sol. Cells*, vol. 144, pp. 740–747, 2016.
- [13] B. Kafle *et al.*, "Plasma-free dry-chemical Texturing process for high-efficiency multicrystalline silicon solar cells," *Energy Procedia*, vol. 92, no. September, pp. 359–368, 2016.

## CHARACTERISATION OF ANGULAR DEPENDENT OPTICAL PROPERTIES OF DIFFERENT COLORING TECHNOLOGIES EMPLOYED IN BIPV PRODUCTS

Markus Babin, Adrian A. Santamaria Lancia\*, Anders Thorseth, Sune Thorsteinsson  
 Department of Photonics Engineering, Technical University of Denmark  
 Frederiksborgvej 399, 4000 Roskilde, Denmark

\*Corresponding Author: aasl@fotonik.dtu.dk; +45 46774584

**ABSTRACT:** Accurate determination of the angular dependent color of BIPV products is necessary to aid architects in matching BIPVs to surrounding building materials. A methodology for the study and characterization of visual appearance at different viewing angles is presented. This includes measurements of spectra of reflected light from BIPV samples for the determination of single-plane BRDF and IAM. BRDFs are converted to CIELAB color coordinates to analyze lightness, chroma and color saturation. Samples of three different technologies (printed ceramic inks, thin-film coatings and colored interlayers) are investigated. Results show vastly different angular dependency for sample groups, ranging from almost uniform (ceramic ink) to iridescent (thin-film coating) appearance. Differences are also observed between ceramic inks of different colors with correlation between specularly of reflection, IAM and angular constancy of appearance. For thin-film coated samples, correlation is shown between reflectance spectra, IAM and iridescence. Samples with colored interlayers show irregular angular appearance due to a textured glass surface.

**Keywords:** Building Integrated PV (BIPV), Experimental Methods, Optical Properties, Performance, Color

### 1 INTRODUCTION

Building integrated photovoltaics (BIPV) present an important new market for energy production and reduction of carbon emissions by using photovoltaic materials as construction material while at the same time producing energy. While offering great potential, BIPV is faced with the challenge of achieving acceptance as part of architectural design in terms of aesthetics and visual appearance. This requires the development of new methods for customizing the appearance of the PV devices, to either match the appearance of other building materials or to achieve customized and creative designs. These requirements have led to the development of various technologies for coloring of PV modules, ranging from colored glass or encapsulants to mineral or thin-film coatings. [1]

A correlated, major interest by architects is to accurately predict the appearance of BIPV facades during building design. For some BIPV coloring technologies, this is a challenging task due to changes in color appearance with view angle, in extreme cases even showing changes in hue (iridescence). This requires predictions of the appearance for different viewing angles as well as different light incidence angles (corresponding to different times of day). Thus, there is a requirement for the characterization of various BIPV coloring technologies regarding their angular dependent reflections.

Each of the currently available BIPV coloring technologies offers its own advantages and disadvantages regarding spatial and angular color uniformity and efficiency losses. [1] On the one hand, colored or printed glass and mineral coatings suffer from relatively high efficiency losses due to light absorption by the coloring materials. Thin-film coatings on the other hand, while achieving low efficiency losses, present high variation of color with view angle and can appear highly iridescent.

Several studies have been carried out regarding the efficiency of the different technologies and their theoretical limits. [2]–[4] Although there is some disagreement over the results, efficiency losses can be characterized relatively well. Angular dependent optical properties, however, are less well studied, especially in terms of comparisons between technologies.

This paper aims to bridge this gap and allow easier predictions of angular dependent appearance of BIPV products for the use in architectural design and planning.

### 2 DEVICES UNDER TEST

The devices under test (DUT) consist each of a single 6” mono-Si cell laminated with a black backsheet and different types of cover glass. The dimensions of the samples (width x length) are of 20 x 30 cm and 20 x 20 cm and the glass thickness is 3.5 mm.

The samples employ three different coloration technologies: Two of these technologies make use of different coatings on the inner side of the glass and the third uses a stack of several interlayers of different colors. A graphical representation of the sample composition is shown in Figure 1, with further details described below.

Printed Ceramic Ink (PCI) samples feature inkjet printed ceramic ink on the inner side of the solar glass cover. Coloration is achieved through light absorption in the ink pigments, leading to similar spectra of transmitted and reflected light. Samples of seven different colors using this technology are investigated.

Thin film coating (TFC) samples achieve coloration through spectrally selective reflection of light by thin-film coatings deposited on the inner side of their cover glass, with an anti-reflective coating (ARC) on top of the glass. Six differently colored samples of this type are measured.

Colored Interlayer (CIL) samples contain colored interlayers, stacked between layers of encapsulant between the glass cover and the PV cell. Two differently colored samples are investigated, both featuring a textured glass surface.

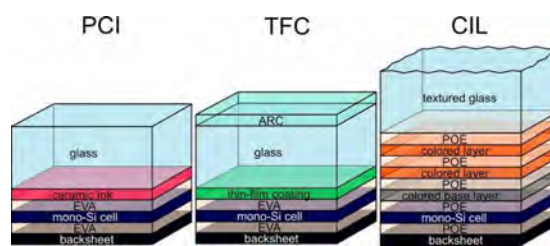


**Figure 1:** Composition of PCI, TFC and CIL samples

For each of the 3 coloring technologies, a reference sample using the same cell and black backsheet was provided with the intention of comparing the effects of the different coloration on the studied parameters.

However, of the reference samples supplied, only the one for the PCI technology had identical materials as the colored samples and was suitable for comparison. In the TFC case, the reference glass had a different ARC than the rest of the samples and is therefore only partially suited for comparisons. For the CIL reference sample, the glass we were provided with was flat instead of textured, so it has almost no use for this study.

### 3 METHODOLOGY

In order to understand the optical properties and the perceived visual aspect of samples under illumination, it is important to obtain measurements of the light reflected from the sample and to quantify changes in intensity and spectrum shape. This allows the translation of these quantities into perceived color changes and specular and diffuse reflected intensity. Measurements obtained at different view angles allow the geometrical distribution of these acquired parameters.

For this purpose, multidirectional reflectance measurements are performed in this work to compute the bidirectional reflectance distribution function (BRDF). Studies of BRDF has been used in a wide range of industries and laboratories to improve the understanding of the bidirectional reflectance characteristics of either natural or man-made surfaces [5].

The general formulation of the BRDF as defined by Nicodemus [6] is as follows:

$$B(\phi_i, \theta_i, \phi_r, \theta_r) = \frac{dL_{\Omega,r}(\phi_r, \theta_r)}{dE_i(\phi_i, \theta_i)}$$

The BRDF is defined as the ratio between the reflected radiance  $L_{\Omega,r}$  and the incident irradiance  $E_i$  on the sample. The angles  $\phi_i$  and  $\theta_i$  refer to the incident light, while  $\phi_r$  and  $\theta_r$  refer to the reflected light.

A laboratory setup for the measurement of the single-plane spectral BRDF was developed. It consists of a collimated light source and a gonioreflectometer, which allow variation of incidence angle and measured reflectance angle on the sample surface. The sample is mounted on a motor allowing variations in incidence angle ( $\theta$ ). Below in the same rotational axis, an independent motor rotates a mechanical arm that holds the input optics to a spectrometer. Measurements are obtained on a single axis in the range of  $\pm 90$  degrees of input optic relative to the sample, and a set of angular data per each sample/light source angle is obtained. The BRDF setup is shown in Figure 2.

The light source is a broadband laser-driven light source (LDLS), Energetiq EQ-99X. Light output source is a high brightness 100  $\mu\text{m}$  size Xe plasma in the range from 170 to 1700 nm. The light is collimated using three off-axis parabolic (OAP) mirrors and a pinhole. An UV-filter cutting light below  $\sim 320$  nm is included to achieve a spectrum closer to that of the sun. The maximum spot size is 38 mm in diameter at the sample plane and can be reduced to fit within the size of the solar cell at all measured angles.

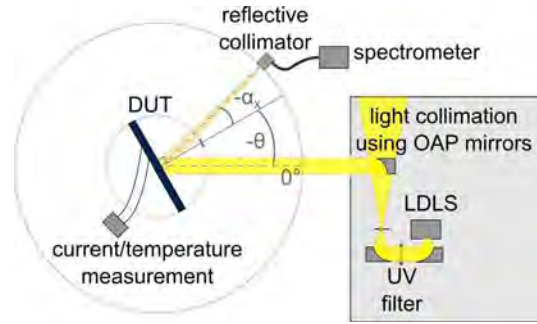


**Figure 2:** Experimental measurement setup for single-plane spectral BRDF:  $\alpha_x$  denotes the view angle and  $\theta$  denotes the incidence angle of light.

Spectra are acquired through independent rotation of a reflective collimator (Thorlabs RC04SMA-F01) around the sample, collecting reflected light, which is transferred to an Ocean Optics QE65000 spectrometer using a 600  $\mu\text{m}$  optical fiber. The reflective collimator is mounted at a distance of 28 cm from the sample and is adjusted to be situated  $4^\circ$  below the plane of irradiance so as not to occlude the incoming light, allowing measurements of the single-plane spectral BRDF.

In addition to the angular dependent optical characteristics of each of the different samples, it is also of interest how they impact the power performance. Therefore, measurements of DUT short circuit current ( $I_{sc}$ ) and temperature ( $T_{DUT}$ ) are carried out during simultaneous rotation of the sample respect to the incident light to compute the incidence angle modifier (IAM). For the particular case of our measurement setup, all the incident light is contained within the samples at all angles and no cosine factor is required, resulting in the following equation:

$$IAM(\theta) = \frac{I_{sc}(\theta)}{I_{sc}(0^\circ)}$$

IAM measurements are carried out using the same setup, but  $I_{sc}$  and  $T_{DUT}$  are acquired using a National Instruments NI 9213 acquisition system with a 24-bit ADC.  $I_{sc}$  is acquired by measuring the voltage across a 0.5  $\Omega$  precision shunt resistor and each measurement is an average over 20 acquired samples to reduce electrical noise variations. Device temperature is measured at the back of the sample with a J-type thermocouple and averaged over 3 measurements at each angle.

As a final electrical performance characterization, IV curves at STC conditions are performed on all the samples using a PASAN class AAA flash solar simulator for cells. Temperature is measured at the base plate and the voltage sweep is performed with a 4-quadrant electronic load.

The analysis of color appearance variations is carried out by calculating coordinate values mapped within the CIELAB color space.

The measured spectral BRDF is used to calculate the XYZ tristimulus values for each measurement point in the CIE 1931 color space via color matching functions and the D65 standard illuminant. Using a measured white reference sample (Spectralon), these coordinates are then transferred to CIELAB color coordinates, yielding device independent values.

Coordinates in the CIELAB color space can be interpreted as functions of Hue ( $h^\circ$ ), Chroma (colorfulness,  $C^*$ ) and Lightness ( $L^*$ ), as represented in Figure 3.

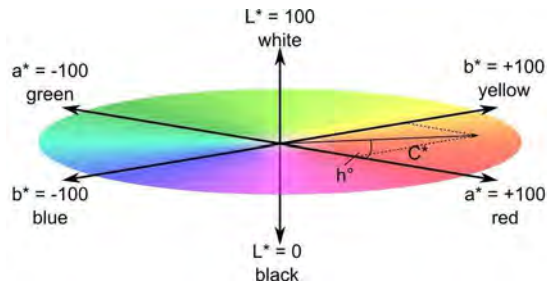


Figure 3: CIELAB color space

Chroma ( $C^*$ ) in the CIELAB is defined as the Euclidean distance to a point on the  $a^*-b^*$ -plane, while the hue ( $h^\circ$ ) is described using the 4-quadrant arctangent of the  $a^*$  and  $b^*$  coordinates. This results in the following equations:

$$C^* = \sqrt{a^{*2} + b^{*2}}$$

$$h^\circ = \text{atan2}(a^*, b^*)$$

CIELAB color coordinates can further be translated to the CIELUV color space which also defines a saturation parameter  $s_{uv} = C^*_{uv} / L^*$ , where  $C^*_{uv}$  is the chroma in the CIELUV space and  $L^*$  is the lightness parameter.

## 4 EXPERIMENTAL RESULTS

### 4.1 BRDF Characterization

#### 4.1.1 PCI Samples

Figure 4 shows the BRDF measurement results for the PCI samples. The spectral BRDF at the center position ( $\alpha_x = \theta = 0^\circ$ ) highlights the large differences in reflectance spectra between colors. Additionally, the total BRDF with changing view angle is shown, with the peak at  $\alpha_x = 0^\circ$  giving an indication of the amount of specular reflections. While most samples show very little specularity, the blue sample shows significant specular reflections, followed by the red and white sample.

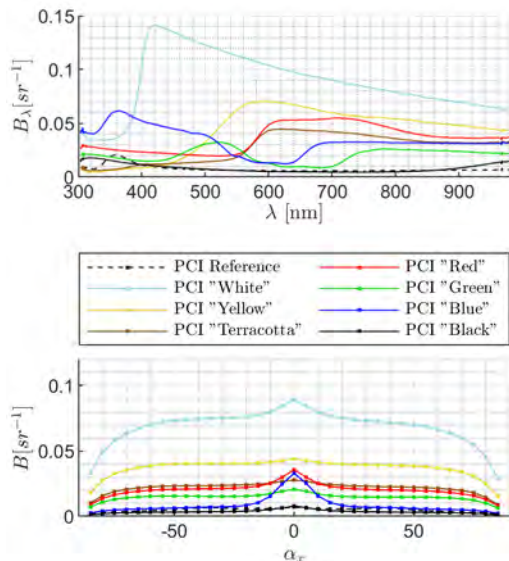


Figure 4: Spectral BRDF at  $\alpha_x = \theta = 0^\circ$  (top), total BRDF at  $\theta = 0^\circ$  (bottom) for PCI samples

#### 4.1.2 TFC Samples

The BRDF measurements of the TFC samples are shown in Figure 5. TFC “Terracotta” seems misnamed, as it appears green-yellow with high iridescence.

The samples can be separated into several groups according to spectrum shape. For one, these are the blue, green and terracotta samples, which all show two distinct peaks within 300-600nm. Secondly, the gold and bronze sample show an almost identical spectrum with a higher reflectance at longer wavelengths. Lastly, the gray sample shows only one peak at  $\sim 360\text{nm}$ , from which the reflectance declines almost linearly for longer wavelengths. While differences between colors in a group are most likely caused by differences in coating thickness, differences between groups are most likely due to different coating materials.

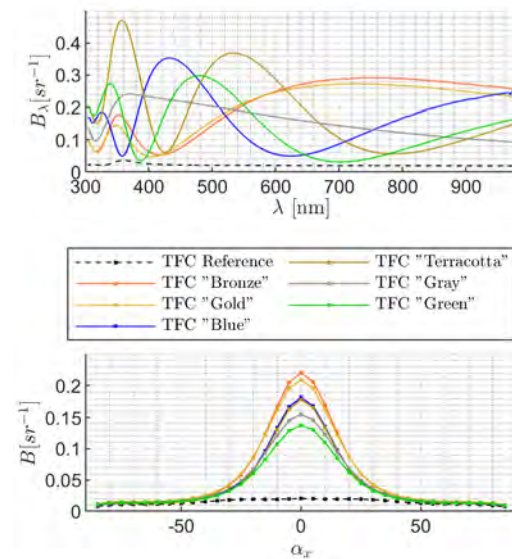


Figure 5: Spectral BRDF at  $\alpha_x = \theta = 0^\circ$  (top), total BRDF at  $\theta = 0^\circ$  (bottom) for TFC samples

#### 4.1.3 CIL Samples

The BRDF graphs of the CIL samples are shown in Figure 6. The flat shape of the reflectance spectra indicates low color saturation for the samples studied.

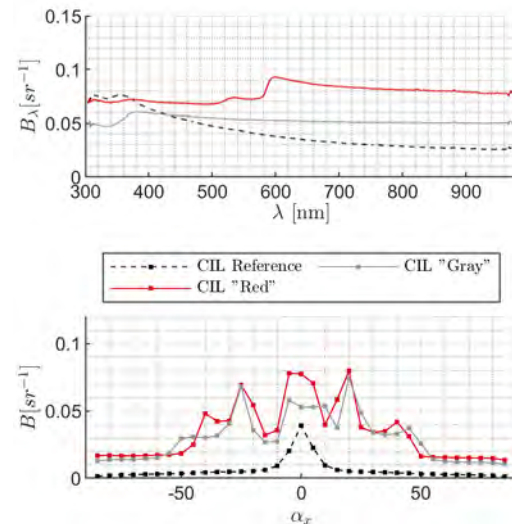


Figure 6: Spectral BRDF at  $\alpha_x = \theta = 0^\circ$  (top), total BRDF at  $\theta = 0^\circ$  (bottom) for CIL samples

In the total BRDF plot, irregular changes in total BRDF values with view angle are observed, and this effect can be mainly attributed to the textured glass surface.

This observation is reinforced by the measurement of the reference sample, which has a non-textured glass, as its total BRDF shows a shape more similar to the other technologies.

#### 4.2 CIELAB Color Space

##### 4.2.1 PCI Samples

Colorimetry calculations are performed for two selected PCI samples, namely PCI “Blue” and PCI “Terracotta”, with photographs shown in Figure 7.

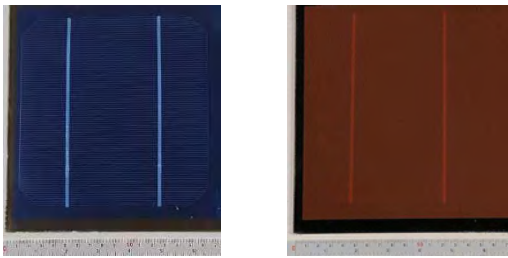


Figure 7: Photos of PCI “Blue” and PCI “Terracotta”

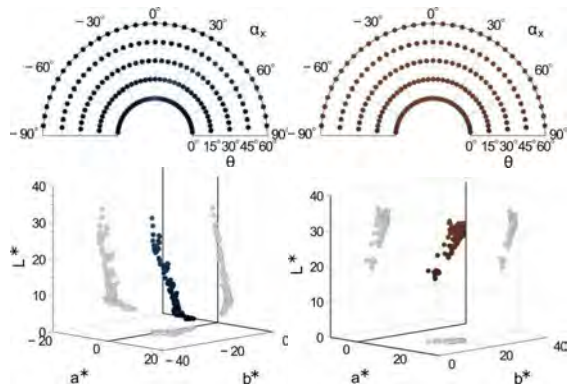


Figure 8: PCI “Blue” (left) and PCI “Terracotta” (right) in angular color representation and CIELAB color space

The PCI samples appear visually uniform from all angles, with changing lightness for samples with high specular reflections, as shown in Figure 8. For the terracotta sample, the CIELAB coordinates are clustered closely together, with only slight variations in chroma and lightness, indicating high color constancy.

The PCI “Blue” sample shows the highest amount of specular reflections, resulting in a less uniform angular appearance due to very low lightness outside of specular reflection angles ( $\alpha_x = \theta$ ).

##### 4.2.2 TFC Samples

For the TFC samples, again two selected samples are analyzed in greater detail. Photos of the samples, TFC “Blue” and TFC “Gold” are shown in Figure 9.

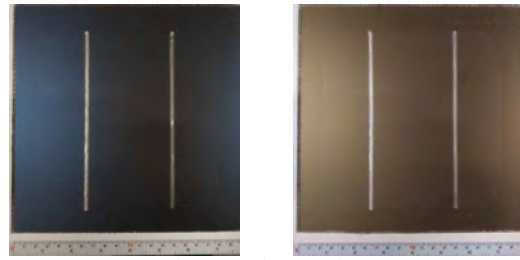


Figure 9: Photos of TFC “Blue” and TFC “Gold”

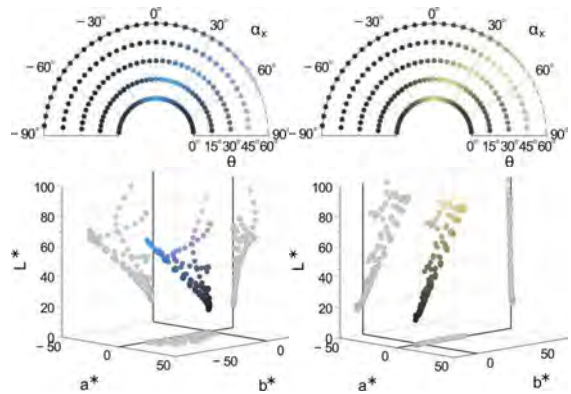


Figure 10: TFC “Blue” (left) and TFC “Gold” (right) in angular color representation and CIELAB color space

Angular color representations and CIELAB color coordinates are shown in Figure 10. While both samples show significant angular dependency of appearance, the blue sample appears iridescent, while the gold sample does not. Similarly, iridescence can be observed for the green and terracotta samples, but not for bronze and gray, though not shown here. Iridescence therefore follows the separation into groups described in Section 4.1.2.

The iridescent nature of the TFC “Blue” sample is shown in more detail in Figure 11. With increasing incidence angles, the color shifts towards magenta, with the specific color depending on the view angle. This is observed with the gradual shift of the points towards more positive values in the  $a^*$  axis as incidence angle increases. The difference between positive and negative view angles similarly increases with incidence angle.

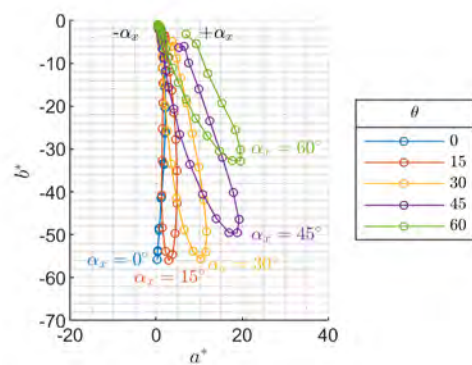


Figure 11: TFC “Blue” color coordinates in  $a^*$ - $b^*$ -plane with changing angles

4.2.3 CIL Samples

Photographs of the two CIL samples, CIL “Gray” and CIL “Red” are shown in Figure 12. Compared to the photographs of other sample groups, irregular reflections caused by the textured surface glass are visible.



Figure 12: Photos of CIL “Gray” and CIL “Red”

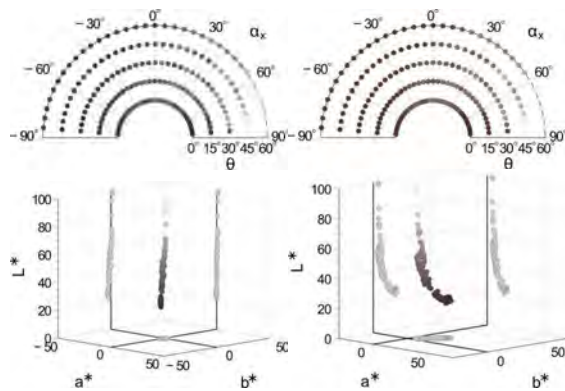


Figure 13: CIL “Gray” (left) and CIL “Red” (right) in Angular color representation and CIELAB color space

Figure 13 shows a representation of the angular dependent color and the CIELAB color coordinates for the CIL samples. Due to the irregular reflections caused by the textured glass surface, the apparent sample color varies with view angle, showing an intermediate average color saturation.

Opposed to the other sample groups, CIL samples show lower chroma at specular reflection angles ( $\alpha_x = \theta$ ), while both PCI and TFC samples show increasing chroma at specular reflection angles. This can also be observed in the CIELAB color space, where the measurement points for the CIL “Red” sample form an asymptotic curve with high chroma (increasing away from the axis origin) at low lightness, while the other sample groups show measurement points that can be extrapolated to cross the origin. This results in lower average color saturation for the CIL samples and is most likely a consequence of the textured glass surface.

4.3 IAM Characterization

4.3.1 PCI Samples

Figure 14 shows the IAM for the PCI samples. The primary observation is that apart from the black colored sample, all samples show a similar IAM curve. Additionally, the IAM for all colored samples is below that of the reference sample.

Secondly, there is a relationship between IAM and the amount of specular reflections (see Section 4.1): For colors with higher specular reflections (blue, white, red), a higher IAM is measured compared to samples with few specular reflections.

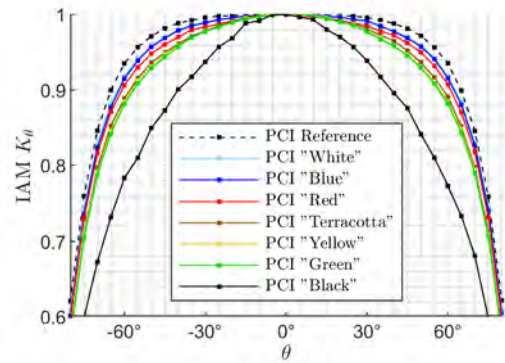


Figure 14: IAM for PCI samples

4.3.2 TFC Samples

The IAM of the TFC samples is shown in Figure 15. Due to the ARC, all samples show a high IAM compared to the other sample groups. Despite also having an ARC, the reference sample shows a significantly reduced IAM.

Differences in IAM between colors follow the sample groups shown in Section 4.1.2: The non-iridescent samples (gray, gold, bronze) show a higher IAM than the iridescent samples (blue, green, terracotta).

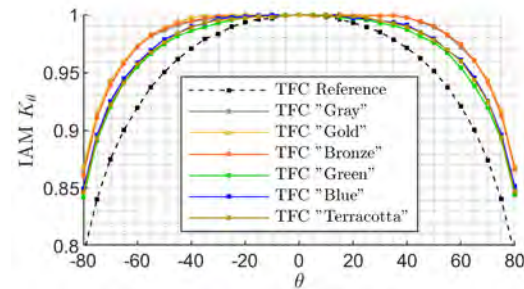


Figure 15: IAM for TFC samples

4.3.3 CIL Samples

IAM measurements of the CIL samples are shown in Figure 16. They present a generally lower IAM compared to other sample groups, with the red sample achieving a slightly higher IAM than the gray sample.

It can be observed that this lower IAM characteristic is mainly an effect of the textured glass, as evidenced when compared to the reference sample, which uses a flat glass.

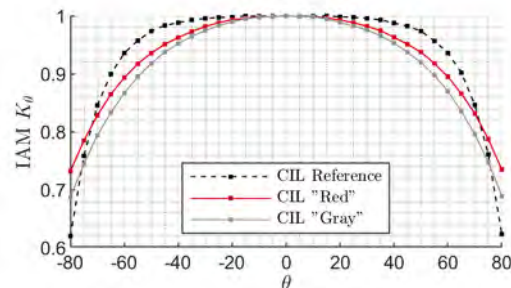


Figure 16: IAM for CIL samples.

4.4 Intercomparison

While the sample groups cannot be directly compared due to the differences in module structure, especially regarding the cover glass, a few trends can be identified:

Both PCI and TFC samples show increasing chroma and lightness around specular reflection angles ( $\alpha_x = \theta$ ),

while CIL samples show decreasing chroma and increasing lightness. It is believed that this is mostly due to the cover glass, showing irregular reflections.

Table I shows the average color saturation of different samples as well as its standard deviation. The PCI samples show the highest color saturations, while the TFC samples show the lowest. Conversely, PCI samples show low average lightness, resulting in saturated but dark colors.

**Table I:** Mean color saturation and standard deviation

Sample	$S_{uv}$	$\sigma$
PCI "White"	0.19	0.01
PCI "Yellow"	0.96	0.02
PCI "Terracotta"	1.18	0.05
PCI "Red"	1.9	0.31
PCI "Green"	1.03	0.08
PCI "Blue"	1.66	0.23
PCI "Black"	0.14	0.10
TFC "Terracotta"	0.26	0.20
TFC "Bronze"	0.30	0.20
TFC "Blue"	0.52	0.47
TFC "Gold"	0.27	0.19
TFC "Gray"	0.18	0.06
TFC "Green"	0.41	0.26
CIL "Gray"	0.09	0.05
CIL "Red"	0.66	0.40

## 5 OVERALL TRANSMISSION AND EFFICIENCY

IV-curve measurements of the colored samples in relation to their specific reference samples results in the relative short circuit currents and relative maximum power which are shown in Table II. Both give an indication of transmission losses caused by the coloring technology.

**Table II:** Performance parameters for PCI samples

Sample	rel. $I_{sc}$	rel. $P_{mpp}$
PCI "White"	68.4 %	69.4 %
PCI "Blue"	83.0 %	83.2 %
PCI "Red"	49.7 %	50.5 %
PCI "Terracotta"	57.5 %	58.6 %
PCI "Yellow"	63.6 %	64.6 %
PCI "Green"	66.5 %	67.6 %
PCI "Black"	11.0 %	10.5 %

PCI samples show high variations in short circuit currents. This is due to their different transmittance spectra, which are similar to the reflectance spectra shown in Figure 4, as coloration is achieved through light absorption.

**Table III:** Performance parameters for TFC samples

Sample	rel. $I_{sc}$	rel. $P_{mpp}$
TFC "Gray"	98.3 %	96.0 %
TFC "Gold"	94.4 %	94.9 %
TFC "Bronze"	93.9 %	94.0 %
TFC "Green"	96.5 %	96.3 %
TFC "Blue"	96.2 %	95.8 %
TFC "Terracotta"	96.4 %	96.3 %

TFC samples, on the other hand, show relatively low losses for all colors (see Table III), with the gray sample performing the best, followed by the iridescent samples (blue, green, terracotta) and the remaining non-iridescent samples. However, since the reference differs in anti-

reflective coating in respect to the colored samples, there is an uncertainty contribution on the accuracy of these absolute values and a future study will address this to confirm the trend presented here.

**Table IV:** Performance parameters for CIL samples

Sample	rel. $I_{sc}$	rel. $P_{mpp}$
CIL "Gray"	81.6 %	83.5 %
CIL "Red"	80.6 %	83.3 %

For the CIL samples, results for the relative short circuit current and relative maximum power, shown in Table IV, have values strongly influenced by the differences in glass between reference and colored samples, therefore contribution of coloring on the performance cannot be assessed for this particular case and warrants further investigation.

## 6 CONCLUSIONS

A methodology for characterizing the angular dependence of visual appearance of BIPV products has been presented. Measurements of the single-plane spectral BRDF of single cell BIPV devices has been performed allowing description of angular dependent color appearance using the CIELAB color space. Additionally, optical losses in electrical performance were studied performing IAM and IV curve measurements. Using this methodology, samples of three coloring technologies were measured.

Samples with printed ceramic ink show highest color constancy and saturation but also highest losses in short circuit current. Additionally, a clear correlation can be observed between specularly of reflection, IAM and angular constancy of appearance.

Samples with thin-film coatings show higher average efficiency with high angular dependency. For the blue, green and terracotta samples, iridescence is observable. Additionally, samples can be separated into two groups with similar IAM and angular dependency. This leads to the conclusion, that for thin film coatings, the choice of layer material, affecting the number of reflectance and transmittance peaks in the visible range, is of high importance for the angular dependency of both appearance and efficiency.

Samples with colored interlayers show intermediate color saturation and transmission losses. Contrary to the other technologies, these samples also show decreased color saturation at specular reflection angles due to the textured glass surface.

The presented methodology allows accurate determination of angular dependent sample color. Differences between coloration technologies and individual samples highlights the need for further research to obtain highly efficient BIPV coloration technologies.

As the individual coloration technologies could not be directly compared to each other, due to differences in sample structure, further measurements with new sample batches of more uniform composition will be performed. This should allow direct comparison of color saturation and thus coloration efficiency between technologies.

## 7 ACKNOWLEDGEMENTS

The authors would like to acknowledge the support

from EUDP by project 64019-0029 as part of their Energy Technology Development and Demonstration program.

## 8 REFERENCES

- [1] G. Eder, G. Peharz, R. Trattnig, P. Bonomo, E. Saretta, F. Frontini, C. S. P. López, H. R. Wilson, J. Eisenlohr, N. M. Chivelet, S. Karlsson, N. Jakica, A. Zanelli, Coloured BIPV: Market, Research and Development, International Energy Agency (2019)
- [2] G. Peharz, A. Ulm, Quantifying the influence of colors on the performance of c-si photovoltaic devices, *Renewable Energy* 129 (2018) 299–308
- [3] A. Røyset, T. Kolås, B. P. Jelle, Coloured building integrated photovoltaics: Influence on energy efficiency,”*Energy and Buildings* 208 (2020) 109
- [4] J. Halme, P. Mäkinen, Theoretical efficiency limits of ideal coloured opaque photovoltaics, *Energy & Environmental Science* 12 (2019) 1274–1285
- [5] S. R. Sandmeier, A. H. Strahler, BRDF Laboratory Measurements, *Remote Sensing Reviews* 18 (2000) 481-502
- [6] F. E. Nicodemus, Directional reflectance and emissivity of an opaque surface, *Applied Optics* 4 (1965) 767-775

# Vertical reflector for bifacial PV-panels

Michael Linde Jakobsen<sup>a</sup>, Sune Thorsteinsson<sup>\*,a</sup>, Peter Behrendorff Poulsen<sup>a</sup>, Peter Melchior Rødder<sup>b</sup> and Kristin Rødder<sup>b</sup>

<sup>a</sup> Department of Photonics Engineering, Technical University of Denmark, Frederiksborgvej 399, Building 130, 4000 Roskilde, Denmark, \*mlja@fotonik.dtu.dk, phone: +45 46774556

<sup>b</sup> SolarLab, Gunnar Clausens Vej 9, DK-8260 Viby J., Denmark

**Abstract** — Bifacial solar modules offer an interesting price/performance ratio, and much work has been focused on directing the ground albedo to the back of the solar cells. In this work we design and develop a reflector for a vertical bifacial panel, with the objective to optimize the energy harvest for the winter. Raytracing modelling is used to simulate the reflector, and initial simplified simulations indicates a significant gain in energy harvest that increase with increasing latitude for the winter. The simulations also show energy gain for the summer, however, not as significant as for the winter and the summer gain is almost independent of latitude.

## I. INTRODUCTION

Bifacial solar modules has in the recent years become an attractive commercially available newcomer to the solar industry, due to the fact that the energy performance of a bifacial cell in the right orientation increases the energy harvest significantly, while only providing an additional module cost of approximately 30 % [1]. Several works have proven that adding reflectors to bifacial panels mounted at a certain optimized tilt, increases the energy harvest even further [2]-[4], and bifacial panels has offered new solutions as e.g. PV based fences [5]. For PV-systems mounted at a tilt, the reflectors will in many cases be placed underneath the PV panel to reflect incident light from surroundings e.g. the albedo. Since these reflectors are not exposed to rain they do not have the same self-cleaning ability as the PV panels itself and the resulting energy harvest is decreased due to soiling [2], [4]. It has also been modeled that the use of bifacial PV panels in solar farms can reduce the needed storage for the power system, since the peak power times can be shifted closer to the power demand [6].

In this work we propose a system using a vertical mounted bifacial panel using vertical reflectors at an angle to both reduce the soiling problem, but also to optimize the energy harvest during winter, where there is shortage of solar energy. The reflector is optimized using raytracing modelling of the optical rays, where the details of the reflections at the optical interfaces are taken into consideration.

## II. REFLECTOR DESIGN AND RAY-TRACING

For this initial design a bifacial panel being one cell wide is used. A preliminary system design is shown in Fig. 1, which is comprised of a vertical bifacial panel which for simulation is oriented east west, and two reflector plates extending in angles

( $\delta$ ) of  $\geq 45$  deg. relative to the bifacial panel. The working principle is shown in Fig. 1. The design offers a tubular embodiment with a “hat” on top, which in combination with the vertical surfaces reduces the soiling of the system significantly. In a further development where the reflectors could be concentrating the sun, the tubular design can be optimized for efficient natural convection.

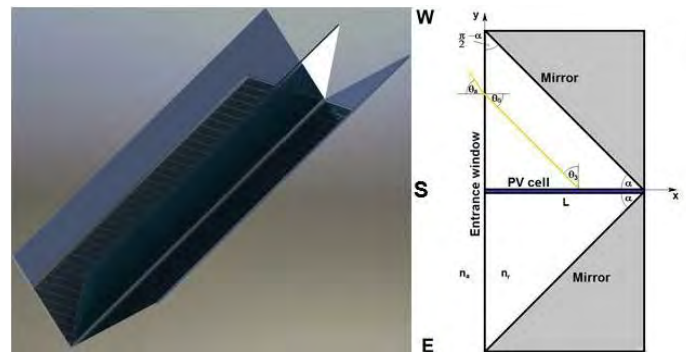


Fig. 1. Illustration of the reflector system.

The optical paths of the light incident on the retro-reflector are modelled with our Ray tracing model with the objective of winter optimization.

The volume inside the retroreflector is filled with a medium with a refractive index  $n_r$ , which optionally can be different from the refractive index ( $n_a$ ) of air. If  $n_r = n_a$  the model ignores the medium. In case  $n_r \approx n_a$  the medium is present in the model and it will encapsulate the retroreflector with a flat window (the entrance window to the retroreflector) opposing the top angle of the reflector, see Fig. 1.

The optical paths of the light incident on the retro-reflector are modelled with our ray tracing model.

The PV-module is a glass-glass module, with EVA as encapsulant. In case we select  $n_r = 1.5$  (the refractive index of glass) for the medium inside the retroreflector the interface to this laminate vanish and in that case we assume that the PV cells absorb all the incoming light – independent of its angular incidence. This allows us to consider only three paths of the incoming light, and these are illustrated in Fig. 2.

1. Refraction at the entrance window and then propagation to the PV-cell.
2. Refraction at the entrance window, then propagation to the mirror, where reflection occurs and then propagation to the PV-cell.
3. Refraction at the entrance window, then propagation to the mirror, where reflection occurs, then propagation to the entrance window, where refraction and reflection occurs and the reflected part propagates to the PV-cell.

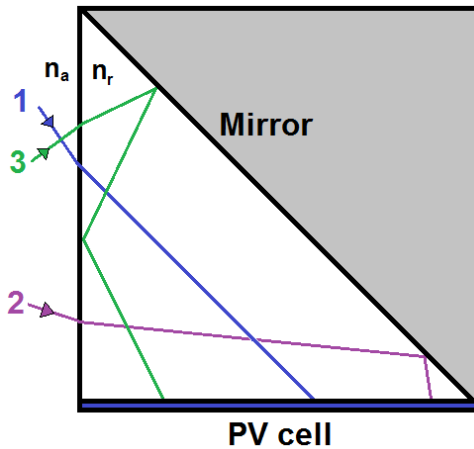


Fig. 2. Relevant paths in one half of the retroreflector, when assuming that the PV cell absorbs all light.

In case we select  $n_r = 1.0$  for the medium inside the retroreflector the interface to the PV laminate will be dealt with as a dielectric interface, and the Fresnel equations are used. When the ray intersects with a mirror interface we use a reflection coefficient of 95%, as an average value for the reflection coefficient of alumina throughout the spectral range of c-Si. The solar elevation ( $\rho$ ) is determined from the local latitude ( $\mu$ ), the declination of the sun ( $\gamma$ ) and the azimuth angle ( $\tau$ ) of the sun relative to the local true south:

$$\rho \cong \sin^{-1} \sqrt{\sin^2 \mu \sin^2 \gamma + \cos \mu \cos \gamma \cos \tau} \quad (1)$$

The schematic illustrates the model of the vertical retroreflector, and its orientation relative to earth. At the moment, the model does not include the diffuse solar contribution as well as optical absorption in the medium inside the retroreflector. This preliminary model does not include variations in sun intensity but considers only the projection of the AM 1.5 spectrum and resulting scattering due to the Fresnel equations.

### III. RESULTS

As a reference to our simulations on the retroreflector, the light incident on vertical mono-facial panel of the same size

facing south is simulated, calculating the sun path for the specific latitude. The integral of the irradiance curve is then used as reference. An example of a reference curve is shown in Fig. 3.

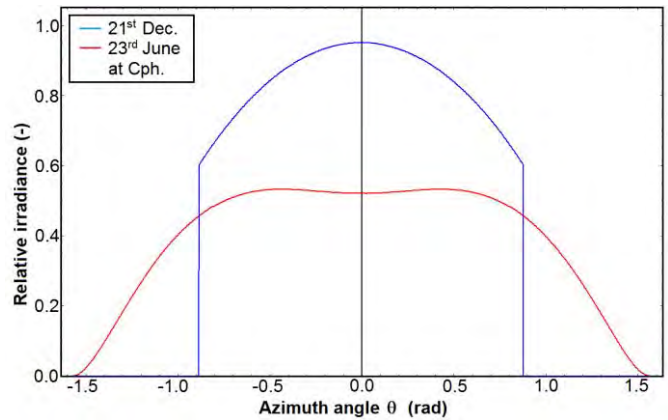


Fig. 3. The simulated relative irradiance for the reference case located in Copenhagen.

The small decrease at noon for the summer is owing to the sun height, and the vertical mounted panel, and the sharp winter cut-off is due to the fact that only the projection of the direct sunlight is considered. Four cities placed at different latitudes and very similar longitudes are chosen to for the simulations: Trondheim (Norway latitude 63.5°N), Copenhagen (Denmark lat. 55.7°N), Munich (Germany lat. 48.1°N) and Rome (Italy lat. 41.9°N). The shortest and the longest days of the year are simulated and the relative irradiances as a function of azimuthal angle are used to normalize for the energy harvest.

The retroreflector is simulated with the reflector volume containing air ( $n_r=1$ ), and the glass laminate on the PV-cell reflects light according to Fresnel's equations.

A plot of the relative irradiance from East to South, is shown in Fig. 3 for the longest day of the year. In these simulations the irradiation is symmetrically around 0°, since clear sky days are modelled, and the modules bifaciality is ignored (bifaciality is the ratio of the modules front side and back side efficiency, which in most cases differs slightly). The plot in Fig. 4 illustrates the different contributions from the optical paths present in the retroreflector.

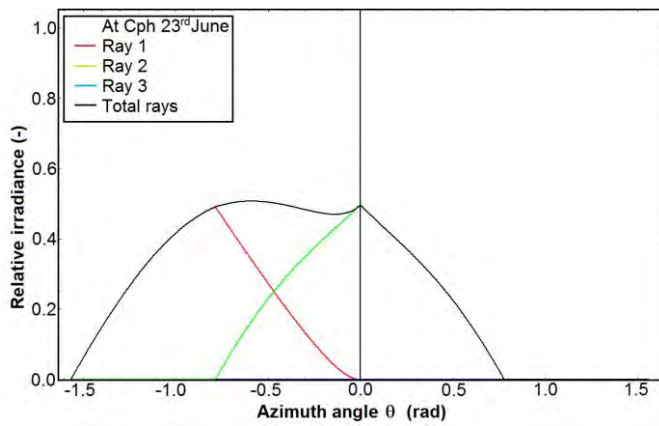


Fig. 4. The simulated relative irradiance for the upper half of the bifacial PV-cell with the retroreflector

The red curve is the light incidence directly onto the PV-cells (1). The green curve illustrates light, being reflected in the retroreflector before it hits the PV-cells (2). The third option is not present for  $n_r = n_a$ . The total irradiance for the entire retroreflector is plotted in Fig. 5 for Copenhagen with a  $n$  index matched medium.

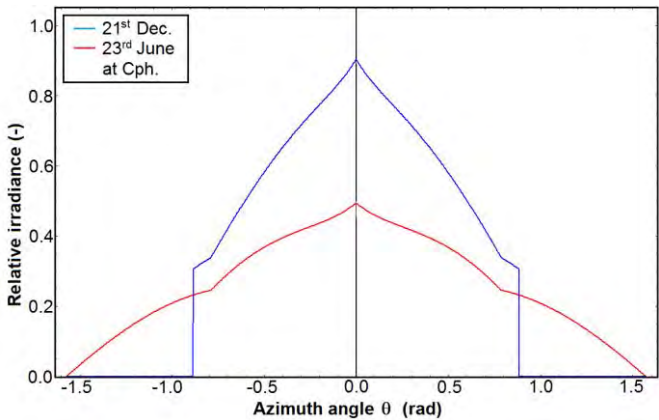


Fig.5. The simulated relative irradiance for the upper half of the bifacial PV-cell with a retroreflector filled with a medium with a refractive index of 1.5.

Table 1 shows the energy gain for the longest and the shortest day at the chosen locations compared to the mono-facial south oriented reference. Since all simulations are normalized the same area, being the area of the reference setup at normal incidence, the non-concentrating retro reflector can give a maximum energy gain of 2. Our intensions are to design a reflector that can deliver an energy output at a value as close to two as possible.

TABLE I.  
IMPROVEMENT COMPARED TO MONO-FACIAL REFERENCE.

Place	Latitude	Improvement December	Improvement June
Trondheim	63.5	1.68	1.36
Copenhagen	55.7	1.45	1.35
Munich	48.1	1.39	1.33
Rome	41.9	1.38	1.35

#### IV. DISCUSSION

Initial simulations, have shown that the retroreflector increases the energy output on a winter day by 30 – 70% relative to our reference setup, and a constant gain of approximately 35 % for the summer, almost independent of latitude. The improvement could be extended further by inserting an index matched medium discussed above, inside the retroreflector, however due to the long optical path optical absorption needs to be considered.

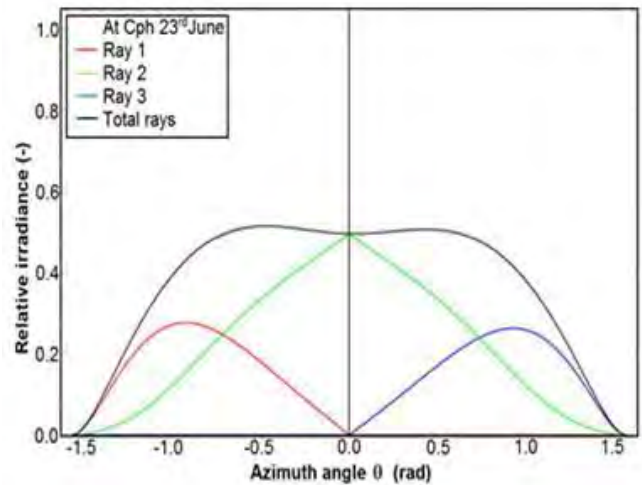


Fig 6. The simulated relative irradiance for the upper half of the bifacial PV-cell with a retroreflector filled with a medium with a refractive index of 1.5.

Fig 6 illustrates that the third optical path appears as a significant contribution approximately 33% to the total irradiance for the longest day, and the relative contribution depends on the latitude. In the four cases listed in Table 1 the gain is highest at the highest latitude, however this figure might change once diffuse meteorological irradiation data is used.

#### V. SUMMARY AND FUTURE WORK

An optical model for the retroreflector has been created based on raytracing. Initial simulations, have shown that the retro reflector increases the energy output on a winter day by 30 – 70% relative to the reference setup and is strongly

increasing with latitude. The next steps are to field test a reflector model at our Copenhagen based laboratory and advance the model with diffuse contribution and meteorological irradiation data.

#### REFERENCES

- [1] G. João, "Testing bifacial PV cells in symmetric and asymmetric concentrating CPC collectors," *Engineering*, vol. 05, no. 01, pp. 185–190, 2013.
- [2] A. Moehlecke, F. S. Febras, and I. Zanesco, "Electrical performance analysis of PV modules with bifacial silicon solar cells and white diffuse reflector," *Sol. Energy*, vol. 96, pp. 253–262, 2013.
- [3] G. E. Ahmad and H. M. S. Hussein, "Comparative study of PV modules with and without a tilted plane reflector," *Energy Convers. Manag.*, vol. 42, no. 11, pp. 1327–1333, 2001.
- [4] A. Luque, E. Lorenzo, G. Sala, and S. López-Romero, "Diffusing reflectors for bifacial photovoltaic panels," *Sol. Cells*, vol. 13, no. 3, pp. 277–292, 1985.
- [5] R. J. Magasrevy, "Bifacial efficiency at monofacial cost Building Integrated photovoltaic Energy Solutions for the World," p. 25, 2007.
- [6] S. Obara, D. Konno, Y. Utsugi, and J. Morel, "Analysis of output power and capacity reduction in electrical storage facilities by peak shift control of PV system with bifacial modules," *Appl. Energy*, vol. 128, pp. 35–48, 2014.

## RAY TRACING MODELLING OF REFLECTOR FOR VERTICAL BIFACIAL PANEL

Michael Linde Jakobsen<sup>a</sup>, Sune Thorsteinsson<sup>a\*</sup>, Peter Behrendorff Poulsen<sup>a</sup>, Peter Melchior Rødder<sup>b</sup>, Kristin Rødder<sup>b</sup>

<sup>a</sup>Department of Photonics Engineering, Technical University of Denmark, Frederiksborgvej 399, Building 130, 4000 Roskilde, Denmark,

<sup>b</sup>SolarLab, Gunnar Clausens Vej 9, DK-8260 Viby J, Denmark

\*Phone: +45 46774521, E-mail: sunth@fotonik.dtu.dk

**ABSTRACT:** Bifacial solar panels have recently become a new attractive building block for PV systems. In this work we propose a reflector system for a vertical bifacial panel, and use ray tracing modelling to model the performance. Particularly, we investigate the impact of the reflector volume being filled with a refractive medium, and shows the refractive medium improves the reflector performance since it directs almost all the light incident on the incoming plane into the PV panel.

**Keywords:** Solar cells, Ray tracing, PV applications, Reflector, Energy systems

## 1 INTRODUCTION

Bifacial solar modules offers in the right orientation a significantly improved energy harvest, while only providing an additional cost of 30 % [1], and these are now an attractive commercially available building block that allows for innovative concepts where both side of the PV-panel can be utilized. Several works have proven that adding reflectors to bifacial panels mounted at a certain optimized tilt, increases the energy harvest even further [2]-[3], and bifacial panels has offered new solutions as e.g. PV based fences [4]. For PV-systems mounted at a tilt, the reflectors will in many cases be placed underneath the PV panel to reflect incident light from surroundings e.g. the albedo. Since these reflectors are not exposed to rain they do not have the same self-cleaning ability as the PV panels itself and the resulting energy harvest is decreased due to soiling [2], [4]. It has also been modeled that the use of bifacial PV panels in solar farms can reduce the needed storage for the power system, since the peak power times can be shifted closer to the power demand [5].

In this work we propose a system using a vertical mounted bifacial panel equipped vertical reflectors at an angle to both reduce the soiling problem, but also to optimize the energy harvest. Here we particularly consider the impact of a refractive medium inside the reflector volume. The reflector is optimized using raytracing modelling of the optical rays, where the details of the reflections at the optical interfaces are taken into consideration.

## 2 THEORY AND MODEL

### 2.1 Theory

Two types of optical losses are modelled within this work:

- Fresnel losses, which are optical losses at interfaces between dielectric media, having different refractive indices.
- Material absorption losses, which are losses owing to the absorption in the bulk material and at metallic surface.

The Fresnel losses are determined by using the Fresnel equations, and here the reflection losses at an optical interface are calculated, and within this work averaging

the transverse electric (TE) and transverse magnetic (TM) polarization reflection coefficients. Material absorption losses occur either due to absorption, when light propagates inside a transparent dielectric material, or due to absorption, when light is reflected at a metallic surface.

### 2.2 Model

Initially, a design according to Figure 1 is used for the raytracing model, and in the first design the mirrors are plane surfaces and thus provide no concentration of the sunlight. The system is comprised of a vertical bifacial panel which for simulation purposes is oriented east-west, and two reflector plates extending in angles ( $\alpha = \pm 45$  deg.) relative to the bifacial panel (a picture of a prototype is shown in Figure 2).

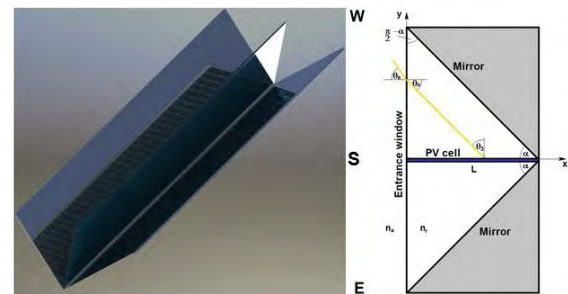


**Figure 1:** Rendering (left) and illustration (right) of the reflector system.

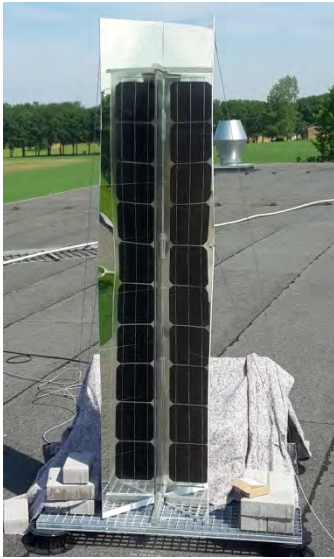


**Figure 2:** Prototype of the reflector.

Ray tracing, where many optical rays are modelled and finally the weighted output is integrated, are performed on this system. The volume inside the reflector can be bulk and thus be filled with a medium with refractive index  $n_r$ . The medium can be index matched to that of glass, where the Fresnel losses at the surface of the PV-module will be eliminated, or it can be air, removing the optical interface at the entrance window or any other transparent material.

We assume that all light incident into the PV cell and its laminate of glass is absorbed. This allows us to consider only three paths of the incoming light, and these are illustrated in Figure 3. This allows us to omit surface reflections at the PV-module and to omit the optical paths derived from these reflections, which in fact are insignificant.

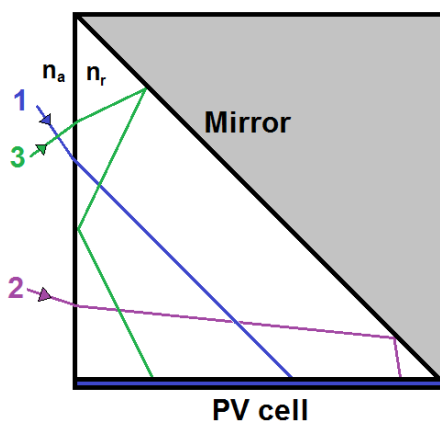


**Figure 3:** Relevant paths in one half of the retroreflector, when assuming that the PV cell and its glass laminate absorb all light.

The paths are:

1. Refraction at the entrance window and then propagation to the PV-module where refraction occurs again - *the direct path*.
2. Refraction at the entrance window, then propagation to the mirror, where reflection occurs and then propagation to the PV-cell, where refraction occurs again - *the reflected path*.

3. Refraction at the entrance window, then propagation to the mirror, where reflection occurs, then propagation to the entrance window, where refraction and reflection occurs and the reflected part propagates to the PV-cell, where refraction occurs again - *the back multiple reflected path*.

When the ray intersects with a mirror interface we use a reflection coefficient of 95%, as an average value for the reflection coefficient of alumina throughout the spectral range of c-Si. The solar elevation ( $\psi$ ) is determined from the local latitude ( $\varphi$ ), the declination of the sun ( $\delta$ ) and the azimuth angle ( $\theta$ ) of the sun relative to the local true south:

$$\psi = \sin^{-1}[\sin \varphi \sin \delta + \cos \varphi \cos \delta \cos \theta] \quad (1)$$

The schematic of Figure 1 illustrates the model of the vertical retroreflector, and its orientation relative to earth. At the moment, the model does not include the diffuse solar contribution. The preliminary model does not include variations in sun intensity but considers only the projection of the AM 1.5 spectrum and resulting scattering due to the Fresnel equations.

### 3 RESULTS

Four cities placed at different latitudes and very similar longitudes are chosen for the simulations: Trondheim (Norway latitude 63.5°N), Copenhagen (Denmark lat. 55.7 °N), Munich (Germany lat. 48.1 °N) and Rome (Italy lat. 41.9 °N). The shortest and the longest days of the year are simulated and the relative irradiances as a function of azimuthal angle are used to normalize for the energy harvest.

As reference for the simulations, a monofacial panel facing south with the same area as a single side of a bifacial panel, is used. A reference scenario is calculated for each position. An example of a reference simulation is shown in Figure 4.

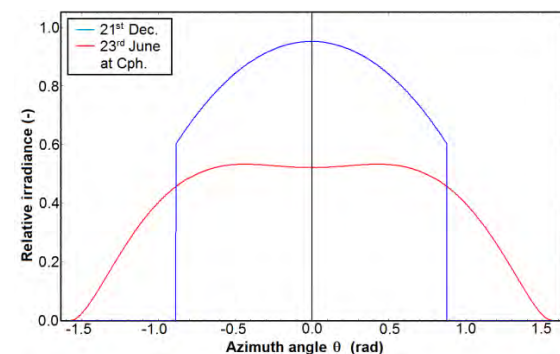


**Figure 4:** Reference simulation for Copenhagen.

In Figure 5 and Figure 6, two reflectors located in Copenhagen have been simulated. Figure 5 plots the simulation of a reflector filled with air ( $n_r = 1.0$ ), Figure 6 plots the simulation for a reflector filled with acrylic ( $n_r = 1.49$ ). The contributions from the three different ray paths are illustrated in Figure 5 and Figure 6 with three different colors. The bulk optical absorption losses are omitted. As can be seen, the 3. ray path contributes significantly to the total light flux. The index matched reflector improves the energy harvest by 32%, when bulk

losses are neglected.

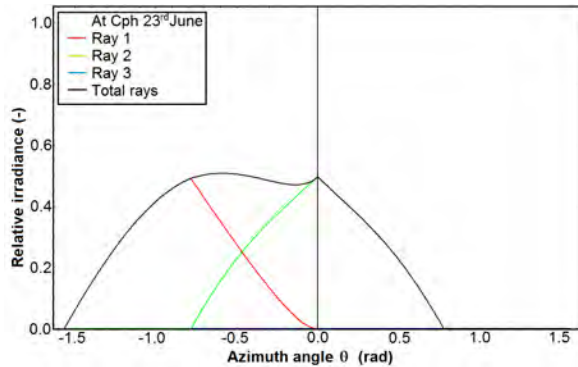


Figure 5: Ray contributions for a reflector filled with air.

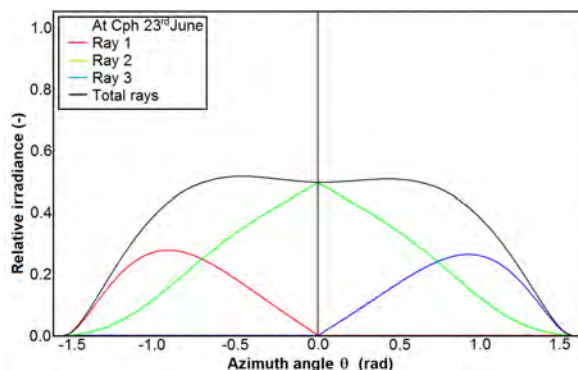


Figure 6: Ray contributions for a reflector filled with acrylic.

The impact of optical absorption and non-ideal mirrors are considered in the following. As it can be seen from table I, going from ideal glass to an acrylic filled reflector and with mirrors with a reflection coefficient of 95 % the power output is reduced by approximately 5 %, and hence fairly optimal materials give acceptable performance.

Table I: Influence of non-idealities

Material	Reflection	Absorption	Loss
Ideal	100 %	0	0 %
BK 7	95 %	0.3151	3.9 %
Acrylic	95 %	0.115	4.9 %

In table II simulations comparing the energy harvest on the longest day and the shortest day of the year at four different latitudes are shown. Bulk optical absorption in the acrylic material is taken into account and the mirrors are assumed to reflect 95 % of the light.

Table II. Simulation for 4 different latitudes, comparing energy harvest with an air filled reflector with an acrylic filled reflector.

Location	Latt.	Improvement			
		December		June	
		Air	Acrylic	Air	Acrylic
Trondheim	63.5	1.61	1.91	1.36	1.92
Copenhagen	55.7	1.45	1.91	1.35	1.92
München	48.1	1.39	1.91	1.33	1.92
Rome	41.9	1.38	1.92	1.35	1.92

It can be seen that the air filled reflector is performing significantly worse compared to the acrylic

filled reflector and the performance of the air based is strongly dependent on the location and the time of year – i.e. the solar angles.

#### 4 DISCUSSION

The results from table II (visualized in Figure 5 and Figure 6), shows that for this initial reflector design (filled with air) that approximately 30 % of the light entering the reflector is lost when reflected back out through the entrance window. Table I shows, that that low optical absorption and good reflectance gives the best performance, however good performance can be achieved with less than the best performing materials.

#### 5 CONCLUSION AND FUTURE WORK

In this work we have proposed an energy system using a vertical bifacial PV-panel with a reflector system that captures almost all the light incident on the entrance window. The reflector volume has to be filled up with a medium with a refractive index matched to that of glass and with low optical bulk absorption. Future work includes testing the fabricated prototype to validate the model, upgrading the model to take diffuse light into account, and use simulations based on real weather data. Further developments include a new reflector design which will direct the reflected light propagating back out through the entrance window into the PV-panel and thereby omitting the need for the air gap being filled with an index matched material.

#### 6 REFERENCES

- [1] G. João, “Testing bifacial PV cells in symmetric and asymmetric concentrating CPC collectors,” *Engineering*, vol. 05, no. 01, pp. 185–190, 2013.
- [2] A. Moehlecke, F. S. Febras, and I. Zanesco, “Electrical performance analysis of PV modules with bifacial silicon solar cells and white diffuse reflector,” *Sol. Energy*, vol. 96, pp. 253–262, 2013.
- [3] A. Luque, E. Lorenzo, G. Sala, and S. López-Romero, “Diffusing reflectors for bifacial photovoltaic panels,” *Sol. Cells*, vol. 13, no. 3, pp. 277–292, 1985.
- [4] R. J. Magasrevy, “Bifacial efficiency at monofacial cost Building Integrated photovoltaic Energy Solutions for the World,” p. 25, 2007.
- [5] S. Obara, D. Konno, Y. Utsugi, and J. Morel, “Analysis of output power and capacity reduction in electrical storage facilities by peak shift control of PV system with bifacial modules,” *Appl. Energy*, vol. 128, pp. 35–48, 2014.



## Bifacial PV cell with reflector for stand-alone mast for sensor powering purposes

**Jakobsen, Michael Linde; Thorsteinsson, Sune; Poulsen, Peter Behrendorff; Riedel, Nicholas; Rødder, Peter M.; Rødder, Kristin**

*Published in:*  
Aip Conference Proceedings

*Link to article, DOI:*  
[10.1063/1.5001437](https://doi.org/10.1063/1.5001437)

*Publication date:*  
2017

*Document Version*  
Publisher's PDF, also known as Version of record

[Link back to DTU Orbit](#)

*Citation (APA):*  
Jakobsen, M. L., Thorsteinsson, S., Poulsen, P. B., Riedel, N., Rødder, P. M., & Rødder, K. (2017). Bifacial PV cell with reflector for stand-alone mast for sensor powering purposes. *Aip Conference Proceedings*, 1881, [070004]. <https://doi.org/10.1063/1.5001437>

---

### General rights

Copyright and moral rights for the publications made accessible in the public portal are retained by the authors and/or other copyright owners and it is a condition of accessing publications that users recognise and abide by the legal requirements associated with these rights.

- Users may download and print one copy of any publication from the public portal for the purpose of private study or research.
- You may not further distribute the material or use it for any profit-making activity or commercial gain
- You may freely distribute the URL identifying the publication in the public portal

If you believe that this document breaches copyright please contact us providing details, and we will remove access to the work immediately and investigate your claim.

## Bifacial PV cell with reflector for stand-alone mast for sensor powering purposes

Michael L. Jakobsen, Sune Thorsteinsson, Peter B. Poulsen, N. Riedel, Peter M. Rødder, and Kristin Rødder

Citation: [AIP Conference Proceedings](#) **1881**, 070004 (2017); doi: 10.1063/1.5001437

View online: <http://dx.doi.org/10.1063/1.5001437>

View Table of Contents: <http://aip.scitation.org/toc/apc/1881/1>

Published by the [American Institute of Physics](#)

---

### Articles you may be interested in

[TwinFocus<sup>®</sup> CPV system](#)

AIP Conference Proceedings **1881**, 030006 (2017); 10.1063/1.5001417

[Spectrally-resolved optical efficiency using a multi-junction cell as light sensor: Application cases](#)

AIP Conference Proceedings **1881**, 030011 (2017); 10.1063/1.5001422

[Impact of the atmospheric conditions to the bandgap engineering of multi-junction cells for optimization of the annual energy yield of CPV](#)

AIP Conference Proceedings **1881**, 070002 (2017); 10.1063/1.5001435

[Many-junction photovoltaic device performance under non-uniform high-concentration illumination](#)

AIP Conference Proceedings **1881**, 070005 (2017); 10.1063/1.5001438

[Is it CPV? Yes, but it is a partial CPV](#)

AIP Conference Proceedings **1881**, 080001 (2017); 10.1063/1.5001439

[A review of the promises and challenges of micro-concentrator photovoltaics](#)

AIP Conference Proceedings **1881**, 080003 (2017); 10.1063/1.5001441

---



**SUMMER SALE!**

**30% OFF**  
**ALL PRINT**  
**PROCEEDINGS!**

**AIP** | Conference Proceedings

ENTER COUPON CODE  
SUMMER2017

# Bifacial PV Cell with Reflector for Stand-alone Mast for Sensor Powering Purposes

Michael L. Jakobsen<sup>1, c)</sup>, Sune Thorsteinsson<sup>1, b)</sup>, Peter B. Poulsen<sup>1, a)</sup>, N. Riedel<sup>1</sup>,  
Peter M. Rødder<sup>2</sup> and Kristin Rødder<sup>2</sup>

<sup>1</sup> *Department of Photonics Engineering, Technical University of Denmark, mlja@fotonik.dtu.dk, Roskilde, Denmark.*

<sup>2</sup> *SolarLab, pmr@solarlab.dk, Viby J., Denmark.*

<sup>a)</sup>Corresponding author: ppou@fotonik.dtu.dk

<sup>b)</sup>sunth@fotonik.dtu.dk

<sup>c)</sup>mlja@fotonik.dtu.dk

**Abstract.** Reflectors to bifacial PV-cells are simulated and prototyped in this work. The aim is to optimize the reflector to specific latitudes, and particularly northern latitudes. Specifically, by using minimum semiconductor area the reflector must be able to deliver the electrical power required at the condition of minimum solar travel above the horizon, worst weather condition etc. We will test a bifacial PV-module with a retroreflector, and compare the output with simulations combined with local solar data.

## INTRODUCTION

Bifacial solar modules are commercially attractive, due to the fact that the total energy producing area increases by a factor of two, and only to an additional module cost of approximately 30 %.<sup>1</sup> However, the challenge is to guide light onto both sides sufficiently efficient. Several works have proven that adding reflectors to bifacial panels mounted at a certain optimized tilt, increases the energy harvest even further,<sup>2-3</sup> and bifacial panels has offered new solutions as e.g. PV based fences.<sup>4</sup> For PV-systems mounted at a tilt, the reflectors will in many cases be placed underneath the PV panel to reflect incident light from surroundings e.g. the albedo. Since these reflectors are not exposed to rain they do not have the same self-cleaning ability as the PV panels itself and the resulting energy harvest is decreased due to soiling.<sup>2,4</sup>

Earlier, we have proposed a system, using a vertical mounted bifacial panel and two vertical reflectors<sup>5</sup> mounted at an angle to partly reduce the soiling problem, but also to optimize the energy harvest. The schematics is illustrated in figure 1. The investigation of this system has been based on raytracing with different assumptions to simplify the model. One of the assumptions is that the irradiance of sunlight incident onto a surface, being normal to the sun all day, is constant.

The conclusions on the following investigations were that the bifacial PV-cell, combined with a retroreflector, including a transparent filling material, could collect 96 % of all light, incident onto a plane surface with the same area as both sides of the bifacial PV-cell together.<sup>6</sup> With and without the filling the simulated amount of incident light is plotted in figure 2 as a function of azimuth angular position of the sun.

In this work, we will include experimental solar data to estimate a more realistic incidence of sunlight in our simulations to finalize our model, and to compare it with data from an experimental prototype (see figure 3). This will bring us to a discussion where we can compare this device with a bifacial PV-cell without a reflector.

## THE MODEL

The modelling starts by identifying the possible paths of rays, dependent on their initial position and angle. When all ray paths have been identified we focus on the relevant rays, which will be incident on the PV surface. The individual rays will be weighted by the different losses they experience on their path through the model. The angle of incidence and path for a given ray are important in order to calculate the Fresnel, absorption and reflection loss:

- Fresnel loss occurs when light travels through a flat interface between two dielectric media. Generally, the light beam will be divided into a refracted (transmitted) light beam and a reflected light beam without suffering any further losses. The transmission ( $T$ ) and reflection ( $R$ ) coefficients are listed below as functions of angle of incidence ( $\theta$ ), the refractive indexes of the first ( $n_1$ ) and second ( $n_2$ ) medium, respectively<sup>7</sup>:

$$T(\theta, n_1, n_2) = \begin{cases} \frac{\sin(2\theta) \sin\left(2 \sin^{-1}\left(\frac{n_1}{n_2} \sin(\theta)\right)\right)}{\sin^2\left(\theta + \sin^{-1}\left(\frac{n_1}{n_2} \sin(\theta)\right)\right) \cos^2\left(\theta - \sin^{-1}\left(\frac{n_1}{n_2} \sin(\theta)\right)\right)} & \text{for the TM polarization} \\ \frac{\sin(2\theta) \sin\left(2 \sin^{-1}\left(\frac{n_1}{n_2} \sin(\theta)\right)\right)}{\sin^2\left(\theta + \sin^{-1}\left(\frac{n_1}{n_2} \sin(\theta)\right)\right)} & \text{for the TE polarization} \end{cases} \quad (1)$$

$$R(\theta, n_1, n_2) = \begin{cases} \left[ \frac{\tan\left(\theta - \sin^{-1}\left(\frac{n_1}{n_2} \sin(\theta)\right)\right)}{\tan\left(\theta + \sin^{-1}\left(\frac{n_1}{n_2} \sin(\theta)\right)\right)} \right]^2 & \text{for the TM polarization} \\ \left[ \frac{\sin\left(\theta - \sin^{-1}\left(\frac{n_1}{n_2} \sin(\theta)\right)\right)}{\sin\left(\theta + \sin^{-1}\left(\frac{n_1}{n_2} \sin(\theta)\right)\right)} \right]^2 & \text{for the TE polarization} \end{cases} \quad (2)$$

- Material absorption losses are caused by bulk absorption in a material, which the light propagates through. The absorption coefficient  $\gamma$  is the material parameter, while  $A$  defines the relative intensity transmitted after a traveled distance in the material of  $L$ <sup>7</sup>:

$$A(L) = \exp(-\gamma L) \quad (3)$$

- Reflection at metallic surfaces. In principle, the Fresnel equations could describe these losses. However, the refractive index and the significant absorption for metals are often uncertain and difficult to establish. Therefore, the experimentally determined reflection coefficient for a polished metal surface will be used here, instead. We assume that the reflection coefficient is a constant, independent on the wavelength and angle of incidence.

In this case, the PV cell is laminated with a thin glass layer. Therefore, the Fresnel equations are used to determine the loss occurring as light enters the laminate. At first incidence we sum up the power of light transmitted into the glass and assume that all this light will be absorbed by the PV cell. For further pursue of the ray reflected of the glass laminate we also determine the power of the rays reflected after a direct incidence onto the glass laminate,

and can derive a simple angular dependence for their next incidence on the PV surface. In case that, their original incidence is more than 45 deg. relative to the normal of the PV surface they will all hit the PV cell again. Again, we assume that all the transmitted light is absorbed by the PV cell, and now that the second reflection will escape. In Eq.1 and Eq.2 we only consider interfaces, where light enters from air into glass, thus, the refractive indexes, used for air ( $n_a = 1.00$ ) and glass ( $n_g = 1.50$ ), can be substituted as  $n_a \rightarrow n_1$  and  $n_g \rightarrow n_2$ .

Material absorption losses occurring when light propagates inside a transparent dielectric material will be neglected ( $\gamma = 0$ ) here, because the glass laminate above the PV cells is thin ( $< 1$  mm). However, the reflection coefficients for the metallic surfaces are significant, and here they are set to 95% as it would be for enhanced alumina.

The design, used for the raytracing model, is illustrated in Fig.1(a) for a horizontal cross section. In this design the mirrors are plane surfaces and provide no concentration of the sunlight. The system is a vertical standing bifacial panel, which for simulation purposes is oriented east west. The two reflector plates are connected to the PV cell, and each spans an angle of  $\alpha = \pm 45$  deg. relative to the bifacial panel. In this work, the reflector only encapsulates half the length of the PV cell. The total length of the illustrated PV cell is  $2 L_p$ .

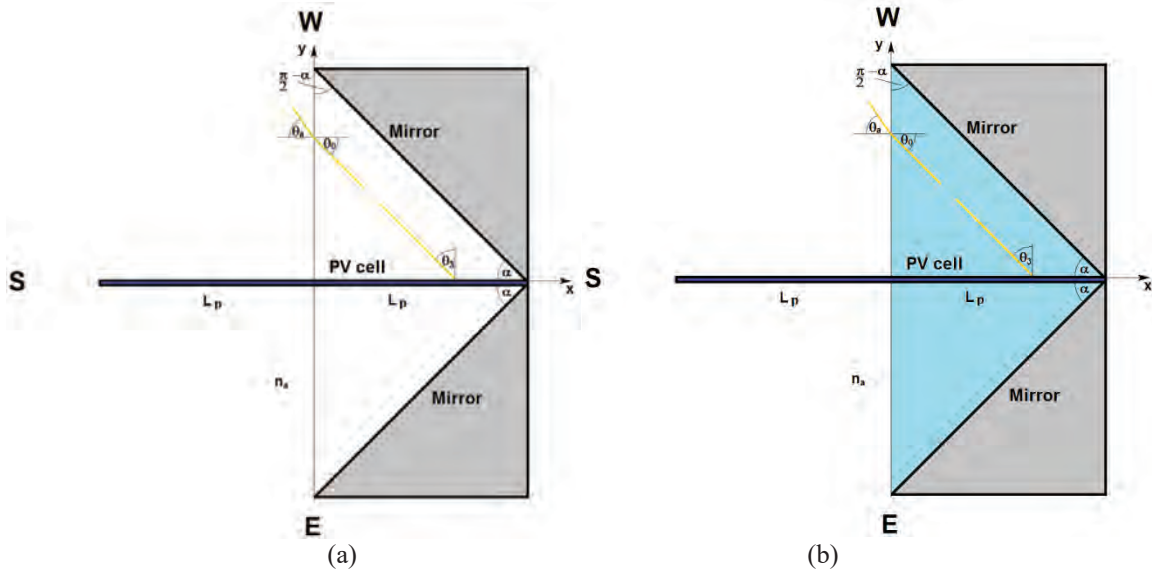


FIGURE 1. (a) Illustration of the current reflector system. (b) Illustration of an earlier reflector system.

Earlier designs (Fig.1(b)) had a bulk material (glass or plastic) inside the reflector, in order to capture light reflected by the reflector in an unfortunate direction, and thus leaving the retroreflector. The capture is achieved by internal reflection or even total internal reflection. However, in this case the volume inside the reflector consists of air only. The extension of the PV cell by the length of  $L_p$  away from the retroreflector means that all these escaping light rays are captured directly by the PV cell itself.

Using the model and its assumptions concerning the number of reflections described above, we only need to consider two paths of light entering the retroreflector:

1. Direct incidence onto the PV cell.
2. Reflection in the retroreflector and then incidence onto the PV-cell.

Similarly, the part of the PV cell sticking out from the retroreflector can be handled by two paths as well:

1. Direct incidence onto the PV cell from left.
2. Direct incidence onto the PV cell from the right.

Every time (max. 2) a ray is reflected by a alumina surface we use a reflection coefficient of 95%, as an average value for the reflection coefficient throughout the spectral range of c-Si. The solar elevation ( $\psi$ ) is determined from the local latitude ( $\phi$ ), the declination of the sun ( $\delta$ ) and the azimuth angle ( $\theta$ ) of the sun relative to the local true south:

$$\psi = \sin^{-1} [\sin \phi \sin \delta + \cos \phi \cos \delta \cos \theta] \quad (4)$$

The schematics of Fig.1 illustrate the models of the vertical retroreflector, and their orientation relative to earth poles. The model combines the ray tracing with solar irradiation data, obtained by a Si-photodetector, which tracks the sun across the sky, and discards the diffuse contribution.

## EXPERIMENTS

The solar irradiance is measured with the tracking solar measurement station illustrated in Fig.2. The tracking device maintains at all time normal incidence of the sun light onto the detector. Further, the solar station provides measurements of the diffuse optical contribution onto a horizontal surface (thermopile detector) as well as wind speed and temperature. The solar station is mounted above roof height to ensure no shadowing effects from the surroundings.



**FIGURE 2.** The tracking solar setup measures the normal incidence of light from the sun. The black sphere obstructs direct sunlight to a horizontal detector, which measures the diffuse light.

The prototype is illustrated in Fig.3. The prototype has a cross section which is very similar to the schematics drawn in Fig.1, see Fig.3(a). The height of the PV cell is 1.8 m, while its width and thickness is 0.16 m and 5 mm, respectively. The height of the reflector and the opening in the cabinet is 2 m in order to avoid shadowing effects near the top and bottom of the PV cell. The prototype is mounted at ground level (Fig.3(b)), and therefore, there will be shadowing effects from the surroundings. Specifically, a tree will provide shadow until midday. The data are obtained for direct comparison with our simulations.



**FIGURE 3.** (a) The prototyping setup of the bifacial PV cell with its retroreflector as illustrated in Fig.1. (b) The prototype is mounted on ground level.

The raw data from the systems are sampled with a sample rate of 0.1 S/s. Both, the solar data and the electrical current from the prototype are then low pass filtered with a current averaging algorithm with a flat kernel to an effective sample rate of 0.0042 S/s or approximately 1.0 S/deg. (azimuth angle).

## RESULTS

The latitude is set to  $55.676^\circ$  North, which corresponds to the latitude of Copenhagen. The shortest day (21/12), the longest day (23/6) of the year and the day of data acquisition (10/4) are simulated in our model. Preliminary, we assume that the radiance from the sun is constant during its travel across the sky. The simulations are plotted in Fig.4(a) as the normalized irradiances as a function of azimuthal angle (rad.).

As a reference for the simulations we simulate a bifacial panel facing east-west with the same area as PV cell in the retroreflector a well. Figure 4(b) illustrates the simulations for the bifacial panel.

In Table1 the relative integrated power from the individual curves in Fig.4(a) and Fig.4(b) are listed.

**TABLE 1.** The normalized power obtained in Fig.4 are integrated through a day and listed for the three dates.

System\Seasons	23 <sup>rd</sup> of June	10 <sup>th</sup> of April	21 <sup>st</sup> of Dec.
Bifacial with retroreflector	0.314	0.333	0.230
Bifacial with no reflector	0.424	0.347	0.102

Clearly, the bifacial PV without a reflector perform best during the summer time when the sun travels through a large azimuth angular interval. However, the bifacial PV cell with the retroreflector perform best during the winter periods where the sun travels through a short angular interval, and with low sun height.

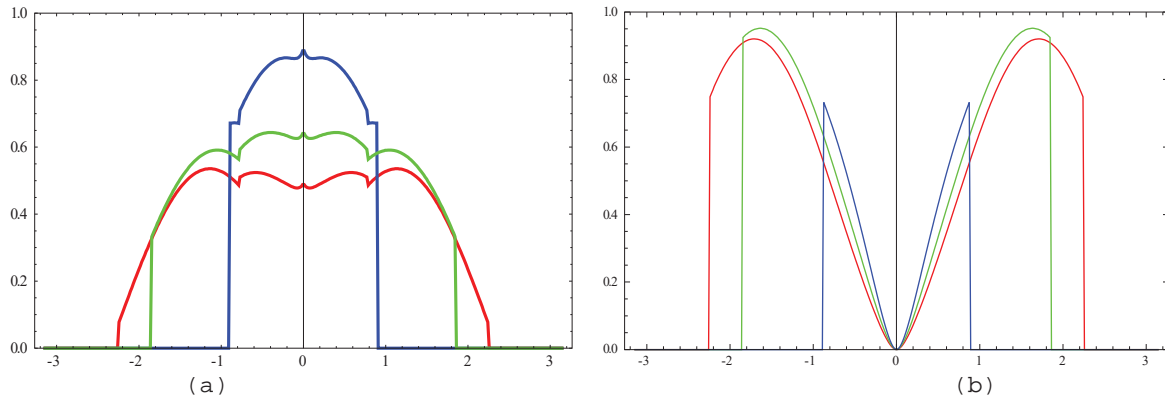


**FIGURE 4.** The simulations of the bifacial PV cell with the retroreflector (a) and the bifacial PV cell without the reflector (b) plotted versus azimuth angle (rad.). Latitude:  $55.676^\circ$  North, Dates: (red) 23/6, (green) 10/4 and (blue) 21/12.

In Fig.5(a) the direct solar irradiance at normal incidence is plotted as a function of azimuth angle. The data are obtained the 10 of April 2017 near Copenhagen. The sky is not entirely cloud free during the morning. However, during the afternoon we have a reasonably good measurement for comparison with the simulations. Diffuse light is eliminated in this measurement. The diffuse contribution to a detector mounted horizontally is plotted in Fig.5(b).

If we multiply the curve in Fig.5(a) with the simulation in Fig.4(a) we find the following simulation for the irradiance incident onto the bifacial PV cell with the retroreflector. The result is plotted it in Fig.6(a). In Fig.6(b) the simulated curve in Fig.4(b) of the reference PV is multiplied with the curve in Fig. 5(a) as well. The integrated power from the two systems for the entire day are  $56 \times 10^3$  and  $49 \times 10^3$  respectively. The ratio of these two power values indicating that the bare bifacial PV cell collects only 88% of the power collected by the bifacial PV cell with the reflector.

We have not included the diffuse light in the two curves in Fig.5 because, they are not horizontally mounted as the solar detector, which is responsible for this measurement. Secondly, that the two bifacial PV configurations have different opening angles for diffuse light.

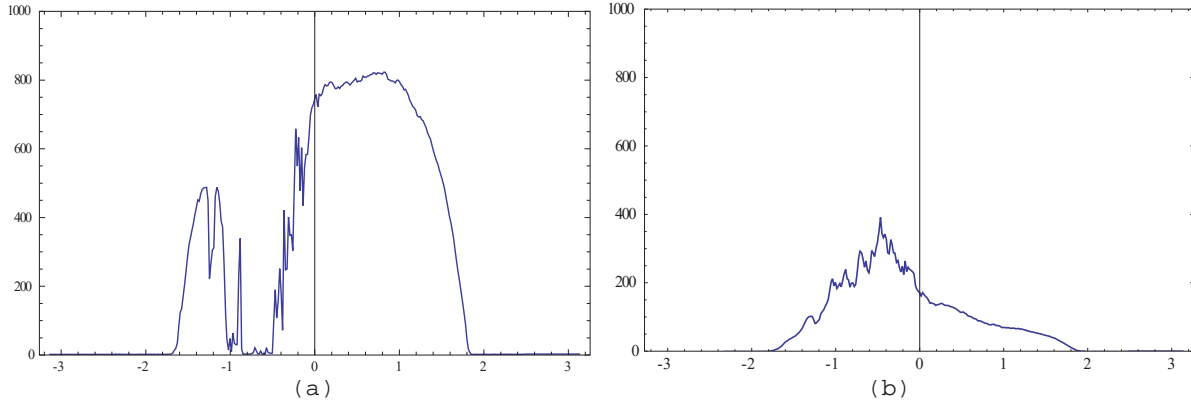


**FIGURE 5.** Solar data obtained near Copenhagen at the 10<sup>th</sup> April 2017 are plotted as a function of azimuth angle (rad.). (a) Illustrates the normal incident light from the sun only, while (b) illustrates the diffuse light contribution to a horizontal surface.

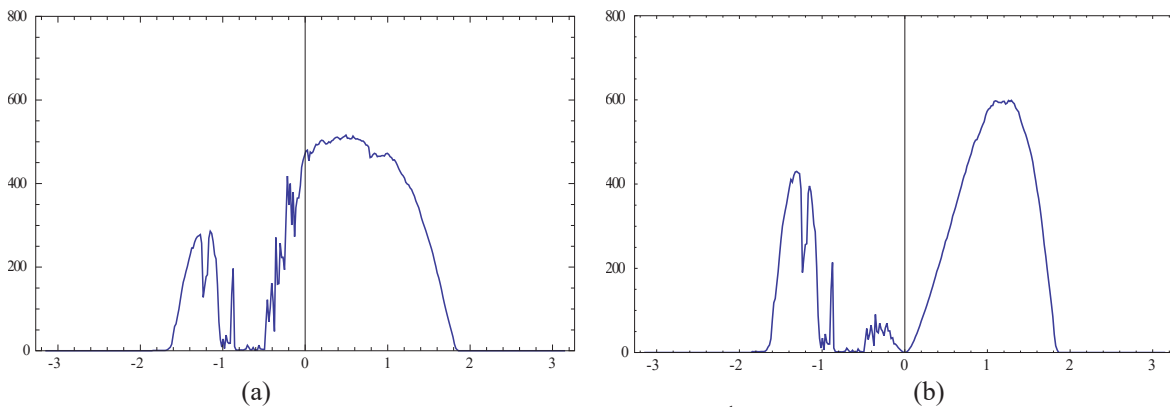


**FIGURE 6.** Simulations of solar power obtained near Copenhagen at the 10<sup>th</sup> April 2017 are plotted as a function of azimuth angle (rad.) for the prototype PV (a) and the reference PV (b) with no reflector.

In Fig.7(a) the measurement from the prototyping bifacial PV cell with retroreflector is plotted. These data are acquired simultaneously with the solar data. In Fig.7(b) the simulated curve including the solar light at normal incidence (Fig.5(b)) has been added half the amount of diffuse light as a simple approach to include the diffuse contribution from only half a hemisphere.

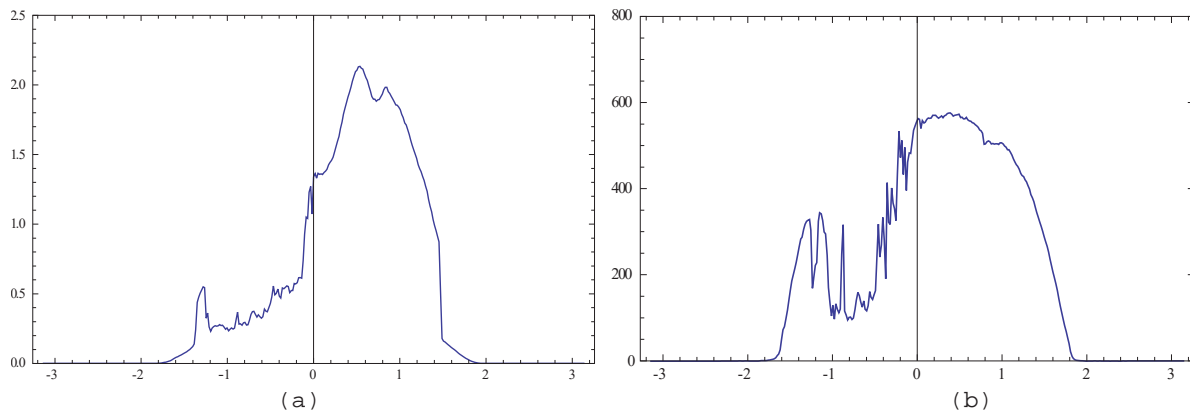


**FIGURE 7.** (a) Solar data obtained near Copenhagen at the 10<sup>th</sup> April 2017 by the prototyping bifacial PV cell with retroreflector is plotted as a function of azimuth angle (rad.) (b) The simulated irradiance including solar data for normal incidence and half the measured amount of diffuse light.

## DISCUSSION

The results in Table 1 indicates that by integrating the curves in Fig.4 the prototype and the reference PV provides the same total power for the acquisitions obtained at the 10<sup>th</sup> of April. However, the curves in Fig.6 provide different results for the prototype and the reference PV, which indicates that the reference PV only collects 88% of power collected by the prototype. This is likely to be caused by the attenuation in radiance near sunset, which severely affects the reference PV – compare Fig.4 with Fig.5.

The difference between the measured current produced by the prototype in Fig.7 and the simulated optical irradiance in Fig.6(a) could be caused by several issues. The model includes all rays, which experiences either none or a single reflection. In case of rays reflected of the laminated glass, we still ignore contributions, which are reflected by the reflector before reflection at the laminated glass. Additionally, in case of rays with direct incident on the laminated and at an angle of incidence smaller than 45 deg., few of these might also contribute to the photo current, but are not accounted for in this model.

Of experimental issues we have that the semiconductors do not fill out the PV cell entirely as it is assumed for the simulations. Minor variations in efficiency are expected for the different sub elements in the PV cell. Shadowing effects from trees or buildings have not been included in the model. Specifically, the drop in current, occurring in Fig.5(a) within the range of azimuth angle from -1.2 to -0.5, is caused by clouds on the sky, while the lack of current within the azimuth angular range from -1.6 to -0.2 is caused by the shadowing effect of a nearby tree. Therefore, Fig.7(a) and Fig.7(b) should be compared only for the positive angular range. At the moment we do not have a model to including the diffuse light properly in our simulation. However, by simply adding half the measured diffuse irradiation the observed drop in irradiance (Fig.7(b)) in the interval between -0.8 rad. to -0.6 rad. seems reasonable compare with the measured current Fig.7(a).

## CONCLUSION AND FUTURE WORK

In this work we have completed our simulation by combining the raytracing model with real solar data. Clearly, the simulations conclude that the reflector can have a strong influence on the application of the PV cell. As Table1 illustrates it, the reflector tested with the prototype here has its clear advantages on a Northern latitude compare to the bare bifacial PV cell. Additionally, we have processed our first power measurement from the prototype and compared them with our simulations.

## ACKNOWLEDGMENTS

The project is funded by the Danish Energy Technology Development and Demonstration Programme, project number 64014-0508 “SENSORPOWER – Bifacial PV Energy Reflector Tower”.

## REFERENCES

1. G. João, “Testing bifacial PV cells in symmetric and asymmetric concentrating CPC collectors,” *Engineering*, vol. 05, no. 01, pp. 185–190, 2013.
2. A. Moehlecke, F. S. Febras, and I. Zanesco, “Electrical performance analysis of PV modules with bifacial silicon solar cells and white diffuse reflector,” *Sol. Energy*, vol. 96, pp. 253–262, 2013.
3. A. Luque, E. Lorenzo, G. Sala, and S. López-Romero, “Diffusing reflectors for bifacial photovoltaic panels,” *Sol. Cells*, vol. 13, no. 3, pp. 277–292, 1985.
4. R. J. Magasrevy, “Bifacial efficiency at monofacial cost Building Integrated photovoltaic Energy Solutions for the World,” p. 25, 2007.
5. S. Thorsteinsson, M. L. Jakobsen, P. B. Poulsen, P. M. Rødder and K. Rødder, “Vertical reflector for bifacial PV-panels“, part of: IEEE 43rd Photovoltaic Specialist Conference 2016 (ISBN: 9781509027248), pages: 2678-2681, 2016, IEEE.D. L. Davids, “Recovery effects in binary aluminum alloys,” Ph.D. thesis, Harvard University, 1998.
6. M. L. Jakobsen, S. Thorsteinsson, P. B. Poulsen, P. M. Rødder and K. Rødder, “Ray Tracing modelling of a reflector for a vertical bifacial panel“, part of: Proceedings of the 2016 European Photovoltaic Solar Energy Conference and Exhibition 2016, 2016.
7. M. Born and E. Wolf, “*Principles of Optics*” (Pergamon Press, Oxford, 1980).

## PV LED ENGINE CHARACTERIZATION LAB FOR STANDALONE LIGHT TO LIGHT SYSTEMS

Sune Thorsteinsson<sup>1</sup>, Peter Behrendorff Poulsen<sup>1</sup>, Johannes Lindén<sup>1</sup>, Søren Stentoft Hansen<sup>1</sup>, Carsten Dam Hansen<sup>1</sup>, Maria del Carmen Mira Albert<sup>2</sup>, Arnold Knott<sup>2</sup> and Poul Norby<sup>3</sup>

<sup>1</sup>Department of Photonics Engineering, Technical University of Denmark, Roskilde, Denmark, (sunth@fotonik.dtu.dk)

<sup>2</sup>Department of Electrical Engineering, Technical University of Denmark, Lyngby, Denmark

<sup>3</sup>Department of Energy Conversion and Storage, Technical University of Denmark, Roskilde, Denmark

**ABSTRACT:** PV-powered lighting systems, light-to-light systems (L2L), offer outdoor lighting where it is elsewhere cumbersome to enable lighting. Application of these systems at high latitudes, where the difference in day length between summer and winter is large and the solar energy is low requires smart dimming functions for reliable lighting. In this work we have built a laboratory to characterize these systems up to 200 Wp from “nose to tail” in great details to support improvement of the systems and to make accurate field performance predictions.

**Keywords:** Solar cells, PV applications, Characterization, Energy Systems

### 1 INTRODUCTION

Light-to-light systems are typically solar powered stand-alone lamps using LEDs as light source. Park lights and bollards are examples of L2L systems and these systems offers lighting solutions, for places where lighting is not feasible due to very high cabling costs of e.g. 700 €/m in Copenhagen. At low latitudes dimensioning of such products is relatively easy, since there is plenty of sun and the difference between day length between summer and winter is small. However in locations further away from equator, the difference in day length between summer and winter increases, and the solar potential is less. Therefore construction of reliable lighting with feasible dimensions requires intelligent harvesting and efficient usage of energy becomes crucial [1]. Since high power MPPT-charge regulators are not subjected to any standards e.g. [2] not all charge regulators comply with the manufactures specification [3], and within this work low maximum power point tracking (MPPT)-efficiencies of commercially available regulators are measured, and therefore this work emphasize the importance of full system testing.

In this work we have build a laboratory where we can measure all the parts of such light-to-light systems, and use the data for optimization of products and accurate prediction of field performance.

### 2 THE LAB

#### 2.1 IV Characterization

A Newport class AAA solar simulator is used for illumination of the panels, and IV-curves from 50 W/m<sup>2</sup> to 1000 W/m<sup>2</sup> are recorded, using a Keithley 2401 SourceMeter for small panels. An example of such series of measurement is shown in Figure 1.

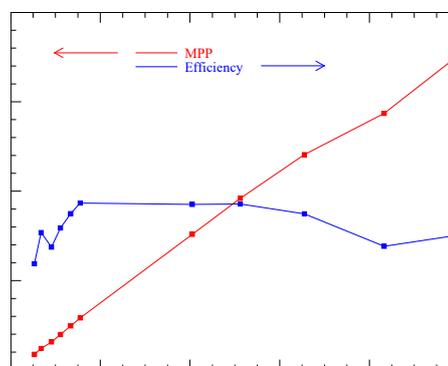


**Figure 1:** Measurement of the Solar panel at different illumination levels. An IV-curve is recorded for each measurement point.

#### 2.2 Electronic characterization

We characterize 4 electronics features on the electronic controller board:

- The MPP-tracking efficiency.
- The Charge conversion efficiency.
- The efficiency of the LED supply.
- The standby consumption.

The electronic characterization lab consists of 3 different emulators and a 3 channel power analyzer to measure the power flow. The equipment is as follows:

- Two Agilent B2962 - 2 Channel programmable source measure unit, 30 W pr. channel. The channels are floating enabling serial and parallel connection of the channels.
- One Agilent Solar Array Simulator E4360A mainframe with a E4361A DC module (0-65 V and 0 8.5 A).
- One Keithley 2651A High Power SourceMeter (200 W 2000 W pulsed).
- One Tektronix Power Analyzer PA4000 3CH.

The charge part of the characterization is done using either an Agilent E4361A Solar Array Simulator for larger PV modules and for smaller PV modules an Agilent B2962 Source Measure Unit (SMU) as an emulator. The SAS is not very accurate for power levels

under 5 - 10 watts. As battery the Keithley 2651A Source meter is used in constant voltage mode and since charge currents is typically below 0.2 C the constant voltage emulates the battery fairly well. The devices supports though more advanced battery emulation.

All voltages and currents are measured using the power analyzer.

As input to the solar emulators the measured sets of  $V_{OC}$ ,  $I_{SC}$ ,  $V_{MP}$  and  $I_{MP}$ , recorded at different light intensities are used. The set of IV-curve parameters is measured for different relevant battery voltages, and thereby a full mapping of the working ranges is obtained for a specific system. The measurement and data acquisition is automated in LabVIEW.

Based on these measurements the tracking efficiency and the conversion efficiency are obtained and examples are shown in figures 2 and 3.

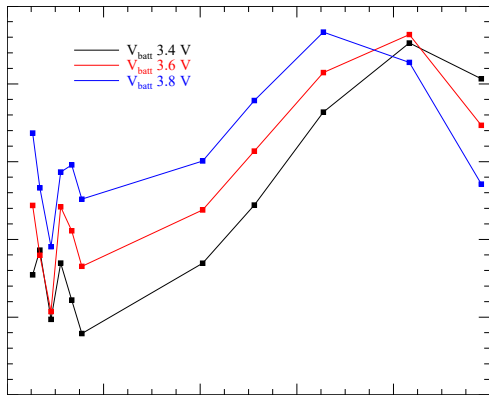


**Figure 2:** The powerpoint tracking efficiency as a function of irradiation. The efficiencies above 100 %, is explained by the accuracy of the emulator, in this case the Agilent E436x SAS system.

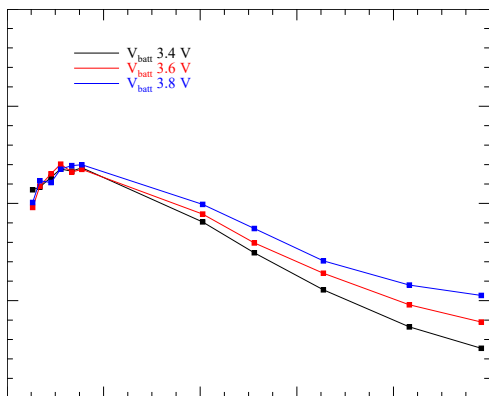


**Figure 3:** The conversion efficiency of the charger. This chargers seems to be optimized for low power.

The LED driver is also tested by letting the Keithley 2651A emulate a battery in constant voltage mode, vary the battery voltage and using the real LED as sink. The system tested here is simple without a clock and therefore it turns the LED on once the PV Energy is decreased to zero. Therefore, for this system, a LED output can be

stimulated with a constant battery voltage and a solar input for a short while e.g. a minute. The LED output is stimulated after the solar input is turned on. However some controllers are time based why it is sometimes hard to stimulate a LED output for the controller.

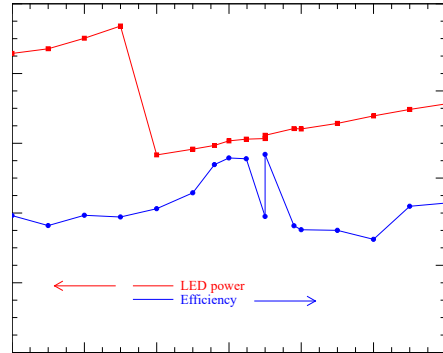


**Figure 4:** The LED driver efficiency and Power. The sudden decrease in power level at 3.5 volts has no explanation, but is a reproducible system behaviour.

The Power analyzer has a special standby mode, where it measures the standby power by integrating the power over a period set by the user with a very high sampling rate and then output the average power. With a similar approach as for the LED driver, the standby power consumption can be measured when the LED is disconnected. The measurement in figure 3 also includes the standby power in the efficiency calculation and therefore this measurement provides sufficient information for a field performance prediction. However, the standby power consumption measurement is a powerful tool to differentiate the converter loss and standby power consumption enabling a more targeted product improvement.

### 2.3 Battery characterization

Charge and discharge curves are recorded using an ELV ALC 8500 Expert battery tester. This device can charge and discharge the battery at a specified rate, and record the data, and an example of such measurement is showed in figure 5.

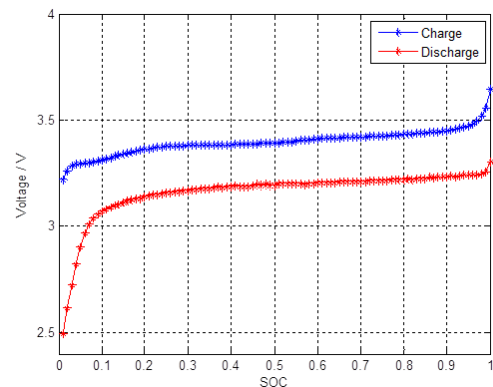


**Figure 5:** Charge and discharge curve of a NiMH battery.

### 2.4 Luminaire testing

The LED is characterized at DOLL quality lab [4], where both a goniophotometer (Techno Team, Rigo 801), and an integrating sphere (Instrument Systems, ISP 1000 and ISP 2000), which are both equipped with a spectrometer (Instrument Systems, CAS 140, 380-1040 nm) and a high quality luxmeter (PRC Krochman,  $f_1 < 1.2$ ).

The integrating sphere measures the total luminous flux, and the goniophotometer measures the light distribution from a luminaire.

Figure 6 shows an example of a measurement in the integrating sphere, where the luminous flux is measured as a function of voltage and current.

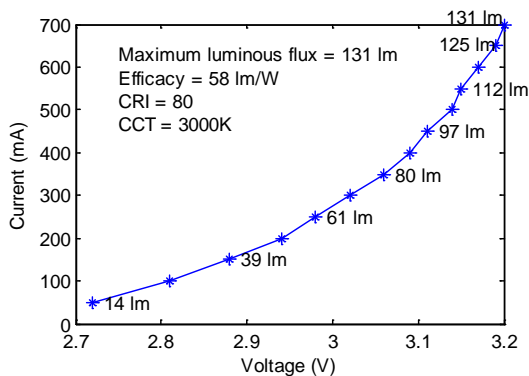


**Figure 6:** Characterization of an LED

### 3 MEASUREMENTS

A measurement on a commercial high end PV powered LED lighting bollard system was done, and the results can be found in figures 1-6. The average conversion efficiency is 78% and the tracking efficiency is 93.5 % giving the controller a total charging efficiency of 72 %. The average battery efficiency is 94 % and the average LED driver efficiency is 77% i.e. approximately only 53% of the incoming electric power is available for the LED.

### 4 CONCLUSION

These preliminary measurements provide a deep insight in the losses and the behavior of these smaller light-to-light systems. Further the preliminary measurements indicate that the electronic controller in the L2L systems has the highest potential for improvement.

Future work includes, implementing the shown laboratory measurement in the PV LED engine software [5], and use these data for accurate field prediction.

### 5 ACKNOWLEDGEMENTS

The project is funded by the Danish Energy Technology Development and Demonstration Programme, project number 64011-0323, "The PV LED Engine - new generation of intelligent solar powered LED lighting".

### 6 REFERENCES

[1] Edoardo Cavallaro et. A., Dimming\_Based

Energy Management of PV-Fed LED Lighting System, presented at PCIM Europe 2012.

- [2] EN 50530: Overall efficiency of grid connected photovoltaic inverters.
- [3] Michael Müller et. Al; Performance of MPPT Charge.
- [4] Danish Outdoor Lighting Lab; [www.lightinglab.dk/UK/](http://www.lightinglab.dk/UK/)
- [5] Poulsen et. Al; Simulation tool for designing off-grid PV applications for the urban environment, presented at the 28. EUPVSEC 2013, Paris

## DESIGNING HIGH EFFICIENT SOLAR POWERED OLED LIGHTING SYSTEMS

Rasmus Overgaard Ploug<sup>1</sup>, Peter Behrendorff Poulsen<sup>1,\*</sup>, Sune Thorsteinsson<sup>1</sup>, Anders Thorseth<sup>1</sup>, Dennis Dan Corell<sup>1</sup>, Jesper Wolff<sup>1</sup>, Carsten Dam-Hansen<sup>1</sup>, Arnold Knott<sup>2</sup>

<sup>1</sup>Department of Photonics Engineering, Technical University of Denmark, Frederiksborgej 399, Building 130, DK-4000 Roskilde, Denmark

<sup>2</sup> Department of Electrical Engineering, Technical University of Denmark, Richard Petersens Plads 325, DK-2800 Kgs. Lyngby, Denmark

\*Phone +45 21325110, E-mail: ppou@fotonik.dtu.dk

**ABSTRACT:** OLEDs used in solar powered lighting applications is a market of the future. This paper reports the development of electronic Three-Port-Converters for PV OLED product integration in the low-power area respectively for 1-10 Wp and 10-50 Wp with a peak efficiency of 97% at 1.8 W of PV power for the 10 Wp version. Furthermore, we present measurements of state-of-the-art commercial available OLED with regards to the luminous flux, luminous efficacy, luminance homogeneity, temperature dependency and IV characteristic of the OLED panels. In addition, solar powered OLED product concepts are proposed.

**Keywords:** Stand-alone PV Systems, High-Efficiency, Design, OLEDs.

### 1 INTRODUCTION

Organic Light-Emitting Diodes (OLEDs) are a promising new lighting technology, as they are very thin uniform light sources which are pleasing to look directly at without the need to encapsulate it in heavy optical components to hide the light source. By employing optically transparent components, transparent organic light emitting diodes (TOLEDs) have also been realized. When operating, TOLEDs emit light from both their bottom and top surfaces, while in non-operational mode they look like ordinary transparent glass. TOLEDs can be applied to a variety of window-like displays, bi-directional lighting facilities and eyewear displays [1]. It also makes them suited for combinations with photovoltaics, since the same area can be used to harvest solar radiation energy and irradiate light. Furthermore, OLEDs brings new possible form factors into the lighting sectors which makes new design possibilities available for innovative lighting products. Their ability to be deposited on a flexible substrate making flexible light sources available to the market gives unique opportunities in differentiations in the lighting market with similar arguments as flexible solar panels of thin-film, organic and polymer photovoltaics. OLEDs are still very expensive compared to other lighting technologies but in the display market they are competitive to LCD and have the later years gained ground in the display market e.g. in mobile phones, TVs and laptops.

Light-2-Light (L2L) stand-alone self-powered products (as sketched in figure 1) based on photovoltaics, OLEDs and batteries has not yet been seen on the market to the author's knowledge. Since OLEDs are very sensitive to e.g. humidity, oxygen and solar radiation it requires extra care in the encapsulation of the OLEDs when used outdoor. Many scientific problems are yet to be solved and successful solar powered OLED products might first reach the market some years in the future.

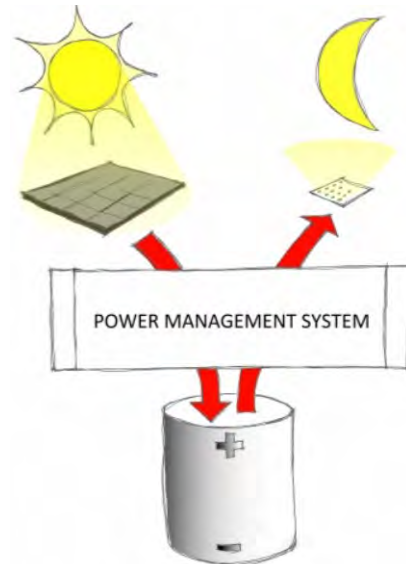


**Figure 1:** Principle sketch of a Light-2-Light system.

OLED technology is interesting for L2L due to the electric characteristics, which resembles conventional LED, and the potentially very low production cost of OLEDs when roll-to-roll techniques can be used for mass production [2]. In this paper we present measurements of state-of-the-art commercial available OLED products. The investigation will focus on the performance with regards to light output vs. electrical input. The characteristics studied are: the luminous flux and luminous efficacy as a function of power and luminance homogeneity and IV characteristics of the OLED panels.

Furthermore, in this work it is sought to lower the barrier towards design and implementation of solar powered OLED products by proposing a topology to a high efficient converter system for use in L2L OLED systems and investigates new concepts that could potentially exploit the uniqueness of the OLED and photovoltaics in combination.

## 2 OLED LIGHTING

The OLEDs have been characterized in the nearfield goniophotometer at DTU Department of Photonics Engineering, which for the 10×10 cm samples can measure the intensity distribution, luminance and spectral radiant intensity in the visible range. This paper presents measurements of luminous flux, luminous efficacy, luminance homogeneity, IV characteristics and the result of a temperature dependency investigation.

In figure 2 the measurement of luminous flux and luminous efficacy is shown as a function of the power consumption from low currents up to the rated maximum. It can be seen that the efficacy decreases with increasing power consumption with the decrease falling off rapidly in the low power range.

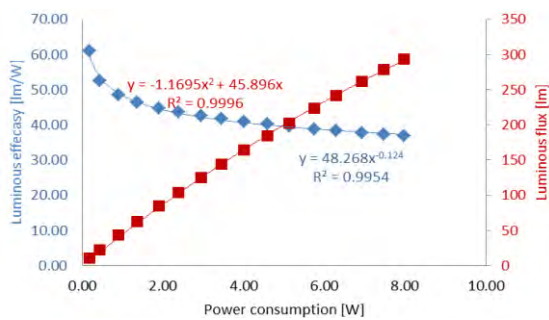


**Figure 2:** Luminous flux and luminous efficacy as a function of the consumed power.

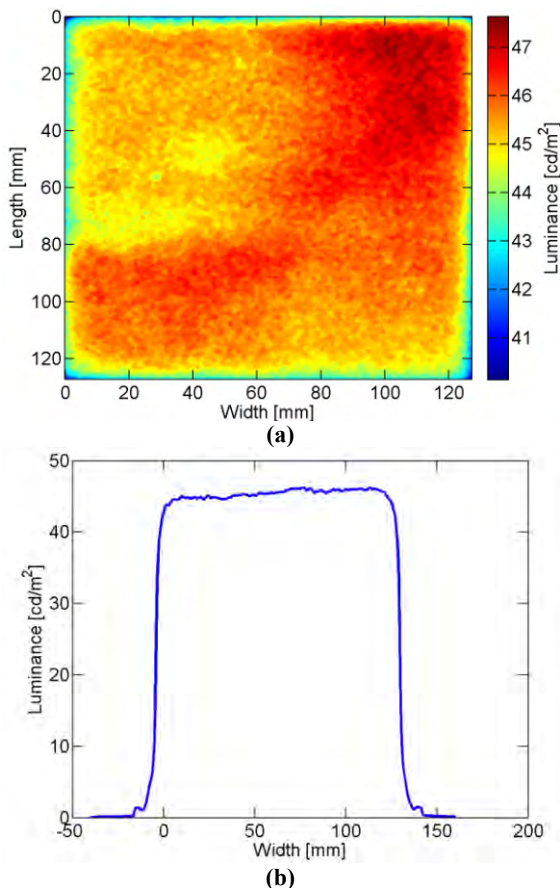


**Figure 3:** Luminance map of an OLED with the colours used as intensity scale i.e. not colour distribution (a) and

a horizontal cross-section taken in the centre of the map (b).

The OLEDs have also been measured using an imaging luminance meter, which shows the uniformity of the appearance. The results are shown in figure 3. The luminance of an OLED tile like this, with a 4% gradient in the cross section might in some cases seem disturbing to a human viewer.

The forward IV characteristics of an OLED was measured and plotted in figure 4. The OLED shows a diode characteristic with a threshold voltage around 7.5 V.

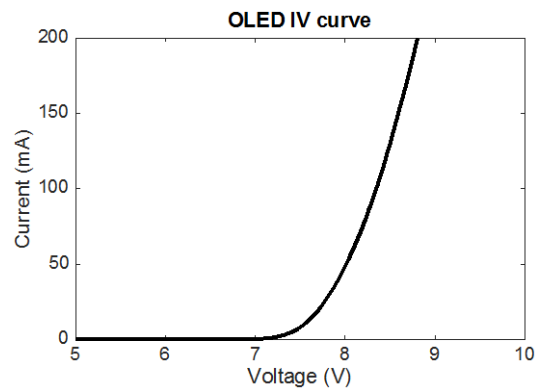


**Figure 4:** OLED IV characteristics. The OLED shows a diode characteristic with a threshold voltage around 7.5 V.

Lastly the temperature dependence of selected OLED was investigated. The temperature dependency is a critical parameter in outdoor applications due to the potentially large variations in weather conditions. For one OLED panel we measured a very small reduction in light output of 0.04% per °C in the temperature range 33-50 °C, with the temperature measured on the mounting plate of the OLED. Another OLED showed higher temperature dependence with a reduction of 0.14 % per °C.

## 3 ELECTRONIC CONVERTER

In order to design an efficient electronic converter for an outdoor L2L system two operating modes for the system are identified as

1. Energy harvesting during the day: Conversion of energy from the PV panel to the energy storage with high efficiency maintaining Maximum Power Point Tracking (MPPT) to harvest as much energy as possible
2. Energy usage during the night: Conversion of energy from the energy storage to satisfy the electrical operating point of the OLED panel.

To fulfil these two operating modes a switch-mode Three-Port-Converter (TPC), as shown in figure 5, has been developed.

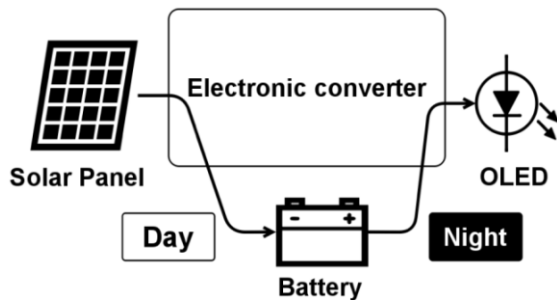


**Figure 5:** System design of the electronic three-port-converter for the L2L application.

### 3.1 Topology

For this study the voltage restrains for the PV panel, battery and OLED was chosen such that the PV panel voltage and the OLED operating voltage must be larger than the maximum battery voltage. Hence, in the daytime, the PV voltage has to be stepped down to the battery voltage (buck-type conversion) and during the night the battery voltage has to be stepped up to meet the OLED requirements (boost-type conversion). While one could design two separate converters – one for each of the operating modes – a conceptual topology has been suggested to meet both demands in one topology in order to reuse components between each operating mode and thereby save on total cost. This topology is shown in figure 6. It can be seen that the inductor  $L1$  and switch  $Q2$  are reused between each operating mode while  $Q4$  and  $Q5$  serve as power control switches (either fully on or fully off) preventing unwanted currents to run in the system. The electrical design and properties of this topology have been documented in [3] and a slightly different version with a tapped-boost step-up converter in [4]. In order to cover a full range of applications covering panels from 1-50 Wp, a low power range of 1-10 Wp and a high power range optimized for 10-50 Wp is developed. This project documents the 1-10 Wp prototype.

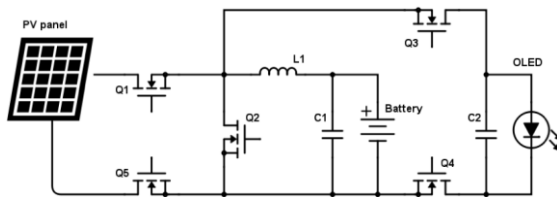


**Figure 6:** Three-port-converter topology. Buck operating mode:  $Q1$  is the control switch,  $Q2$  is the synchronous rectifier,  $Q5$  is on,  $Q3$  and  $Q4$  is off. Boost operating mode:  $Q2$  is the control switch,  $Q3$  is the synchronous rectifier,  $Q4$  is on,  $Q1$  and  $Q5$  is off.

### 3.2 Implementation and results

Apart from seeking a high efficiency energy conversion by proper component selection and converter switching frequency, it is furthermore sought to optimize the converter switching behaviour for having highest efficiency in the lower part of its operating range. It is desired to have a high performance in a L2L system also on days with low solar irradiation. Efficiency wise this means that the system should be optimized for having its highest efficiency in its low power operating area as this would be the 'bottleneck' in securing high reliable performance. Furthermore, L2L products are often placed in areas with a lot of shadows on the solar panels e.g. in parks or in the urban environments, making peak power

operation rare. An optimization for the electronic power converter for this low power area was described in [3] and the resulting energy conversion efficiency graphs can be seen in figure 6. The converters peak efficiency is 97 % when operating at 1.8 W with PV panel voltage of 9 V. The conversion from battery to light is of similar efficiency.

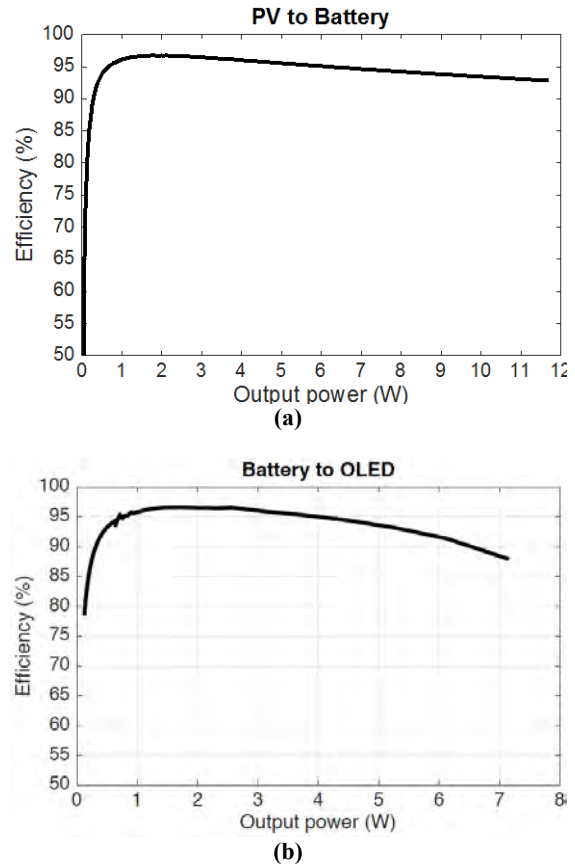


**Figure 7:** (a) Measured efficiency curve of the 10 W converter when harvesting energy from PV panel to the battery. It can be seen that the converter excels in having its highest efficiency at the lowest power obtaining 94 % at 0.5 W and peaking at 97% at 1.8 W. (b) Efficiency curve of the converter operating in boost mode. The converter reaches 96 % efficiency at the 1.275 W corresponding to an OLED operating point of 8.5 V at 150 mA.

A more in depth view of the efficiency during energy harvesting of the electronic converter can be seen in figure 8.a. Here the efficiency has been measured in the entire converter operating range in order to assess the energy harvesting behaviour for all possible solar irradiation conditions. This was done in an automated setup using a solar array simulator as the PV and a source meter unit as the battery. Also the tracking efficiency of the MPPT algorithm was measured as well using panel characteristics with 1 maximum power point (figure 8.b). These two measurements were then combined in order to estimate the total energy harvesting yield (figure 8.c). Note that the converter efficiency measurements differ slightly from figure 7.a since, in the latter measurements are made with a 4.0 V fixed voltage source-meter instead of a battery with a voltage floating in the range 3.2 V to 4.2 V.

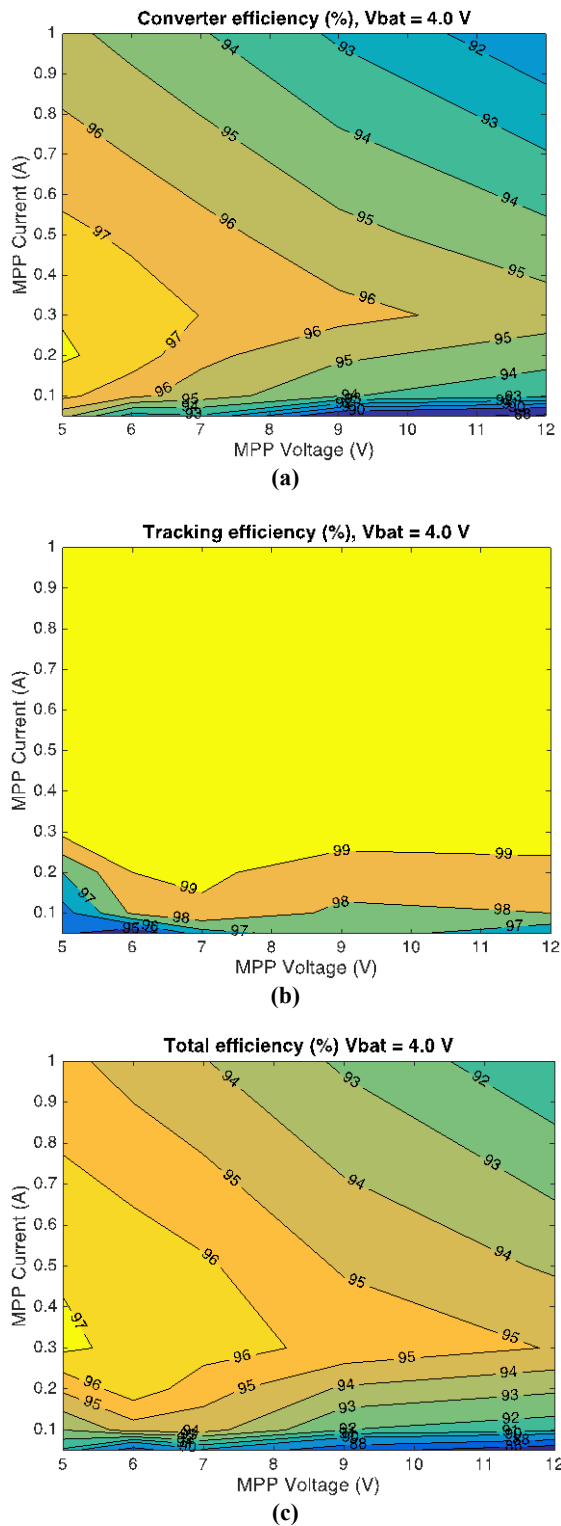


**Figure 8:** Converter energy harvesting efficiency measured in its entire operating range. (a) shows converter efficiency, (b) shows the MPP tracking efficiency and (c) shows the converter and tracking combined efficiency.

#### 4 SOLAR POWERED OLED LIGHTING CONCEPTS

The OLED technology brings many new unique

design possibilities into the market of stand-alone self-powered lighting. New designs should utilize the surface light concept in new products with new possibilities in mating the very thin and flat OLED structure with PV panels which also are flat structures. Transparent OLED (TOLED) technology could also lead to new ‘sandwich’ structures simply by placing the TOLED on top of a PV-panel making small devices that are able to both illuminate and harvest energy from the same surface. Also flexible OLEDs paired with flexible PV-panels can potentially introduce new unique design possibilities.

As an example of a product idea it is suggested to use the OLED lighting structure to give the possibility of making self illuminating signs which are perfect examples of utilizing self-powered L2L systems in remote locations where grid-connection is not an opportunity. A possible design concept for a L2L OLED sign is included in figure 9 for inspiration purposes.



**Figure 9:** OLED based sign with PV integrated in the mast.

#### 5 CONCLUSIONS

OLEDs used in solar powered lighting applications are a market of the future. To break down the barriers towards exploiting the unique potentials of PV and OLEDs in combination we have reported the development of a Three-Port-Converter for PV OLED product integration for the 1-10 Wp range with a peak efficiency of 97% at 1.8 W of PV power. Furthermore, we have presented measurements of state-of-the-art commercial available OLED with regards to the luminous flux, luminous efficacy, luminance homogeneity and IV-characteristic select OLED panels. In addition, solar

powered OLED products are elaborated and a design suggestion of a solar powered OLED sign is presented.

#### REFERENCES

- [1] C. W. Joo, J. W. Shin, J. Moon, J. W. Huh, D. H. Cho, J. Lee, S. K. Park, N. S. Cho, J. H. Han, H. Y. Chu, and J. I. Lee, "Highly efficient white transparent organic light emitting diodes with nano-structured substrate," *Org. Electron. physics, Mater. Appl.*, vol. 29, no. 2016, pp. 72–78, 2016.
- [2] R. R. Søndergaard, M. Hösel, and F. C. Krebs, "Roll-to-Roll fabrication of large area functional organic materials," *J. Polym. Sci. Part B Polym. Phys.*, vol. 51, no. 1, pp. 16–34, Jan. 2013.
- [3] R. O. Ploug, A. Knott, "Photovoltaic OLED Driver for Low-Power Stand-Alone Light-to-Light Systems", *Elektronika Ir Elektrotechnika*, vol 22, no. 3, 2016. Available: <http://dx.doi.org/10.5755/j01.eic.22.3.15314>
- [4] M. C. Mira, A. Knott, M. A. E. Andersen, "Three-port converter for low-power stand-alone light-to-light systems (submitted for publication)", *IEEE Energy Conversion Congress & Expo (ECCE) 2016*.

## DESIGN, CHARACTERIZATION AND MODELLING OF HIGH EFFICIENT SOLAR POWERED LIGHTING SYSTEMS

Peter Nymann<sup>a</sup>, Frederik Svane<sup>a</sup>, Peter Behrendorff Poulsen<sup>a,\*</sup>, Sune Thorsteinsson<sup>a</sup>, Johannes Lindén<sup>a</sup>, Rasmus Overgaard Ploug<sup>a</sup>, Maria C. Mira<sup>b</sup>, Arnold Knott<sup>b</sup>, Ib Mogensen<sup>c</sup>, Kris Retoft<sup>c</sup>

<sup>a</sup>Department of Photonics Engineering, Technical University of Denmark, Frederiksborgvej 399, Building 130, 4000 Roskilde, Denmark

<sup>b</sup>Department of Electrical Engineering, Technical University of Denmark, Richard Petersens Plads 325, DK-2800 Kgs. Lyngby, Denmark,

<sup>c</sup>Out-sider, Kigkurren 8A, Islands Brygge, 2300 København S, Denmark

\*Phone: +45 21325110, ppou@fotonik.dtu.dk

**ABSTRACT:** This paper discusses some of the major challenges in the development of L2L (Light-2-Light) products. It's the lack of efficient converter electronics, modelling tools for dimensioning and furthermore, characterization facilities to support the successful development of the products. We report the development of 2 Three-Port-Converters respectively for 1-10Wp with a peak efficiency of 99.1% at 1.5 W output power at PV to battery and almost similar characteristics for a 10-50 Wp. Furthermore, a modelling tool for L2L products has been developed and a laboratory for feeding in component data not available in the datasheets to the model is described. A living lab facility is realized to field test prototypes of L2L lighting products in their development state to validate the modelling tool and tweak the parameters in the system for optimized performance the product. Finally, the model was validated against a field test from the living lab over a four-day period with an offset of 5.3 %.

**Keywords:** Stand-alone PV Systems, High-Efficiency, Design, Modelling, Simulation

### 1 INTRODUCTION

In the last few years significant progress has been made in research and development of renewable energy systems. Solar energy is one of the most reliable, daily available and environment friendly renewable energy sources, being unlimited, clean and free [1], [2]. Furthermore, due to the ability of generating off-grid electricity, sustainable energy systems have attracted research interest in the last decades [3]. Due to the rapidly increasing efficiency of light emitted diodes (LEDs) stand-alone combinations of PV modules, battery storage and LED luminaires are becoming more attractive for a variety of lighting applications [4]. The systems operate entirely on DC and are often called Light-to-light (L2L) systems, see figure 1.

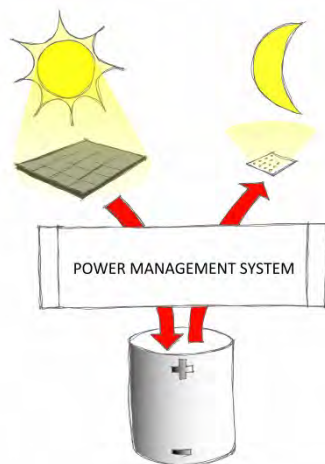


**Figure 1:** A principle sketch of a Light-2-Light system

Park lights and bollards are examples of L2L systems and these systems offer lighting solutions, for places where lighting is not feasible due to very high cabling costs of up to e.g. 700 €/m in Copenhagen and up to 2000€/m in Berlin [5]. Some of the major obstacles still

remaining for successful L2L systems are 1) the lack of efficient converter electronics for small PV systems, (PV powers of 1-50 Wp) 2) the lack of a dimensioning and assessment tool for L2L systems and 3) the knowledge centers and laboratory facilities to support the complicated process of designing successful L2L products. The latter being an interdisciplinary technical task involving at least knowledge, tools, and test equipment for the technology fields of lighting, photovoltaics and power electronics. A series of Danish research projects has addressed these issues and the results are reported here.

### 2 ELECTRONIC CONVERTER

An electronic converter for outdoor light-to-light purposes should be able to work in two modes:

1. In the daytime: Convert energy from the PV panel while maintaining Maximum Power Point Tracking (MPPT) in order to harvest as much energy to the battery from the available solar energy as possible.
2. In the night: Convert stored energy from the battery to the operating point of the LED panel.

Hence this application calls for a Three-Port-Converter (TPC) with two operating modes.

To cover the full range of 1-50 Wp of solar panels with high efficiency, 2 versions of converters was developed. A low range for PV powers 1-10 Wp and a high power range of 10-50 Wp, giving the versatility of choosing solar panels in the whole span. The efficiency curve for the 10 Wp version is shown in figure 2 and figure 3. It is sought to achieve the peak conversion efficiency in the lower part of its operating range since L2L products often are placed in areas with a lot of shadows on the solar panels e.g. in parks or in the urban environments, making peak power operation rare.

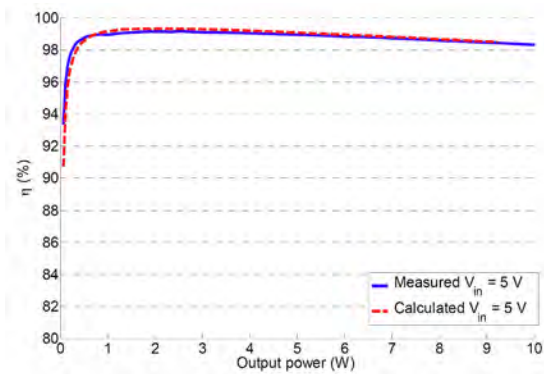


**Figure 2:** Efficiency curve of the 10 W converter when harvesting energy from PV panel to the battery.

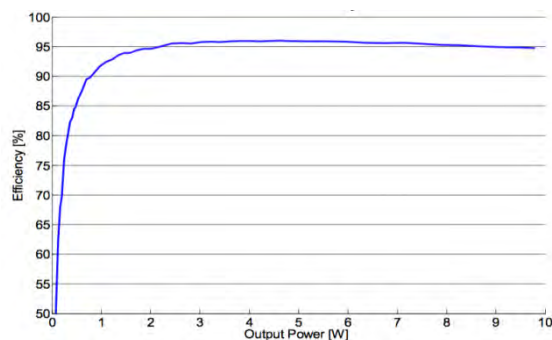


**Figure 3:** Efficiency curve of the LED driver stage peaking at 3W output power with 97.3%

The converters peak efficiency is 99.1 % when operating at 1.5 W. The output power and the LED driver stage present a peak efficiency of 97.3% at 3W output power. The electronics converter work is documented in [6] and [7].

### 3 SOFTWARE FOR DIMENSIONING AND SIMULATION OF PV LED APPLICATIONS

The authors have investigated several software tools on the market and none was found suited for the task of dimensioning and simulating performance of solar powered L2L products. A customized tool is therefore developed in MATLAB as a starting point with input from several specialized tools. The block diagram, figure 4, shows the design of the simulation tool, which essentially is a computer model of a basic PV application, including PV panel, electronics, battery and power consumption in the form of an LED luminaire. The L2L dimensioning tool differs since it uses highly time resolved weather data in 1-minute resolution. This is important when modelling solar products operating most of its time in the shadows from buildings and other artefacts. The efficiency curve, figure 2 of the developed converter is rather flat in the whole irradiation interval from 0-1 sun. The full electronic controller unit, however, consists of both converter and controller with a microcontroller operating in several states, running algorithms, and controlling other external devices as a battery management system, motions sensors etc. The real energy conversion functions are therefore usually far from linear and depend heavily on irradiation level on the

PV panel, temperature, battery voltage and other parameters which need to be modelled for precision. The energy flow is basically made up of:

1. Energy flow from the sun to the PV panel
2. Energy flow from the panel – through the charger – and into the battery
3. Energy flow from the battery – through the discharger – into the LEDs
4. Stand-by consumption of the electronics controller due the intelligent disposition of the energy for lighting (the lighting scheme) and the loss in its external components (if any).

The datasheets of small solar panels, PV/LED controllers and batteries are rarely having data for this type of modelling to be done.

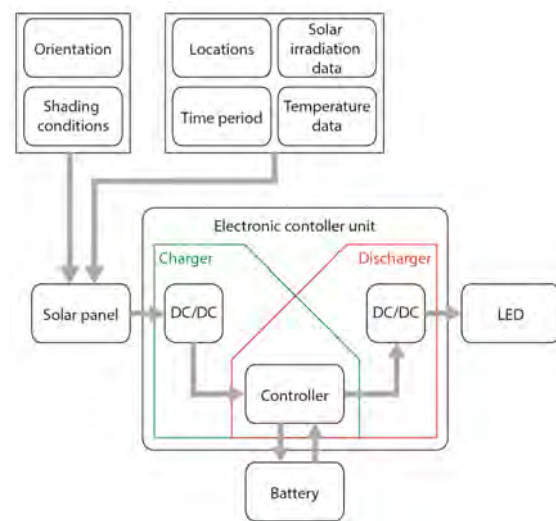


**Figure 4:** Block diagram of L2L modelling tool

### 4 LABORATORIES FOR CHARACTERIZATION AND MONITORING OF L2L PRODUCTS

There has been installed two laboratories, a specialized lab to feed the mathematical simulation tool with accurate and sufficient data for modelling of L2L products and support the development of successful solar powered LED products, and a living lab for installation and monitoring the energy flow inside the L2L products. This will be expanded in the coming years at the university campus of the Technical University of Denmark around the building of Department of Photonics Engineering in Roskilde. The modelling tool can thereby be validated against periods with known weather data where data logging has been implemented in the products. The differences between simulated performance of a product and the logged performance is due to inaccuracies in the model and is a valuable tool to optimize it. Figure 5 shows the data feed-back loop.

The specialized lab is composed of the following facilities:

#### *Component characterization*

- Solar cell electrical (I, V, Irradiation 0-1 sun AM 1.5)

- Solar panel electrical (I, V, Irradiation 0-1 sun AM 1.5)
- Battery (I, V, Charge, Temp)
- LED electrical and photometrical (I, V, lumens)
- Electronics controller
  - Charging efficiency (Emulation of the PV panel and the battery, allowing mapping of the full operating range for the charger)
  - Discharge efficiency ( $V_{bat}$ ,  $I_{LED}$ ,  $V_{LED}$ )
- Shade measurement/simulation

- Goniophotometry

The measurements are tailored to fit into the L2L modelling tool and are more or less automated to characterize the individual components in the many different operating states needed. The luminaire characterization is not part of the model but a part of the process of creating highly efficient high end L2L products. The light rays need to illuminate the desired object nicely without the light being lost in reflectors and diffusers, giving rise to glare or other waste mechanisms. Here good optical engineering can reduce the total amount of light needed, and thus improving the efficiency. The relevant metric is useful lux or useful lumens which can be modelled by use of e.g. DIALux and RELUX which in turn can be used iteratively with the L2L model.

**Luminaire characterization**

- Spectroradiometry
- Photometry
- Goniospectroradiometry

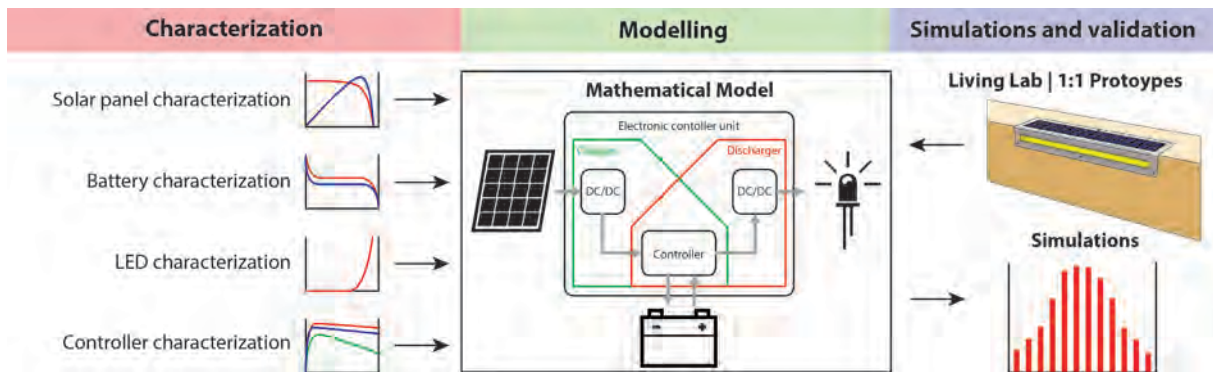


**Figure 5:** Diagram of the data feed-back loop for simulation of L2L products and validation of the model

**5 MODEL VALIDATION**

The model has been validated using the components of the “Lighttube” developed by Out-sider, which consists of a 4 W mono crystalline silicon cell, a NiMH 3.6V 4Ah battery, the control unit discussed and eight 0.3 W LEDs (Samsung LM561B Plus). For this validation weather data from the weather station at DTU RISØ Campus has been used for the simulation, alongside a logging device connected to similar components placed in the Living lab at DTU RISØ. The shading profile used in the simulation was created with a Solmetric SunEye, which is basically a fish eye camera that captures a picture of the hemisphere. It is then adjusted for the model and can be seen in figure 6.

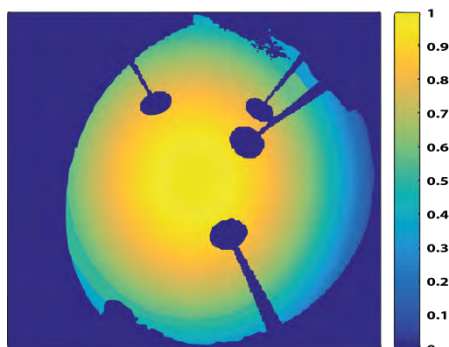


**Figure 6:** The shading profile of the field tested device at the Living Lab @ DTU RISØ Campus.

Since standalone systems are straight forward products they usually are not equipped with Sun tracking technology, therefore the Sun’s position for all times of the year has been calculated from the SunEye’s compass and the belonging software. This shade profile and the Sun’s position are used to calculate the direct irradiation and the fraction of open sky, used to determine the contribution of the diffuse light, assuming that the diffuse light is isotropically distributed. The contribution of the diffuse light is calculated to be 81 % of the total diffuse light, with a fraction of open sky at 70 %, due to the angle dependency of light from normal incident. Using the shadow profile created by the fish-eye picture from the SunEye the weighting, which can be seen in figure 6 as the scale, is calculated by giving each pixel a coordinate corresponding to the distance from normal incident, i.e. the center of the picture, from which the corrected contribution of diffuse light is calculated. This could have been done more exact by projecting the corrected contribution down onto the plane of the panel, but was not done, because of SunEye’s high pixel resolution.

The models assumes that the shadows are binary, meaning that they either cover the entire panel completely or not at all, which is assumed to be an acceptable approximation for small PV panels. This approximation will not be valid for larger panels with bypass diodes. Data from four days in May and June have been used to compare the model to the device in the lab. The comparison has been made between the effects of the different components of the device, which can be seen in figure 7 with 1 minute resolution.

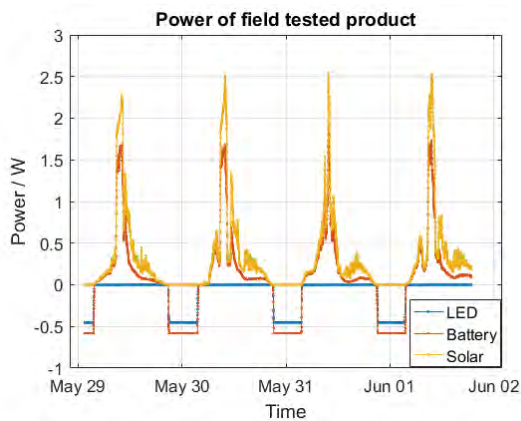


**Figure 7:** The power of the field tested device at the living lab @ DTU RISØ Campus

The differences in power from the PV panel to the battery and from the battery to the LED are the losses in the system, e.g. during conversion and standby. On the logged plot it can be seen that the power increases slowly when the PV panel is exposed to increasing irradiation in the early hours, where as it can be seen from the simulated plot in figure 8 that the power increases abruptly.

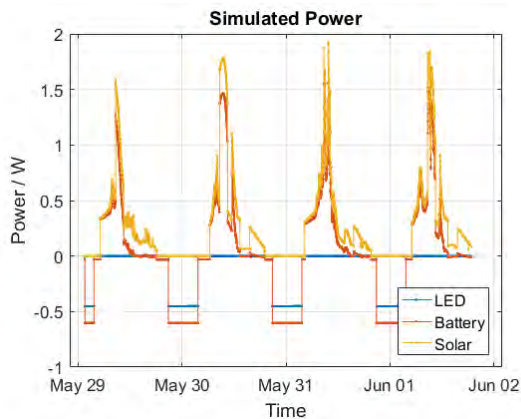


**Figure 8:** The power simulated by the model

This is due to the PV panel not being characterized for low levels of irradiance, which results in the current over the PV panel cutting off until the irradiance value has surpassed a certain value. This however is not of great importance since the lowest levels of irradiation do not produce very significant amounts of energy.

From figure 9, it can be seen that around midday the power on the battery drops relatively compared to the power on the solar cell, and the power on the solar cell begins to fluctuate, which is due to the battery being nearly fully charged. This consequence is not as eminent on the plot of the simulated power, which is a combination of the battery not being completely characterized, and the fact that the simulated battery is fully charged earlier than the logged battery. The characterization of the battery during charge and discharge has not been done for varying currents, resulting in the assumption; the voltage on the battery is equal to the open circuit voltage on the battery which in turn results in deviations from the field tested device when the current is either high or low relatively. This however does not play an important role in the total

amount of energy accumulated. The fact that the simulated battery is fully charged earlier than the logged battery, can be explained by looking at the morning hours on figure 9. Here it can be seen that after the abrupt increase in power for the simulated solar panel, the effect is much larger than for the field tested device, i.e. the simulated battery is charged more during the early hours. This also explains why the peaks of the simulated and field tested powers are so different from 9 to 10 o'clock, since the current drops when the battery is almost fully charged. The field tested battery thus has a higher power than the simulated in the time interval from 9 to 16 o'clock, where the simulated battery has a higher power from 5 to 9 o'clock. This fallout is also believed to be caused by lacking characterization of the PV panel at low levels of irradiance, and is of much higher significance than the first missing hour by the abrupt start caused by the same lack of characterization.

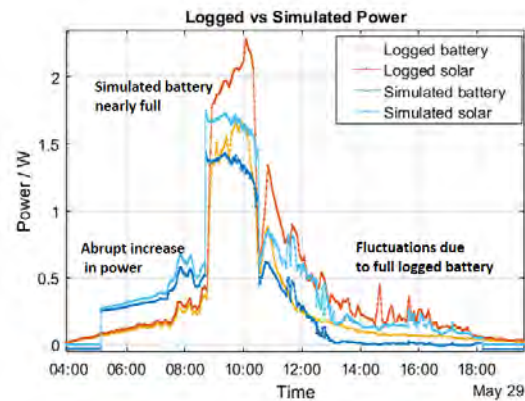


**Figure 9:** Comparison of the logged and simulated power on the 29.th of May

When integrating the power of the different components over the entire time span, the total change in energy is found. The relative differences in energy flow can be seen in table 1. These indicate that over a period of 4 days, the simulated values of energy harvested and consumed are very close to the logged values. However, as can be seen from figure 9, the solar power is not harvested simultaneous in the simulation and for the logged device.

**Table I:** Energy flow over the entire time period.

	Solar	Battery	LED
Logged	29.4 Wh	3.1 Wh	12.0 Wh
Simulated	30.2 Wh	3.3 Wh	12.6 Wh
Relative deviation	2.9 %	4.5 %	5.3 %

## 6 CONCLUSION

Three major challenges in the development of L2L products is the lack of efficient converter electronics, modelling tools for dimensioning and furthermore, characterization facilities to support the successful development of the products. Above we report the development of 2 Three-Port-Converters respectively for 1-10Wp and 10-50 Wp PV panels with a peak efficiency of 99.1% at 1.5 W of output power for the 10 Wp version PV to battery conversion state. Furthermore, a modelling

tool for L2L products has been described and validated, but still allow for small improvements through a better characterization of the battery and of the PV panel. A laboratory for feeding in component data not available in the datasheets to the model is described. A living lab for field test of L2L product to validate the modelling tool and assisting in the development process of L2L products is also under further development.

## 7 REFERENCES

- [1] G. Spagnuolo, G. Petrone, S. Araujo, C. C. Araújo, E. Friis-Madsen, E. Gubía, D. Hissel, M. Jasinski, W. Knapp, M. Liserre, P. Rodriguez, R. Teodorescu, and P. Zacharias, "Renewable energy operation and conversion schemes: A summary of discussions during the seminar on renewable energy systems," *IEEE Ind. Electron. Mag.*, vol. 4, no. 1, pp. 38–51, 2010.
- [2] A. Al Nabulsi and R. Dhaouadi, "Efficiency optimization of a dsp-based standalone PV system using fuzzy logic and dual-MPPT control," *IEEE Trans. Ind. Informatics*, vol. 8, pp. 573–584, 2012.
- [3] S. S. Thale, R. G. Wandhare, and V. Agarwal, "A Novel Reconfigurable Microgrid Architecture With Renewable Energy Sources and Storage," *IEEE Trans. Ind. Appl.*, vol. 51, no. 2, pp. 1805–1816, 2015.
- [4] D. L. Meier, L. Harvest, and S. Marys, "Stand-Alone Solar Generator with LED Floodlights for Outdoor Sign Illumination," pp. 2748–2750, 2014.
- [5] P. B. et al. Poulsen, "Udvikling af CO2 neutralt byrumsarmatur, Final report," 2013.
- [6] M. C. Mira, A. Knott, and M. A. E. Andersen, "Three-Port Converter for Low-Power Stand-Alone Light-to-Light Systems."
- [7] R. O. Ploug and A. Knott, "Photovoltaic OLED Driver for Low-Power Stand-Alone Light-to-Light Systems," no. V, 2016.



## Designing high efficient solar powered lighting systems

**Poulsen, Peter Behrendorff; Thorsteinsson, Sune; Lindén, Johannes; Ploug, Rasmus Overgaard; Knott, Arnold; Mira Albert, Maria del Carmen; Mogensen, Ib; Retof, Kris**

*Published in:*  
Proceedings of IEEE 43rd Photovoltaic Specialist Conference 2016

*Link to article, DOI:*  
[10.1109/PVSC.2016.7750143](https://doi.org/10.1109/PVSC.2016.7750143)

*Publication date:*  
2016

*Document Version*  
Peer reviewed version

[Link back to DTU Orbit](#)

*Citation (APA):*  
Poulsen, P. B., Thorsteinsson, S., Lindén, J., Ploug, R. O., Knott, A., Mira Albert, M. D. C., Mogensen, I., & Retof, K. (2016). Designing high efficient solar powered lighting systems. In *Proceedings of IEEE 43rd Photovoltaic Specialist Conference 2016* (pp. 2712-2714). IEEE. <https://doi.org/10.1109/PVSC.2016.7750143>

---

### General rights

Copyright and moral rights for the publications made accessible in the public portal are retained by the authors and/or other copyright owners and it is a condition of accessing publications that users recognise and abide by the legal requirements associated with these rights.

- Users may download and print one copy of any publication from the public portal for the purpose of private study or research.
- You may not further distribute the material or use it for any profit-making activity or commercial gain
- You may freely distribute the URL identifying the publication in the public portal

If you believe that this document breaches copyright please contact us providing details, and we will remove access to the work immediately and investigate your claim.

# Designing high efficient solar powered lighting systems

Peter Behrendorff Poulsen<sup>\*,a</sup>, Sune Thorsteinsson<sup>a</sup>, Johannes Lindén<sup>a</sup>, Rasmus Overgaard Ploug<sup>b</sup>, Arnold Knott<sup>b</sup>, Maria del Carmen Mira Albert<sup>b</sup>, Ib Mogensen<sup>c</sup>, Kris Retoft<sup>c</sup>

<sup>a</sup> Department of Photonics Engineering, Technical University of Denmark, Frederiksborgvej 399, Building 130, 4000 Roskilde, Denmark, \*ppou@fotonik.dtu.dk, phone: +45 46774572

<sup>b</sup> Department of Electrical Engineering, Technical University of Denmark, Kgs. Lyngby, Denmark

<sup>c</sup> Outsider, Kigkurren 8A, DK-2300 København S, Denmark

**Abstract** — Some major challenges in the development of L2L products is the lack of efficient converter electronics, modelling tools for dimensioning and furthermore, characterization facilities to support the successful development of the products. We report the development of 2 Three-Port-Converters respectively for 1-10Wp and 10-50 Wp with a peak efficiency of 97% at 1.8 W of PV power for the 10 Wp version. Furthermore, a modelling tool for L2L products has been developed and a laboratory for feeding in component data not available in the datasheets to the model is described.

## I. INTRODUCTION

Due to the rapid increasing efficiency of light emitted diodes (LEDs) stand-alone combinations of PV module, battery storage and LED luminaires is becoming more attractive for a variety of lighting applications [1]. The systems operate entirely on DC and is often called Light-to-light (L2L) systems, see Fig. 1. Park lights and bollards are examples of L2L systems and these systems offers lighting solutions, for places where lighting is not feasible due to very high cabling costs of up to e.g. 700 €/m in Copenhagen and up to 2000€/m in Berlin [2]. Some of the major obstacles still remaining for successful L2L

systems are 1) lack of efficient conversion electronics for small PV systems, (PV powers of 1-50 Wp) 2) lack of a dimensioning and assessment tool for L2L systems and 3) knowledge centers and laboratory facilities for supporting the complicated process of designing successful L2L products. The latter being an interdisciplinary technical task involving at least knowledge, tools, and test equipment for the technology fields of lighting, photovoltaics and power electronics. A

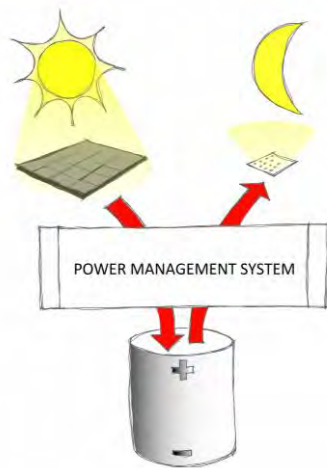


Fig. 1. A principle sketch of a Light-2-Light system.

series of Danish research projects has addressed these issues and the results are reported here.

## II. ELECTRONIC CONVERTER

An electronic converter for outdoor light-to-light purposes should be able to work in two modes:

1. In the daytime: Convert energy from the PV panel while maintaining Maximum Power Point Tracking (MPPT) in order to harvest as much energy to the battery from the available solar energy as possible.
2. In the night: Convert stored energy from the battery to the operating point of the LED panel.

Hence this application calls for a Three-Port-Converter (TPC) with two operating modes as sketched in Fig. 2.

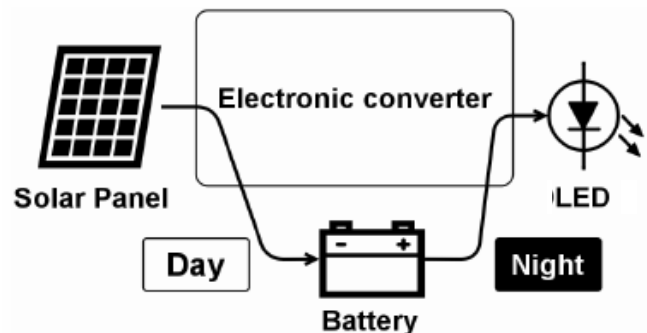


Fig. 2. Working principle of the converter

To cover the full range of 1-50 Wp of solar panels with high efficiency, 2 versions of converters was developed. A low range for PV powers 1-10 Wp and a high power range of 10-50 Wp, giving the versatility of choosing solar panels in the whole span. The efficiency curve for the 10 Wp version is shown in Fig. 3. It is sought to achieve the peak conversion efficiency in the lower part of its operating range since L2L products often are placed in areas with a lot of shadows on the solar panels e.g. in parks or in the urban environments, making peak power operation rare.

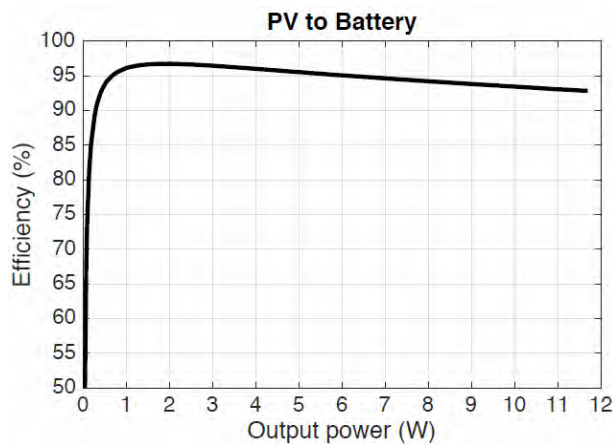


Fig. 3. Efficiency curve of the 10 W converter when harvesting energy from PV panel to the battery. It can be seen that the converter excels in having its highest efficiency at the lowest power obtaining 94 % at 0.5 W and peaking at 97% at 1.8 W.

The converters peak efficiency is 97 % when operating at 1.8 W. The conversion from battery to light is of similar efficiency. The electronics converter work is documented in [3] and [4].

### III. SOFTWARE FOR DIMENSIONING AND SIMULATION OF PV LED APPLICATIONS

The authors have investigated several software tools on the market and none was found suited for the task of dimensioning and simulating performance of solar powered L2L products. A customized tool is therefore developed in MATLAB as a starting point with input from several specialized tools.

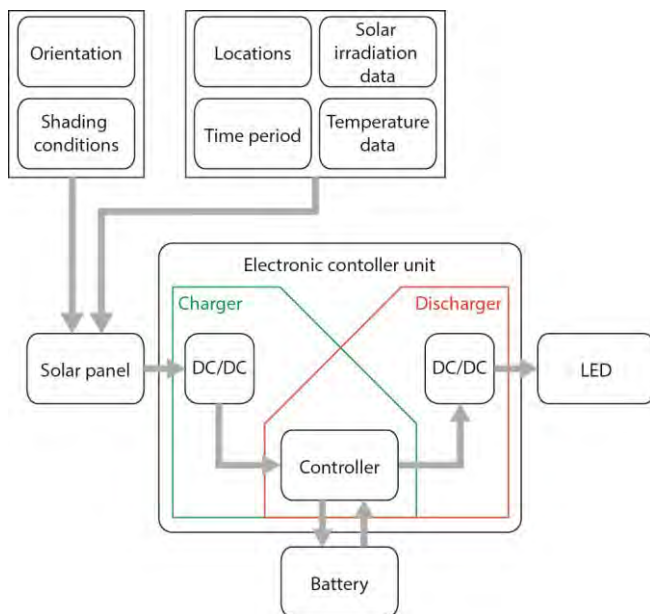


Fig. 4. Block diagram of L2L modelling tool.

The block diagram in Fig. 4. shows the design of the simulation tool, which essentially is a computer model of a basic PV application, including PV panel, electronics, battery and power consumption in the form of an LED luminaire. The L2L dimensioning tool differs since it uses highly time resolved weather data in 1-minute resolution. This is important when modelling solar products operating most of its time in the shadows from buildings and other artefacts. The efficiency curve in Fig. 3. of the developed converter is rather flat in the whole irradiation interval from 0-1 sun. The full electronics controller unit, however, consist of both converter and controller with a microcontroller operating in several states, running algorithms, and controlling other external devices as a battery management system, motions sensors etc. The real energy conversion functions are therefore usually far from linear and depend heavily on irradiation level on the PV panel, temperature, battery voltage and other parameters which need to be modelled for precision. The energy flow is basically made up of

1. Energy flow from the sun to the PV panel
2. Energy flow from the panel – through the charger – and into the battery
3. Energy flow from the battery – through the discharger – into the LEDs
4. Stand-by consumption of the electronics controller due the intelligent disposition of the energy for lighting (the lighting scheme) and the loss in its external components (if any).

The datasheets of small solar panels, PV/LED controllers and batteries are rarely having data for this type of modelling to be done.

### IV. LABORATORY FOR CHARACTERIZATION OF L2L PRODUCTS

A specialized laboratory has been built, to feed the mathematical simulation tool with accurate and sufficient data for modelling of L2L products and support the development of successful solar powered LED products. It is composed of the following facilities

#### Component characterization

- Solar cell electrical (I, V, Irradiation 0-1 sun AM 1.5)
- Solar panel electrical (I, V, Irradiation 0-1 sun AM 1.5)
- Battery (I, V, Charge, Temp)
- LED electrical and photometrical (I, V, lumens)
- Electronics controller
  - Charging efficiency (Emulation of the PV panel and the battery, allowing mapping of the full operating range for the charger)
  - Discharge efficiency ( $V_{bat}$ ,  $I_{LED}$ ,  $V_{LED}$ )
- Shade measurement/simulation

## Luminaire characterization

- Spectroradiometry
- Photometry
- Goniospectroradiometry
- Goniophotometry

The measurements are tailored to fit into the L2L modelling tool and are more or less automated to characterize the individual components in the many different operating states needed. The luminaire characterization is not part of the model but a part of the process of creating highly efficient high end L2L products. The light rays need to illuminate the desired object nicely without the light being lost in reflectors and diffuser, giving rise to glare or other waste mechanisms. Here good optical engineering can reduce the total amount of light needed, and thus improving the efficiency. The relevant metric is useful lux or useful lumens which can be modelled by use of e.g. DIALux and RELUX which can be used iteratively with the L2L model.

## IV. CASE

Several products have been designed parallel in the process of developing the L2L converter electronics, the L2L simulation tool and L2L laboratory. The products were developed together with the company, Outsider, who is designing, producing and distributing high-end solar powered lighting product for the urban environments. 2 Products were developed together with Outsider and the Architecture company, Snøhetta, for the King Abdulaziz Centre for World Culture in Dhahran Saudi Arabia, see Fig. 5. below.



Fig. 5. King Abdulaziz Center for World Culture - Rendering Snøhetta/Mir.

One of the products are called LIGHT-TUBE and is inspired by bulrushes swaying gently in the wind, shown Fig. 6. Especially the shade modelling was a special challenge of this product along with temperature modelling of the systems that had to be done to fit the data to the model. The PV is integrated in the base of the product and the LEDs in the end of the metal stick where luminaires is composed of edge-lit acrylic wave guides sandblasted on the sides.



Fig. 6. LIGHT-TUBE

## VI. SUMMARY

3 major challenges in the development of L2L products is the lack of efficient converter electronics, modelling tools for dimensioning and furthermore, characterization facilities to support the successful development of the products. Above we report the development of 2 Three-Port-Converters respectively for 1-10Wp and 10-50 Wp PV panels with a peak efficiency of 97% at 1.8 W of PV power for the 10 Wp version. Furthermore, a modelling tool for L2L products has been described and a laboratory for feeding in component data not available in the datasheets to the model is proposed.

## REFERENCES

- [1] D. L. Meier, L. Harvest, and S. Marys, "Stand-Alone Solar Generator with LED Floodlights for Outdoor Sign Illumination," 40th IEEE Photovoltaic Specialist Conference, pp. 2748–2750, 2014.
- [2] Poulsen, P.B. et al. , Udvikling af CO2 neutralt byrumsarmatur, Final report, ELFORSK project 343-021, www.elforsk.dk, 2013.
- [3] Maria C. Mira, Arnold Knott and Michael A. E. Andersen, "Three-Port Converter for Low-Power Stand-Alone Light-to-Light Systems (submitted for publication)", IEEE Energy Conversion Congress & Expo, 2016.
- [4] Rasmus Overgaard Ploug and Arnold Knott, "Photovoltaic OLED Driver for Low-Power Stand-Alone Light-to-Light Systems" (submitted for publication)", Elektronika ir Elektrotechnika, 2016

## SUN HUB – ENERGY HUB FOR OUTDOOR TABLES

Peter B. Poulsen<sup>1</sup>, Gisele A. dos Reis Benatto<sup>1</sup>, Nicholas Riedel<sup>1</sup>, Sune Thorsteinsson<sup>1</sup>, Adrian Alejo Santamaria Lancia<sup>1</sup>, Joanna Karolina Symonowicz<sup>1</sup>, Kris Retoft<sup>2</sup> and Ib Mogensen<sup>2</sup>

<sup>1</sup>Department of Photonics Engineering, Technical University of Denmark, Frederiksborgvej 399, 4000, Roskilde, Denmark, ppou@fotonik.dtu.dk

<sup>2</sup>Outsider, Kigkurren 8A, Islands Brygge, Copenhagen, Denmark

**ABSTRACT:** Solar cells integrated into products are attracting more and more attention especially due to the dramatically declining cost of solar cells. Furthermore, we are getting more dependent on portable units like mobile phones, tablets and PCs which has to be charged to be of any use. Especially on festivals where people camps for several days it can be hard to have your portable units charged. In this this work we report a solar powered hub, as an add-on to a table in the urban environment for charging mobile phones and tablets and other handheld devices through USBs, charging laptops through AC connections, providing opportunity to stream music via Bluetooth and play it from a handheld device to the table and lastly to provide LED lighting on the table during the dark hours. 3 prototypes of the system was built and tested at the Roskilde Festival 2017. Electrical logger units were built into the 3 Sun Hubs to monitor the overall energy system and the consumption of each functionality in the table.

**Keywords:** Stand-alone PV Systems

### 1 INTRODUCTION

Solar cells integrated into products are attracting more and more attention especially due to the dramatically declining cost of solar cells. Furthermore, the cost of batteries is being driven down by the increasing market for electrical cars being a major driver with e.g. Tesla investing heavily in both. Lithium based secondary batteries are now approaching prices for Lead Acid, which gives some major advantages in solar cell product design, since lighter and more compact form factors can be used without introducing a major extra costs. Moreover, Lithium battery chemistry is getting to a level where it can survive so many cycles that it in many cases don't need to be changed in in the lifetime of the product which earlier on has been one of the major disadvantages of solar products. Especially when addressing the western countries markets, where labor cost is high and battery change is often a showstopper. The recent year's development in the solar and battery market mentioned above has made major difference for the feasibility of solar powered product that will just become more and more feasible in the future.

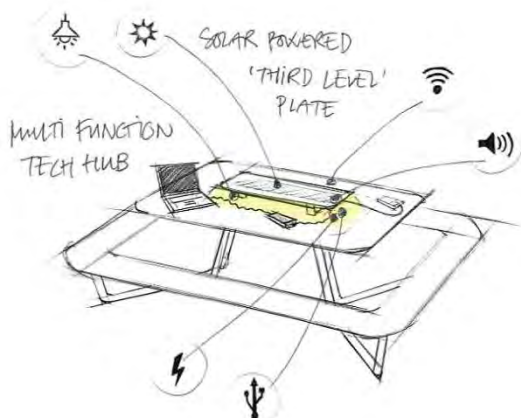


**Figure 1:** Sketch of the Sun Hub concept on top of the Plateau table produced and sold by the company outsider in Denmark.

Solar products has earlier on been more primitive,

basically powering products from the sun to save on cables which in e.g. a lighting installation in Denmark represent around the same cost as the cost of the lamp being installed. In this study we report a solar powered hub, as an add-on to a table in the urban environment for charging mobile phones and tablets and other handheld devices through USBs, charging laptops through AC connections, providing opportunity to stream music via Bluetooth and play it from a handheld device to the table and lastly to provide LED lighting on the table during the dark hours.



**Figure 2:** The Plateau table without Sun Hub

### 2 METHODOLOGY

A sketch of the Sun Hub can be seen on Figure 1. For dimensioning, some assumptions were made to both fit the dimensions of the Plateau table where the hub can be mounted as an add-on feature, and to satisfy the need for the different functions the Sun Hub makes available to the user. A mock-up was made to find the best size of the hub leaving enough space around it for working with also a relatively large laptop. 3D software models were made to extend this study virtually and an image from this process can be seen in Figure 3.

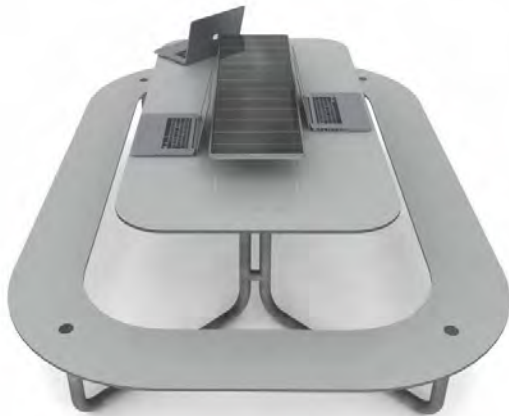


**Figure 3:** 3D drawing of the Plateau table with the Sun Hub and some different sizes of laptops.

When the best compromise between size of solar panel for energy production and space for the user to work around the hub was reached, the active components for the hub could be chosen. The major components are listed below.

- 2x 30 Wp Monocrystalline silicon panels for shade tolerance ( $V_{oc}$ : 25.65V,  $I_{sc}$ : 1.48A for each panel)
- 2x Panasonic LC-CA1212P 12V Lead Acid Battery 12Ah.
- 18 W LED flex band (3014 Sidelight SMD LED - IP 67) to be dimmed down.
- Charge regulator: GenaSun GV-5 (Lead Acid)
- 12V Inverter Hama Safety 100W
- LeaningTech 50 W 4.0 Wireless Digital Bluetooth with Audio Receiver Amplifier Board
- 4x 2.5" full range speakers
- 2x PIR motion sensors looking 180 degrees out of each of the ends.

A rendering of the Sun Hub with the above components embedded is shown below on figure 4.

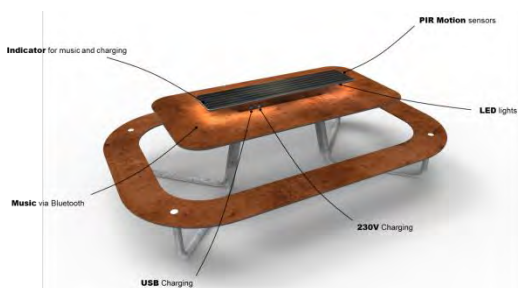


**Figure 4:** Rendering of Sun Hub with the suggested components implemented in the commercial Plateau table.

In figure 5 a diagram of the electrical components in the systems is shown schematically. Due to the limited resources in the project it was chosen to find commercial components on the market and connect them by a custom electronical driver system controlling them. More cost effective solutions would be to build the electronics into one printed circuit board which will be a task for the future.

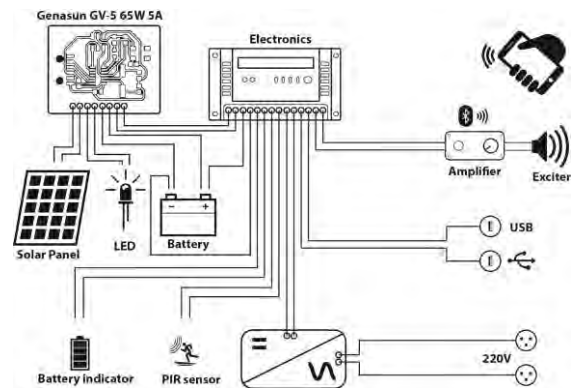


**Figure 5:** Diagram of the electrical components in the Sun Hub.

An electronic mock-up was made to test the component and especially the losses in the system. Since, as stated above, the project did not have financing for developing dedicated and optimized electronics, e.g. a low power commercial inverter needed to be used being very inefficient and having a 6W standby consumption. The charge efficiency was found to around 80% when charging close to 100W and much lower when charging at lower wattages. Also, a commercial board with Wireless Digital Bluetooth with Audio Receiver Amplifier was used having about 0.6 W standby consumption. The energy consumption while playing music was for the selected board around 3W at the maximum volume. Since the Bluetooth will be searching for a phone to pair with it was decided to turn this function on only, when PIR was activated opening a window of 10 minutes (being renewed every time PIR is activated again). So when no PIR was activated the power to the whole audio board was turned off.

The hub has 2 sockets for USB charging and 2 sockets for AC charging. The latter is sharing the 100 W inverter, so only 100W can be drawn from the 2 sockets in total. This means that very powerful laptops cannot charge at maximum rate, but will have a longer charging time which is a compromise that has to be made. A rather simple microcontroller based controller PCB was made to control the individual components and with the measured losses in the system, a mathematical model could be made. Assuming that the Sun Hub are placed in a not shadowed environment in Denmark in a typical meteorological year (TMY), an energy balance could be made (see figure 6) based on the measurements of the charge efficiencies and standby consumptions of the components.

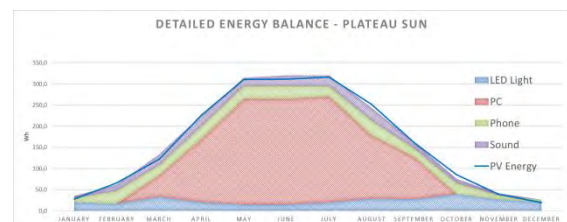


**Figure 6:** Energy balance of the functions offered by the Sun Hub.

The power consumption is very different for the different functions, and the availability is controlled by the microprocessor prioritizing:

1. USB charging
2. Streaming music
3. AC charging of laptops



**Figure 7:** Energy prioritizing for the individual functions

The microcontroller turns off the individual functionality at different programmed thresholds changing the indicator from green to red. The table always leaves energy for lighting to the night – even when all indicators are red. 3 prototypes of the Sun Hub were built and can be seen on Figure 8.



**Figure 8:** 3 prototypes of the Sun Hub.

On figure 9 it can be seen how the electronics is mounted and fitted into the hub.

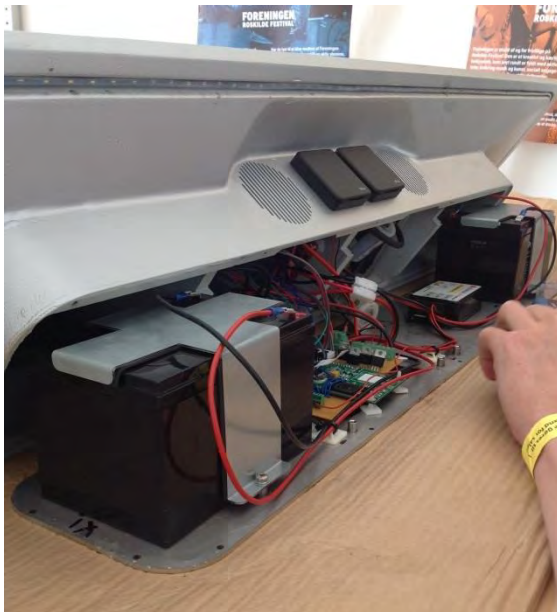


**Figure 9:** Inside look of the Sun Hub.

The 3 prototypes was field tested at the Roskilde Festival 2017. A photo can be seen on Figure 10.



**Figure 10:** Photo of field test of a Sun Hub integrated into a Plateau table at the Roskilde Festival 2017.

### 3 RESULTS AND DISCUSSION

The 3 prototype hubs were observed by a group of 6 students from the Technical University of Denmark. The aim of this was to identify if the user interfaces has been designed in an intuitive way. Furthermore an anthropology study was made to identify how the user felt about the table, its functions, its user interface etc.



**Figure 11:** A Sun Hub with LEDs turned on and all the other functions off during a rainy day at the Roskilde Festival 2017.

Some interesting observations were that many users used the 230V AC socket for charging their mobile devices. That is seen from the table a very inefficient way of using the energy since it is converted from 12V DC to 230 V

AC and back to DC by the portable unit's charger. A lot of loss will come in each conversion step, and the DC/AC inverter is very inefficient at low power consumption. A technical challenge was the high stand-by consumption of the DC/AC inverter. A magnet relay was built into the lid of the 230VAC socket to only turn on the inverter when the lid was opened (expectedly to insert a plug for charging). This magnet relay was not really working well leaving the inverter on unintentionally and draining the battery even when no charging was going on. In the software of the Sun Hubs controller electronics a threshold was made turning off the 230VAC charger and preventing this feature for being used by when the battery was under a chosen state of charge as shown on Figure 7. This saved some energy for the other functionality of the Sun Hubs. In the user survey the users was asked how they felt about not having all functionalities available at all times e.g. due to bad weather or heavy use of the table earlier in the day. The users really didn't complain as they saw it as the nature of a solar product that its services vary with the weather. This is a really important attitude of the users for securing satisfied customers to the product. The user interfaces seem to have been made successfully intuitive. The indicators of service (as shown on Figure 7) though gave rise to some confusion and some users tried to press them as a button to try to make the service available that was automatically had been disabled. The energy system was dimensioned well providing the services very similar to the calculated in the energy balance (Figure 6). The problem with the magnet switch was creating the biggest deviation from the calculations and that problem has to be solved before making it into a product.

#### 4 CONCLUSIONS

A solar powered hub for charging laptops, phones, streaming/playing music and providing light for an outdoor table was researched, developed, prototyped and tested. 3 prototypes was constructed and tested at the Roskilde Festival 2017. The energy system was dimensioned well and providing the calculated services to the user when using solar irradiation data for a TMY in Denmark end of June where the hubs was tested at the Roskilde Festival 2017. The user survey showed that people accepted that the hubs services were not always available due to bad weather (the Roskilde Festival 2017 had very few sun hours this year). The 12V DC to 230V AC inverter had very high stand-by consumption and a rather low efficiency and a good solution for only turning this on when a connection is made to the plug is still to be found.

#### 5 ACKNOWLEDGEMENTS

The work was supported by Innovation Fund Denmark under the Innobooster programme. The project was granted support for developing the Sun Hub solution in one grant and a special grant was giving to support testing it at the Roskilde Festival 2017. The Sun Hub is designed by Holscher Design, who was not a partner in the project but a very active subcontractor. The project partners will also like to thank the 6 students from the Technical University of Denmark who made the observations during the festival.



## Synchronization of Solar Stand-alone Devices and Autonomous Energy Management through Solar Time Measurements

Santamaria Lancia, Adrian Alejo; Riedel, Nicholas; Ploug, Rasmus Overgaard; Thorsteinsson, Sune; Poulsen, Peter Behrendorff; Benatto, Gisele Alves dos Reis

*Published in:*  
Proceedings of 7th World Conference on Photovoltaic Energy Conversion

*Link to article, DOI:*  
[10.1109/PVSC.2018.8548183](https://doi.org/10.1109/PVSC.2018.8548183)

*Publication date:*  
2018

*Document Version*  
Peer reviewed version

[Link back to DTU Orbit](#)

*Citation (APA):*  
Santamaria Lancia, A. A., Riedel, N., Ploug, R. O., Thorsteinsson, S., Poulsen, P. B., & Benatto, G. A. D. R. (2018). Synchronization of Solar Stand-alone Devices and Autonomous Energy Management through Solar Time Measurements. In *Proceedings of 7th World Conference on Photovoltaic Energy Conversion* (pp. 0632 - 0637). IEEE. <https://doi.org/10.1109/PVSC.2018.8548183>

---

### General rights

Copyright and moral rights for the publications made accessible in the public portal are retained by the authors and/or other copyright owners and it is a condition of accessing publications that users recognise and abide by the legal requirements associated with these rights.

- Users may download and print one copy of any publication from the public portal for the purpose of private study or research.
- You may not further distribute the material or use it for any profit-making activity or commercial gain
- You may freely distribute the URL identifying the publication in the public portal

If you believe that this document breaches copyright please contact us providing details, and we will remove access to the work immediately and investigate your claim.

# Synchronization of Solar Stand-alone Devices and Autonomous Energy Management through Solar Time Measurements

Adrián A. Santamaría Lancia<sup>1</sup>, Nicholas Riedel<sup>1</sup>, Rasmus Overgaard Ploug<sup>2</sup>, Sune Thorsteinsson<sup>1</sup>, Peter Behrendorff Poulsen<sup>1</sup>, Gisele A. dos Reis Benatto<sup>1</sup>

<sup>1</sup>Technical University of Denmark, Department of Photonics Engineering, Frederiksborgvej 399, 4000 Roskilde, Denmark. Tel: +45 46774572. E-mail: ppou@fotonik.dtu.dk

<sup>2</sup>Technical University of Denmark, Department of Electrical Engineering, Elektrovej, B325, 2800 Kgs. Lyngby, Denmark

**Abstract** — This work presents a method for synchronization of a solar device to real solar time for event triggering and energy management. Specifications require the devices to be off-grid and self-adjusting. Measurements of daylight duration were performed using one test device over the course of several months in Denmark. Analysis of viability over the accuracy of solar time determination and potential for self-adjusting energy management was carried out. Measurement results allowed for the development of an algorithm with good potential for performing the required tasks. Influence of variations in weather and different shadowing conditions were tested in two prototype devices. Results show a good potential for daily synchronization between devices and estimation of solar time within less than 5 minutes error.

## I. INTRODUCTION

One of the market possibilities for photovoltaic devices is within innovation in product development. The department of Photonic Engineering of the Technical University of Denmark (DTU) works closely with partners in the industry developing solar-powered electronic systems for diverse leisure activities and outdoor illumination products (Product Integrated PV). These products involve a small solar panel or array of solar cells used to provide energy for charging the battery and powering the application. Examples of the devices embedded in such products are bluetooth connectivity for cellphones, speakers for music playing, charging of cellphones and laptops, LED illumination, among many others.

The project, called 'Solar Clock' for short, started as a collaboration with one of our partners, in order to improve the manufacturing and distribution of one of their products. The product in question is a solar powered, LED illuminated, battery powered off-grid lamp post for outdoors installation. The power consumption of this product is adjusted to the available energy in the battery and thus the lights are dimmed according to the energy in the battery, the length of the dark period and a history based prediction of the incoming energy. A dimming scheme was incorporated within the electronics for each month of the year, and five intervals during the 24 hours of the day. As it has been manufactured so far, our partner has first to receive a purchase order from their customer to know in which location the products are to be installed and their quantity. The required PWM adjustment for energy management was determined according to some estimation of

the solar resource available on the location and each table was programmed in each product individually in factory before shipping. This process is costly and very time consuming.

To improve this situation established the requirements of the Solar Clock. A self-learning algorithm that can estimate the solar time of each day for synchronization purposes and it is able to measure the current daylight duration and make predictions for future daylight durations in order to correct in real time the energy management parameters without human intervention. Another requirement is robustness of the algorithm against shadowing/other environmental effects.

An accurate measurement of daylight duration with a photovoltaic device as a sensor would provide information about daylight duration for each day [1]. The electronic device used as control possess an oscillating clock that would measure the duration of daylight with high resolution. The duration of daylight (DD) between consecutive days can be compared and the difference in daylight duration ( $\Delta dd$ ) can be established. This could allow the algorithm to predict if the days are getting shorter or longer and adjust the energy management settings accordingly. Furthermore, the sun trajectory over the sky over the course of the year and for every location has been determined in a set of astronomical equations that can be used for accurate predictions.

## II. METHODS

The approach used in this work required thorough understanding of the sun position astronomical equations, selecting an appropriate measured variable and understanding the environmental effects that influence the measurements.

For performing this part of the study, the open circuit voltage ( $V_{oc}$ ) was measured in intervals of 10 seconds on two solar panels embedded in LED lampposts placed in our Risø outdoor PV test facilities. The solar panels are facing upwards in the sky. The lamps are named TS08 and TS09 and both are similar in specifications to the product manufactured by our partner. They include LEDs, battery and control/charge electronics.

### A. $V_{oc}$ as Measured Parameter

When a photovoltaic device is used as a sensor, normally its main goal is to measure irradiance through its short circuit

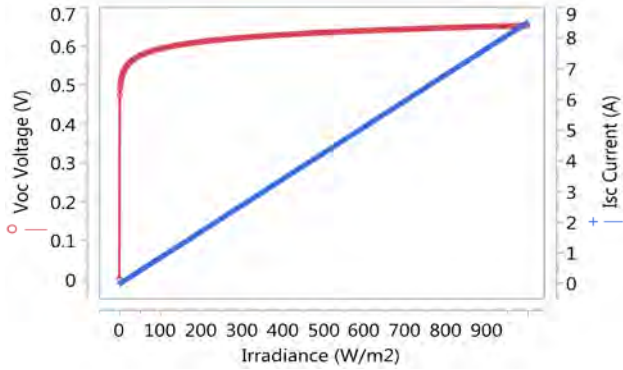


Fig. 1. Dependence of  $V_{oc}$  and  $I_{sc}$  with irradiance.

current ( $I_{sc}$ ). This is under the assumption of linearity of the device with irradiance, which is a good assumption for silicon PV devices. Irradiance during the day, however, is strongly influenced by environmental factors like clouds, shadows on the device, other illumination sources, etc. and it does not constitute a useful parameter. The  $V_{oc}$  has a logarithmic dependence with irradiance and it has been tested to provide excellent sensitivity at low irradiance values, as illustrated in Figure 1. It is able to detect sunrise and sunset diffuse light, and remain at a high, almost constant value until the irradiance level drops down significantly.

Measured values of  $V_{oc}$  are corrected for temperature using a temperature/humidity sensor located close to the lamps location.

A study about the suitability of  $V_{oc}$  as DD measurement parameter has been performed. Global Horizontal Irradiance (GHI) has been recorded simultaneously with  $V_{oc}$  measurements performed on 36 cells, multi-Si modules positioned at the same angle as the sensor. This data shows that irradiance is not always zero before sunrise or after sunset, but is observed to be as high as  $10 \text{ W/m}^2$  when the sun is below the horizon and this level of ambient light is enough to turn on the PV voltage. The mean response time of  $V_{oc}$  for these modules has been measured to be around  $13 \text{ mV/sec}$  for the turn on slope and  $-15 \text{ mV/sec}$  the turn off slope. Both  $V_{oc}$  response time and sensitivity to irradiance are more than adequate.

### B. Sun Position Studies

Out of the solar equations studied, the most important is the one that relates the Duration of Daylight (DD) with the declination ( $\delta$ ) and the latitude ( $L$ ) of the location.

$$\cos\left(\frac{\pi DD}{24}\right) = -\tan\left(\frac{\pi L}{180}\right) \times \tan\left(\frac{\pi \delta}{180}\right) \quad (1)$$

This equation and the calculations and assumptions made for the development of this algorithm are valid for latitude values between  $-65^\circ$  ( $65^\circ \text{ S}$ ) and  $+65^\circ$  ( $65^\circ \text{ N}$ ).

The declination of the earth towards the Sun is an angle whose value that changes between the values of  $-23.45^\circ$  to  $23.45^\circ$  over the course of 6 months and going back to  $-23.45^\circ$  during the remaining 6 months of the calendar year.

This is what produces the change in seasons during the year. There are four days during the calendar year that mark the beginning and end of the seasons. These are the winter and summer solstices and the autumn and spring equinoxes. The winter and summer solstices the longest and shortest daylight duration of the year respectively, and the minimum  $\Delta dd$  within neighboring days.

The characteristics of these days that are directly measurable by the voltage of a photovoltaic sensor are the Daylight Duration (DD) and the Difference in Daylight Duration between the few previous and following days ( $\Delta dd$ ). Both parameters are different in value depending on the Latitude, but follow the same pattern in all locations regarding their properties during the solstices and equinoxes.

The duration of daylight has a unique value for each day of the year and each latitude value regardless being N or S (or  $\pm L$ ). In opposite latitudes, the same daylight duration occurs in different days of the year.

If it would be possible to measure the daylight duration of a single day with an error of less than 3 minutes and 20 seconds, then the Latitude can be obtained after either one of the Solstices occur. This error value is smaller than the smallest difference of daylight duration between two consecutive latitudes (3 minutes 28 seconds at the equator).

If the Latitude of the location can be obtained, then it would be possible to predict accurate future DD values calculating them from the astronomical equation.

### C. Measurements Performed

Measurements of  $V_{oc}$  were performed on both TS08 and TS09 lamps for several months in 2017 and it is currently ongoing at the time of this manuscript writing.

Since the solar panel in both lamps are connected to the battery charger controller, the measurements values over the course of a day contain many fast and significant variations, which mainly correspond to switching of the electronic device and battery voltage levels when  $V_{batt}$  differs from  $V_{oc}$ .

In order to assess the accuracy and environmental effects over the daylight duration, the control electronics was turned off on TS08 and the panel of this device was left in permanent open circuit mode. Measurements were performed in these conditions during Denmark's winter solstice and the time of this writing. This time interval represents the minimum difference in daylight duration between consecutive days, and could provide a good test of the resolution of the device.

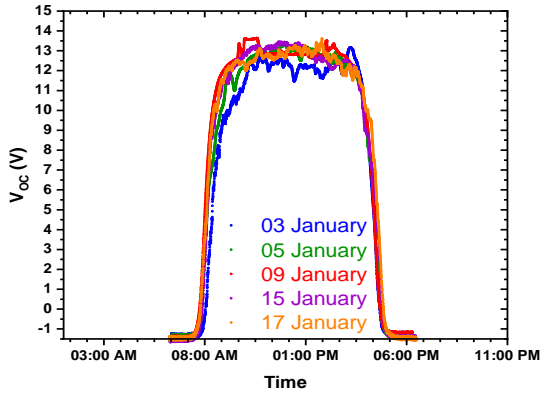


Fig. 3. Measurements of  $V_{oc}$  showing changes in daylight duration after the Winter Solstice.

As it can be observed in Fig. 2, weather conditions such as cloudiness can affect the shape of the slope and the flat zone of the  $V_{oc}$  measurement. Measurements performed in different days would either yield a smoother slope or a more irregular one. During these days, the daylight duration calculation can deviate significantly from the theoretical one, and the previously measured ones. These could be marked as outliers when determining sunset/sunrise times.

A proper selection of threshold voltage values to generate the detection of a sunrise and sunset event is also very important parameter that can affect the daylight duration measurements and were studied with new devices deployed in our campus at Risø.

#### D. Sunset and Sunrise point determination

The rise/decrement slope of  $V_{oc}$  has a duration over time that can take close to 25 minutes to rise from 0 V to 60 % of  $V_{oc}$ . Afterwards, the curve begins to stabilize to the  $V_{oc}$  maximum value. For the algorithm to work, it must be able to select a point of the curve every day for both sunset and sunrise slopes, in which the day duration interval is consistent when comparing the days with each other. One method was developed, in which 5 points of each slope were measured and a median value was taken to mark the sunset (or sunrise) point.

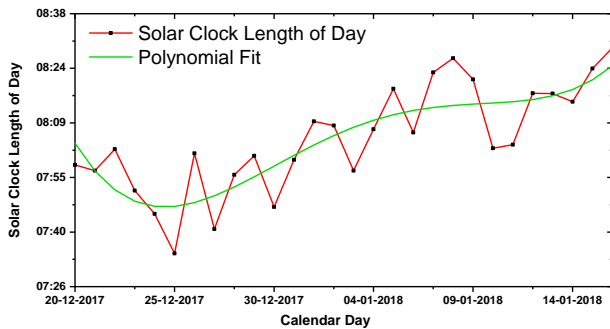


Fig. 2. Measurements of daylight duration for 10 consecutive days and polynomial fit. Improvement can be made removing outliers.

The values of DD calculated with this method were compared between consecutive days and it is shown in Fig. 3.

It can be seen that the dispersion between individual daylight durations is significant and can reach differences beyond 25 minutes in certain cases. However, they do follow the tendency of increasing in value after the winter solstice, which correspond with the daylight hours increasing by each passing day towards the summer.

#### E. Daylight Duration Measurement under Different Environmental Conditions.

Three measurement devices were constructed to evaluate the performance of the daylight duration measurement under different environmental conditions. Each device consisted of a photovoltaic 3 Volts DC, 250mA PV mini-module, a Texas Instrument programming board for an MSP432P401 microcontroller and a battery pack to power the board under stand-alone conditions. All the electronics were enclosed in a weather resistant box with the solar panel attached facing up on the top cover. The battery pack allowed for an autonomy of only 4 days of measurement, due to the consumption of the JTAG programming interface of the board, which also provides regulated 3.3 V to the microcontroller. Disabling this part of the board would have produced substantial consumption drop, however it was not possible to do this in a practical way. Measurements were performed in sets of 4 days and the data downloaded and analyzed in between.

The microcontroller was programmed to log the  $V_{oc}$  of the photovoltaic panel and determine the daylight duration when the voltage level passed certain threshold value. Two threshold values of 1.0 V and 1.5 V were tested. Both levels were implemented with a 0.2 V hysteresis for 300 seconds period. This means that for the 1 V threshold, the behavior of the device from day to night is that it initialize counting the 300 seconds when PV voltage is beneath 0.9 V and it continues the counting as long as the PV voltage is beneath 1.1V. When the 300 seconds have passed it declares shift from day to night. The same process is repeated from night to day. Daylight Duration measurement for both levels were recorded.

Due to malfunction of Device 2, only two devices were deployed in three different locations. Device 1 was placed on top of the Fotonik building in Risø (where the Weather Station sensors that monitor irradiance conditions are installed, abbreviated WSt). This location has a completely unobstructed exposure to sunlight. Device 3 was placed against the wall of a neighbor building. The wall is facing West, and the device is completely under the shadow until the late afternoon (West Facade, abbreviated WFc). The Sunrise moment detected by this device will be due to diffuse light only. Finally, Device 3 was placed against a north oriented wall, having no exposure to direct light (Total Shadow, abbreviated TSw). Both sunrise and sunset points will be detected by diffuse light.

Device 1 and Device 3 were placed next to each other under unobstructed sunlight to compare their measurements under same conditions. The measurements in Daylight Duration of

both devices had consistently a difference of 12 minutes maximum (Device 1 measures longer DD than Device 3). This is also true for both threshold levels. The cause for this particular difference is under study.

### III. ANALYSIS

The resolution and inaccuracy of the photovoltaic device acting as a sensor, plus all environmental factors affecting the measurement of the daylight duration does not allow to obtain daylight duration values directly comparable in resolution with the calculated ones from the equations for every single day.

#### A. Weather Dependence and Threshold Voltage Values

For assessing the influence of weather conditions on the DD measurements, the measured values from Weather Station (Device 1) were compared to the ones obtained for each day of the year through astronomical equations, at the latitude of our Risø campus in Denmark (55.64 N approx.) as shown below.

TABLE I

Calculated values for the interval of days under study using Equation 1.

Day	Calculated Daylight Duration (Hours)	Calculated Daylight Duration (Minutes)	Calculated $\Delta$ dd (Minutes)
20-Apr-18	14.25	854.8	4.51
21-Apr-18	14.32	859.3	4.49
22-Apr-18	14.40	863.8	4.47
04-May-18	15.26	915.5	4.15
05-May-18	15.33	919.6	4.11
06-May-18	15.39	923.7	4.08
10-May-18	15.66	939.6	3.91
11-May-18	15.72	943.4	3.86
12-May-18	15.79	947.3	3.81

TABLE II

Measured values of Daylight Duration. Device 1 is located in Weather Station and Device 3 in West Façade. Threshold values comparison from Device 1.

Day	Weather Conditions	Weather Station vs. Calculated (Minutes)	West Façade vs. Calculated (Minutes)	Weather Station vs. West Façade (Minutes)	Threshold 1.0 V - 1.5 V (Minutes)
20-Apr-18	All day very sunny	57.6	38.5	19.0	16.3
21-Apr-18	All day very sunny	61.8	43.2	18.6	15.8
22-Apr-18	All day very sunny	60.0	40.4	19.6	14.7
04-May-18	Cloudy morning, sunny	65.9	45.3	20.6	16.7
05-May-18	Sunny with few clouds	67.7	47.2	20.5	16.0
06-May-18	All day very sunny	67.8	46.6	21.2	16.7
10-May-18	Very sunny, rain in evening	33.8	14.3	N/M	16.1
11-May-18	Cloudy, covered sky	44.0	2.1	N/M	26.1
12-May-18	Partially Sunny and cloudy	54.3	18.1	N/M	21.0

Under sunny conditions, the difference in DD ranges between 57 and 68 minutes with a 63.5 average. Cloudy and sky covered days produce shorter DD durations, due to the irregularities of the voltage slope as shown in Figures 4 and 5. Difference between calculated and measured DD values decreased 20 and 30 minutes and were closer to the calculated ones than the sunny days. Moreover, they are caused by a single slope being distorted by cloudiness (morning or evening, but not both at the same time). The measurements produced under these circumstances are not a reliable measurement of daily daylight duration.

TS08 Daylight Duration Measurements (19 of April to 22 of April) at Risø

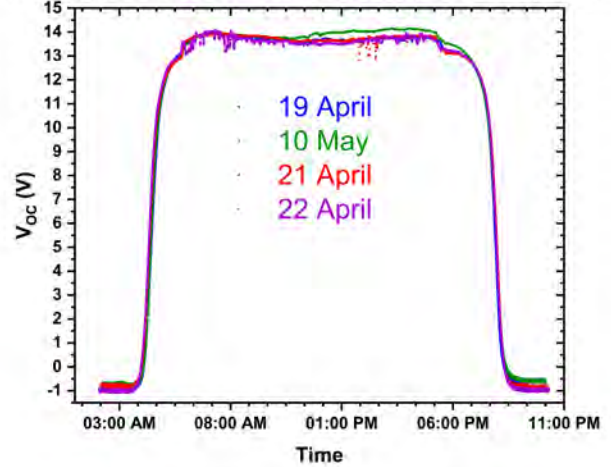


Fig. 4: Daylight Duration measurements on very sunny days. Voltage slope is smooth under clear sky conditions.

TS08 Daylight Duration Measurements (09 of May to 13 of May) at Risø

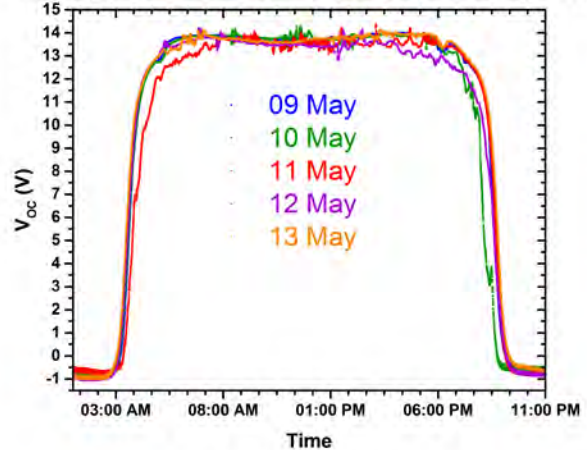


Fig. 5: Daylight Duration measurements showing the effect of cloud sky in the voltage slope for the morning (11 of May) and late afternoon (10 of May and 12 of May). These weather effects produce an erroneously shorter DD.

Design of an appropriate threshold level has also influence on how close the measured values are to the calculated ones. Figure 6 shows the TS08 voltage curve and calculated Solar Elevation Angle for 22<sup>th</sup> of April and at the Risø campus location. The voltage slopes are produced with enough intensity

of diffuse light in the sky, since at these times the sun is still below the horizon.

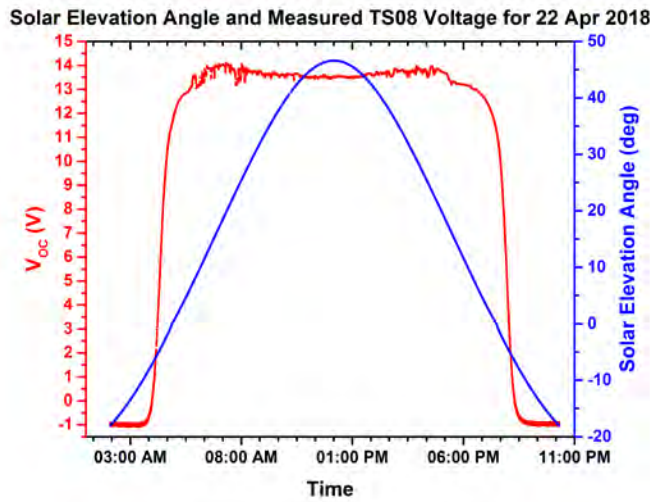


Fig. 6: Daylight Duration measured and calculated Solar Elevation Angle for Risø site. The voltage slopes occur when the sun has less than  $-5^\circ$  elevation angle (it is below the horizon). The presence of diffuse light alone produces the desired voltage increment. The voltage threshold selection is a relevant parameter for comparison against calculated values.

For the Devices, the higher threshold value of 1.5 V produced DD values 14 to 17 minutes closer to calculated ones than the 1.0 V level under sunny conditions, though this cannot be taken as direct correlation. Further threshold levels should be tested to evaluate if better match to calculated values degrades or improve DD measurement performance due to other effects.

### B. Environmental Shadow Conditions

Synchronization of the devices exposed under different conditions of light shadowing is an important parameter to be assessed from the industry point of view. Several devices placed inside the same location but under different light obstruction situations (trees, buildings, neighbor light sources) should be able execute the programmed tasks (e.g. switch on LEDs) at the same time or as close as possible. Some minutes delay between devices is acceptable for outdoors lightning.

Measured Daylight Duration (DD) was compared between Weather Station and the other two locations. It was shown that roughly 22 minutes difference exists with West Facade location under sunny conditions. The DD is measured to be shorter when the device loses exposure to direct incident light in the mornings.

A similar difference of 20 minutes was measured with the Total Shadow location under sunny days. However, on more cloudy days DD differences of a maximum of 42 minutes were measured in comparison with WSt values. This suggest that changes in weather conditions may increase even more the

differences in measurements between devices under various shadow conditions.

### C. Effects on Devices Synchronization

An estimation of the daily synchronization delay between devices should be considered to verify it is in acceptable range. The sources of deviations and the magnitude of their contributions have been evaluated. Measurement performed on the day  $n-1$  is used to determine the new 24-hour time duration for the current  $n$  day. This 24-hour interval is calculated as the summation of the DD measured on the previous  $n-1$  day and the night duration (ND) until the next sunrise detected on the  $n^{\text{th}}$  day. Midday and midnight are calculated as half the measured  $DD_{n-1}$  and  $ND_{n-1}$  values, and are established as zero points to which reference the amount of hours to trigger events. Comparison between the measured solar and the internal oscillation clock 24-hour intervals, allows obtaining daylight duration increment or decrement ( $\Delta dd$ ) for energy management and periodical internal synchronization adjustments.

In between consecutive days, the event triggering time will vary due to all effects studied in the  $DD_{n-1}$  measurement. An event expected to be triggered at 18 hours solar time every day, will occur within a certain amount of minutes before or after, which will be different each day and per device.

Results from this study allow us to do some estimations about the total error per day that can be introduced. A worst-case scenario would be one with a very cloudy sky at sunset time on the day  $n-1$ , and very cloudy sky at sunrise time on the day  $n$ . These atmospheric effects make for an artificially shorter daylight duration, and their occurrence simultaneously would result in an inaccurately longer night duration. Assuming a detected sunrise 25 minutes later than in a sunny day (earlier for sunset), a total error in the 24-hour interval due to cloudiness only would be around 50 minutes.

As per the differences in DD between devices at the same position, which was found to be maximum 12 minutes, a conservative total of 20 minutes is assumed since only two devices were tested in this experiment and it cannot be taken as a maximum delay value at the moment.

Two devices under different shadow conditions could be expected to have an additional difference in DD measurement between 15 and 25 minutes.

These estimations and assumptions combined would introduce a total of 70 minutes increment between previous and current day calculation of the 24 hour interval, and a total of 45 minutes for devices under different shadowing conditions on the same day. This will introduce an error in event triggering time between consecutive days of almost 3 minutes, and between devices in the same day and weather conditions, the delay would be no more than 2 minutes. For our partner's purpose of synchronization or triggering of events regarding

illumination in urban areas, this resolution for time measurement is acceptable.

#### D. Energy Management

Determination of  $\Delta d$  to assess the amount of solar resource and predict future values is also possible. Day by day comparison yields unreliable information on whether DD is bigger or smaller than the previous day, but it does follow the season trend in intervals of a number of days. The number of days for each segment were chosen as 10 and measurements of DD for each of the days can be carried out. After the interval acquisition is finished, a polynomial fit is used to have an estimated interval total difference in daylight duration ( $\Delta dN^k$ ) as shown in Figure 3. For the predicted difference in day duration for the next interval to be measured ( $p_{\Delta d10^k}$ ), a look-up table is used. This table will contain DD values for 10 days intervals during the year, and for each Latitude in steps of  $1^\circ$ . The algorithm will find the DD value closest to the fitted one obtained, and relate it to the Latitude. Then, the value from the table corresponding to the same latitude  $L$ , but next interval of the year  $k+1$  will be selected. This value will be used in energy management to predict how much solar resource will be available, how long the night will be, and adjust the PWM for the LED

#### IV. CONCLUSIONS

In this work, the effect of diverse weather and environmental conditions over the determination of duration of daylight have

been studied. Despite the significant variations in measurements of daylight duration between devices in different locations, it is possible to estimate solar time for each day and implement synchronized events with an acceptable margin of error. This study suggest synchronization issues between devices and event triggering time in worst cases studied can amount to maximum 5 minutes. Future work should focus on obtaining more days of DD measurement to further validate these findings, and obtain more evidence of the correlation between the irregularities on the acquired curve and weather conditions. This can be achieved through the calculation of a diffuse ratio obtained from the weather station measurements. Prediction of solar resource and adjustment of energy management are also possible using intervals of few days. Additionally to the polynomial fit approach being considered to minimize the propagation of errors in the calculation of  $\Delta dN^k$ , another possibility is to have part of the algorithm to analyze the shape of the  $V_{oc}$  curve and slopes produced during sunny days and cloudy days to determine outliers or produce an estimation of a true value. With further development aimed to increase understanding of environmental effects and reduce uncertainties, synchronization of stand-alone, self-adjusting photovoltaic devices to real solar time for event triggering and energy management shows great potential.

#### REFERENCES

- [1] Simeon Lisovski, Chris M. Hewson, Raymond H. G. Klaassen, Fränzi Korner-Nievergelt, Mikkel W. Kristensen and Steffen Hahn, "Geolocation by light: accuracy and precision affected by environmental factors," *Methods in Ecology and Evolution* 2012, 3, 603–61